

PL-TR-91-2070

AD-A241 938

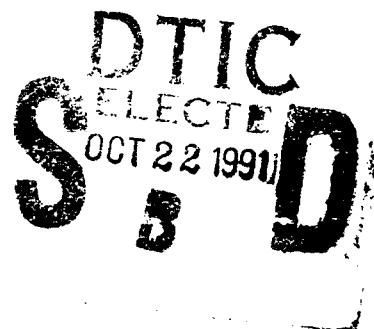


2

**STUDIES OF HIGH-FREQUENCY SEISMIC
WAVE PROPAGATION**

Jean-Bernard Minster
Jonathan Berger

University of California, San Diego
Institute of Geophysics and Planetary Physics
Scripps Institution of Oceanography
La Jolla, CA 92093-0225



29 March, 1991

Final Report
17 October 1988-17 May 1991

APPROVED FOR PUBLIC RELEASE; DISTRIBUTION UNLIMITED

91-13650



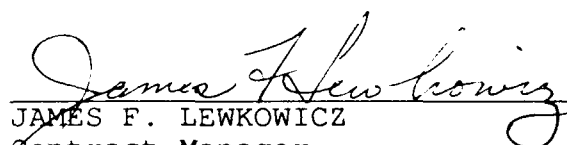
PHILLIPS LABORATORY
AIR FORCE SYSTEMS COMMAND
HANSCOM AIR FORCE BASE, MASSACHUSETTS 01731-5000

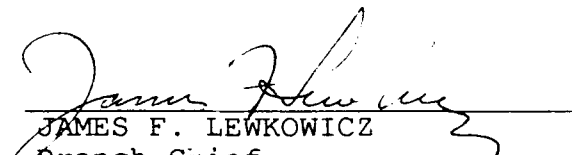
SPONSORED BY
Defense Advanced Research Projects Agency
Nuclear Monitoring Research Office
ARPA ORDER NO. 5299

MONITORED BY
Phillips Laboratory
Contract F19628-88-K-0044

The views and conclusions contained in this document are those of the authors and should not be interpreted as representing the official policies, either expressed or implied, of the Defense Advanced Research Projects Agency or the U.S. Government.

This technical report has been reviewed and is approved for publication.


JAMES F. LEWKOWICZ
Contract Manager
Solid Earth Geophysics Branch
Earth Sciences Division


JAMES F. LEWKOWICZ
Branch Chief
Solid Earth Geophysics Branch
Earth Sciences Division


DONALD H. ECKHARDT, Director
Earth Sciences Division

This report has been reviewed by the ESD Public Affairs Office (PA) and is releasable to the National Technical Information Service (NTIS).

Qualified requestors may obtain additional copies from the Defense Technical Information Center. All others should apply to the National Technical Information Service.

If your address has changed, or if you wish to be removed from the mailing list, or if the addressee is no longer employed by your organization, please notify PL/IMA, Hanscom AFB, MA 01731-5000. This will assist us in maintaining a current mailing list.

Do not return copies of this report unless contractual obligations or notices on a specific document requires that it be returned.

REPORT DOCUMENTATION PAGE			Form Approved OMB No. 0704-0188	
<small>Public reporting burden for this collection of information is estimated to average 1 hour per response, including the time for reviewing instructions, searching existing data sources, gathering and maintaining the data needed, and completing and reviewing the collection of information. Send comments regarding this burden estimate or any other aspect of this collection of information, including suggestions for reducing this burden, to Washington Headquarters Services, Directorate for Information Operations and Reports, 1215 Jefferson Davis Highway, Suite 1204, Arlington, VA 22202-4302, and to the Office of Management and Budget, Paperwork Reduction Project (0704-0188), Washington, DC 20503.</small>				
1. AGENCY USE ONLY (Leave blank)		2. REPORT DATE March 29, 1991		3. REPORT TYPE AND DATES COVERED Final/ 17 Oct. 1988 - 17 May. 1991
4. TITLE AND SUBTITLE Studies of High-Frequency Seismic Wave Propagation			5. FUNDING NUMBERS PR 8A10 TA DA WU AU Contract F19628-88K-0044	
6. AUTHOR(S) Jean-Bernard Minster Jonathan Berger				
7. PERFORMING ORGANIZATION NAME(S) AND ADDRESS(ES) University of California, San Diego SIO/IGPP 0225 8604 La Jolla Shores Dr. La Jolla, CA 92093			8. PERFORMING ORGANIZATION REPORT NUMBER	
9. SPONSORING MONITORING AGENCY NAME(S) AND ADDRESS(ES) Darpa/NMRO 3701 N. Fairfax Dr. #717 Arlington, VA 22203-1714 Phillips Laboratory Hanscom AFB, MA 01731 Contract Manager: J.Lewkowicz/LWH			10. SPONSORING MONITORING AGENCY REPORT NUMBER PL-TR-91-2070	
11. SUPPLEMENTARY NOTES				
12a. DISTRIBUTION AVAILABILITY STATEMENT Approved for public release; distribution unlimited.			12b. DISTRIBUTION CODE	
13. ABSTRACT (Maximum 200 words) <p>This final report summarizes published research conducted over the past 30 months at IGPP on high-frequency seismic waves. Our objectives were (1) to improve our understanding of the high-frequency seismic properties of the crust and upper mantle, with special attention of the eastern Kazakh region of the Soviet Union, (2) to address seismological issues raised in the context of nuclear test monitoring by seismic means, including the use of high-frequency array data, and (3) to investigate the characteristics of very high frequency waves (>20 Hz) and to validate the results by comparison with well-understood areas, such as Anza, California.</p> <p>This final report contains the results of seven studies supported by this contract, which have been accepted for publication in refereed journals. They are:</p> <ol style="list-style-type: none"> 1. A study of the location of regional seismic events using a sparse network, with an application to eastern Kazakhstan [Thurber <i>et al.</i>, 1989] 2. An analysis of high frequency seismic observations collected in eastern Kazakhstan, including in particular calibration chemical explosions [Given <i>et al.</i>, 1990]. 3. A study of the discrimination of quarry blasts from single explosions, using sonogram analysis of data collected in eastern Kazakhstan [Hedlin <i>et al.</i>, 1989] <p style="text-align: right;">(over)</p>				
14. SUBJECT TERMS Discrimination, quarry blasts, Anisotropy, High-frequency Waves, Kazakhstan			15. NUMBER OF PAGES 196	
			16. PRICE CODE	
17. SECURITY CLASSIFICATION OF REPORT Unclassified	18. SECURITY CLASSIFICATION OF THIS PAGE Unclassified	19. SECURITY CLASSIFICATION OF ABSTRACT Unclassified	20. LIMITATION OF ABSTRACT UL	

ABSTRACT (continued)

4. The extension of the discrimination methodology developed in the previous paper to small aperture array data, and application to the automated discrimination between earthquake and quarry blasts at NORESS [Hedlin *et al.*, 1990]
5. The use of a new technique, labelled "beam-stack imaging", to map shallow crust scatterers near a small aperture array, with applications to NORESS [Hedlin *et al.*, 1991]
6. A study of the polarization characteristics of high-frequency borehole seismograms recorded near Anza, California, [Aster and Shearer, 1991a]
7. An analysis of attenuation and site effects on high-frequency seismic waves, using high-frequency borehole seismograms recorded in the San Jacinto fault zone, near Anza, California, [Aster and Shearer, 1991b]

References:

- Aster, R. and P. Shearer, High-Frequency Borehole Seismograms Recorded in the San Jacinto Fault Zone, Southern California Part 1: Polarizations. In press, *Bull. Seismol. Soc. Amer.*, 1991a.
- Aster, R. and P. Shearer, High-Frequency Borehole Seismograms Recorded in the San Jacinto Fault Zone, Southern California Part 2: Attenuation and Site Effects. In press, *Bull. Seismol. Soc. Amer.*, 1991b.
- Given, H., Tarasov, N.T., Zhuravlev, V., Vernon, F.L., Berger, J., and I.L. Nersesov, High-frequency seismic observations in eastern Kazakhstan, USSR, with emphasis on chemical explosion experiments. *J. Geophys. Res.*, **95**, 295-307, 1990.
- Hedlin, M., J.B. Minster, and J.A. Orcutt, The time-frequency characteristics of quarry blasts and calibration explosions recorded in Kazakhstan, USSR, *Geophys. J. Int.*, **99**, 109-121, 1989.
- Hedlin, M., J.B. Minster, and J.A. Orcutt, An automatic means to discriminate between earthquakes and quarry blasts, *Bull. Seismol. Soc. Amer.*, **80**, 2143-2160, 1990.
- Hedlin, M.A.H., J. B. Minster and J. A. Orcutt, Beam-stack imaging using a small aperture array. In press, *Geophys. Res. Lett.*, 1991.
- Thurber, C. H. Given and J. Berger, Regional seismic event location with a sparse network: Application to eastern Kazakhstan, USSR, *J. Geophys. Res.*, **94**, 17,767-17,780, 1989.

Accession For	
NTIS GRA&I	<input checked="" type="checkbox"/>
DTIC TAB	<input type="checkbox"/>
Unannounced	<input type="checkbox"/>
Justification	
By	
Distribution/	
Availability Codes	
Dist	Avail and/or Special
A-1	



Summary

This final report summarizes published research conducted over the past 30 months at IGPP on high-frequency seismic waves. Our objectives were (1) to improve our understanding of the high-frequency seismic properties of the crust and upper mantle, with special attention of the eastern Kazakh region of the Soviet Union, (2) to address seismological issues raised in the context of nuclear test monitoring by seismic means, including the use of high-frequency array data, and (3) to investigate the characteristics of very high frequency waves (>20 Hz) and to validate the results by comparison with well-understood areas, such as Anza, California.

This final report contains the results of seven studies supported by this contract, which have been accepted for publication in refereed journals. They are:

1. A study of the location of regional seismic events using a sparse network, with an application to eastern Kazakhstan [Thurber *et al.*, 1989]
2. An analysis of high frequency seismic observations collected in eastern Kazakhstan, including in particular calibration chemical explosions [Given *et al.*, 1990].
3. A study of the discrimination of quarry blasts from single explosions, using sonogram analysis of data collected in eastern Kazakhstan [Hedlin *et al.*, 1989]
4. The extension of the discrimination methodology developed in the previous paper to small aperture array data, and application to the automated discrimination between earthquake and quarry blasts at NORESS [Hedlin *et al.*, 1990]
5. The use of of a new technique, labelled "beam-stack imaging", to map shallow crust scatterers near a small aperture array, with applications to NORESS [Hedlin *et al.*, 1991]
6. A study of the polarization characteristics of high-frequency borehole seismograms recorded near Anza, California, [Aster and Shearer, 1991a]
7. An analysis of attenuation and site effects on high-frequency seismic waves, using high-frequency borehole seismograms recorded in the San Jacinto fault zone, near Anza, California, [Aster and Shearer, 1991b]

References:

- Aster, B. and P. Shearer, High-Frequency Borehole Seismograms Recorded in the San Jacinto Fault Zone, Southern California Part 1: Polarizations. In press, *Bull. Seismol. Soc. Amer.*, 1991a.

- Aster, R. and P. Shearer, High-Frequency Borehole Seismograms Recorded in the San Jacinto Fault Zone, Southern California Part 2: Attenuation and Site Effects. In press, *Bull. Seismol. Soc. Amer.*, 1991b.
- Given, H., Tarasov, N.T., Zhuravlev, V., Vernon, F.L., Berger, J., and I.L. Nersesov, High-frequency seismic observations in eastern Kazakhstan, USSR, with emphasis on chemical explosion experiments, *J. Geophys. Res.*, **95**, 295-307, 1990.
- Hedlin, M., J.B. Minster, and J.A. Orcutt, The time-frequency characteristics of quarry blasts and calibration explosions recorded in Kazakhstan, USSR, *Geophys. J. Int.*, **99**, 109-121, 1989.
- Hedlin, M., J.B. Minster, and J.A. Orcutt, An automatic means to discriminate between earthquakes and quarry blasts, *Bull. Seismol. Soc. Amer.*, **80**, 2143-2160, 1990.
- Hedlin, M.A.H., J. B. Minster and J. A. Orcutt, Beam-stack imaging using a small aperture array,. In press, *Geophys. Res. Lett.*, 1991.
- Thurber, C. H. Given and J. Berger, Regional seismic event location with a sparse network: Application to eastern Kazakhstan, USSR, *J. Geophys. Res.*, **94**, 17,767-17,780, 1989.

TABLE OF CONTENTS

	Page
Regional seismic event location with a sparse network: Application to eastern Kazakhstan	1
High-frequency seismic observations in eastern Kazakhstan, USSR, with emphasis on chemical explosion experiments	15
The time-frequency characteristics of quarry blasts and calibration explosions recorded in Kazakhstan, USSR	28
An automatic means to discriminate between earthquakes and quarry blasts	41
Beam-stack imaging using a small aperture array	74
High-Frequency Borehole Seismograms Recorded in the San Jacinto Fault Zone, Southern California Part 1: Polarizations	87
High-Frequency Borehole Seismograms Recorded in the San Jacinto Fault Zone, Southern California Part 2: Attenuation and Site Effects	134

Regional Seismic Event Location With a Sparse Network: Application to Eastern Kazakhstan, USSR

C. THURBER¹

Department of Earth and Space Sciences, State University of New York at Stony Brook

H. GIVEN AND J. BERGER

Institute of Geophysics and Planetary Physics, Scripps Institution of Oceanography, University of California, San Diego, La Jolla

Three-component data from a sparse three-station seismic network in eastern Kazakhstan, surrounding the Soviet nuclear test site, have been analyzed to determine location estimates for regional events recorded by two or three stations. Included among these events are the September 1987 chemical explosions whose locations are known. Locations are calculated using arrival times of *P* and *S* phases and arrival azimuths from first *P*. Location uncertainties are estimated using a combination of a priori and a posteriori data uncertainties. A layered *P* wave velocity model adapted from Soviet Deep Seismic Sounding surveys is employed for calculating travel times, and two *S* models are tried. Location results for the chemical explosions are excellent, even if only two stations are used: absolute location errors are less than 10 km, and estimated 90% confidence uncertainties are only a few kilometers. The data are also adequate to determine correctly their depth (i.e., focus at the surface). The other regional events include numerous suspected mine blasts and two earthquakes from the Tien Shan. The calculated locations of the latter events agree well with a teleseismic location for one of them, falling within a belt of regular seismic activity. Nearly all of the presumed blasts can be associated with mapped mines, and we have been able to identify the source areas for two sets of blasts in high-resolution satellite images. "Before and after" photographs allow us to identify specific active mines. Our location estimates agree quite well with the observed active mines.

INTRODUCTION

Through an agreement between the National Resources Defense Council, Incorporated (NRDC) and the Academy of Sciences of the USSR a three-station seismic network was established in the spring of 1987 in eastern Kazakhstan in the Soviet Union (Figure 1) to collect data relevant to seismic monitoring of nuclear weapons tests [Berger *et al.*, 1987]. Each station site consists of several sets of three-component instruments, including surface and borehole sensors, recorded digitally at 250 samples per second using a triggered system [Berger *et al.*, 1988]. The network recorded numerous seismic events during its operation, including local, regional, and teleseismic events.

One fundamental capability required for treaty verification purposes is the ability to determine reliably the location of regional events (explosions and earthquakes) detected by the network. Due to the sparseness of the NRDC network, however, most regional events do not trigger all three stations. Thus standard earthquake location algorithms that use seismic wave arrival times only cannot be expected to yield satisfactory results. A treaty verification network would likely face this same difficulty. Several recent papers have discussed regional event location using single three-component stations or regional arrays [Magoira *et al.*, 1987; Ruid *et al.*, 1988; Bratt and Bache, 1988].

Our primary objective is to demonstrate the capability of a sparse network of three-component stations to locate re-

gional events even when as few as two stations record a given event. From the catalog of event triggers from the NRDC network we have identified a suite of 20 regional events recorded by at least two stations for analysis. These events occurred between May and September 1987. Included among them are the three chemical explosions detonated in September 1987 as part of the cooperative NRDC-Soviet Academy program [Eissler *et al.*, 1987] (Figure 1). The explosions provide especially valuable data because of their known locations and origin times. They allow us to assess the location method that we use and provide some indication of the precision and accuracy of event location that we can expect in general. Most of the other events are presumed to be mining or quarrying explosions occurring within a few hundred kilometers of the network. Note that network stations were shut down during periods of nuclear testing at the Kazakhstan Test Site as part of the operational agreement.

The event locations are determined from arrival times and azimuths of seismic phases, using the location algorithm TTAZLOC developed by Bratt and Bache [1988]. The azimuthal information is quite valuable for improving the location estimates, particularly for two-station locations. We find that we can typically locate regional events that have occurred within several hundred kilometers of the network with estimated epicentral uncertainties of only about 5-10 km, even with data from only two stations. In most cases the event locations fall in areas of known mining activity. Note that the "true" location errors are known only for the three chemical explosions.

First, we will describe the elements of our location procedure, including some aspects of the location algorithm, the crustal models used, and the techniques for estimating

¹Now at Department of Geology and Geophysics, University of Wisconsin-Madison.

Copyright 1989 by the American Geophysical Union.

Paper number 89JB01540.

0148-0227/89/89JB-01540\$05.00

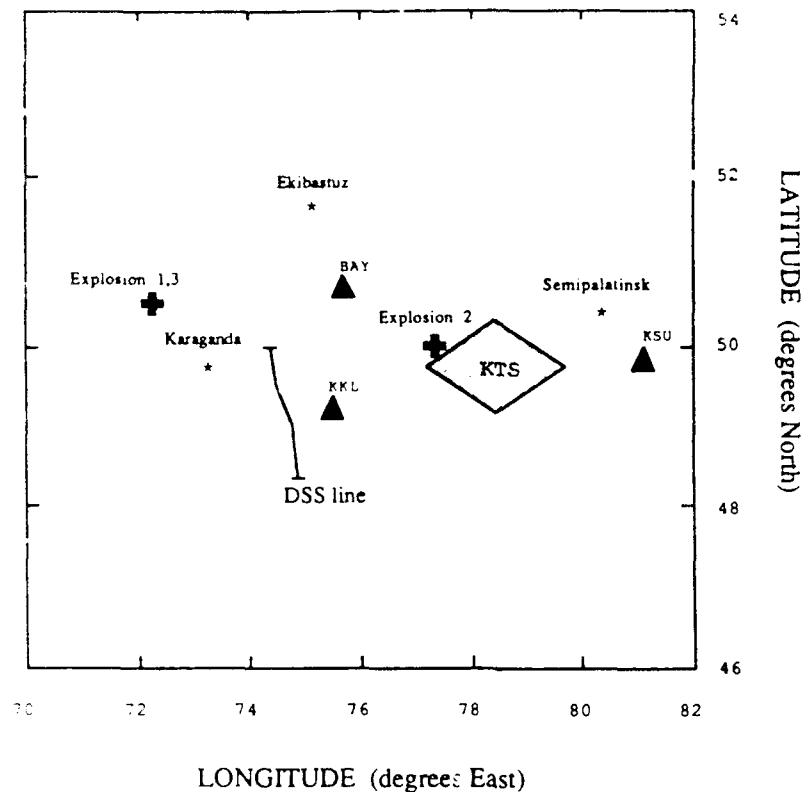


Fig. 1. Configuration of the NRDC-Soviet Academy seismic network, located near the Kazakhstan Test Site (KTS) on the steppes of Central Asia. Stations BAY, KKL, and KSU are indicated by the solid triangles. Also shown are the sites of the September 1987 chemical explosions (crosses) and the location of a deep seismic sounding profile (DSS).

azimuth of phase arrival. Then the chemical explosion data will be examined in some detail, as they furnish critical tests for our location method and provide useful information regarding the appropriateness of the velocity models. Finally, the results for the remainder of the regional events are presented, including assessment of the accuracy of the location estimates for events with independently determined locations. Sources of these independent locations are direct observation, earthquake catalogs, and satellite photos.

LOCATION PROCEDURE

The standard earthquake location method iteratively solves a matrix equation relating hypocenter adjustments to arrival time residuals via the Jacobian matrix, which consists of the partial derivatives of arrival time with respect to the event coordinates and origin time [Lee and Stewart, 1981; Thurber, 1986] with the iterations stopping when some convergence criterion is reached. Arrival azimuth information can be incorporated as additional information for determining the location by adding azimuth residuals to the residual vector and the corresponding rows of partial derivatives to the Jacobian matrix [Bratt and Bache, 1988]. The partial derivatives for azimuth are derived directly from the source-receiver geometry. Both the event depth and origin time are independent of the azimuth. In the algorithm TTAZLOC [Bratt and Bache, 1988] the final solution is obtained using iterative damped least squares. The estimate of location uncertainty is derived using a combination of a priori and a posteriori data uncertainties [Jordan and Sverdrup, 1981]. The a priori uncertainty can incorporate esti-

mated uncertainties due to measurement error and inexact knowledge of velocity structure [Bratt and Bache, 1988; Pavlis, 1986]. In this initial investigation we use the estimated uncertainties in arrival time reading and arrival azimuth determination for the a priori values. The former typically are 0.25 s for *P* and 0.5 s for *S* arrivals, based on subjective estimation of reading quality, while the latter are of the order of 5°, based on the standard deviation of the computed arrival azimuth within the selected window. We also assume a value for the Bayesian parameter *K* of 8 [Jordan and Sverdrup, 1981]. A value for *K* of 8 assigns 8 degrees of freedom to the a priori uncertainty and implies an expected standard deviation of the a posteriori uncertainty of 25% [Jordan and Sverdrup, 1981]. Note that in the discussion and tables all error ellipses will be represented by the major axes of the 90% confidence ellipses. For additional details on the location algorithm and underlying theory, refer to Bratt and Bache [1988] and Jordan and Sverdrup [1981].

A crustal model is required to compute travel times of the various phases. Fortunately, Soviet deep seismic sounding (DSS) surveys have been carried out in the region, including one line just to the west of Karkaralinsk (Figure 1), yielding estimates of crust and upper mantle *P* velocities and crustal thickness. Results from these profiles are summarized by Belyaevsky et al. [1973], Antonenko [1984], and Leith [1987]. Crustal thickness varies between about 45 and 55 km in the immediate vicinity of the network [Belyaevsky et al., 1973]. We have adopted a layered approximation to the *P* wave velocity model reported by Antonenko [1984], shown in Figure 2 and Table 1, modified to account for the low-

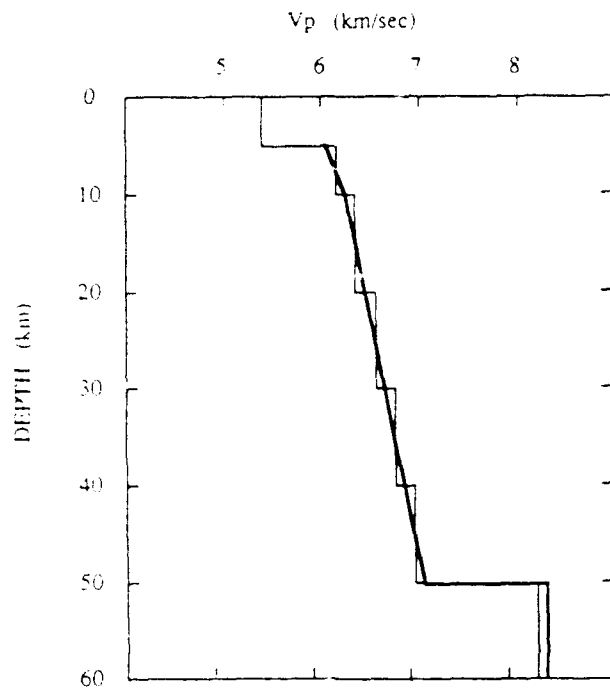


Fig. 2. Layered P wave velocity model (thin line) adapted from the results of the DSS survey (bold line) along the profile indicated in Figure 1, as summarized by Antonenko [1984].

velocity granites that underly the station sites [Leith, 1987]. The model predicts a P_n crossover distance of about 220 km.

There is little published information on the S velocity structure in the region. Priestley *et al.* [1988] carried out a preliminary teleseismic waveform inversion for records at stations BAY and KKL, using the method of Owens *et al.* [1984], deriving a layered model for the S velocity structure beneath those stations. For comparison, taking the DSS profile results and assuming a constant V_p/V_s ratio of 1.73 gives values for V_s that are consistent with the teleseismic waveform analysis of Priestley *et al.* [1988] for the upper crust but are somewhat lower than Priestley *et al.*'s for the lower crust. This is in agreement with the finding of Alekseev

et al. [1988] that V_p/V_s is higher in the upper crust than the lower crust in the area of Kazakhstan near the Tien Shan. Given the uncertainties, however, we have chosen to calculate the event locations using two different S velocity models (Table 1), one with constant V_p/V_s ratio (model A) and another using the model of Priestley *et al.* [1988] (model B).

The location algorithm TTAZLOC is structured to be able to utilize arrival times of secondary phases, assuming that they can be identified and modeled correctly. Travel time calculations for the P velocity model in Figure 2 indicate that an upper crustal refraction along the 6.35 km/s layer at 10 km depth gives the first arrival from surface sources in the distance range of about 100–220 km and also suggests that it might produce a significant secondary arrival beyond that distance. We will denote this phase as P_R , following the notation of Aki and Richards [1980, p. 213]. The phases that we use for locations include P_n , P_R , S_n , and S_R , when observable; we have not used L_R , as we regard it as having a less precisely measurable arrival time.

For seismic arrays or sparse networks the azimuth of arriving phases can provide crucial constraints for determining event locations. We determine arrival azimuths using a method similar to that described by Magotra *et al.* [1987] for estimating the polarization direction of arriving seismic phases. For a polarized signal in the presence of noise the eigenvector corresponding to the largest eigenvalue of the covariance matrix for the signal components gives the direction of polarization, and the ratio of eigenvalues measures the rectilinearity of particle motion [Kanasewich, 1981]. Since we are interested just in the arrival azimuth, the horizontal component seismograms from a station are windowed (usually over 100–250 samples or 0.4–1.0 s) and demeaned, and the 2-by-2 signal covariance matrix C is computed:

$$C = \begin{bmatrix} \text{Var} [NS] & \text{Cov} [NS, EW] \\ \text{Cov} [NS, EW] & \text{Var} [EW] \end{bmatrix}$$

where NS and EW represent the north-south and east-west component time series, respectively. From the eigenvector for the largest eigenvalue of C ,

$$E_{\lambda \max} = [e_1 e_2]$$

the polarization direction ϕ for the time window can be computed from

$$\tan \phi = e_2/e_1$$

For the P wave, ϕ will be the apparent back azimuth to the event. The inherent 180° ambiguity in azimuth can be resolved by using all three components of particle motion [Magotra *et al.*, 1987]. We find that we are consistently able to determine azimuth estimates from the first P arrival, usually with an estimated uncertainty of 5° or less. Particle motion plots are also examined for a simple check of the results.

There are of course a variety of alternative ways to determine arrival azimuth from three-component data. Possibilities include frequency-dependent polarization analysis [Park *et al.*, 1987] or maximum likelihood estimation [Christofferson *et al.*, 1988]. The latter method has been employed successfully for single-station event location [Ruud *et al.*, 1988]. In our simple time domain approach we have not applied any tapering or filtering, nor have we used

TABLE 1. Velocity Models Used for Event Location

Depth Range, km	V_p , km/s	V_s , km/s
<i>Model A</i>		
0–5	5.40	3.05
5–10	6.15	3.50
10–20	6.35	3.60
20–30	6.55	3.70
30–40	6.75	3.85
40–50	6.95	3.95
50+	8.20	4.65
<i>Model B</i>		
0–5	5.40	3.30
5–10	6.15	3.40
10–20	6.35	3.50
20–30	6.55	3.70
30–40	6.75	4.10
40–50	6.95	4.30
50+	8.20	4.70

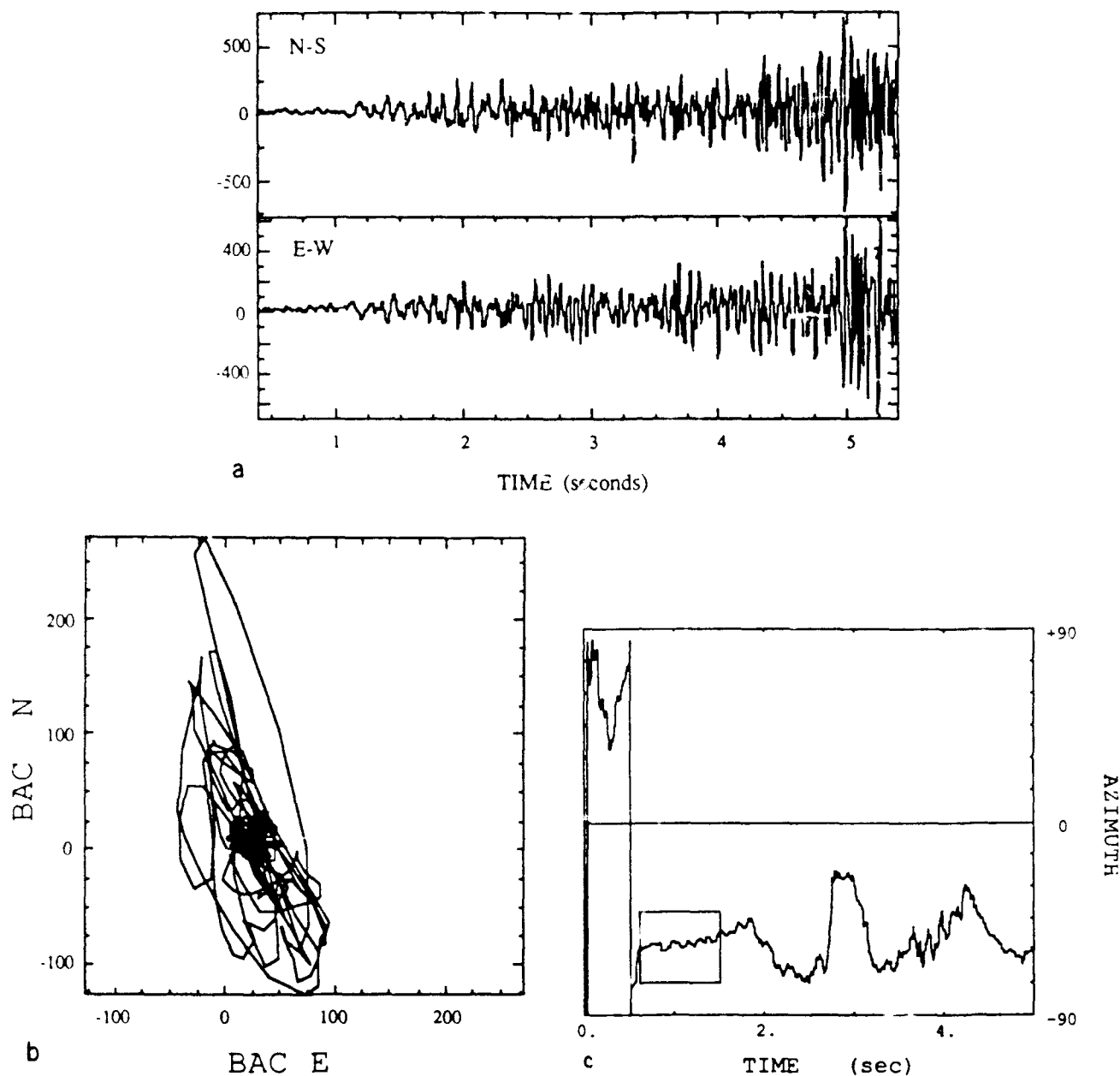


Fig. 3. (a) Initial few seconds of the horizontal component seismograms for a presumed blast (event h) located north of station Bayanaul, near the town of Ekibastuz. (b) Particle motion plot for the first 2 s of the seismograms in Figure 3a. The signal is well polarized and shows a reasonably constant arrival azimuth. (c) Arrival azimuth estimate from covariance analysis for the same portion of the seismogram shown in Figure 3a, computed using a 100-sample (0.4 s) moving window. Following the period of noise at the start of the record, the arrival azimuth estimate is fairly stable for about 1.5 s; then it shows significant variations corresponding to visible differences in the original seismograms. These variations could be due to scattered or direct multipathed arrivals. The box indicates the window selected for azimuth estimation.

smoothing as in the work by Magotra *et al.* [1987]. We prefer to be able to identify portions of the seismogram that show a consistent arrival azimuth, rather than averaging our estimate of arrival azimuth over direct and scattered or multipathed arrivals.

Figure 3 shows a typical example of azimuth determination for a mining blast located near Ekibastuz, recorded at the Bayanaul station. From the initial *P* wave train on the horizontal component seismograms (Figure 3a) we construct a particle motion plot for the first 2 s of the records shown

(Figure 3b) and compute the apparent arrival azimuth using the covariance analysis (Figure 3c). The initial *P* wave has a good signal-to-noise ratio (about 10) and is well polarized, as can be seen in the particle motion plot. The computed arrival azimuth is fairly stable using the 100 sample length (0.4 s) window. However, there appear to be secondary *P* arrivals and/or scattered energy in the record that seem to have measurably different arrival azimuths. Examples can be seen at about 2.5 and 4.3 s, with another strong phase appearing at about 5 s.

TABLE 2. Calculated and True Locations for Chemical Explosions, Using Velocity Models A and B

Explosion	Model	Origin Time	Latitude, °N	Longitude, °E	Error Ellipse, km	True Error, km	Mean Residuals
1	True	0.30	50.281	72.172			
	A	0.65	50.263	72.161	5 × 3 at -84°	1.8	0.08 s, 1.5°
	B	-2.65	50.342	71.815	18 × 10 at -81°	40.1	0.79 s, 2.8°
2	True	5.00	50.000	77.333			
	A	5.23	50.029	77.257	2 × 1 at +19°	8.7	0.24 s, 2.6°
	B	5.30	50.026	77.249	7 × 3 at +20°	9.7	0.60 s, 2.9°
3	True	0.30	50.281	72.172			
	A	1.34	50.278	72.241	18 × 9 at -73°	7.8	0.34 s, 9.9°
	B	-2.05	50.270	71.834	22 × 13 at -90°	37.6	0.39 s, 11.0°

CHEMICAL EXPLOSION LOCATIONS

On September 2 and 3, 1987, three large (10–20 t) chemical explosions were detonated in the vicinity of the network, two at the same location to the northwest of Karaganda and one on the western boundary of the Kazakh test site [Eissler *et al.*, 1987]. Their locations are indicated in Figure 1. Eissler *et al.* [1987] described the characteristics of the seismograms and presented basic analyses of their spectra and size. All three blasts were successfully recorded by each of the network stations. However, we have concentrated our analysis on the data for the first two explosions, as records of the third overlapped a teleseismic arrival from a magnitude 7.2 earthquake in the Macquarie Islands. The event depths were fixed at the surface for the initial set of calculations. In the following discussion it should be kept in mind that the "true" explosion locations may in fact be somewhat in error, perhaps by as much as a few kilometers, as it is not certain how accurate the maps are that were used by the Soviets to provide the locations.

Explosion 1 was located well outside the network, at sufficient epicentral distance from all the stations for P_n and S_n to be clear first arrivals. A strong crustal refracted phase (P_g) is also observed at stations BAY and KKL, both about 250 km from the shot site. Despite the unfavorable location with respect to the network, the availability of data at three stations, including numerous secondary arrivals, removes the necessity of incorporating azimuthal information to yield a stable location. We included the azimuthal data in all the calculations, though, as they will be essential in constraining regional event locations when only two stations provide data, as discussed below.

The location estimates for explosion 1 using the two S velocity models are listed in Table 2 and are compared to the true location in Figure 4a. The constant V_p/V_s model (model A) yields vastly superior results, both in terms of the accuracy of location and the data fit (and hence the location precision). Even the origin time is well estimated. In contrast, in the case of model B the 18 by 10 km error ellipse does not even encompass the true location, and the origin time is 3 s early. The excellent fit for model A is somewhat surprising. The existence of significant lateral heterogeneity in crustal thickness and P_n velocity in the region [Antonenko, 1984], combined with the location of the shot outside the network, would lead one to expect far less favorable results. On the one hand, it is true that the DSS profile that is used to provide the P velocity model is located between the shot point and the network, so the P structure itself may be reasonably appropriate. On the other hand, we

would have expected to obtain better results with model B, which has an S structure that is consistent with both DSS and teleseismic receiver structure results.

For comparison, we also show the location results for explosion 3 in Table 2. Despite the overlapping teleseism, the results are nearly identical to that for explosion 1. As before, only the estimated origin time is off significantly, over 1 s late for model A and 2 s early for model B. This 3-s difference in calculated origin time for the two velocity models also mirrors the result for explosion 1. In terms of the input data the only differences are the absence of a measured P_n azimuth for station KKL and the fact that the data from station KSU were obtained from a high-pass-filtered version of the seismogram. Perhaps the 1-s shift in fit to the origin time between explosions 1 and 3 is due to the masking of smaller-amplitude initial arrivals by the interfering teleseism.

Explosion 2 was located within the network at a distance range from stations BAY and KKL (about 150 km) such that the first seismic phases are crustal arrivals. Unfortunately, this removes the availability of $P_n - P_g$ arrival differences as constraints for the location and also probably makes the identification of the first S arrival somewhat less reliable. The separation between shot 2 and station KSU is comparable to that between shot 1 and stations BAY and KKL, so mantle-refracted waves are the first arrivals and a secondary crustal P phase is again observed. Azimuthal data are included in the calculations, although they were not required to produce acceptable location estimates.

Table 2 contains the location results for the two crustal models, and Figure 4b shows their comparison with the true location. The two estimated locations are nearly identical: they are both shifted about 9 km west of the true location, which falls outside the error ellipse in each case. Comparison of the observed and calculated travel times indicates that the P velocity model is too slow in the upper layers, causing the shift in location toward stations BAY and KKL. The only major difference in the results for the two models is the S_n residual at KSU, which is about 1 s late for model A but over 3 s late for model B. This suggests that the S velocities in the deeper layers of model B are systematically too high. This is consistent with the model B results for explosion 1, for which the calculated S arrival times were significantly early.

Since most of the regional event locations discussed below are determined using data from only two stations (BAY and KKL), it is informative to test the two-station location capability on the chemical explosions. The locations were recalculated (using model A) excluding the data from station

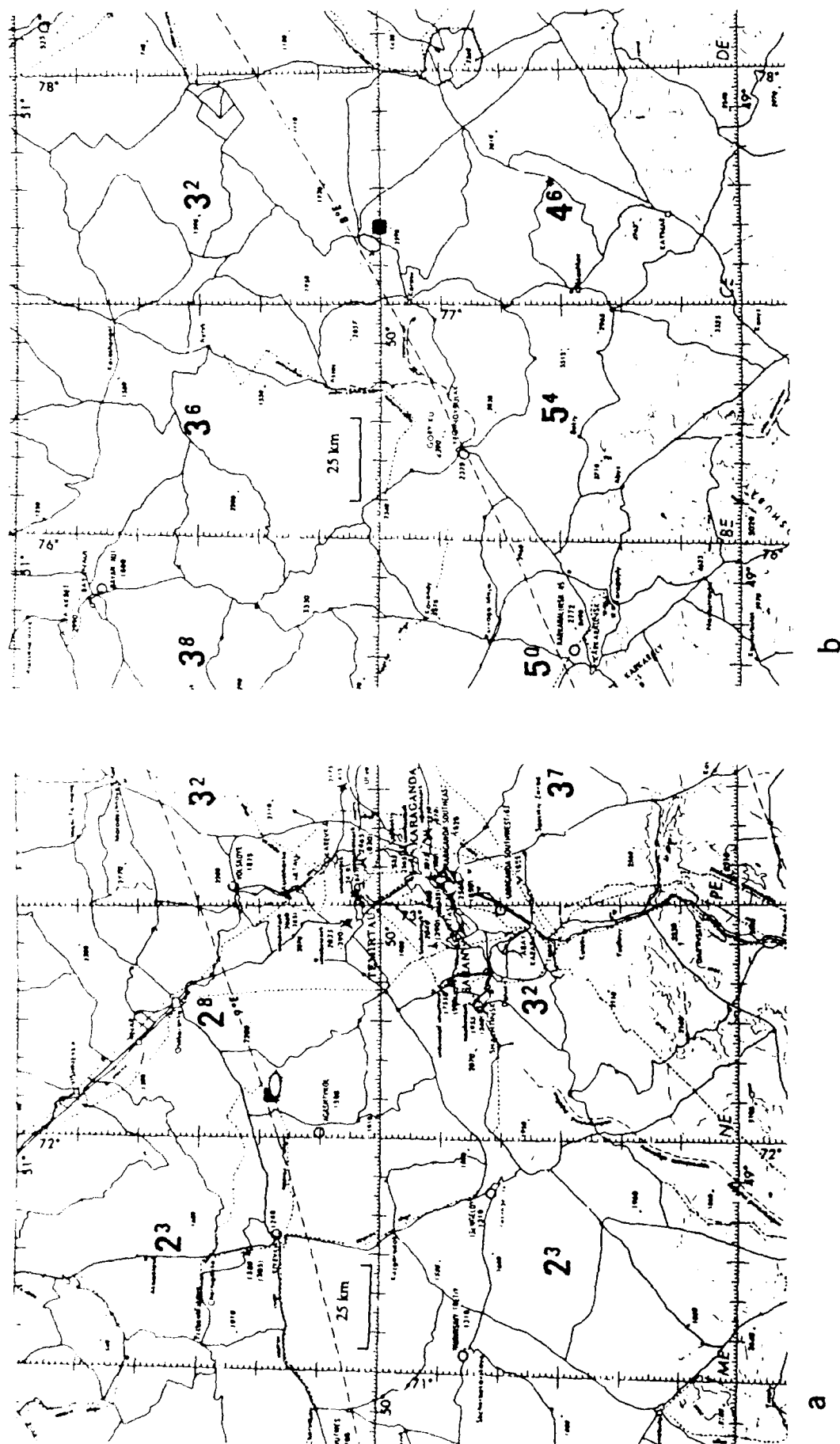


Fig. 4. Comparison between true and estimated locations for chemical explosions (a) 1 and (b) 2. The squares are the reported true locations, while the ellipses represent the 90% confidence limit for our locations. (a) Results are shown for model A and (b) results are shown for model B. Base map is taken from DMA [1983].

KSU, with little or no significant effect on the results. In the case of explosion 1 the epicenter and origin time are essentially unchanged, although the error ellipse expands by 10%. For explosion 2 the epicenter shifts 2 km westward and the origin time is 0.25 s later. However, the error ellipse does enlarge significantly, to 8.5 by 1.5 km. Thus in these two cases where the true event locations are known, we can derive reasonable location estimates using data from only two stations. The success of this test gives us considerable confidence in the reliability of the regional event locations discussed below, which were mostly obtained using data from two stations.

For our final location tests with the chemical explosions we examined the question of focal depth constraint. Ruud *et al.* [1988] suggest that focal depths for regional events can be determined from a single station, particularly if S_n is observed. With some degree of pessimism we relocated chemical explosions 1 and 2 first with depth fixed at 5 km and then with depth free, again using velocity model A. For both events the fixed 5-km depth solutions were notably worse than the original fixed 0-km depth solutions: the mean absolute arrival time residuals increased from 0.08 to 0.87 s for explosion 1 and from 0.24 to 0.68 s for explosion 2. Furthermore, for the solutions with focal depth left free the final calculated location was in fact at 0 km depth in each case, with estimated focal depth uncertainties of 0.6 and 1.3 km for explosions 1 and 2, respectively. If we further eliminate the data from station KSU, the location quality remains essentially unaltered for explosion 1 but degrades significantly for explosion 2. In the latter case, constraint on source depth is completely lost. With data from only a single station (either BAY or KKL), the solution for explosion 1 is still stable and reasonably accurate, falling within 8 km in epicenter and 1 km in depth. We attribute these surprisingly successful results for explosion 1 to the availability of multiple secondary arrivals (P_g and S_n). Thus we would agree with the claim of Ruud *et al.* [1988] that focal depth can be determined from data at a single station. A far more thorough analysis will be required to establish the conditions under which depths of regional events can be adequately constrained in general.

In addition to providing a general check on the location method and the network location capability the chemical explosion data are extremely useful for investigating the polarization properties of regional signals for the purpose of azimuth determination. The results of the covariance analysis for explosions 1 and 2 are illustrated in Figure 5, and Table 3 shows the comparison between the true and estimated back azimuths. The estimated azimuths were obtained from selected portions of the initial P arrival, chosen on the basis of azimuth stability, and the $\pm 1 \sigma$ level represents the standard deviation of the azimuth estimate within the window selected. A more formal uncertainty estimate could probably be derived from the eigenvalue analysis. The windows chosen are indicated in Figure 5. The accuracy of the estimates is quite good, with the largest errors for the seismograms in which P_g is the first arrival (explosion 2, stations BAY and KKL). The apparent misfit is near to or exceeds $\pm 2 \sigma$ for all stations for explosion 2 and for KKL for explosion 1. This suggests that the a priori uncertainty assumed for azimuth data should be somewhat larger than our simple estimate. Further analysis is required to determine possible station bias in arrival azimuth or

possibly to find optimum frequency bands for azimuth estimation.

We note also the large swings in estimated azimuth following the initial arrivals in Figure 5. Many of these azimuth changes correspond to sizable transverse arrivals, presumably near-receiver P to S conversions. Other less dramatic azimuth shifts, such as at 1 s in the BAY record for explosion 2, may reflect off-azimuth arrivals due to lateral heterogeneity in structure or perhaps minor contamination by scattered or converted waves. Data from an array of three-component stations might permit a more complete analysis of such arrival azimuth variations.

REGIONAL EVENT LOCATIONS

We have estimated the locations for 17 regional events recorded by either two or three stations of the network, using arrival time and azimuth data as available. The locations were all determined using velocity model A, given its success in locating the chemical explosions. The source depths of all the events presumed to be blasts were fixed at the surface. The calculated locations are listed in Table 4 and mapped in Figure 6. The events cover an estimated epicentral distance range of 25–1000 km. Their origin times are given in local time.

To the best of our knowledge, only two of these 17 regional events are earthquakes, both from the Tien Shan area. It is likely that all the remaining events are near-surface explosions, either mine or quarry blasts. A number of factors support this supposition. The Kazakh region is relatively aseismic, although it is bounded to the south by major earthquake zones. However, Kazakhstan is known as a major quarrying and coal mining region. All of the suspected blasts occurred during the morning or early afternoon. The vast majority of the seismograms for these events display strong short-period R_g phases, indicative of very shallow focus [Kafka, 1988]. Hedlin *et al.* [1989] find clear evidence for ripple-fired sources in the spectra of many of these events. Finally, almost all our event locations can be associated with mines mapped on regional navigational charts [Defense Mapping Agency (DMA), 1983], and as will be shown below, some of the mines are readily visible in satellite photographs of the area. Unfortunately, it has not been possible to obtain direct independent confirmation of the true locations of the majority of these events. However, the good two-station results obtained above for the chemical explosions provide some degree of assurance that these location estimates are valid. In addition, the adequate location agreement that we find for a number of these regional events with independently determined locations provides further confidence in our technique.

Two of the events for which locations have been determined independently are a quarry blast near the town of Karagayly, just east of station KKL (event e) and a regional earthquake in the northeastern Tien Shan (event l). The Karagayly blast occurred at a time when only stations KKL and BAY were operating. First P and S arrivals and P azimuths from these two stations were used to calculate the event location. The network installation crew noted the site of the active quarry, estimating its location to be 49.35°N, 75.72°E. The operational navigational chart (ONC) for the area [DMA, 1983] also indicates an active quarry there. Although this places our calculated location some 8 km to

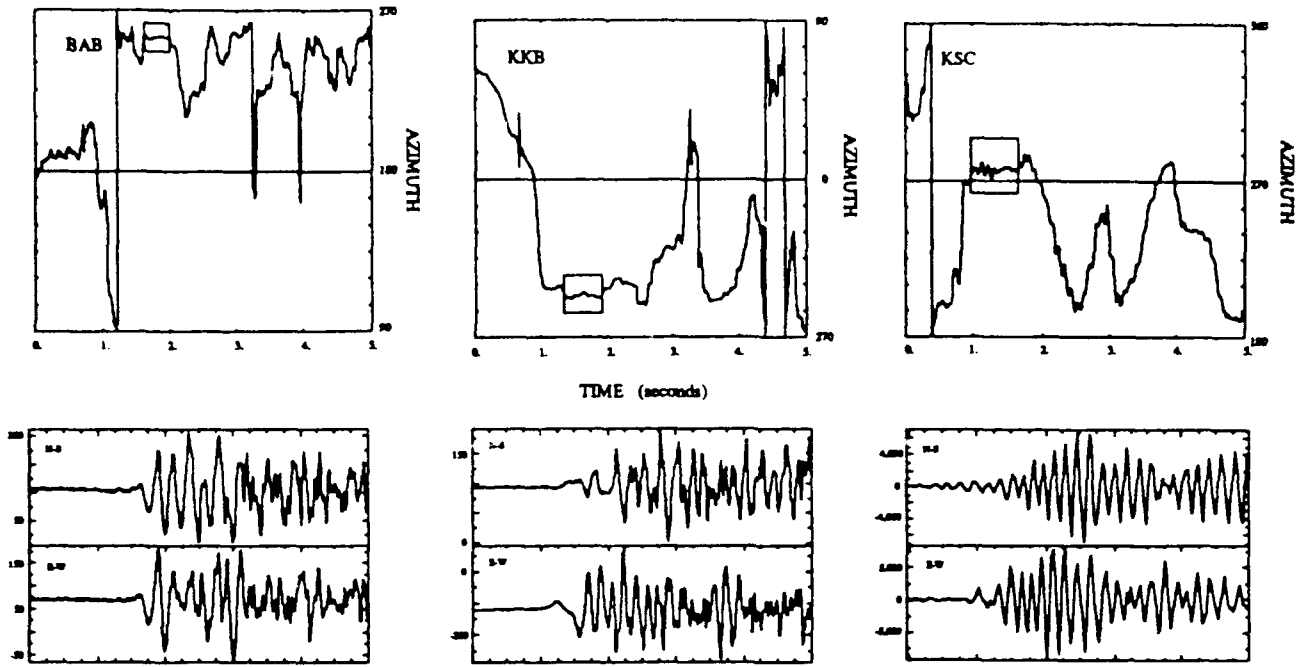


Fig. 5. Arrival azimuth estimates from covariance analysis (top) for chemical explosions 1 and 2 computed over 100-sample (0.4 s) windows for 5 s of the horizontal component seismograms (bottom). The boxes indicate the window chosen for determination of the *P* wave arrival azimuth at each station. Significant off-azimuth, scattered, and/or converted energy is present in all the seismograms.

the south of true, it is at the proper epicentral distance from station KKL (about 25 km). Since the event origin time is unknown, we cannot directly compare the calculated travel times to the actual absolute travel times. Therefore it is uncertain whether the crustal *P* velocity is slightly too slow or *S* too fast, causing the location to be displaced away from station BAY. The azimuths estimated from the first *P* arrivals fit extremely well with the true quarry location.

The Tien Shan earthquake of August 22, 1987, is reported in the preliminary determination of epicenters (PDE) [U.S. Geological Survey, 1987] as a magnitude 4.4 event at 43.81°N, 85.29°E, and 58 km depth, based on only seven reporting stations. This location places it approximately 200 km west of Urumqi, People's Republic of China. Fixing the source at that same depth and using data from all three stations, we determine a location that is offset just 40 km to

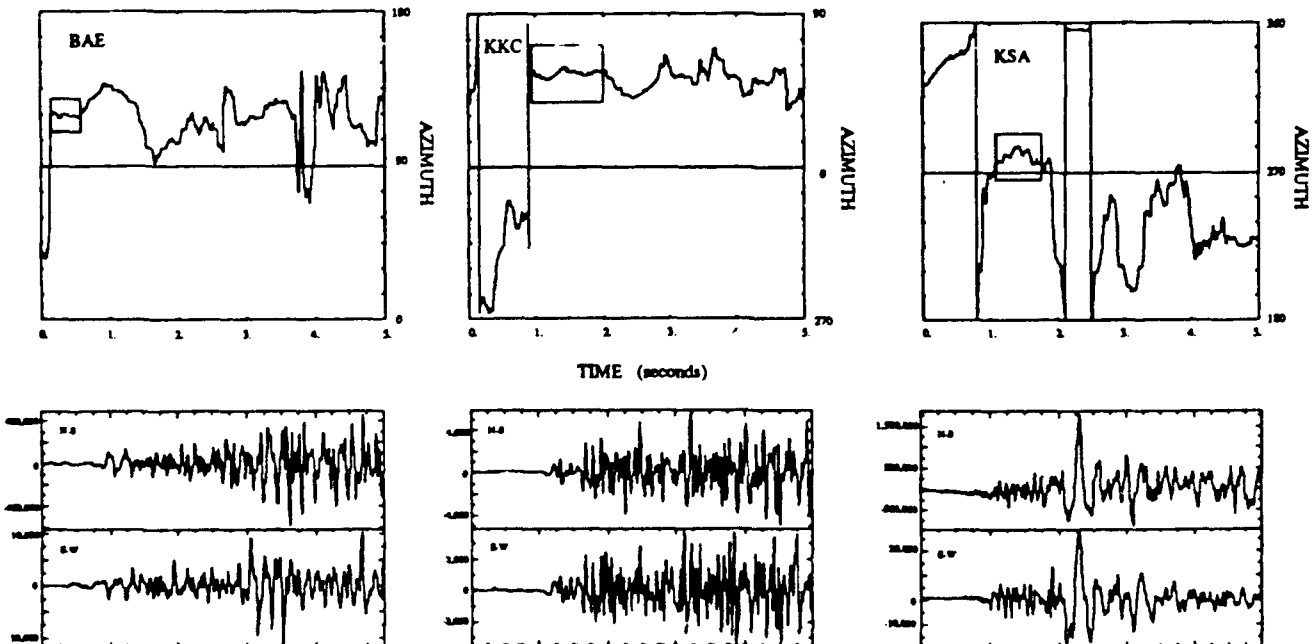


Fig. 5. (continued)

TABLE 3. Estimated and True Arrival Azimuths for Chemical Explosions 1 and 2

	Explosion	BAY	KKL	KSU
Estimated ($\pm 1 \sigma$)	1	255 ± 2	293 ± 1	276 ± 2
True		257	296	277
Estimated ($\pm 1 \sigma$)	2	121 ± 2	56 ± 2	279 ± 4
True		125	61	272

the east, with an rms arrival time misfit of 0.7 s. We consider the agreement to be surprisingly good: the event is over 700 km from KSU, the nearest network station, so control on the epicenter is relatively weak; given the small number of stations used in the teleseismic solution, that location may not be well constrained either. Another smaller earthquake occurred in the same vicinity on September 1 (event o) but did not appear in the PDE. Only two stations triggered on the *P* wave for this event (KKL and KSU). Our estimated location is about 60 km east of our location for the August 22 event. Our locations for both events fall within a narrow east-west trending belt of seismicity along the northern border of the Tien Shan adjacent to the Dzungarian Basin [Nelson *et al.*, 1987]. Eventually, we hope to obtain independent location estimates for both of these events from regional catalogues of the People's Republic of China and/or the Soviet Union. We may be able to use data from the Urumqi station of the China Digital Seismic Network to improve our location estimates for these earthquakes.

The remainder of the events can be grouped corresponding to three areas: Lake Balkash, Ekibastuz, and Karaganda. Of these, only two of the events were recorded by all three stations: event n in the Lake Balkash area and event q in the Ekibastuz area. Unfortunately, the former event was overlapped by an apparently more distant, unidentified regional event, so that in addition to three first *P* arrivals, only one *S* arrival time and *P* azimuth could be obtained. However, the resulting solution is relatively well constrained with small residuals. A second event 5 days later (event p) was recorded by stations KKL and KSU, and it locates within error at nearly the same place in the Lake Balkash area, providing some added confidence in the reliability of the

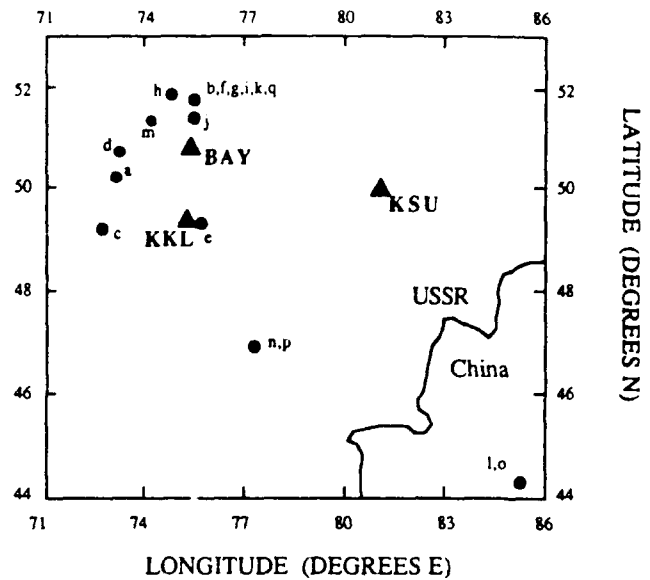


Fig. 6. Map of two- and three-station locations for regional events in the time period May to September 1987. See Table 4 for a list of the locations and their uncertainties.

location. The seismograms from these two events at station KKL resemble that from chemical explosion 1, which was at a roughly comparable epicentral distance.

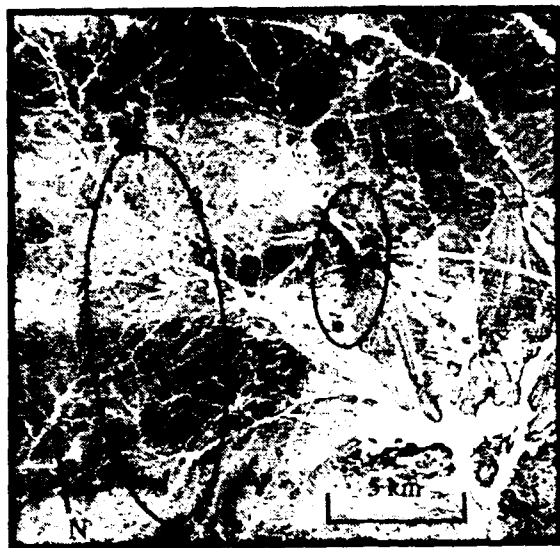
In order to obtain further evidence of the true locations of these events, two photographs taken by the French satellite SPOT covering an area encompassing these locations have been examined for evidence of mining activity, one from June 1986 and the other (requested by us) from October 1988. The original photos cover a region roughly 60 by 60 km centered on 47°02'N, 77°15'E, with a nominal spatial resolution of 30 m and a geographic location accuracy of 300 m. A 21-km square portion of the 1986 photo is shown in Figure 7, with the 90% confidence ellipses for our two event locations indicated. Two mine areas are visible (labeled A and B), and both fall near the error ellipses of the two events. Comparison of the appearance of the mines in the 1986 photo with the 1988 photo of the same region (Figure 8) indicates

TABLE 4. Catalog of 1987 Two- and Three-Station Event Locations

ID	Origin Time		Latitude °N	Longitude °E	Error Ellipse	Type	Area
	Day	Time					
a	134	0936:16.4	50.190	74.157	26 × 3 at -85°	blast	Karaganda
b	135	0908:35.2	51.709	75.514	8 × 4 at +74°	blast	Ekibastuz
c	135	1035:00.3	49.304	72.712	3 × 2 at +53°	blast	Karaganda
d	141	0916:43.3	50.744	73.279	2 × 2 at -80°	blast	Karaganda
e	143	0849:22.7	49.275	75.738	5 × 2 at -34°	blast	Karagayly
f	145	0926:43.7	51.670	75.454	12 × 3 at +84°	blast	Ekibastuz
g	145	0956:40.9	51.743	75.316	10 × 2 at +74°	blast	Ekibastuz
h	146	0531:04.8	51.819	74.797	6 × 4 at -85°	blast	Ekibastuz
i	146	0833:26.5	51.760	75.571	15 × 6 at -83°	blast	Ekibastuz
j	162	1241:04.9	51.454	75.488	7 × 5 at +16°	blast	Ekibastuz
k	162	1250:34.3	51.677	75.525	17 × 7 at +88°	blast	Ekibastuz
l	234	0021:50.7	44.129	85.363	12 × 6 at -69°	quake	Tien Shan
m	239	0852:53.0	51.213	74.302	13 × 5 at -26°	blast	Ekibastuz
n	239	0938:34.8	46.900	77.389	6 × 3 at +23°	blast	Balkash
o	244	0344:38.8	43.808	85.948	6 × 5 at +14°	quake	Tien Shan
p	244	0908:52.0	46.924	77.241	14 × 5 at +15°	blast	Balkash
q	245	0802:10.2	51.639	75.481	12 × 6 at -69°	blast	Ekibastuz

47°03'N 77°13'E

47°00'N 77°31'E



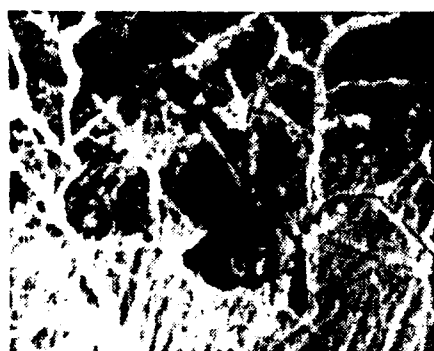
46°50'N 77°09'E

46°47'N 77°27'E

Fig. 7. Reproduction of a 21-km square portion from a SPOT satellite image north of Lake Balkash. The Sayak air field is visible in the lower right. Two mine areas are marked A and B. Also indicated are the epicenters and 90% confidence ellipses for events n and p. (Base photo, © 1986, CNES/SPOT Image Corporation.)

that the eastern site (mine B) was significantly more active over this time period. A new open pit is clearly visible at the northeastern corner of the mining area. Event n, located using all three stations, falls less than 10 km south of the eastern mine. This agreement is quite good considering that the nearest station (KKL) is more than 300 km from the mines. We tentatively conclude that event n did in fact originate from mine B and that event p probably did as well. No other mining activity is visible within the 60 by 60 km region, giving us high confidence that we have correctly identified the source area of these explosions. However, we cannot be absolutely certain at present whether or not both of the events originated from the same mine.

The majority of the regional events occurred just to the north of station BAY, in the area around the town of Ekibastuz. In all but one case they were recorded only by stations BAY and KKL. As indicated in Figure 6, six of the nine Ekibastuz events appear to be from the same site, with the other three at distinctly different sites. We have examined a May 1986 SPOT photo centered on 51°46'N, 75°17'E, encompassing the six estimated event locations, and numerous large mines are clearly identifiable. Several of these mines are also present (and accurately mapped) on the 1983 ONC for the region. An approximately 35-km square blow-up from the photo (Figure 9) shows a ring of seven mines (marked A-G) that appear to be active (and a number of what are probably abandoned water-filled mines); also indi-



A



B



Fig. 8. Comparison of the appearance of the two mines north of Lake Balkash in 1986 (left) versus 1988 (right), from SPOT satellite images. Mine B has an obvious new pit in the north-center section of the mine complex. (Base photo, © 1986 and 1988, CNES/SPOT Image Corporation.)

51°52'N 75°17'E

51°48'N 75°44'E



51°36'N 75°08'E

51°31'N 75°35'E

Fig. 9. Reproduction of a 35-km square portion from a SPOT satellite image around the town of Ekibastuz (at left center) showing obvious mining activity. Seven individual mines in a partial ring around the town are marked A–G. The largest mine (A) is about 5 km across. Also indicated are the epicenters and 90% confidence ellipses for events b, f, g, i, k, and q. (Base photo, © 1986, CNES/SPOT Image Corporation.)

cated are the 90% confidence ellipses for our estimated locations for the six events. The event locations generally cover the region of mining activity, with no particular pattern that can be related to the actual distribution of the mines. Due to uncertainties in absolute locations, it is of course impossible to associate unambiguously a given event with a particular mine. However, inspection of a September 1988 SPOT photo acquired for the same region suggests that the mines labeled A, B, D, and G were particularly active during the intervening period. The appearance of all six mines in 1986 and 1988 are compared in Figure 10. Mine A shows a major new cut through the middle, while mine B has a new linear cut west of the central pit. Mine D has two new major cuts spanning almost the entire mine, while mine G

has increased in area more than 100%. One or more of these four mines are overlapped, or nearly so, by all the error ellipses for the six events.

We have also compared these six event locations to the catalog of regional events recorded by the NRDC network produced by the Center for Seismic Studies (CSS). While our locations are quite tightly clustered, the CSS locations for these events are scattered rather widely in longitude. For some of the events, the location agreement is reasonable. For example, the CSS locations for events f and k are both shifted only about 10 km WNW, while event q is shifted in a similar direction and event b in the opposite direction by about 30 km each. In contrast, event g is shifted 75 km ESE and event i is shifted over 100 km WSW. Although we do not

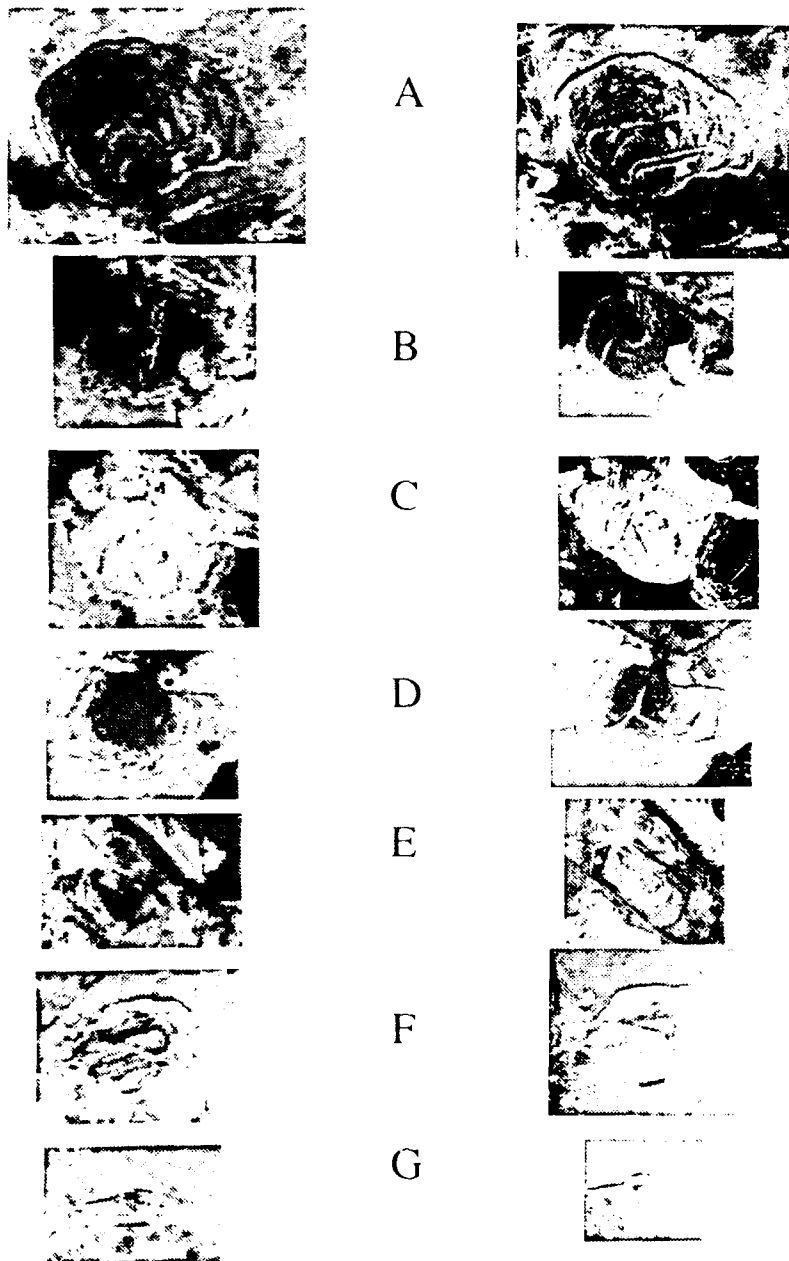


Fig. 10. Comparison of the appearance of the seven Ekibastuz mines in 1986 (left) versus 1988 (right), from SPOT satellite images. Mines A, B, D, E, and G show the clearest evidence of activity in the intervening period. (Base photo, © 1986 and 1988, CNES/SPOT Image Corporation.)

know the exact procedure used by CSS to determine the locations in their catalog, it is clear that careful event location incorporating azimuth data can provide quite reliable location results compared to routine catalog locations.

We are confident that the remaining three events in the Ekibastuz area (events h, j, and m) are from different sites and are not simply mislocated. For example, visual comparison of the seismograms for event m with other events indicates that event m lies at an epicentral distance from station BAY very similar to the typical Ekibastuz event but that KKL is within the P_n crossover distance while the others (h and j) lie beyond it. Event j occurred just 9 min before event k (one of the Ekibastuz cluster), suggesting that it originated from a different mine, and the two indeed show

markedly different seismograms at both BAY and KKL. Finally, event h took place on the same morning as event i (another of the Ekibastuz cluster), and again the two sets of seismograms appear markedly different.

The remaining three events (a, c, and d) are scattered around the town of Karaganda, in the general vicinity of the site of chemical explosions 1 and 3. The Karaganda area is a particularly active mining region, based on the presence of a large number of mapped mines in the area [DMA, 1983]. Event a is located only about 30 km north of Karaganda. The other two events are located well away from Karaganda, but each is near a town with mapped mines [DMA, 1983]. Event c falls within 20 km of the town of Yuzhnyy, while event d is at a comparable distance from the town of

Molodezhnoye. We plan to obtain additional SPOT images to attempt to corroborate the existence of mines in the vicinity of these sites.

CONCLUSIONS

We have demonstrated the capability of the three-station NRDC-Soviet Academy of Sciences network in Kazakhstan to locate regional events accurately over a wide area. Locations are determined using arrival times and arrival azimuths of observed phases, in most cases with data from only two stations. The September 1987 chemical explosions can be located with reasonable precision and accuracy either with data from all three network stations or using just two (BAY and KKL). Furthermore, the data are sufficient to determine correctly the depths of the chemical explosions (i.e., surface focus). We have also derived a well-constrained epicenter for an event in the Tien Shan at a distance of 700 km from the nearest station that agrees well with the published PDE location. Many other events are located in areas of mining activity identified in satellite photos and/or navigational charts, and the spectral characteristics of many indicate that they are ripple-fired explosions [Hedlin *et al.*, 1989], but the precise location of each individual event cannot be unambiguously determined. Analysis of "before and after" satellite photo images in these areas helps to identify specific active mining sites, and the success in locating events at or near these active sites adds confidence in our ability to locate accurately regional events with data from as few as two stations.

There are several extensions to the present work that we intend to pursue. One is the use of relative event location techniques, including waveform correlation to determine precise arrival time differences [Console and Di Giovambattista, 1987]. This can be applied to clusters of events such as at Ekibastuz, where it might be possible to match the pattern of relative event locations to the distribution of active mines observed in the satellite images. In this way it should also be possible to verify whether or not other events from the same general vicinity (events h, j, and m) were from distinct sites. At the same time, additional satellite images will be examined to seek potential alternative sites of explosions. Finally, one of the most pressing issues is the routine determination of source depth. Ruud *et al.* [1988] claim that depths can be constrained using data from a single station. Analysis of the chemical explosion data indicates that depth can be constrained if multiple secondary arrivals (such as P_g and S_n) are available. Our future work will include further testing of this claim for the data from other regional events in Kazakhstan, as well as an examination of the problem on a theoretical basis.

Acknowledgments. We are grateful to Steve Bratt for providing a copy of his location algorithm and for numerous helpful discussions and to Bill Leith for alerting us to some of the information on crustal structure in Kazakhstan. C. Thurber thanks the Seismology Group of Lamont-Doherty Geological Observatory for constructive comments and logistical support while on sabbatical during the beginning stages of this research. H. Given acknowledges support from the Institute on Global Conflict and Cooperation, University of California. We also thank Eric Chael for a helpful review, Jean McPhetres of AFGL and Ed Chabot of DMA for their assistance in obtaining the SPOT photos, and Joe Tull of LLNL for the provision of and assistance with SAC. Installation and operation of the Kazakh network was funded by the National Resources Defense

Council and the Soviet Academy of Sciences. This work was supported by the Defense Advanced Research Projects Agency under contracts F19628-88-K-0037 and F19628-88-K-0044 (monitored by the Air Force Geophysics Laboratory).

REFERENCES

- Aki, K., and P. G. Richards, *Quantitative Seismology: Theory and Methods*, 932 pp., W. H. Freeman, New York, 1980.
- Alekseev, A. S., A. V. Egorkin, and N. I. Pavlenkova, Shear waves in lithosphere studies on the territory of the U.S.S.R., *Tectonophysics*, 154, 227-239, 1988.
- Antonenko, A. N., *Deep Structure of the Earth's Crust in Kazakhstan* (in Russian), 274 pp., Academy of Science of Kazakh SSR, Alma-Ata, USSR, 1984.
- Belyaevsky, N. A., A. A. Borisov, V. V. Fedynsky, E. E. Fotiadis, S. I. Subbotin, and I. S. Volvovsky, Structure of the Earth's crust on the territory of the U.S.S.R., *Tectonophysics*, 20, 35-45, 1973.
- Berger, J., et al., A new U.S.-U.S.S.R. seismological program, *Eos Trans. AGU*, 68, 110-111, 1987.
- Berger, J., H. Eissler, F. L. Vernon, I. L. Nersesov, M. B. Gokhberg, O. A. Stolrov, and N. D. Tarassov, Studies of high-frequency seismic noise in eastern Kazakhstan, *Bull. Seismol. Soc. Am.*, 78, 1744-1758, 1988.
- Bratt, S. R., and T. C. Bache, Locating events with a sparse network of regional arrays, *Bull. Seismol. Soc. Am.*, 78, 780-798, 1988.
- Christofferson, A., E. S. Husebye, and S. F. Ingate, Wavefield decomposition using ML-probabilities in modelling single-site 3-component records, *Geophys. J.*, 93, 197-213, 1988.
- Console, R., and R. Di Giovambattista, Local earthquake relative location by digital records, *Phys. Earth Planet. Inter.*, 47, 43-49, 1987.
- Defense Mapping Agency, Operational navigation chart, *ONCE 6*, Washington, D. C., 1983.
- Eissler, H., J. Berger, F. Vernon, J. Gombert, D. Chavez, N. T. Tarassov, and V. I. Zhuravlev, Observations of chemical explosions on the steppes of central Asia, *Eos Trans. AGU*, 68, 1363-1364, 1987.
- Hedlin, M. A. H., J. B. Minster, and J. A. Orcutt, The time-frequency characteristics of quarry blasts and calibration explosions recorded in Kazakhstan, U.S.S.R., *Geophys. J.*, in press, 1989.
- Jordan, T. H., and K. A. Sverdrup, Teleseismic location techniques and their application to earthquake clusters in the south-central Pacific, *Bull. Seismol. Soc. Am.*, 71, 1105-1130, 1981.
- Kafka, A. L., Investigation of R_g waves recorded from earthquakes and explosions in New England, paper presented at 10th Annual DARPA/AFGL Seismic Research Symposium, Def. Adv. Res. Projects Agency, 1988.
- Kanasewich, E. R., *Time Sequence Analysis in Geophysics*, 480 pp., University of Alberta Press, Edmonton, Canada, 1981.
- Lee, W. H. K., and S. W. Stewart, Principles and applications of microearthquake networks, *Adv. Geophys.*, Suppl. 2, 293 pp., 1981.
- Leith, W., Geology of NRDC seismic station sites in eastern Kazakhstan, USSR, *U.S. Geol. Surv. Open File Rep.*, 87-597, 1987.
- Magotra, N., N. Ahmed, and E. Chael, Seismic event detection and source location using single-station (three-component) data, *Bull. Seismol. Soc. Am.*, 77, 958-971, 1987.
- Nelson, M. R., R. McCaffrey, and P. Molnar, Source parameters for 11 earthquakes in the Tien Shan, Central Asia, determined by P and SH waveform inversion, *J. Geophys. Res.*, 92, 12,629-12,648, 1987.
- Owens, T. J., G. Zandt, and S. R. Taylor, Seismic evidence for an ancient rift beneath the Cumberland Plateau, Tennessee: A detailed analysis of broadband teleseismic P waveforms, *J. Geophys. Res.*, 89, 7783-7795, 1984.
- Park, J., F. L. Vernon III, and C. R. Lindberg, Frequency dependent polarization analysis of high-frequency seismograms, *J. Geophys. Res.*, 92, 12,664-12,674, 1987.
- Pavlis, G. L., Appraising earthquake hypocenter location errors: A complete, practical approach for single-event location, *Bull. Seismol. Soc. Am.*, 76, 1699-1717, 1986.
- Priestley, K. F., G. Zandt, and G. E. Randall, Crustal structure in

- eastern Kazakh, U.S.S.R. from teleseismic receiver functions, *Geophys. Res. Lett.*, **15**, 613-616, 1988.
- Ruud, B. O., E. S. Husebye, S. F. Ingate, and A. Christoffersson, Event location at any distance using seismic data from a single, three-component station, *Bull. Seismol. Soc. Am.*, **78**, 308-325, 1988.
- Thurber, C. H., Analysis methods for kinematic data from local earthquakes, *Rev. Geophys.*, **24**, 793-805, 1986.
- U.S. Geological Survey, Preliminary determination of epicenters, Reston, Va., Aug. 1987.
- J. Berger and H. Given, Institute of Geophysics and Planetary Physics, Scripps Institution of Oceanography, University of California, San Diego, La Jolla, CA 92093.
- C. Thurber, Department of Geology and Geophysics, University of Wisconsin-Madison, Weeks Hall, 1215 W. Dayton St., Madison, WI 53706.

(Received April 5, 1989;
revised July 25, 1989;
accepted July 27, 1989.)

High-Frequency Seismic Observations in Eastern Kazakhstan, USSR, With Emphasis on Chemical Explosion Experiments

HOLLY K. GIVEN,¹ NIKOLAI T. TARASOV,² VLADIMIR ZHURAVLEV,² FRANK L. VERNON,¹
JONATHAN BERGER,¹ AND IGOR L. NERSESOV²

Two temporary three-station seismic networks, deploying surface and 100-m borehole high-frequency seismometers, of the order of 200 km from the Kazakh test site in the USSR and the Nevada test site in the United States are discussed, with emphasis on chemical explosion experiments. Seismograms attained from the detonation of three buried explosions (10 t, 20 t, 10 t) in eastern Kazakhstan at distances between 156 and 637 km are examined in the frequency band of 1-80 Hz. Observed signal-to-noise (S/N) ratios were high, reaching a maximum of 400 for P_g waves and 200 for L_g waves. Good signal-to-noise levels persisted to high frequencies; S/N = 2 at about 50 Hz for L_g waves about 250 km from the source, and at about 14 Hz at 680 km distance. For P_g waves, S/N = 2 at about 50 Hz 270 km from the source. Shapes of displacement amplitude spectra were similar, characterized by a broad maximum in signal-to-noise levels between 4-8 Hz, and a decay at higher frequencies (e.g. above 10 Hz) of about $f^{-3.5}$ - $f^{-4.1}$ for L_g waves, and $f^{-3.1}$ - $f^{-4.5}$ for P_g , uncorrected for distance. Magnitudes estimated from L_g time domain amplitudes for the 10 t explosion are between 2.8 and 3.3, depending on the magnitude relation used. Spectral characteristics are used to put some constraint on L_g Q . P_g Q is poorly constrained by the data. A similar experiment in southern Nevada showed much lower P_g and L_g signal-to-noise levels above 1 Hz, although Kazakh and Nevada absolute noise levels are comparable.

1. INTRODUCTION

In 1987, three high-frequency borehole-equipped digital seismic stations were deployed in eastern Kazakhstan as part of a joint project between the Natural Resources Defense Council, an American environmental organization, and the Academy of Sciences of the Union of Soviet Socialist Republics. The stations were of the order of 200 km from the Kazakh Test Site (Figure 1). The primary purpose of the project was to acquire data relevant to an in-country seismic monitoring scenario in the event of new agreements limiting underground testing of nuclear weapons. A nearly identical network operated near the Nevada Test Site in the western United States for most of 1988 (Figure 2).

The amount of data is limited by the short duration of the deployment, the sparseness of station distribution, and some periods of operational difficulty. Yet the data quality is high, which has led to studies that are useful both in illustrating the possibilities of high-frequency data in general and in describing the seismic properties of a geographic area of high interest where data were previously unavailable. For example, *Thurber et al.* [1989] showed that regional events can be located with remarkable accuracy with only two stations using secondary phases and three-component data and compared computed locations of suspected mining explosions in Kazakhstan to satellite photos of known mining centers. *Hedlin et al.* [1989] distinguished simultaneously fired explosions from sequentially fired mining explosions in the data set on the basis of the time-frequency characteristics of the seismograms. *H. Gurrola et al.*

(Analysis of high-frequency seismic noise in the western U.S. and eastern Kazakhstan, USSR, Submitted to *Bulletin of the Seismological Society of America*, 1989) systematically analyzed levels of ambient ground noise and their dependence on wind conditions and sensor depth in a comparative study between eastern Kazakhstan and the western United States.

As an example of the seismic observations obtained during the Kazakh deployment, we will discuss three large underground chemical explosions (10-20 t of TNT) that were detonated to determine transmission levels of high-frequency signals and their dependence on distance and source yield in the vicinity of the Kazakh test site. The experiment provided seismograms at distances from 156 to 637 km from the sources. This example gives an indication of expected signal-to-noise levels from small explosions as well as some implications for crustal attenuation in Kazakhstan. Results from the Kazakh network are compared with those from a similar explosion experiment with the Nevada network.

2. DESCRIPTION OF DEPLOYMENT

Sensors, data logging equipment, and ambient ground noise levels at the Kazakh stations have been discussed by *Berger et al.* [1988]. Each station was equipped with three-component borehole seismometers (using Teledyne Geotech S750 sensors) at a depth of approximately 100 m and two sets of three-component seismometers in a well-constructed surface vault (Teledyne Geotech GS-13 and Kinemetrics S-1 sensors). The signal was digitized at 250 samples per second; low-pass filters provide antialiasing processing above 80 Hz. At the low-frequency end, the corner frequencies of the borehole and GS-13 surface seismometers are 0.2 Hz and 1 Hz, respectively. When both high- and low-gain channels of all seismometers are considered, the available dynamic range of the system is 180 dB.

The data acquisition software was modified from that of the ANZ network [*Berger et al.*, 1984]. The basic recording mode is event-triggered, although the operator can manually turn the recording system on or preprogram periods of continuous recording. The trigger algorithm employs a standard short-term

¹ Institute of Geophysics and Planetary Physics, Scripps Institution of Oceanography, University of California, San Diego, La Jolla.

² Institute of Physics of the Earth, Academy of Sciences of the USSR, Moscow.

Copyright 1990 by the American Geophysical Union.

Paper number 89JB01572.

0148-0227/90/89JB-01572\$05.00

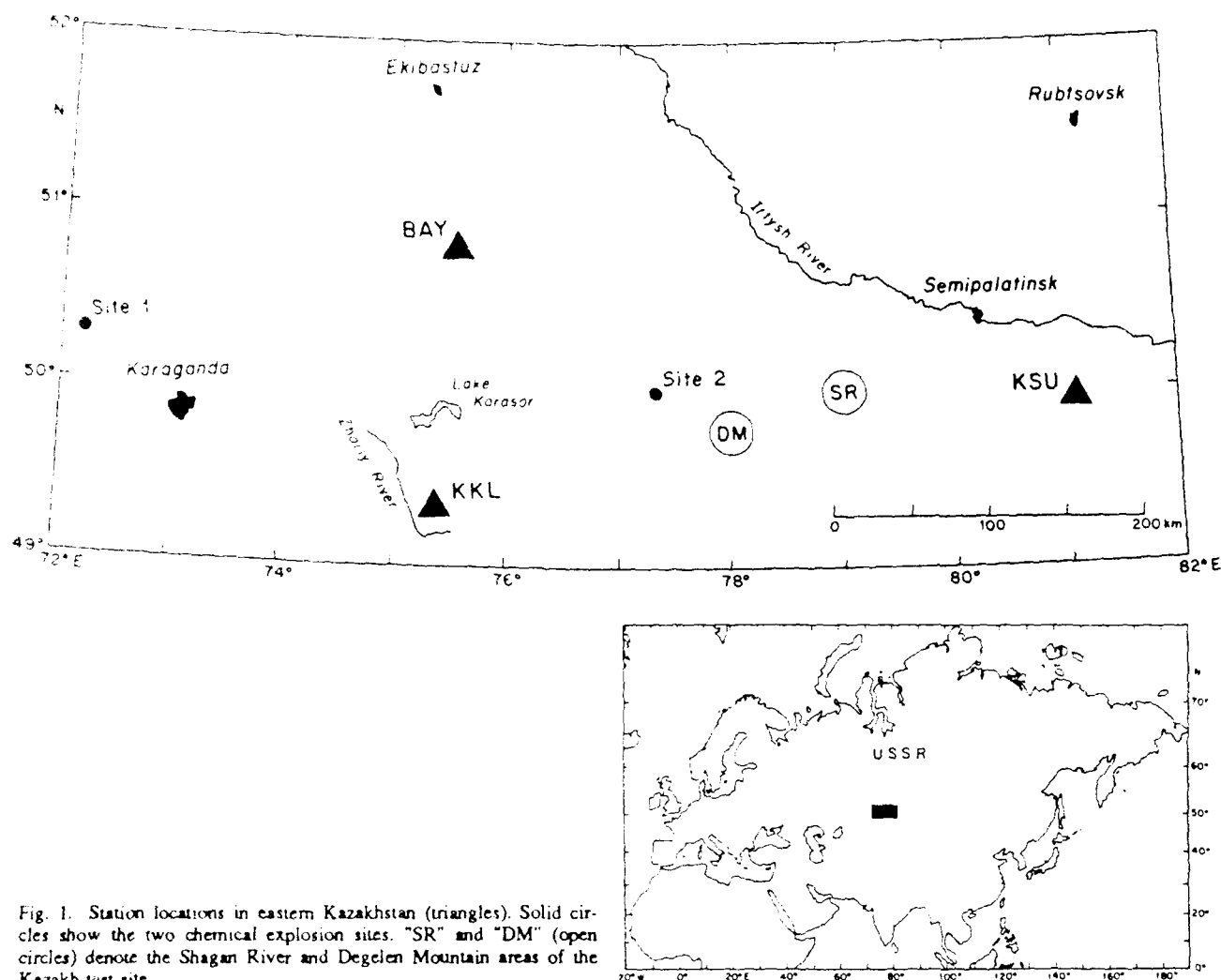


Fig. 1. Station locations in eastern Kazakhstan (triangles). Solid circles show the two chemical explosion sites. "SR" and "DM" (open circles) denote the Shagan River and Degelen Mountain areas of the Kazakh test site.

average to long-term average ratio criterion, where the window lengths are set by the operator. The amount of preevent leader and postevent trailer to be recorded can be set by the operator. The system accepts the designation of any or all data channels as trigger channels; for example, if there is an unusual amount of surface noise, the operator may choose to trigger on borehole channels only. Physically, the components of the data acquisition system fit in an equipment rack housed in a recording trailer, and the digitized signals are transmitted to the recording trailer via underground cable.

The seismic equipment used at the Nevada stations was almost identical to the Kazakh equipment, but there was a fundamental difference in the data acquisition systems. Data were recorded on site in the Kazakh network, and there was no link between stations. There was no on-site recording at the Nevada stations. Data were sent via satellite to Scripps Institution of Oceanography, where an interface unit formed data buffers with information from all three stations for input to the detection algorithm. This increases flexibility in network control; for example, the operator could designate trigger channels such that only events that trigger two or three stations are recorded. This is obviously a preferable design, in that the expense of three separate data loggers is spared; also, one set of presumably related events is obtained rather than three sets of events that

must be associated after the fact. Satellite telemetry was not considered for the Soviet stations at the time of the Kazakh deployment due to logistical and technical considerations.

Sites for the Kazakh stations were chosen to be far from industrial noise and on large granitic intrusions. The geology of the Kazakh sites has been discussed by Leith [1987], who concluded that that granitic intrusions are similar in composition to the Degelen Mountain intrusion on the Kazakh test site, in which nuclear tests are conducted. Similarly, Nevada stations were sited in granitic areas.

The Kazakh data set contains roughly 65% local events, most of which are mining explosions within 250 km of the stations; these explosions occurred of the order of a few per day. Many of them occurred near the cities of Ekibastuz, north of the network, and Karaganda, west of the network, which are major coal producing centers (Figure 1; also Thurber *et al.* [1989]). Natural seismicity in this area of Kazakhstan is rare, providing little opportunity to study local (i.e., ≤ 300 km) earthquakes and explosions at comparable distances. Roughly 10% of the triggers are regional events, predominantly earthquakes from the tectonic areas of the Pamir-Tien Shan mountain region approximately 1000 km to the south of the network, and roughly 25% are globally distributed teleseismic events. About 20% of the Kazakh triggers were recorded on two or more stations. Logistical and

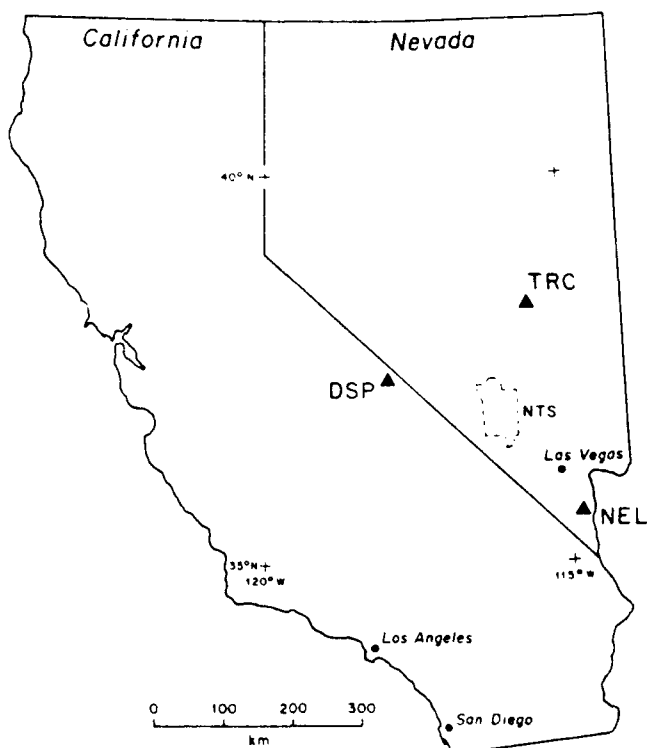


Fig. 2. Station locations for the Nevada network, showing the Nevada Test Site. Station coordinates are given in Table 1.

operational difficulties resulted in only 3 weeks of simultaneous operation of three stations around the time of the chemical explosion experiments described below.

In the Nevada data set there is a more continuous distance range of local and regional events, mainly earthquakes, although there are some mining explosions. Several nuclear explosions were recorded on scale on the low-gain channels. Unlike Kazakhstan, there are observations of earthquakes and explosions at comparable distances. There are a higher number of two- and three-station events due to the difference in the data logging arrangement. A qualitative comparison between the Kazakh and Nevada data sets shows that eastern Kazakhstan is much more efficient in the transmission of high-frequency energy (>20 Hz) than the area around the Nevada Test Site. To quantify this, we now discuss the explosion experiments at length.

3. CHEMICAL EXPLOSION EXPERIMENTS: SITE PREPARATION AND DATA EXAMPLES

Explosion sites are shown in Figure 1 and listed in Table 1. Two 10-t explosions, one day apart, were detonated at site 1, west of the city of Karaganda approximately 450 km from the Kazakh test site. To prepare the shots, 30 boreholes were drilled to a depth of 25 m in water-saturated clay, with a horizontal grid spacing of 10 m. The TNT was distributed equally among the boreholes, and all boreholes were detonated simultaneously. The shot time is known to an accuracy of at least ± 10 ms. The borehole grid for the second explosion at this site was 150 m from the first. Both explosions were fully contained underground. (These shots will be referred to as explosions 1 and 3.) Signals from explosion 3 arrived at the stations in the coda of a teleseism in the MacQuarie Islands ($M_s = 7.2$), but the events can be separated by filtering. Explosion 3 is basically redundant

with explosion 1, except that some instrument gains were changed between the explosions to provide better resolution at higher frequencies for some data channels; in these cases we use data from explosion 3. Figure 3 shows an example of the data from explosion 3, recorded on the borehole seismometer 254 km away at site KKL; Figure 4 shows data from KSU, 637 km from the source. The records have been high-pass filtered for plotting purposes with a 1-Hz corner frequency to eliminate background microseisms and emphasize high-frequency arrivals.

The 20-t shot at site 2 was situated in a 17-m-deep preexisting horizontal mining tunnel in granitic rock, accessible through two shafts. This site is near the center of the network, on the western boundary of the test site. This explosion blew out to the surface along the shafts and thus the signal levels were at best comparable to the 10-t shots in clay. (This shot will be referred to as explosion 2.) Figure 5 shows an example of the high-pass filtered borehole seismogram at KKL, 159 km from the source; Figure 6 shows the record at KSU, 269 km from the source. Note that for both shot sites the geometry is such that two stations (KKL and BAY) are nearly equidistant but at different azimuths, and the third (KSU) is farther.

Thurber *et al.* [1989] matched the locations of the chemical explosions using observed P_g , P_n , L_g , and S_n arrival times and azimuths and a crustal structure modified from the Soviet literature [Antonenko, 1984; Leith, 1987]. This model has a Moho depth of 50 km and a mantle compressional velocity of 8.2 km s^{-1} (Table 2). The predicted $P_n - P_g$ crossover distance is about 230 km; thus P_g dominates the P wave train in most of the records. By $\Delta = 269$ km (Figure 6), P_n arrives about 1 s before P_g . S and P wave trains have comparable amplitudes on the vertical and radial components for both explosions. S amplitudes are roughly equal on vertical, radial, and transverse components, indicating predominance of the L_g phase. There is a long coda after the P and S phases, which is most clear in the P coda on transverse components, indicating high-frequency scattering. S_n is not well observed at the nearer stations but is clear in the record at 637 km at about 150 s (Figure 4).

4. SPECTRAL CHARACTERISTICS OF CHEMICAL EXPLOSION SEISMOGRAMS

L_g and P displacement amplitude spectra were calculated from the borehole vertical channels for the six source-station pairs. We use the multitaper spectral estimation technique of Thomson [1982], as applied by Park *et al.* [1987], where the time series is tapered with a sequence of prolate spheroidal functions is transformed and the results are averaged. We have found that multitaper analysis provides notable improvement over standard single-window methods, particularly where there is still substantial high-frequency coda energy at the end of the window. The variance of the spectral estimate is also much less. Lower frequencies were heavily smoothed for the window lengths used, and thus we restrict discussion to frequencies above 1 Hz.

A group-velocity window of $3.6\text{--}2.7 \text{ km s}^{-1}$ was necessary to window the L_g wavetrain at distances less than 200 km, where the ray paths are affected by lower velocities in the upper crust. Differences between spectra calculated for this window and a $3.6 \text{ km s}^{-1}\text{--}3.0 \text{ km s}^{-1}$ window are negligible for distances over 200 km. L_g amplitude spectra are shown in Figure 7 from explosion 3 and in Figure 8 from explosion 2. Upper traces are signal and lower (dashed) traces are a pre- P noise sample. The solid line fit to the signal spectra were calculated using an algo-

TABLE 1. Explosion and Station Locations

Name	Origin Time		Latitude	Longitude
	Year-Day	Time		
Explosion 1 (10 t)	1987-245	0700:00.32	50°16'50"	72°10'20"
Explosion 2 (20 t)	1987-245	0927:04.95	50°00'00"	77°20'20"
Explosion 3 (10 t)	1987-246	0700:00.06	50°16'50"	72°10'20"
Broken Hills (14 t)	1988-121	1900:00.00	39°03'51"	-117°58'49"
USSR stations				
Karkaralinsk (KKL)			49°20'	75°23'
Bayanaul (BAY)			50°49'	75°33'
Karasu (KSU)			49°57'	81°05'
U.S. stations				
Deep Springs, CA (DSP)			37°22'	-117°58'
Troy Canyon, NV (TRC)			38°21'	-115°35'
Nelson, NV (NEL)			35°39'	-114°51'

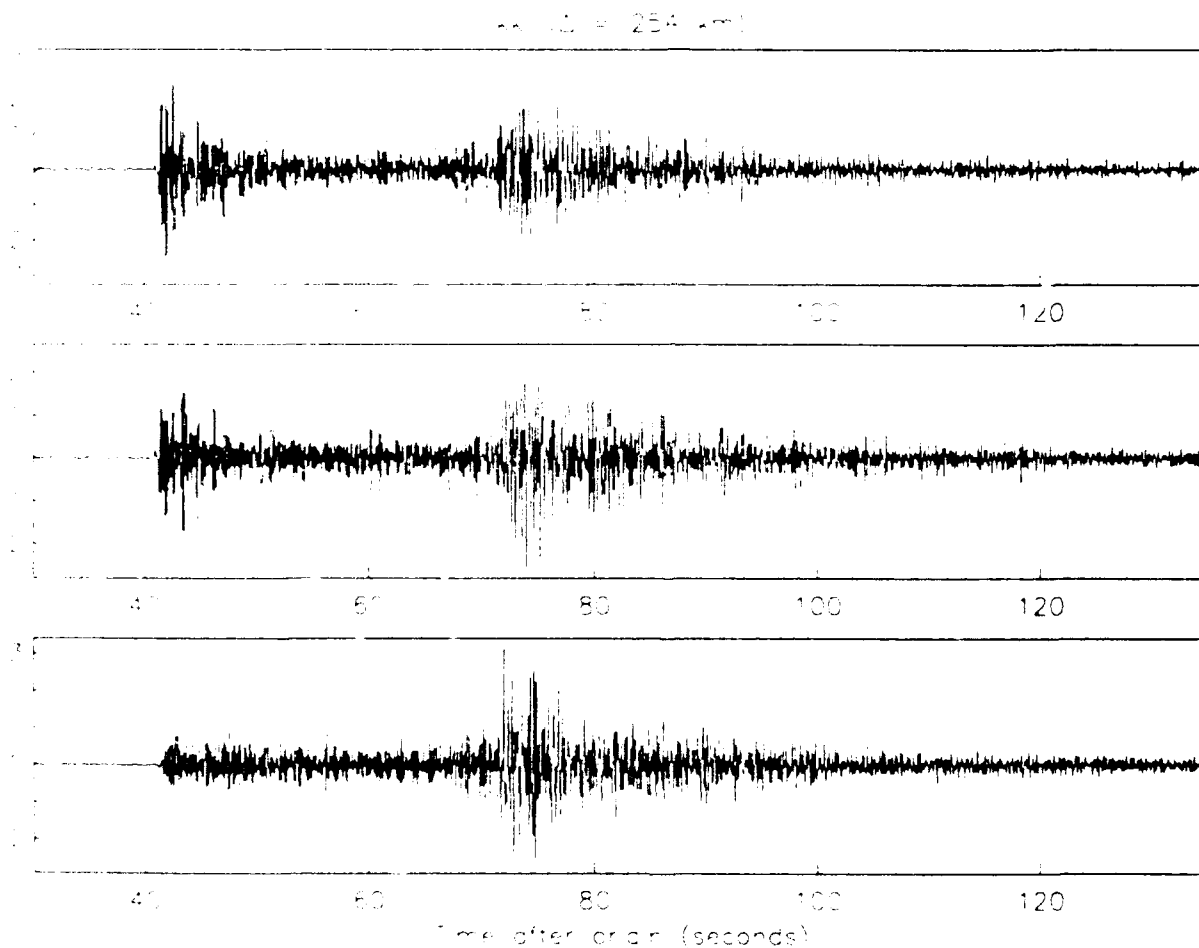


Fig. 3. Three-component seismogram from explosion 3 recorded on the borehole channel at station KKL, 254 km from the source. The records were high-pass filtered with a 1-Hz corner frequency for this plot.

algorithm described by Vernon [1989], which uses the variance output of the multitaper analysis to estimate the best values of high frequency spectral slope, long period spectral level (in this case, 1 Hz), and apparent corner frequency. These parameters are given in Table 3. Although this parameterization is somewhat rigid, all the chemical explosion spectra show similar characteristics that are well described by this model: a fairly constant spectral level up to about 4 Hz and a fairly constant slope above about 10 Hz.

L_p signal levels are high. For explosion 3, maximum signal-to-noise levels are between a factor of 130 and 200 between 5 and 6 Hz at KKL and BAY and reduce to a factor of 13 between 1 and 2 Hz for KSU at a distance of 637 km. The highest frequency where signal amplitudes are above noise amplitudes is about 60 Hz at the KKL and BAY; this reduces to about 14 Hz for KSU. Spectral slopes were estimated only in the frequency band where S/N was at least 2 or greater. Slopes were identical at KKL and BAY at 3.8, increasing only slightly

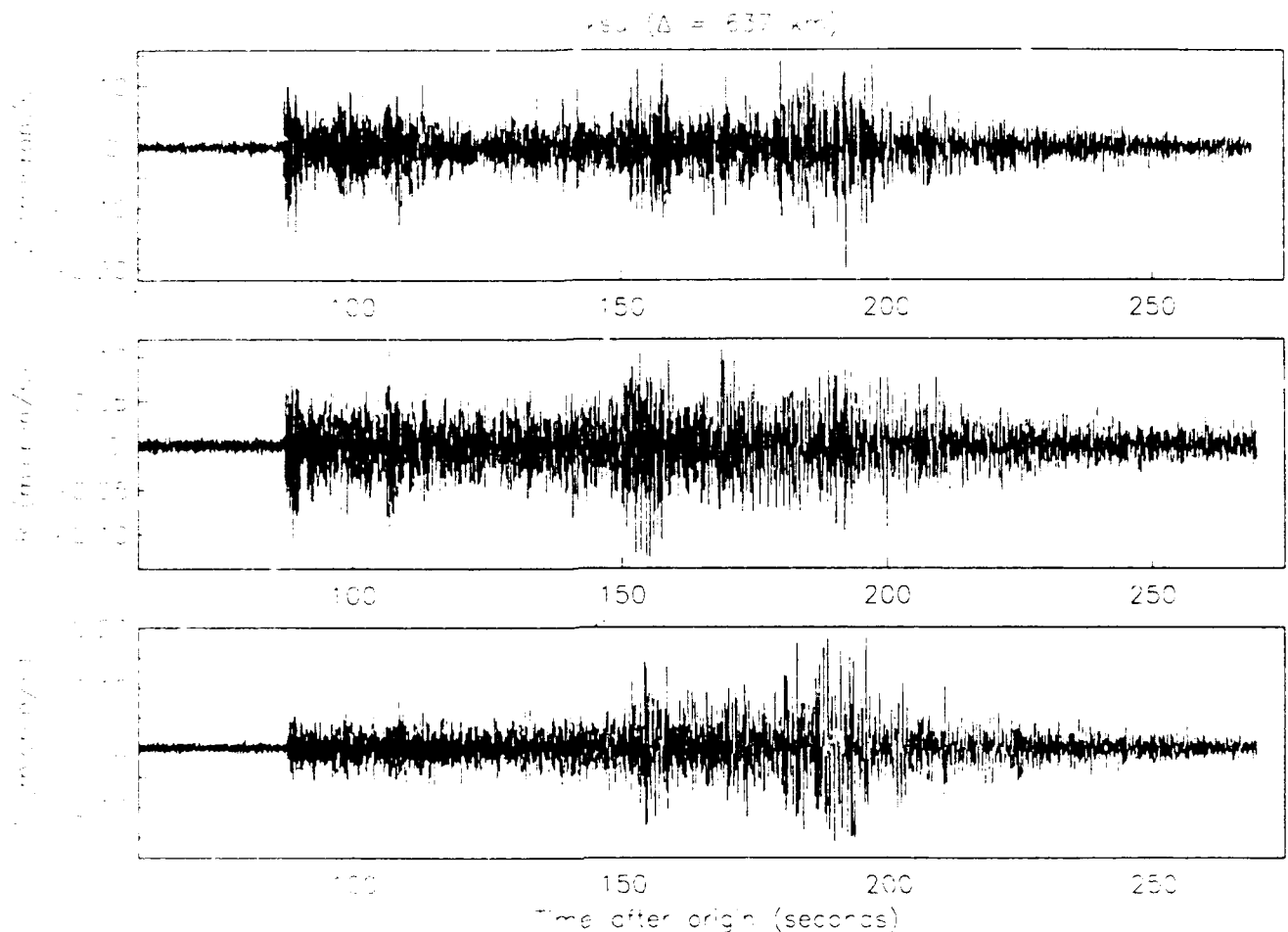


Fig. 4. Three-component seismogram from explosion 3 recorded at KSU, 637 km from the source.

to 4.1 for KSU at 637 km. Explosion 2 L_g spectra (Figure 8) are similar; the maximum signal-to-noise ratio is 200 at 4 Hz at BAY and about 70 at 6 Hz at KKL, decreasing to 50 between 4 and 7 Hz at KSU at 269 km. Note that resolution is lost at KKL and BAY at about 50 Hz, where both signal and noise spectra flatten out due to least count noise from the digitizer because gains were set down on the low-gain channels shown. (High-gain channels clipped at KKL and BAY.) Signal levels are apparent out to 50 Hz at KSU.

Overall, there is little difference between L_g spectra from the two explosions. High-frequency slopes change little if at all with distance, and in most cases the spectral shapes are identical. Absolute spectral levels are more variable and not simply explained by geometric spreading. For example, for explosion 2, spectral levels vary as much between the two equidistant sites as between the near and far sites.

Characteristics of P spectra were more variable. In most cases, P_g was the first arrival or near enough to the first arrival to be clearly identified in the wavetrain. Figure 9 shows signal (upper trace) and pre- P noise spectra (lower trace) from explosion 3 at the western shot site, and Figure 10 shows data from explosion 2 near the test site. A window length of 5 s beginning slightly before the initial arrival was used. Window lengths from 2 to 10 s were tested, but the window had only a minor effect on the gross spectral characteristics. At stations where P_n arrived within 1 s of P_g , inclusion of P_n in the window had almost no effect on the spectra. In Figure 9, P_n is visible as a very low amplitude, lower-frequency arrival preceding the larger

crustal phase by about 0.4 s in the seismograms at BAY and KKL. P_n is the first arrival at KSU at 637 km, and P_g can be seen as the increase in coda at about 10 s (Figure 4). Spectra were calculated for P_n and different parts of the P coda at KSU, but we found that the basic features of the spectra such as the 1-Hz level and high-frequency slope changed very little. The P_n spectrum is shown in Figure 9. For explosion 3, P_g spectral shapes and levels are almost identical for the nearly equidistant stations at KKL and BAY, about 250 km from the source. Maximum signal-to-noise levels are about a factor of 300–400 at these sites, reached at about 7 Hz. The maximum signal-to-noise level for P_n is about 22 at 7 Hz at KSU at 637 km, and appreciable signal levels are seen to about 35 Hz. P_g levels from explosion 2 (Figure 10) are lower than from explosion 3, in spite of the larger source size and smaller distances, most likely due to the effect of the blow out.

Spectra from the crustal phases from the Kazakh chemical explosion experiment in general show high signal levels extending to high frequencies. For comparison with an area of known high crustal attenuation, we computed spectra calculated in the same way from seismograms from a similar explosion experiment in southern Nevada. Figure 11 shows P_g and L_g spectra from a 14-t (TNT) buried explosion, detonated and contained in 48-m-deep boreholes in metamorphic rock, recorded at the Deep Springs and Troy Canyon stations, 188 and 223 km away, respectively. The most dramatic difference is in the signal-to-noise ratios, particularly at high frequencies. S/N approaches 1 between 10 and 20 Hz for P_g and at about 10 Hz for L_g . Noise

KKL ($\Delta = 159$ km)

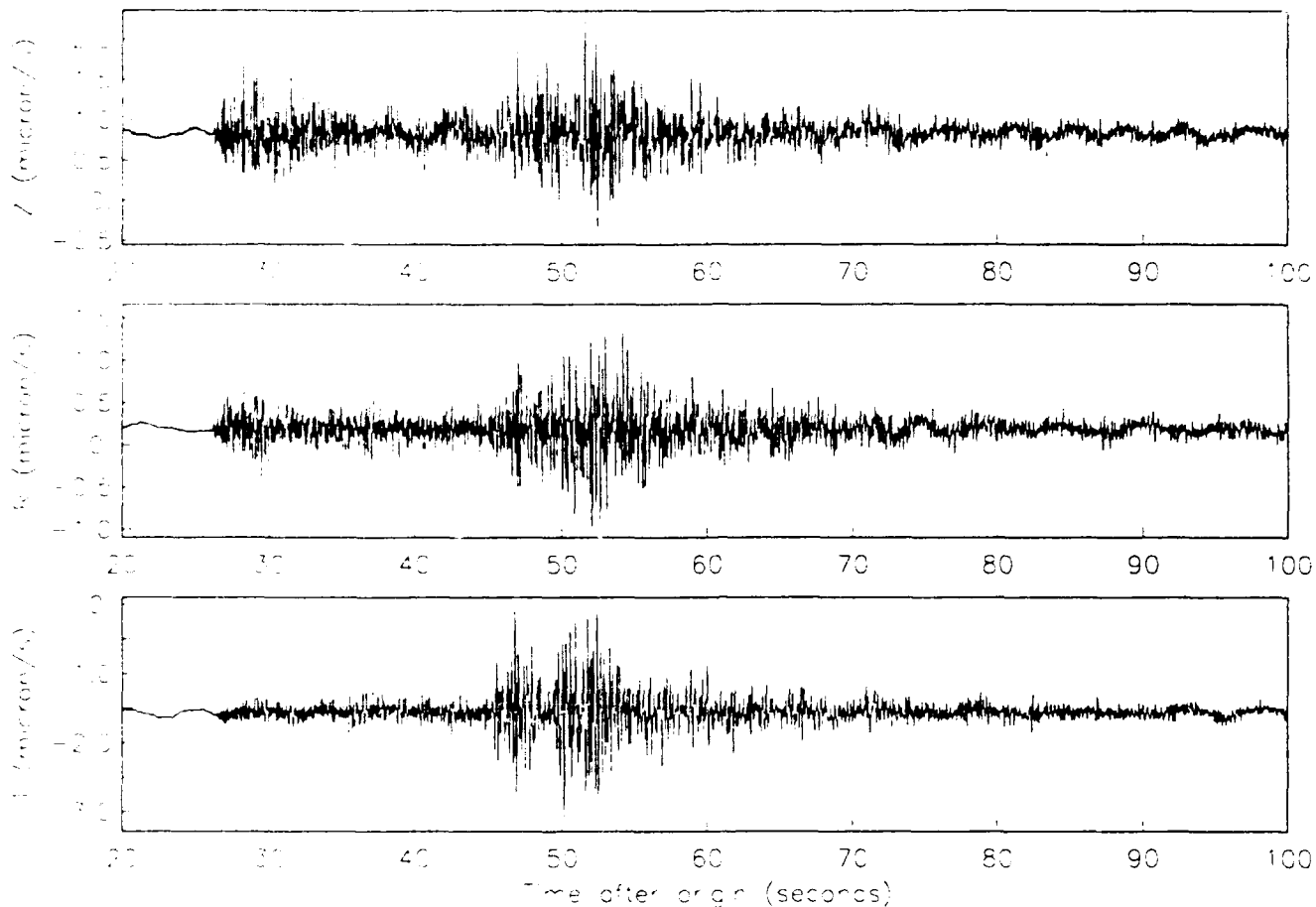


Fig. 5. Seismogram from explosion 2 recorded at KKL, 159 km from the source.

TABLE 2. Layered Crustal Velocity Structure

Depth Range, km	V_p , km s ⁻¹	V_s , km s ⁻¹
0-5	5.40	3.05
5-10	6.15	3.50
10-20	6.35	3.60
20-30	6.55	3.70
30-40	6.75	3.85
40-50	6.95	3.96
>50	8.20	4.65

levels themselves are similar to Kazakh levels. Signal was only about 3 times background noise at the third station, about 400 km away (not shown). Figure 12 compares observed signal-to-noise levels as a function of frequency in Kazakhstan and Nevada.

5. BACK AZIMUTH ESTIMATION FROM *P* WAVE POLARIZATION

We used a method that closely follows *Jurkevics* [1988] to examine the accuracy of event azimuth estimation from three-component *P* waves. A portion of the *P* wave is selected, and the three components are band-pass filtered with a two-pole Butterworth filter centered on a given frequency. A moving window analysis is then done on the filtered seismograms; the data are tapered with a Hanning window, the 3×3 covariance matrix is formed in the window from the three components of ground motion, and the azimuth is taken as the horizontal projection of

the eigenvector of the covariance matrix having the largest eigenvalue. The vertical component is used to resolve the 180° ambiguity by requiring the eigenvector to correspond to a ray arriving from below the station. The strength of this method is that both the time dependence and frequency dependence of the azimuth estimate can be determined.

An example of the azimuth of explosion 1 inferred from the *P* wave arrival at BAY is shown in Figure 13. The azimuth was calculated for four passbands centered on 5, 10, 20, and 40 Hz. The filter width was ± 1 octave around the center frequency. Different lengths for the time window analysis were tested; we found that a window length of $2/f_{center}$, or two cycles of the dominant period of the filtered seismogram, gave stable results for most bands. The window was moved one point at a time, so that the spacing of the azimuth function is the same as the sample rate, 0.004 s. Figures 13b, 13c, 13d, and 13e show the back azimuth as a function of time inferred from 4 s of the *P* wave in the 5-, 10-, 20-, and 40-Hz bands, respectively; the dashed line shows the true back azimuth. For an indication of the signal-to-noise ratio, Figure 13a shows the waveform in the 5-Hz band, and Figure 13f shows the waveform in the 40-Hz band.

The maximum signal-to-noise ratio for the BAY record occurs near 5 Hz (see Figure 9); the azimuth estimation is very stable at this frequency. The 10-Hz band is similar. In the 20-Hz band the initial part of the *P* wave is still well polarized. Signal amplitudes in the 40-Hz band are 0.1 times those in the 5-Hz band (Figure 13f), but the azimuth direction can still be

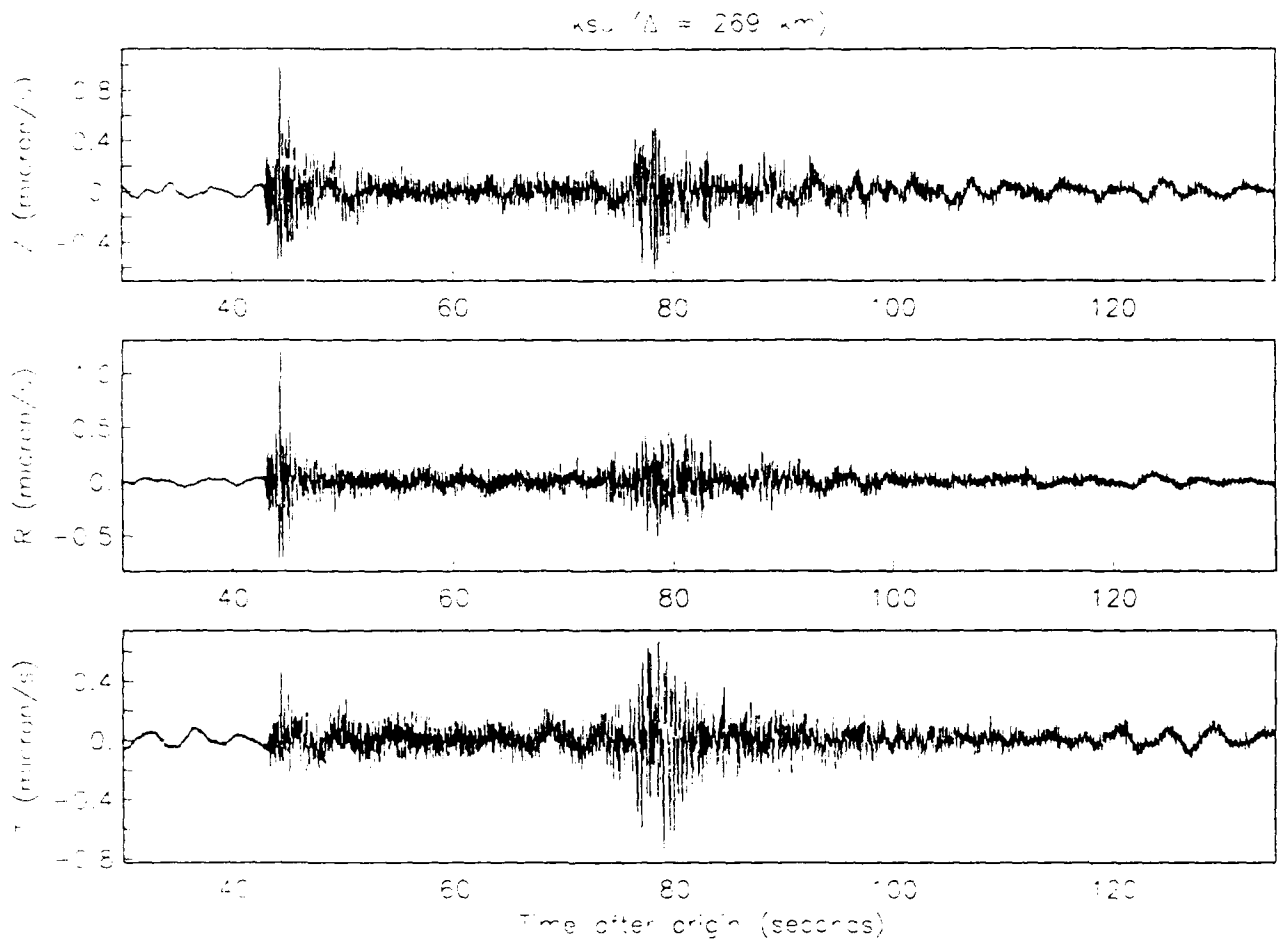


Fig. 6. Seismogram from explosion 2 recorded at KSU, 269 km from the source.

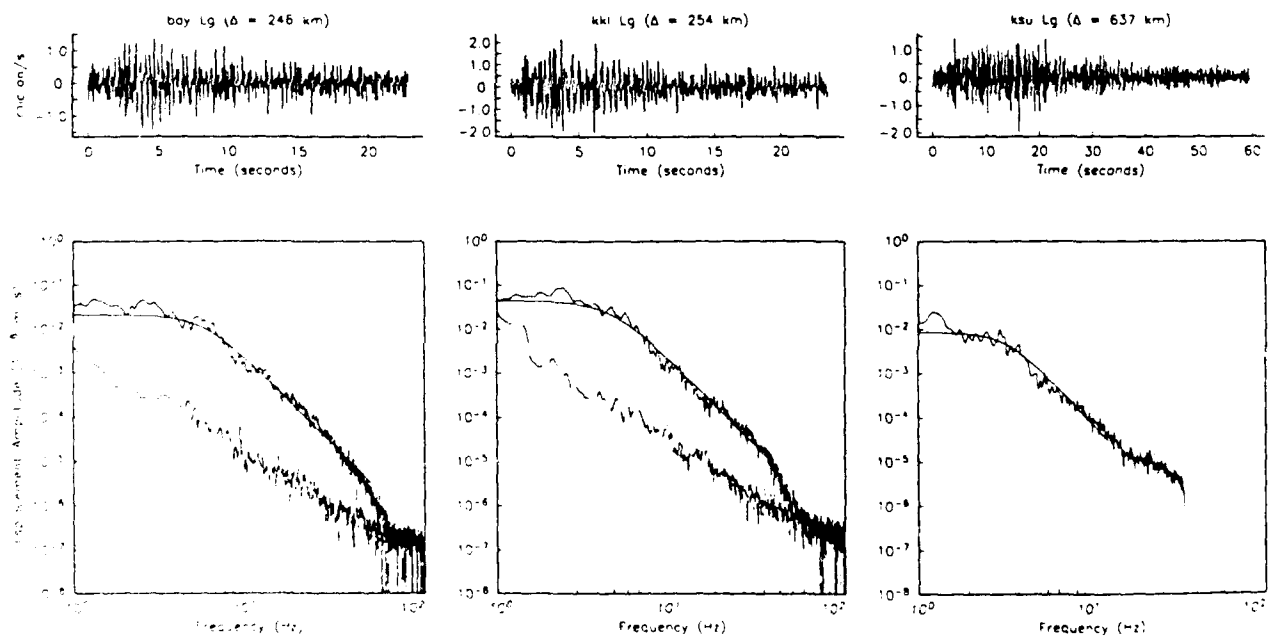


Fig. 7. Displacement amplitude spectra of the L_g wave from explosion 3 (upper traces), shown with noise spectra (lower, dashed) taken just prior to the P arrival. Solid smooth lines represent a parameterized fit to the signal spectra. Velocity time series windows are shown above the spectra.

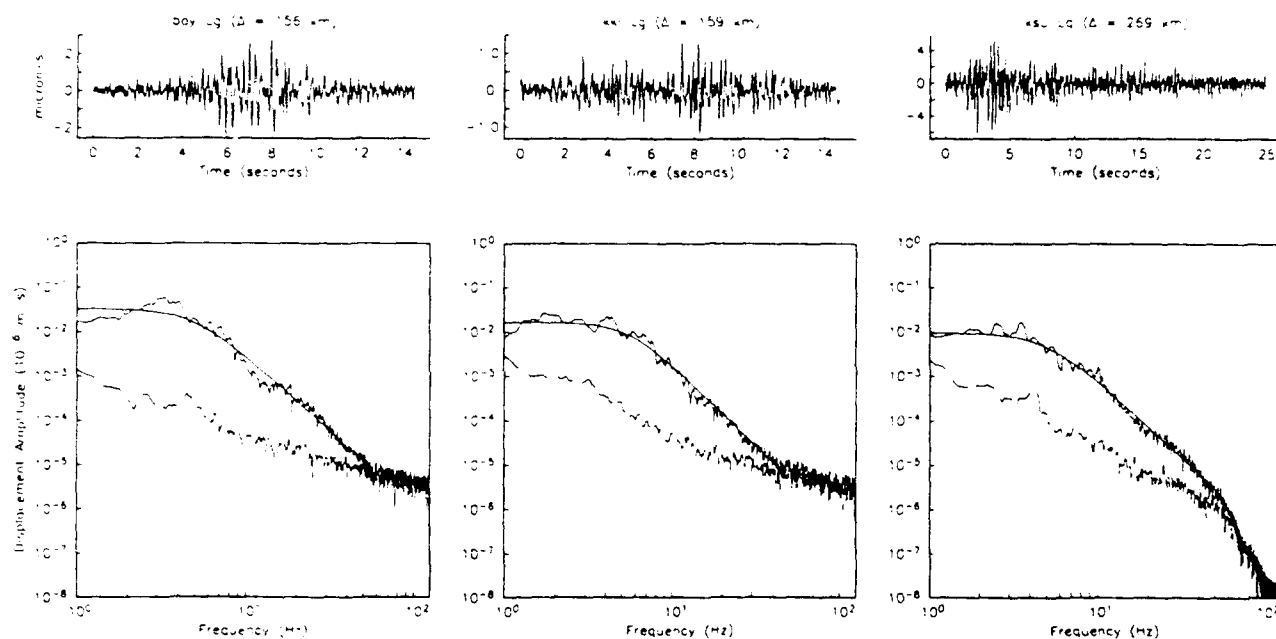


Fig. 8. L_g displacement amplitude spectra observed from explosion 2 shown with pre-P noise.

TABLE 3. Spectral Parameters

Station	Distance, km	Band Fit Hz	1-Hz Level, $\times 10^{-2} \mu s$	f_c , Hz	Slope	S/N_{max}	$f_{S/N_{max}}$	$(L_g/P_g)_1$ Hz
Explosion 3, L_g Waves								
BAY	246	1-60	2.11	6.0	3.8	200	6	1.1
KKL	254	1-50	4.37	4.8	3.8	130	5	2.1
KSU	637	1-14	0.86	5.1	3.4	13	1-2	—
Explosion 2, L_g waves								
BAY	156	1-40	3.29	4.9	3.4	200	4	4.6
KKL	159	1-50	1.64	5.5	3.7	70	6	3.6
KSU	269	1-50	0.95	4.9	3.5	50	6	1.1
Explosion 3, P_g waves								
BAY	246	1-50	1.91	6.8	4.3	400	7	
KKL	254	1-50	2.09	6.9	4.5	300	7	
KSU (P_n)	637	1-35	0.08	6.8	3.7	22	7	
Explosion 2, P_g waves								
BAY	156	1-40	0.72	6.3	3.1	90	7	
KKL	159	1-40	0.45	8.0	3.9	80	10	
KSU	269	1-50	0.84	5.1	3.4	80	8	

recognized; we increased the moving window length to $4/f_{center}$ for more stability. Maximum amplitudes in the 40-Hz waveform occur about 2 seconds after the initial arrival, but the azimuth function is more variable here, implying that the increased later amplitudes are related to P to SV converted energy, increased scattering, or both.

6. CONSTRAINTS ON ATTENUATION FROM CHEMICAL EXPLOSION EXPERIMENTS

Attenuation has a small effect over the distance ranges discussed in the experiment, and thus definitive statements regard-

ing Q are not warranted. As the amplitude spectra shown above revealed, the 1-Hz spectral amplitude levels at farther stations occasionally approached or exceeded those at nearer stations, and the decay of spectral amplitude with increasing frequency changed little with distance. Nonetheless, we will try to estimate apparent crustal attenuation where possible from the explosion data using the standard spectral ratio technique. Note that the geometry of explosion 3 is more suitable for the Q estimate; the range in station azimuth was only 38° , whereas explosion 2 was in the center of the network. Of course, azimuthal heterogeneities and site effects influence amplitude behavior in both cases.

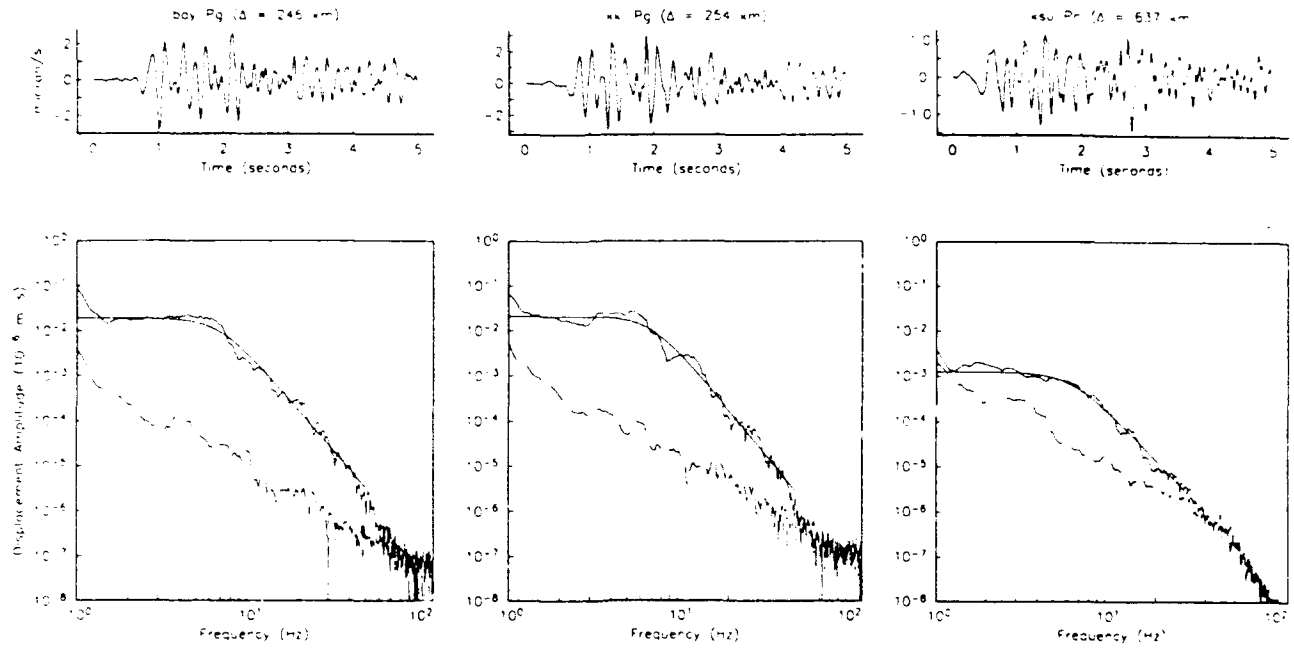


Fig. 9. P_g displacement amplitude spectra from explosion 3, shown with noise. P_n is shown for KSU.

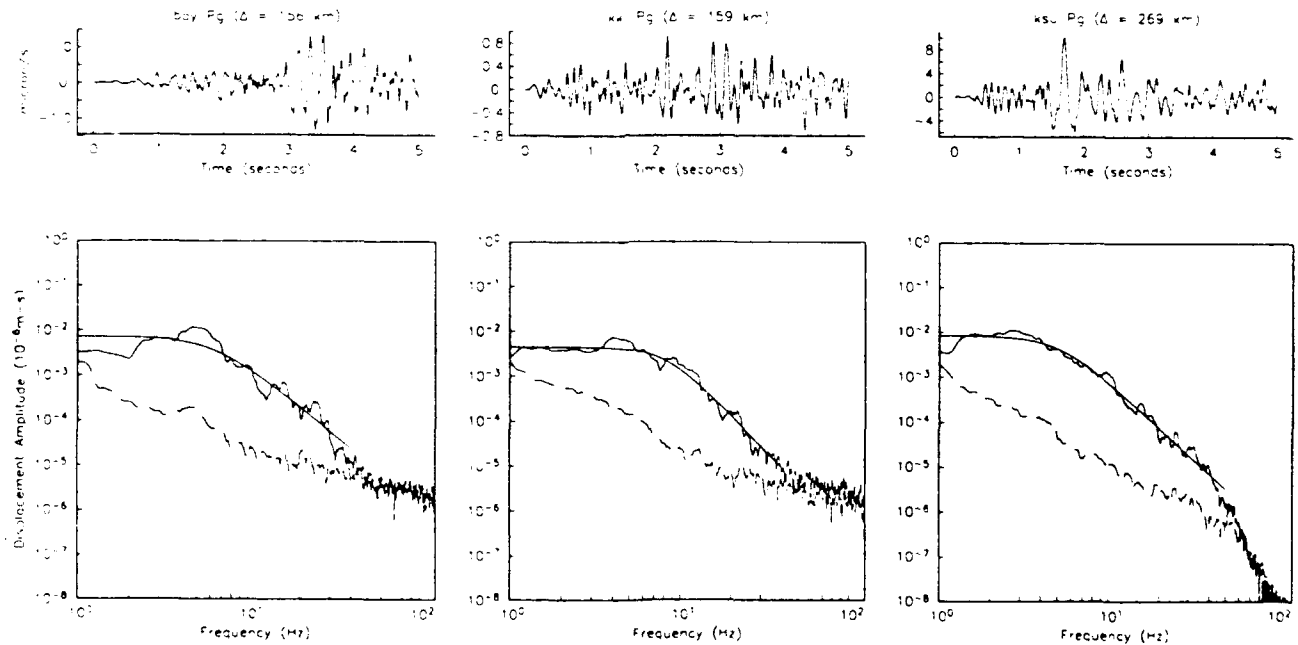


Fig. 10. P_g spectra from explosion 2.

The amplitude spectra $A(f, r)$ is parameterized as

$$A(f, r) = S(f) r^{-\alpha} \exp \left[\frac{-\pi f \Delta}{Q(f) U} \right] \quad (1)$$

where $S(f)$ is the source function, $gexp$ describes geometric spreading, and Δ and U are the source-station distance and group velocity. Assuming there are no azimuthal path heterogeneities or site effects, the quotient of the observed spectra $A_1(f)/A_2(f)$ at two sites of different distances can be used to eliminate the source function and, assuming an appropriate spreading rate, solve for $Q(f)$ via equation (1).

Figure 14 shows $Q(f)$ estimated from various observation pairs of the L_g data. For each explosion, the observed spectra at the nearer stations (KKL and BAY) were divided by the farthest observation (KSU), providing two estimates of Q . Prior to division the spectra were further smoothed by convolution with a cosine function of cycle width 1 Hz; $gexp$ was taken to be 0.5. For explosion 3, the estimate is limited to ≤ 14 Hz by the signal-to-noise quality at KSU at 637 km. The average 1-Hz of Q value is about 500 and increases with frequency, although the dependence is poorly constrained. An approximate dependence of $\sim f^{0.4}$ describes the observation to about 5 Hz, with a possible increased dependence for higher frequencies.

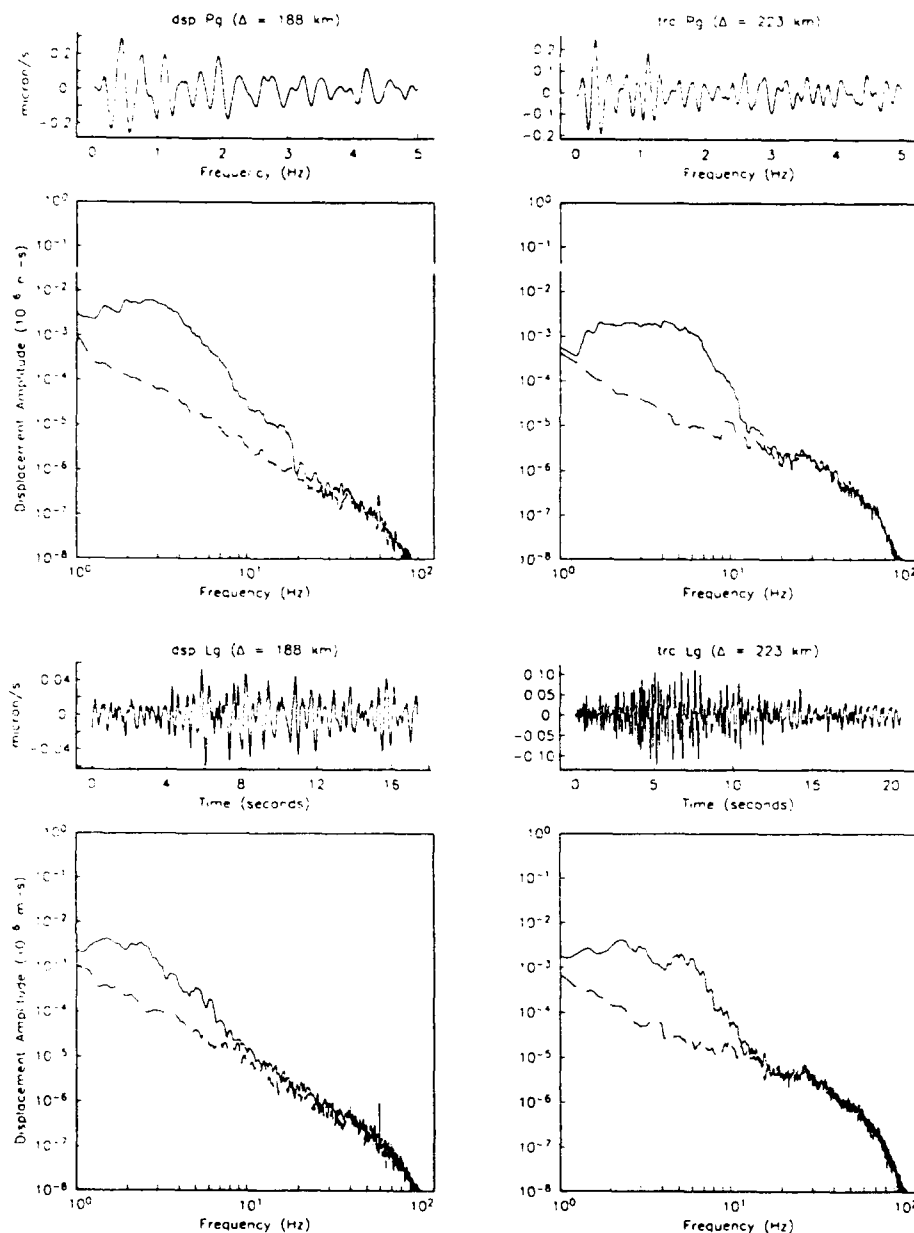


Fig. 11. P_g and L_g displacement amplitude spectra observed at two stations 188 and 223 km from a 14-t borehole explosion in Black Rock, Nevada. Instrumentation and spectral techniques are identical to those used in the Kazakh experiment.

For explosion 2 the distance range and thus the observed change in spectra were less. Remaining modulation in the smoothed spectra caused the observed values of $A(f)$, after correction for spreading, to cross in value at some frequencies, resulting in an unstable estimate. The parameterized fits to the observed spectra are, however, smooth, and these were used in place of $A(f)$ to obtain a Q estimate from the explosion 2 data (Figure 14). The KKL curve from explosion 2 is in general consistent with the explosion 3 observations; BAY gives a lower Q estimate because the broad peak in the observed spectrum at 3–4 Hz caused the fit to be about twice the KKL level, at essentially the same distance (Table 3 and Figure 8).

P_g Q estimates proved to be problematic. P_g was not well observed at 637 km from explosion 3. Explosion 2 P_g spectral levels at 269 km slightly exceeded those at 156 km at lower frequencies, suggesting that the ray paths contributing to the

energy in this window change with distance and thus little can be said about Q without more detailed information regarding the structure. Explosion 2 data above 10 Hz suggest that a lower limit of P_g Q is about 2000, but this is at best a tenuous inference.

Sereno *et al.* [1988] compiled results of L_g Q studies for various geographic regions by many authors from 1 to 7 Hz. The Q estimate from the chemical explosion data falls near the high end of the models, higher than western United States, France, and Africa, somewhat higher than Scandinavia over 3 Hz, and somewhat lower than eastern North America models [Sereno *et al.*, 1988, Figure 4]. This shows promise that a detailed study of the Kazakh data set, using the many quarry blasts and regional earthquakes recorded during the project, can more completely constrain the effective L_g Q . In particular, a larger distance range will guarantee that the average effect of

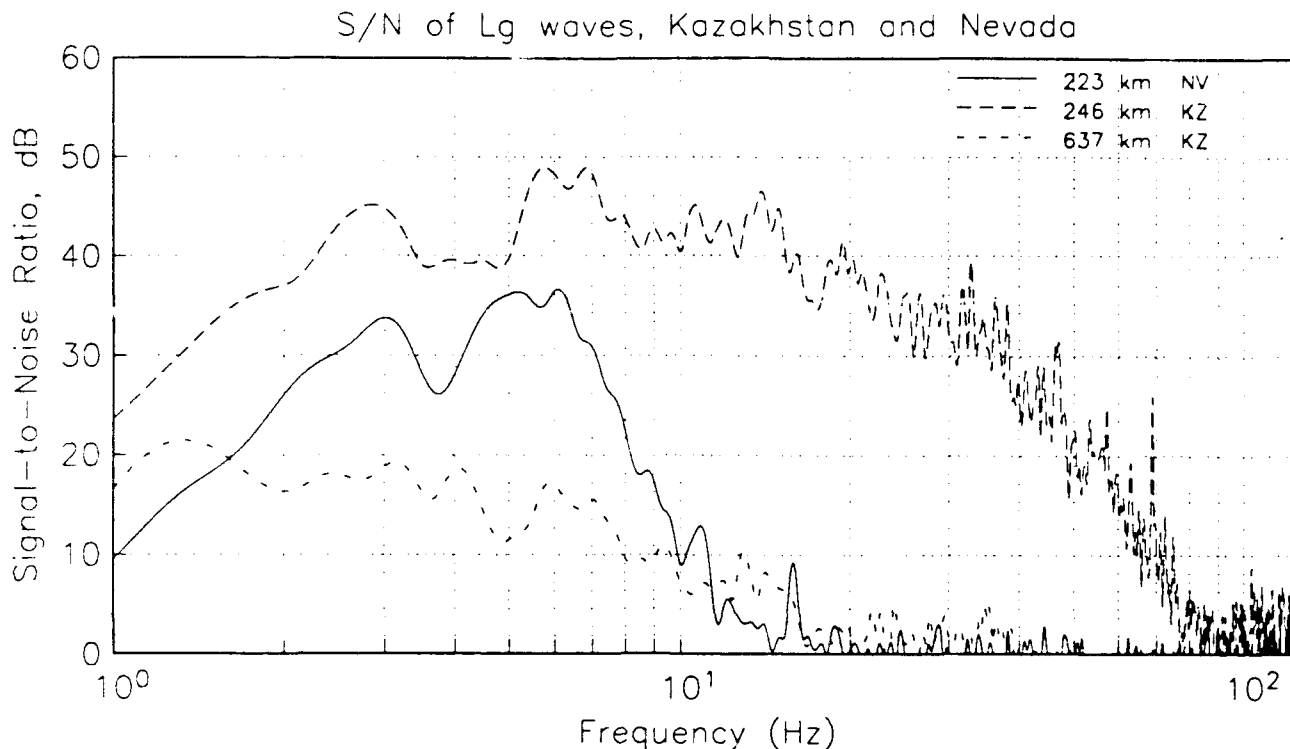


Fig. 12. Signal-to-noise ratios (in dB) for three L_g observations: 10-t explosion in Kazakhstan at 246 and 637 km, and 14-t explosion in Nevada at 223 km. L_g signal levels are sustained at higher levels and to higher frequencies for the Kazakh explosion.

the deeper crustal layers are included, which may result in Q estimates comparable with eastern North America.

For a measure of magnitude, we compare two regional magnitude expressions. The first was derived at Uppsala University for use with small regional events in Scandinavia [Båth *et al.*, 1976]; it is based on Richter M_L magnitude but includes a correction function to M_L that depends on distance and frequency appropriate to Scandinavia. The second is $m_L(f)$, defined by Herrmann and Kijko [1983], which is based on Nuttli's [1973] m_{ML} but is more appropriate for use with instruments where the maximum L_g amplitude occurs at frequencies above 1 Hz. For the Uppsala magnitude the spatial attenuation function is included in the correction factor; for $m_L(f)$, we use $Q(f) \sim 500 f^{0.4}$ estimated above to obtain the spatial attenuation factor γ . In both cases the velocity seismograms were converted into ground motion displacement time series before measuring the maximum L_g amplitude and its frequency from the vertical component. Frequencies of the maximum amplitude ranged from 1.4 to 4.1 Hz. Amplitudes measured from explosion 1 records, with the same source and location as explosion 3, were identical to explosion 3 at all stations.

From the Uppsala relation, the average magnitude of explosion 3 is 2.8, with station values of 3.1 (BAY), 3.0 (KKL), and 2.2 (KSU). Explosion 2 average magnitude is 2.6, with station values of 2.9 (BAY), 2.4 (KKL), and 2.6 (KSU). Thus much smaller values for KSU from explosion 3 suggests that the relation appropriate for Scandinavia may not be the best for Kazakhstan, an issue that more magnitude measurements must address. Using $m_L(f)$, average magnitudes are larger, 3.3 for explosion 3 (3.5 (BAY), 3.4 (KKL), 3.1 (KSU)) and 3.0 for explosion 2 (3.2 (BAY), 2.8 (KKL), 2.9 (KSU)). If Herrmann

and Kijko's [1983] value of γ ($0.001/\text{km } f^{0.7}$) for the eastern United States is used rather than that based on the Q estimate from this study, magnitudes are 0.10–0.15 units smaller.

The energy class parameter K , used more commonly in the Soviet literature, is based on the amplitudes of both P and S waves and is proportional to $\log E$ where E is the energy in Joules. To determine K for the chemical explosions, values were read from calibration charts of Rautian [1964], who first defined the parameter. Average values of K from explosion 2 and 3 are nearly equal at 10.8 and 10.5, respectively.

7. CONCLUSIONS

The major conclusion of the chemical explosion experiment is that crustal signal levels in eastern Kazakhstan from small sources are high and persist to high frequencies. For example, signal-to-noise levels reached a maximum of 400 for P_g waves and 200 for L_g waves 250 km from a 10-t explosion, and S/N for both phases approached 1 at about 50 Hz. This is very different from a similar explosion experiment in Nevada, where signal-to-noise levels were observed to be 140 for P_g waves and 50 for L_g waves for a 14-t explosion at 223 km; S/N approached 1 at 14 Hz for P_g and 10 Hz for L_g .

Crustal phases consistent with a mantle depth of 50 km were observed in Kazakhstan. S_n is large at larger distances and has a velocity of 4.2 km s⁻¹.

Attenuation has little effect on crustal propagation at these distances; we estimated effective attenuation for crustal L_g to be about 500 at 1 Hz, increasing at higher frequencies as about $f^{0.4}$. Q for crustal P is not resolvable from the explosion data. Although the explosion experiment does not constrain Q with much confidence, the high quality of the Kazakh data shows

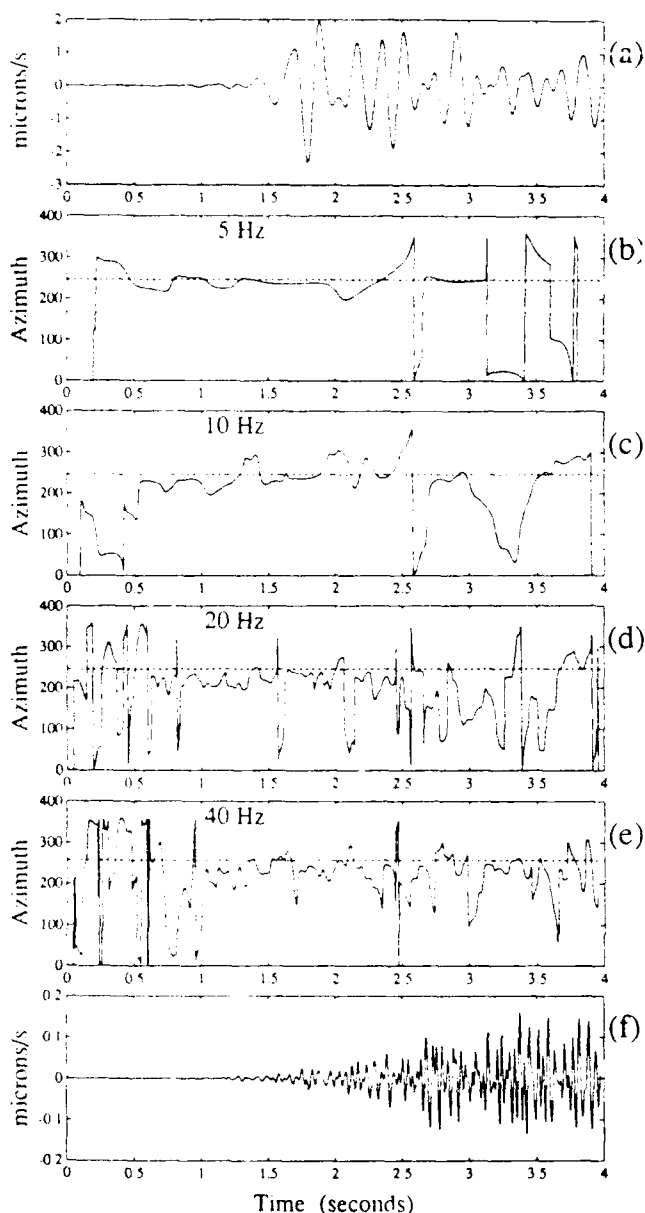


Fig. 13. Back-azimuth from BAY to explosion 1 inferred from polarization analysis of three-component P wave data in different pass bands. (a) Vertical component P wave filtered at 5 Hz; (b) Back azimuth function inferred in the 5-Hz band, where the dashed line indicates the true back azimuth; (c) in the 10-Hz band; (d) in the 20-Hz band; (e) and in the 40-Hz band. The moving window length for the 40-Hz calculation was increased for a smoother estimate. (f) Vertical component P wave filtered at 40 Hz.

promise for in-depth attenuation and other seismological studies, particularly as extended to high frequencies.

Acknowledgments. The Natural Resources Defense Council, Inc., and the Academy of Sciences of the Union of Soviet Socialist Republics jointly operated the seismic stations used in this study and provided funding for the field experiment. Analysis was supported by the National Science Foundation, grant EAR87-08478, the Air Force Geophysical Laboratory, grant F19628-88-K-0044, the Soviet Academy of Sciences, and the Natural Resources Defense Council. H. K. Given acknowledges funding from the Institute on Global Conflict and Cooperation, University of California. Yevgeni Velikov, Mikhail Gokhberg, Nikolai Yuknin, Thomas Cochran, Jacob Scherr, and Charles Archambeau provided advice and organizational support for the explosion exper-

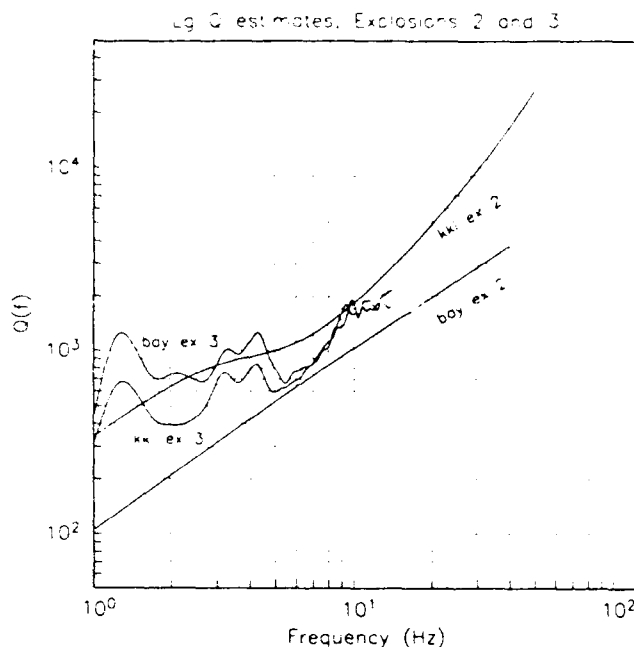


Fig. 14. Estimate of Q vs. frequency from spectral ratios of L_g waves of Kazakh data. Explosion 3 estimates are limited to 14 Hz by the signal levels at 637 km. Explosion 2 estimates used the parameterized fits to the observed spectra rather than the observations themselves.

iment; Felix Tregub supervised the explosion preparations in Kazakhstan, and Elena Anns coordinated transportation. An excellent field team staffed the Kazakh stations: Larry May, Sergei Aptukaev, Joan Gomberg, Daniel Harkins, and especially David Chavez, James Batti, Valeri Kuhnukov, Oleg Rigalov, and Tamara Nagovonskaya, who endured two weeks of tube living on the steppes of central Asia. James Brune sited the Nevada stations, and Bill Honjas supervised their construction as well as the site preparation for the Broken Hills, Nevada, explosion; Ed Crylie supervised detonation. We acknowledge David Chavez, John Ebel, Jeffrey Given, J. Bernard Minster, and the anonymous reviewers for discussion and review.

REFERENCES

- Antonenko, A.N., *Deep Structure of the Earth's Crust in Kazakhstan* (in Russian), 274 pp., Academy of Sciences of the Kazakh SSR, Alma-Ata, 1984.
- Båth, M., O. Kulhánek, T. Van Eck, and R. Wahlström, Engineering analysis of ground motion in Sweden: Fourier and response spectra, attenuation, regional magnitude, energy, acceleration, Rep. 5-76, 48 pp., Seismol. Inst., Uppsala Univ., Uppsala, Sweden, 1976.
- Berger, J., L. N. Baker, J. N. Brune, J. B. Fletcher, T. C. Hanks, and F. L. Vernon, The Anza array: A high dynamic-range, broad-band, digitally recorded, radio-telemetered seismic array, *Bull. Seismol. Soc. Am.*, 74, 1469-1482, 1984.
- Berger, J., H. K. Eissler, F. L. Vernon, I. L. Nersisov, M. B. Gokhberg, O. A. Stolyrov, and N. T. Tarasov, Studies of high-frequency noise in eastern Kazakhstan, *Bull. Seismol. Soc. Am.*, 78, 1744-1758, 1988.
- Hedlin, M. A. H., J. B. Minster, and J. A. Orcutt, The time-frequency characteristics of quarry blasts and calibration explosions recorded in Kazakhstan U.S.S.R., *Geophys. J. R. Astron. Soc.*, in press, 1989.
- Herrmann, R. B., and A. Kijko, Short-period L_g magnitudes: Instrumentation, attenuation, and source effects, *Bull. Seismol. Soc. Am.*, 73, 1835-1850, 1983.
- Jurkevics, A., Polarization analysis of three-component array data, *Bull. Seismol. Soc. Am.*, 78, 1725-1743, 1988.
- Leith, W., Geology of the NRDC seismic station sites in eastern Kazakhstan, USSR, *U.S. Geol. Surv. Open File Rept.*, 87-597, 13 pp., 1987.
- Nuttli, O. W., Seismic wave attenuation and magnitude relations for eastern North America, *J. Geophys. Res.*, 78, 876-885, 1973.

- Park, J., F. L. Vernon III, and C. R. Lindberg, Multitaper spectral analysis of high-frequency seismograms, *J. Geophys. Res.*, 92, 12,675-12,684, 1987.
- Rautian, T. G., On the determination of energy of earthquakes at distances up to 3000 km, *Tr. Inst. Fiz. Zemli Akad. Nauk*, 32(199), 88-93, 1964.
- Sereno, T. J., S. R. Brau, and T. C. Bache, Simultaneous inversion of regional wave spectra for attenuation and seismic moment in Scandinavia, *J. Geophys. Res.*, 93, 2019-2035, 1988.
- Thomson, D. J., Spectrum estimation and harmonic analysis, *IEEE Proc.*, 70, 1055-1096, 1982.
- Thurber, C. H., H. K. Given, and J. Berger, Regional event location with a sparse network: Application to eastern Kazakhstan, USSR, *J. Geophys. Res.*, in press, 1989.
- Vernon, F. L., Analysis of data recorded on the ANZA seismic network, Ph.D. thesis, 191 pp., Univ. of Calif., San Diego, La Jolla, 1989.
- J. Berger, H. K. Given, and F. L. Vernon, Institute of Geophysics and Planetary Physics, Scripps Institution of Oceanography, University of California, San Diego, La Jolla, CA 92093.
- I. L. Nersisov, N. T. Tarasov, and V. Zhuravlev, Institute of Physics of the Earth, Academy of Sciences of the USSR, Bolshaya Gruzinskaya 10, Moscow 123810, USSR.

(Received June 15, 1988;
revised August 3, 1989;
accepted June 25, 1989.)

The time–frequency characteristics of quarry blasts and calibration explosions recorded in Kazakhstan, USSR

Michael A. H. Hedlin, J. Bernard Minster and John A. Orcutt

Institute of Geophysics and Planetary Physics, Scripps Institution of Oceanography, University of California at San Diego, La Jolla, CA 92093, USA

Accepted 1989 April 9. Received 1989 April 7; in original form 1989 January 10.

SUMMARY

In this paper we consider two fundamentally different processes that can be responsible for the organization of energy in seismic coda into discrete time-independent frequency bands. One process involves the resonance of energy in low velocity horizons and the other requires the interaction of time offset wavefields produced by subevents within multiple-event mine explosions (ripple-fired quarry blasts). We examined data collected by high frequency seismometers in Kazakhstan, USSR, and observed regular time-independent spectral modulations in coda resulting from events strongly suspected to be Soviet quarry blasts, but not in the coda from single event calibration explosions detonated at similar ranges. We conclude these modulations are a source effect and due to ripple-firing. This modulation is independent of the source–receiver azimuth and we infer that the spatial array of subshots in each event must be small. We demonstrate that simple linear superposition theory can be used to reproduce effectively the spectral modulation observed in real quarry blasts. On the basis of these observations we attempt to discriminate between the two types of events using a spectral pattern-based algorithm that seeks time-independent features. We consider the detrimental effect that resonant energy in low velocity horizons can have on the successful application of our algorithm.

Key words: explosions, seismic coda, seismic discrimination, USSR

INTRODUCTION

In theory any process that introduces a regular repetition into a seismic wavetrain will impress upon the spectrum of that energy a regularly spaced modulation. Superposed regular modulations were observed in spectra computed from P_n and S_n coda collected in the SW Pacific in 1983 during Scripps' Ngendei expedition. These were explained by Sereno & Orcutt (1985a,b) as being due to the resonance of energy in the water and sedimentary columns near the receiver. This mechanism has provided an elegant alternative explanation to the scattering theory previously held by many as the dominant source of coda generation in the oceanic lithosphere.

We have recently observed very similar spectral modulation in data collected in the Soviet republic of Kazakhstan in 1987. This dataset includes calibration events, where the source–time function is presumably relatively simple, and many other regional events, a large fraction of which are likely mine explosions. This unusual spectral modulation is only observed in the latter events and thus we suspect that it is not a propagation effect, as was the case in the Ngendei dataset. For example, Baumgardt & Ziegler (1988) discuss a commonly used technique in mining known as ripple-firing. In this practice a number of subexplosions

are staggered in time and space to reduce ground motions in areas proximal to the mine as well as to enhance the fracturing of the rock. The most plausible explanation of the spectral modulation we observe in the Soviet data is that it is a source effect which stems from the highly repetitive nature of ripple-fired mine explosion source–time functions.

Although the physics behind these two types of modulations is fundamentally different, the effect they have on the spectra of the recorded energy is strikingly similar. We predict mathematically that both processes are capable of impressing a time-independent modulation on the spectra of seismic wavefields.

We feel the problem of discriminating ripple-fired mine explosions (quarry blasts) from underground nuclear explosions has become increasingly important and deserves close scrutiny. As discussed by Stump & Reamer (1988), a reduced Threshold Test Ban Treaty would bring the magnitude of the largest allowable nuclear explosions down to that of large 'engineering' explosions otherwise known as quarry blasts. The problem of discriminating quarry blasts from other events is not a new one, and has been investigated by several other authors. Aviles & Lee (1986) considered quarry blasts and earthquakes on the west coast of the United States and found they had success in discriminating between the two types of events by

computing ratios of the spectral energy at 1.5 and 12 Hz. They found quarry blasts to be relatively deficient in high frequency energy and proposed a preferred attenuation of high frequency energy near the quarry blast source by near-surface fractures. Although this method may be valid in the western US it seems that its success would be highly dependent on mining practice and the geology of the region in which the discriminant is being used. As we discuss later, the ratios of power in any two frequencies is highly dependent on the geometry and timing of the subshots in the quarry blast sequence.

Many authors have performed cepstral analyses of multiple source events. The cepstrum, which is the Fourier transform of the log of the spectrum (Tribolet 1979), is sensitive to regular spectral modulation in the coda of multiple source events. Baumgardt & Ziegler (1988) showed that cepstra of ripple-fired sources display power highs at certain time dependent on the timing of the shots in the quarry blast sequence. A weakness of studies which employ the cepstrum for discrimination purposes is that simple events (earthquakes and single shot explosions) can possess significant cepstral structure. The cepstra computed by Baumgardt & Ziegler (1988) from the coda of some earthquakes illustrate this point. The problem of discrimination becomes somewhat arbitrary when it must be decided how much structure is sufficient to identify an event as a quarry blast.

Gupta *et al.* (1984) attempted to discriminate between single and multiple-event explosions and earthquakes and explored several methods which were based on the expected differences between the distribution of energy in P_g and L_g phases at a variety of frequencies. The expected differences they discussed were mainly due to the proximity of explosions to the free surface and their omnidirectionality (resulting in their relative inability to generate SH energy). They found that each of the proposed discriminants taken separately had a high failure rate and thus it was necessary to combine all of them into a multivariate discriminant. They observed large differences in the P_g and L_g phases excited by two proximal nuclear explosions and attributed the wide variability in their results to the sensitivity of the P_g and L_g phases to near-source effects.

We feel that a successful discriminant must be relatively independent of the variability of seismic phases, of mining practice and geological setting. In this paper we suggest that the property that best distinguished multiple-shot explosions from all other seismic events is the persistence through time of prominent spectral features in the onsets and coda produced by these complex events. We propose a time versus frequency pattern-based discriminant which seeks long-lived spectral features in seismic coda. The concept of exploiting the time-independence of the spectral modulation induced by ripple-firing the source is not entirely new and was previously suggested by Bell (1977).

SPECTRAL MODULATIONS IN SEISMOGRAMS

Sereno & Orcutt (1985b) demonstrate the significant influence of low velocity horizons in the oceanic environment on coda duration and amplitude. This layer resonance enriches the spectrum of the coda at certain

equispaced eigenfrequencies, determined by the layer thickness and velocity. Considering a relatively simple case in which a wavelet $w(t)$ is reverberating in a single low-velocity surface layer, the linear sum of all reverberations $x(t)$ equals:

$$x(t) = w(t) * \left[\frac{1}{T} \text{III} \left(\frac{t}{T} \right) \cdot e^{-\alpha|t|} \cdot H(t) \cdot e^{-\alpha|t|/T} \right]. \quad (1)$$

The time between successive reverberations is represented by T and to a good approximation equals the two-way vertical travel time in the horizon. The 'shah' function is tapered exponentially to simulate the effect of attenuation and is multiplied by the Heaviside step function to exclude any acausal energy. The final exponential is required by the π phase shift incurred by reflection at the free surface.

By Fourier transforming the preceding equation the authors found that the spectrum of the original wavelet is multiplied by an infinite set of staggered tapering functions which decay at a rate controlled by and proportional to the attenuation parameter α . The amplitude spectrum of the sum of wavelets is given by:

$$|\tilde{X}(f)| = |\tilde{W}(f)| \cdot \left| \text{III} (fT + 1/2) * \left(\frac{\alpha - i2\pi f}{\alpha^2 + 4\pi^2 f^2} \right) \right|. \quad (2)$$

The thicker—or equivalently, the slower—the horizon the more closely spaced the spectral highs will be. In the simple case where one horizon is responsible for the bulk of the resonance and the receiver is a significant distance from the source (so that the incident energy has high phase velocity) the period of the modulation observed on vertical or horizontal component sensors is largely independent of time in the coda (Hedlin, Orcutt & Minster 1988). Sereno & Orcutt (1985b) point out that in situations where two or more different modulations are superposed, either due to more than one resonating horizon or the combination of compressional and shear resonance in the same horizon, the interference of the competing modulations can produce time-dependent behaviour, most likely manifested as an evolution to lower frequency content as time progresses.

We now consider the theory underlying a distinctly different origin of spectral modulation, one originating at the source rather than through propagation. We consider a simple model of a ripple-fired mine explosion (quarry blast) in which all subshots occur at the same point in space and are offset from each other by equal time spans T . In addition we assume that all wavelets produced by each subshot $w(t)$ are identical and superpose linearly. Approaching the problem in the manner of Sereno & Orcutt (1985b) we can compute the seismogram $x(t)$ produced by the entire suite of subshots by convolving the wavelet (coda) produced by each identical subexplosion by the finite duration 'shah' function:

$$x(t) = w(t) * \left[\frac{1}{T} \text{III} \left(\frac{t}{T} \right) \cdot B \left(\frac{t}{D} \right) \right]. \quad (3)$$

The shah function is multiplied by the boxcar function $B(t)$ which lasts D seconds, the duration of the entire suite of subshots in the quarry blast. By Fourier transforming (3) we find that the spectrum of the entire seismogram equals that of an individual shot multiplied by an infinite set of

1,2,3,4,5 shot 100 msec modulations

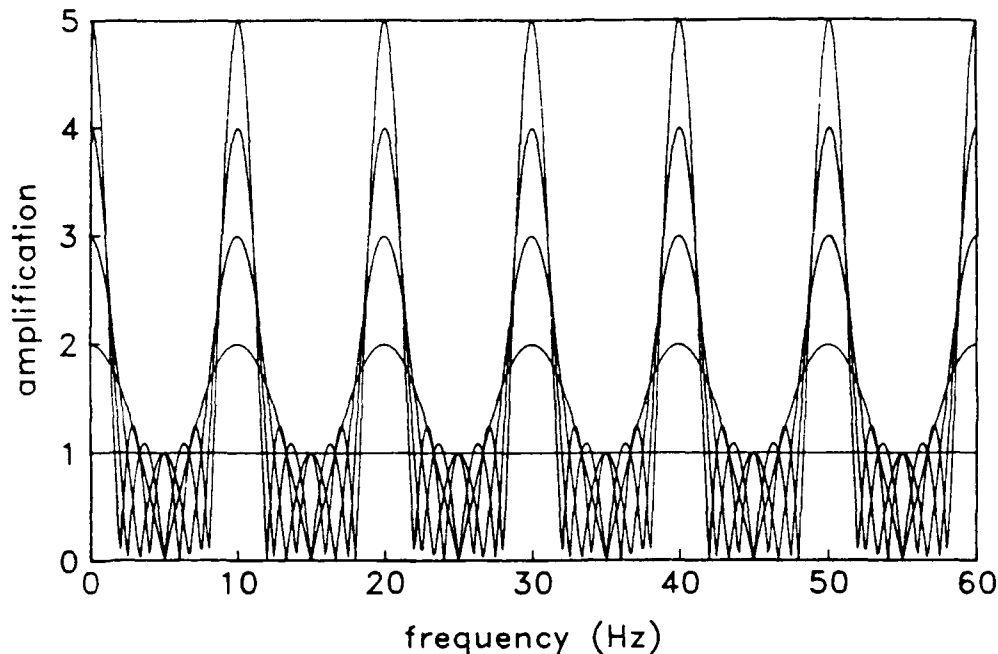


Figure 1. Spectral modulations predicted for events consisting of one to five subshots spaced evenly at 100 ms.

equispaced 'sinc' functions:

$$\bar{X}(f) = \bar{W}(f) \cdot \left(\text{III}(fT) * \frac{\sin(\pi f D)}{\pi f} \right). \quad (4)$$

Although the physics behind the two processes that lead to modulations are fundamentally different, the mathematics that describe them at this simple level are extremely similar. The principal difference between the two models arises from the shah function which convolves the starting wavelet and is truncated by the boxcar describing the abrupt beginning and end of the quarry blast source. In the P_n propagation problem the overall modulation arises from a smoother function which reflects the loss of energy due to attenuation. Figure 1 displays the modulation caused by linearly superposing the wavelets produced by one to five subshots located at the same point in space and delayed 100 ms from each other. The amplification at the preferred frequencies, equals the number of subshots. The degree to which the energy is confined to the preferred frequencies is directly dependent on the duration of the quarry blast set. By inspection of equation (4) one can see that the smaller the spacing between successive shots, the more broadly spaced the modulation in the frequency domain will be. The spacing is equivalent to the inverse of the shot spacing and, as is displayed in Fig. 1, a 100 ms spacing results in a frequency spacing of 10 Hz. In this idealized case the modulation is independent of time.

More general mine explosions, involving arbitrary offsets in time, can be simulated in a similar manner. The theory has been dealt with by Baumgardt & Ziegler (1988) but is similar to that described above provided the scatter of offset times is not too great. Again linear superposition is

assumed.

$$x(t) = \sum_{i=1}^n w(t - T_i). \quad (5)$$

The absolute time of each of the n subevents (relative to the first event) equals T_i . After Fourier transformation we find that the amplitude spectrum of the sum of wavelets equals:

$$\bar{X}(f) = \bar{W}(f) \cdot \left[\left(\sum_{i=1}^n \cos(2\pi f T_i) \right)^2 + \left(\sum_{i=1}^n \sin(2\pi f T_i) \right)^2 \right]^{1/2} \quad (6)$$

The energy from one subevent is multiplied by a sum of sines and cosines, and is still organized preferentially into time-independent frequency bands provided that the scatter of time delays from a constant value is not too great. Figure 2 displays the modulation pattern expected from an event consisting of 50 subshots. The time delays between adjacent events are distributed normally with a mean value of 63 ms and a variance of 6.3 ms. The power is concentrated near the simply predicted frequencies of 16, 32 and 48 Hz, although as the frequency of the overtone increases so does the scatter. This model is undoubtedly more realistic than the first. Although the mining engineers may want their subshots to adhere to a regular time-spacing there may be considerable deviation from this in practice (Stump & Reamer 1988). Using high-speed photographic observations of the subshot blast times in quarries in the eastern US these authors observed that deviations between the intended and actual times were as high as 34 percent. In addition, no true quarry blast consists of a number of discrete events all located at the same point in space. True quarries employ a

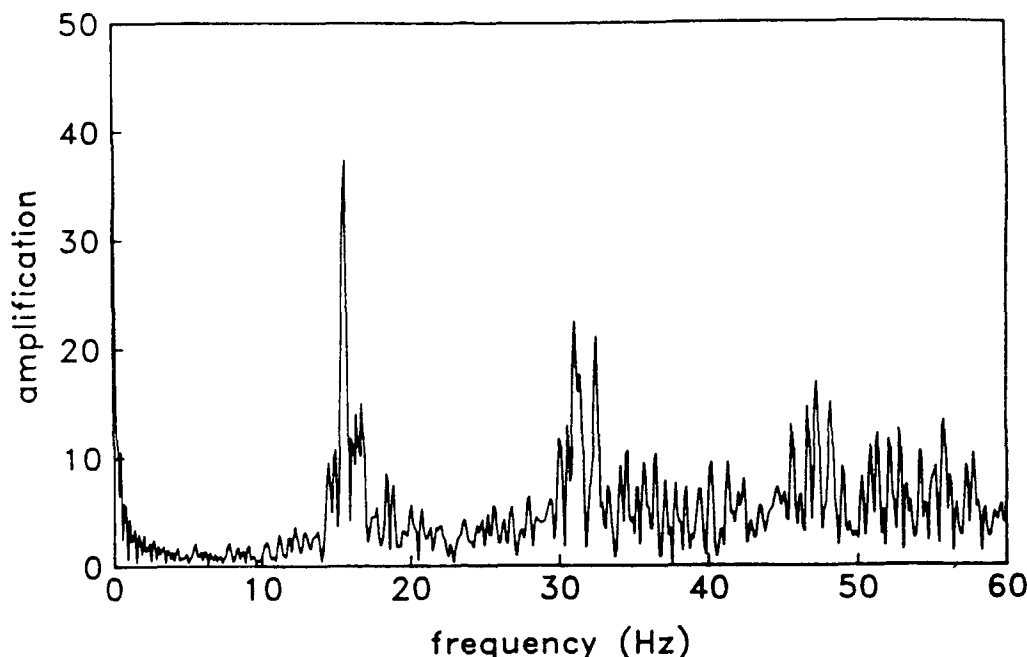
50 shots $t_{av} = 63$ msec, $t_{var} = 6.3$ msec

Figure 2. Spectral modulation predicted for an event consisting of 50 subshots. The offset times are distributed as a Gaussian with a mean of 63 ms and a variance of 6.3 ms.

spatial array of subshots in blasting. These spatial offsets are equivalent to apparent offsets in time that depend on the slowness of the energy being considered and the azimuth from the mine to the receiver. They will, along with the true scatter, introduce a deviation from a regular time spacing but will not altogether destroy the organization of the energy into time-independent bands provided that the shot array dimensions are not too great. Although this is quite easily dealt with (Smith 1989), as will be discussed later it appears that we do not need this refinement to interpret the events we examine in this study.

THE DATA SET

The data used for this study were collected in 1987 in the Soviet republic of Kazakhstan roughly 200 km from the Semipalatinsk underground nuclear test site. Three receiver sites were established in the spring of 1987 in a triangular array near the towns of Bayanaul, Karkaralinsk and Karasu (see Fig. 3). The local crust varies in thickness from roughly 40 km (near Karasu) to 50 km near Karkaralinsk and Bayanaul (Balyaevsky *et al.* 1973; Leith 1987). All three sites were installed on granitic intrusions of Permian to Triassic age and consisted of surface and borehole instruments (deployed at 99, 66 and 101 m, respectively). Although establishing the receivers on granitic outcrops should have eliminated the problem of near-receiver reverberations, the site at Karasu was clearly contaminated by an anomalous site response (Eissler *et al.* 1988) and the data from this site have been excluded from this study.

Teledyne Geotech 54100 seismometers sampling at 250 s^{-1} with a flat response to velocity between 0.2 and

100 Hz were deployed in each of the boreholes (Berger *et al.* 1987). The surface data used in this study were collected by GS-13 seismometers deployed in shallow vaults, which were also sampled at 250 s^{-1} . These instruments have a flat response to ground velocity between 1 and 80 Hz. All seismometers recorded data only after triggering.

Three calibration events detonated in September of 1987 provide the only well-constrained events in this data set. They varied in size from 10 (events 1 and 3) to 20 tons (event 2) and ranged from 157 to 254 km from the receivers (see Fig. 1). Unlike events 1 and 3, event 2 was not fully contained underground. These events were estimated by Eissler *et al.* (1988) to have equivalent seismic moments on the order of 10^{12} – 10^{13} Nm. Since event 3 was detonated at the same site as event 1 and occurred simultaneously with the arrival of a teleseism originating in the MacQuarie Islands, it has not been used in this study.

The region surrounding the seismic network experiences a low level of seismicity (Leith 1987) and is considered to be tectonically stable. We believe that the bulk of the events recorded during the operation of the network are man-made and are likely mine explosions. The events considered in this paper range from 105 to 264 km from the receivers. Compelling support for the identification of one of these events (event i, Fig. 3; Table 1) as a quarry blast comes from a French SPOT photo provided by Dr Clifford Thurber at the State University of New York, Stony Brook. The photo of the area surrounding event i, and a number of other proximal events not discussed in this paper, clearly shows four open-pit mines. All events other than the calibration shots were located by Clifford Thurber (Thurber *et al.* 1988) using the method described by Bratt & Bache (1988).

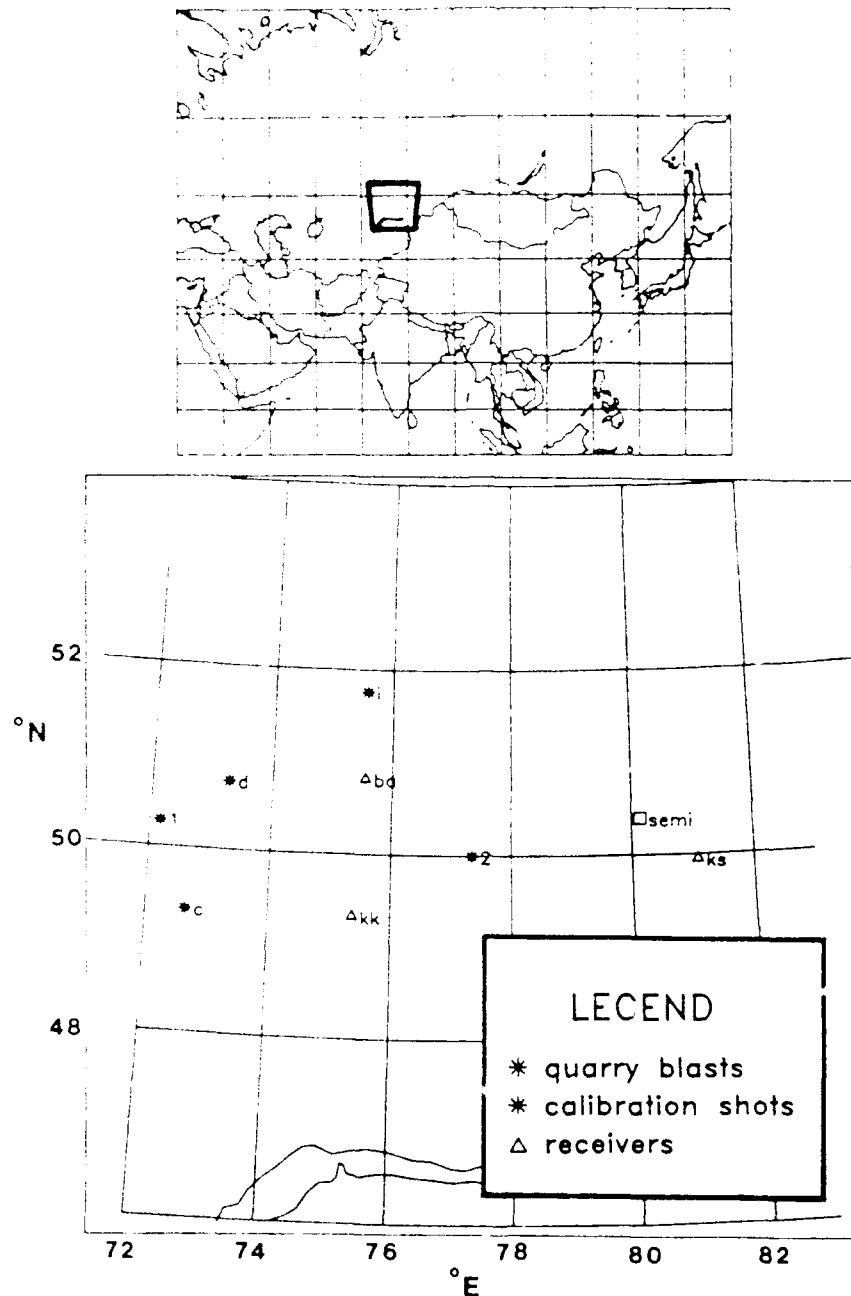


Figure 3. Receiver and event geography.

All spectral estimates displayed in this paper have been computed using an adaptive multitaper algorithm described by Thompson (1982). The spectral leakage that plagues all

estimates, especially the highly-coloured spectra which we encountered in this study, is dealt with in an effective manner by employing several tapers that minimize the leakage from outside a pre-specified bandwidth. Secondly, the analysis of the time dependence of the energy in the coda requires the computation of spectra from short-time series which, especially at the times of onsets, are particularly non-stationary. Park, Lindberg & Vernon (1987) demonstrated the multitaper method is superior in this situation to conventional single-taper algorithms because it employs several tapers that do not overemphasize the data at the centre of the time series and discards significantly fewer data than conventional single-taper algorithms.

Table 1. Event locations.

Event	Latitude (°N)	Longitude (°E)	Origin time (year/day/h.m.s)
CH2	50.000	77.340	87/245/09 27:04.950
ENC	49.333	72.667	87/135/10 35:00.2
EVD	50.742	73.275	87/141/09 16:43.3
EVI	51.760	75.572	87/146/08 33:26.5

DATA ANALYSIS

Since we are looking for the presence or absence of time-independent banding, we have found it useful to calculate frequency-time displays of seismograms, known as sonograms in acoustics (Markel & Gray 1976), because they preserve the time-dependence information.

It is logical to begin the analysis with an event about which we know a great deal. The calibration event Chemex 2 was a 20 T explosion detonated at 50.00°N, 77.34°E at a depth of 17 m in a mining tunnel drilled through granite (see Table 1). The vertical component seismogram for this event recorded at high gain by the GS-13 seismometer and the corresponding sonogram are displayed in Fig. 4. The velocity seismogram has been decimated to one point in 16 (retaining the maximum and minimum amplitudes), and is otherwise unfiltered. The spectral estimates in this and all subsequent figures are of the acceleration amplitude plotted on a linear scale. Each spectral estimate consists of a weighted sum of seven subestimates computed using a time-bandwidth product of 4. Each estimate has been computed from 2 s of data (i.e. 500 samples), padded to 4 s with zeros. A fairly broadband compressional onset occurs 27 s after the event. At this range (157 km) we expect that the onset energy has travelled solely within the crust. A

relatively narrow band, high-amplitude shear onset arrives at 48 s followed roughly 10 s later by a small amplitude surface wave packet. The most striking feature of this sonogram is that the energy is clearly not organized into time-independent frequency bands but, with the exception of the onsets, is distributed fairly randomly.

We strongly suspect that event c (Fig. 3) is a ripple-fired mine explosion. It was recorded by the same seismometer and processed in exactly the same manner as Chemex 2 and is displayed in Fig. 5. The sonograms for this event and Chemex 2 are strikingly different. The energy is clearly organized into time-independent bands regularly spaced at roughly 6 Hz. Considering the regularity of the modulation, it seems reasonable to accept, for now, the initial, simplest, quarry-blast model discussed above. A simple calculation thus suggests that this event consisted of a number of subevents spaced on the order of 167 ms from each other. The actual number of subevents involved is not as simply assessed since the estimation involves using the fall-off rates of the spectral peaks which are much more difficult to compute.

These time-independent bands are observed in virtually all the unidentified events. The primary difference between them is the period of this modulation along the frequency axis. A third event's sonogram, (event i in Fig. 3, located

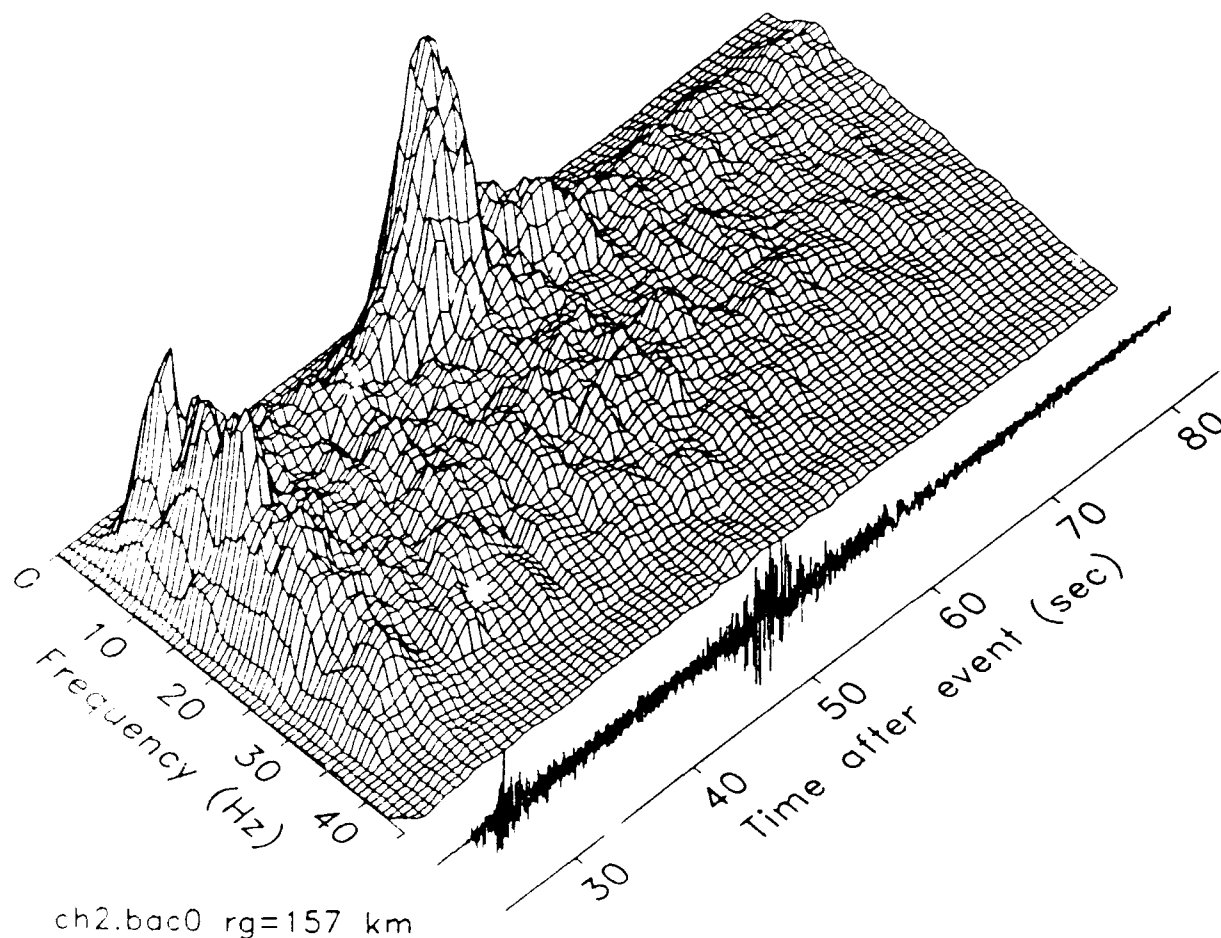


Figure 4. Seismogram resulting from Chemex 2 recorded at a range of 157 km by the vertical surface seismometer at Bayanul and corresponding sonogram.

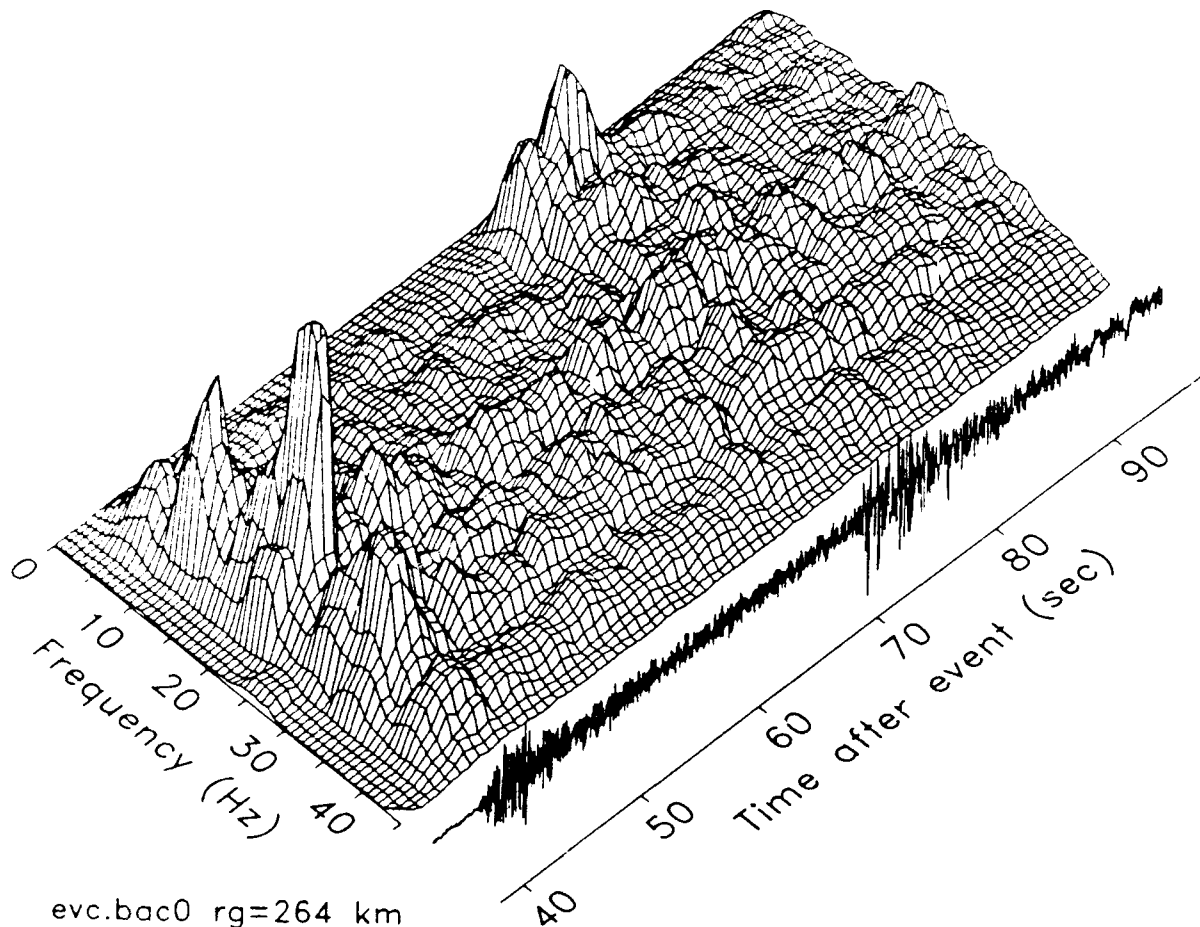


Figure 5. Seismogram resulting from event c recorded at a range of 264 km by the vertical surface seismometer at Bayanaul and corresponding sonogram.

105 km from Bayanaul) is displayed in Fig. 6. The broader spectral spacing ($\Delta f = 16$ Hz) suggests a more closely grouped set of subshots separated by roughly 63 ms.

In order to enhance the time-independent modulation we remove the large-scale structure caused by the compressional and shear onsets as well as the high frequency spectral fall-off. We have found that an effective method involves differencing two versions of each original spectral estimate. As Fig. 7 illustrates we compare a relatively unsmoothed version with one that resolves only the large-scale structure in order to extract the regular modulation. In practice, when analysing the events considered in this paper, the smoothed versions were obtained by simply convolving the original spectral estimates with boxcar functions spanning 2.5 and 1.0 Hz. We represent all regions of the sonogram matrix where the local power is high relative to the more regional average power by a value of +1 (denoted as white in this and all subsequent figures) and where it is low by a -1 (black). In this manner the bulk of the magnitude information is discarded and the true sonogram matrix is 'flattened' to a very simple, yet informative, binary matrix.

The binary matrix representing the first 35 s following the compressional onset of event Chemex 2 recorded at Bayanaul to a frequency of 35 Hz is displayed in Fig. 8. Aside from the suggestion of time-independent structure in the vicinity of 5 Hz, the energy is distributed more or less

randomly. It seems intuitively reasonable that a single-source explosion should give rise to a coda in which the energy is distributed randomly as a function of frequency and time if the dominant coda generation mechanism involves the scattering of energy by a random distribution of randomly sized inhomogeneities. This example suggests that layer resonance, proposed by Sereno & Orcutt (1985a) as the dominant source of coda in the oceanic lithosphere, plays only a supporting role in generating seismic coda in this region of the continental crust. We contrast this result with the coda produced by event c (Fig. 9) which displays obvious time-independent spectral modulation.

We examined a fourth event (event d in Fig. 3) to find that the regular modulation is not restricted to the vertical component. Indeed, as Fig. 10 reveals, the modulation appears to be quite independent of the component of displacement. Only the vertical and radial components are shown, but the transverse component is nearly identical. This observation lends support to the hypothesis that the time-independent spectral modulation is a source and not a propagation effect. This observation is not unique to this event but appears to be shared by all events other than the calibration shots.

The quarry-blast spectral modulation is not only independent of component but appears to be independent of the azimuth from the source to the receiver as well as

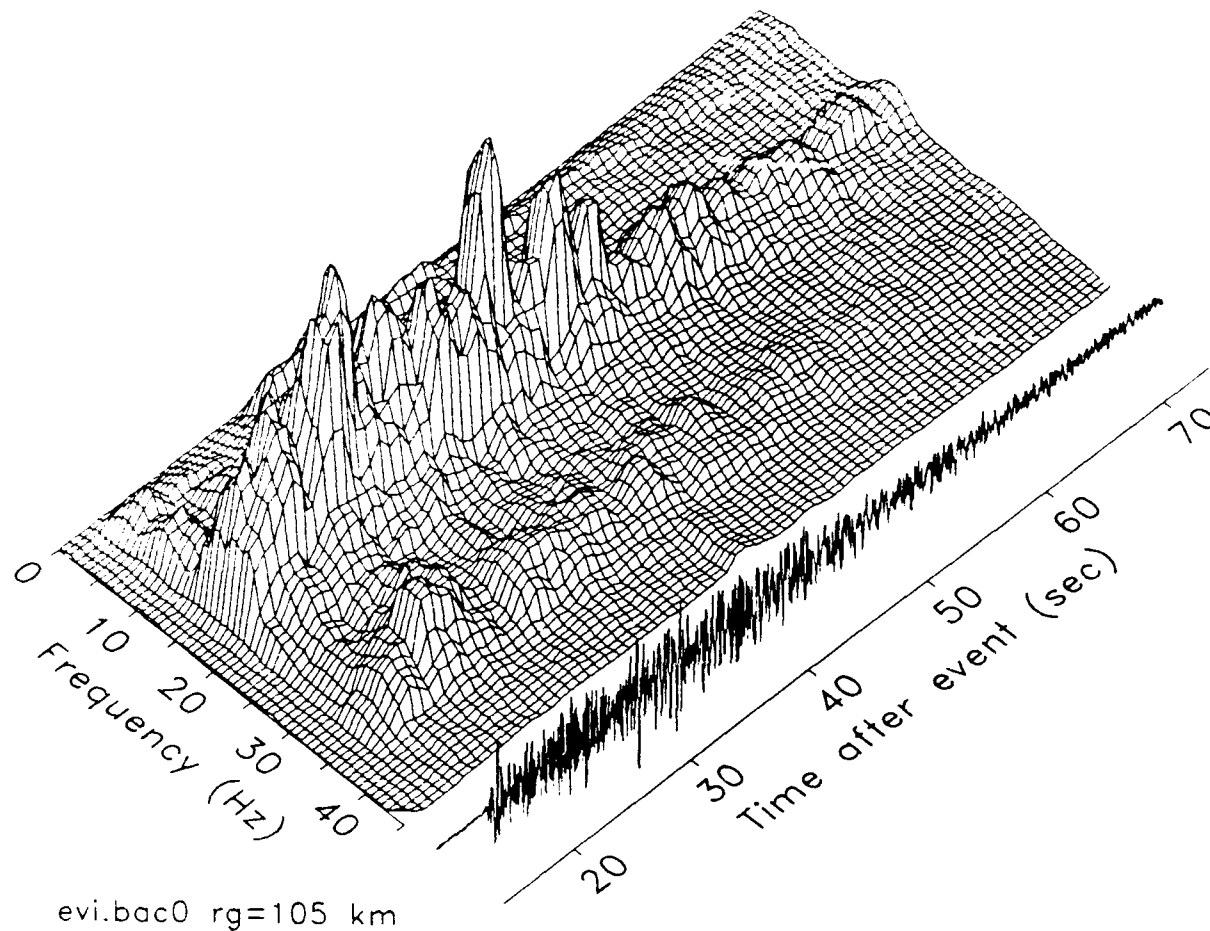


Figure 6. Seismogram resulting from event *i* recorded at a range of 105 km by the vertical surface seismometer at Bayanaul and corresponding sonogram.

source-receiver range. In Fig. 11 we compare the vertical component modulation of event *d* as recorded at Bayanaul (at a range of 159 km and a back azimuth of 268°) and

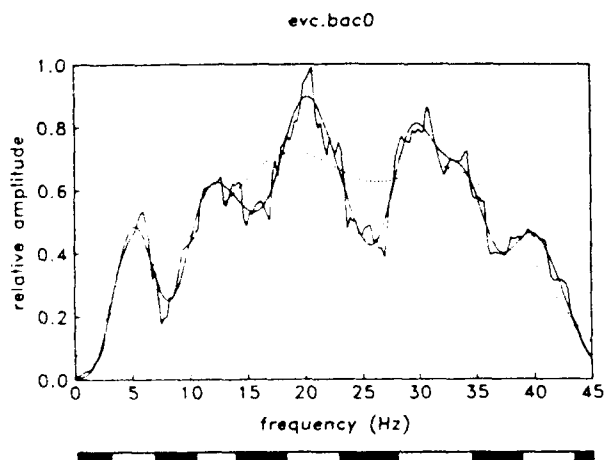


Figure 7. Original spectral estimate and two versions, one relatively unsmoothed and the other relatively highly smoothed. This figure is intended to illustrate the means by which we reduce each spectral estimate to a 'binary spectral estimate'. The regions of locally high power are represented by a +1 (white). Regions deficient in power are represented by a -1 (black).

Karkaralinsk (at a range of 217 km and a back azimuth of 317°). The independence on azimuth suggests that the array of subshots comprising event *d* may be very small. The apparent time offsets caused by spacing the subshots become significant when the array is large and as discussed earlier these apparent offsets have an azimuthal dependence.

To constrain the probable dimensions of a typical quarry blast we employ the formula of Smith (1989) to equate true spatial offsets with apparent time offsets δT_i^a

$$\delta T_i^a = p \sqrt{\delta X_i^2 \sin^2 \theta + \delta Y_i^2 \cos^2 \theta} + \delta T_i \quad (7)$$

Each subevent occurs at point $(\delta X_i, \delta Y_i)$ in space and at time δT_i . The energy under consideration travels at a slowness of p s km⁻¹ along an azimuth from the source to the receiver of θ degrees. To permit a crude calculation we adopt an array consisting of just two shots. We simplify the calculation by aligning the *X* and *Y* axes parallel and perpendicular to the line joining the shots respectively. To use this equation, we must first estimate the dependence of the modulation pattern on source to receiver azimuth. In general it is true in this data set that little difference in the modulation period associated with any single event can be discerned between the recordings made at Karkaralinsk and Bayanaul. Thus, for a crude estimate of the likely source dimensions we model a typical event (*d*, Fig. 10) with subshots arranged spatially to give rise to the maximum

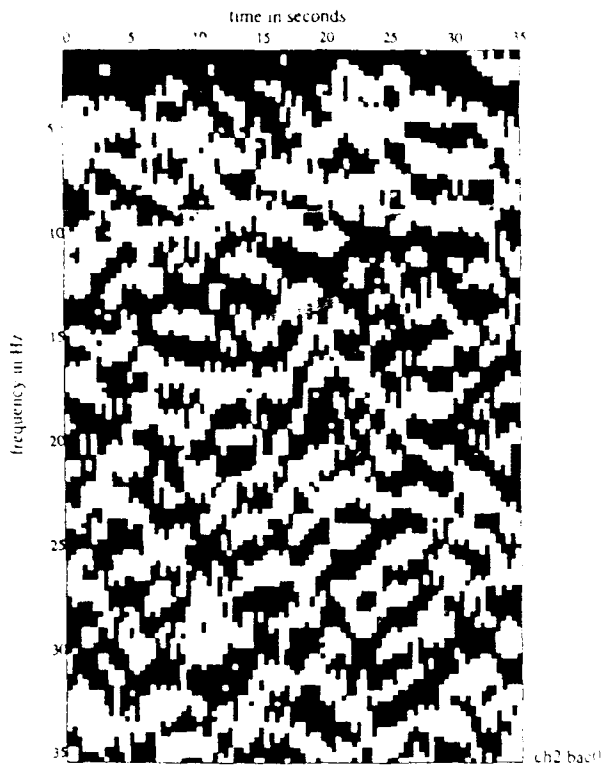


Figure 8. Vertical component binary sonogram matrix corresponding to Chemex 2 recorded at Bayanaul. The first 35 s of coda after the compressional onset are represented in this and all subsequent figures.

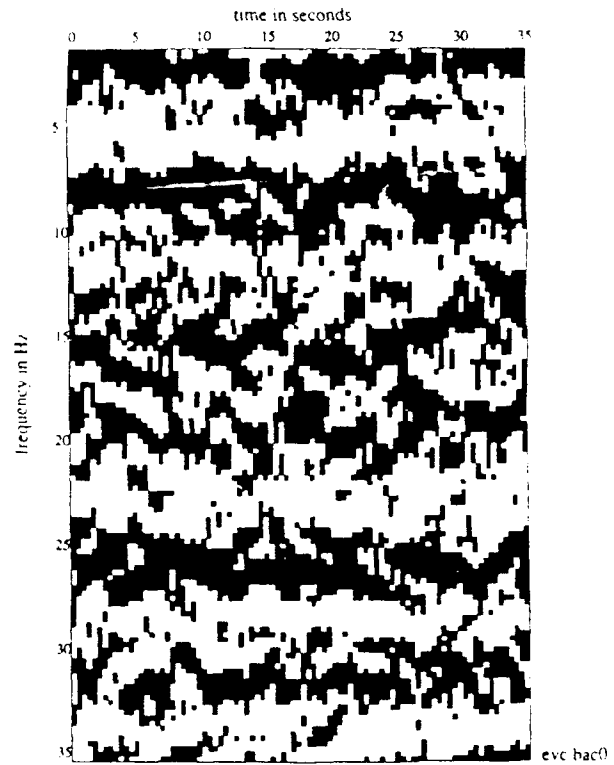


Figure 9. Vertical component binary sonogram matrix corresponding to event c recorded at Bayanaul.

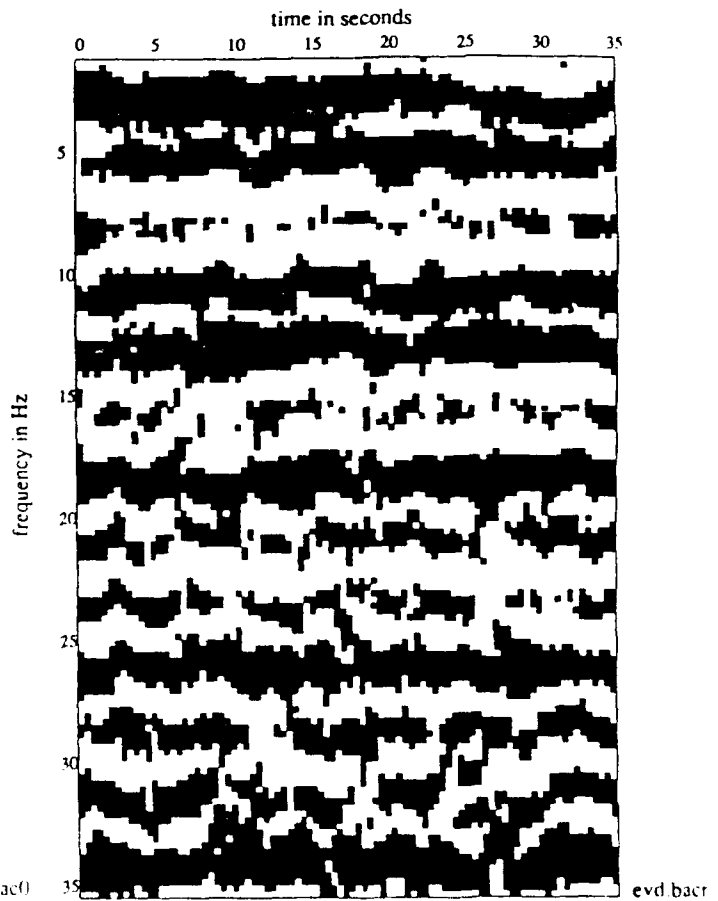
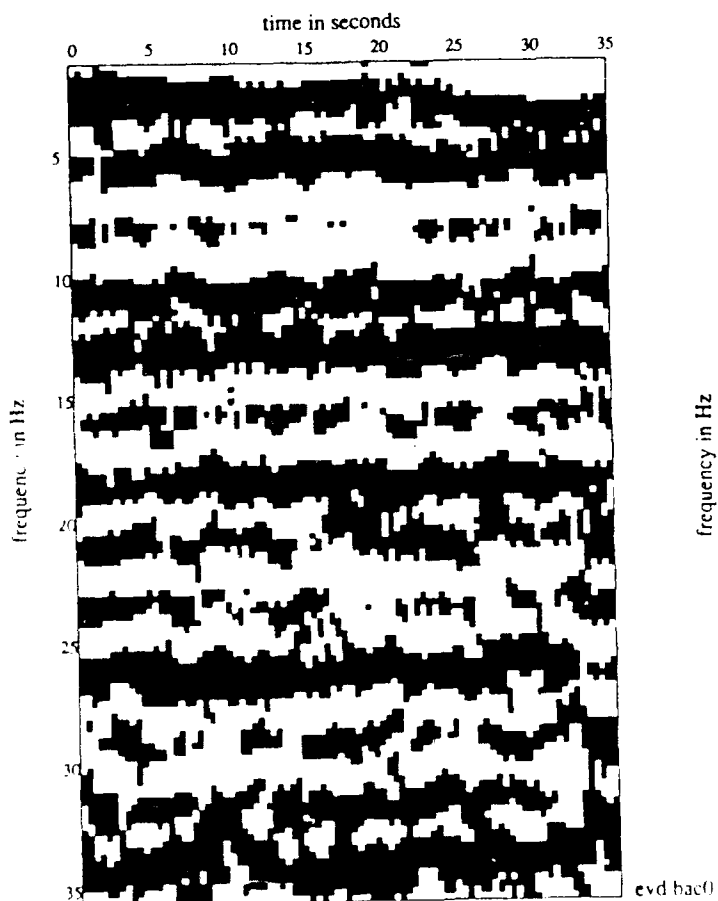


Figure 10. Binary sonogram matrices representing the vertical (a) and radial (b) components of displacement recorded at Bayanaul from event d.

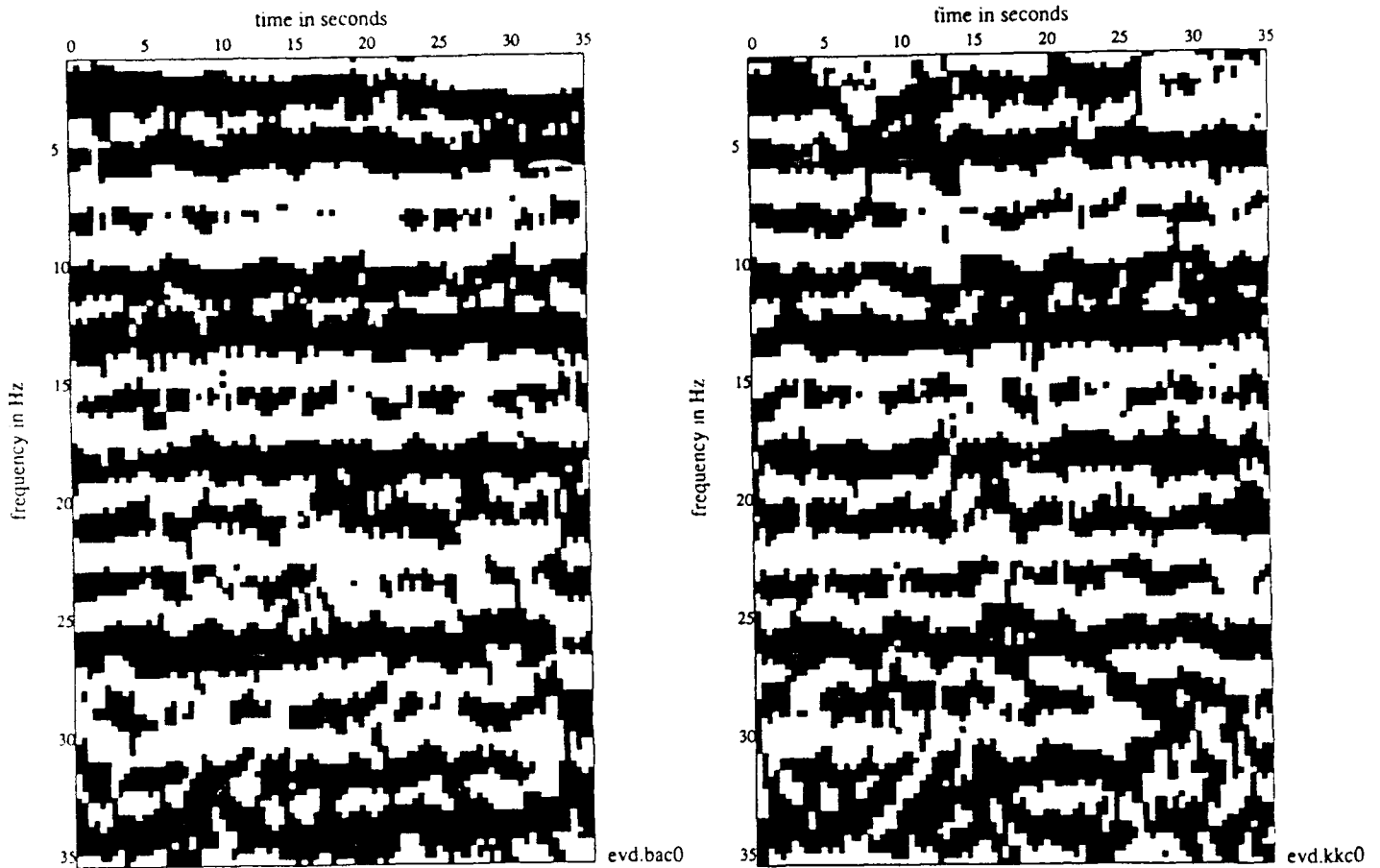


Figure 11. Vertical component binary sonogram matrices corresponding to event d recorded at Bayanaul (a) and Karkaralinsk (b).

possible azimuthal dependence of the spectral modulation when observed at these two stations. We will realize the maximum possible change in modulation period between Bayanaul and Karkaralinsk if we place this dipolar shot array so that the normal to the line joining the shots lies exactly halfway between the two receivers. Using elementary error analysis, and knowing that $\delta T = 1/\delta F$ (where δT is the time offset and δF is the spacing of adjacent peaks in the frequency domain) we find that the change in δT (or $\delta^2 T$) required by a change in the modulation spacing ($\delta^2 F$) is given by:

$$\delta^2 T = -\frac{\delta^2 F}{(\delta F)^2}. \quad (8)$$

If we observe n cycles in the frequency span of ΔF Hz in one recording of an event, and in $\Delta F \pm dF$ Hz in another recording then

$$\delta^2 T = -\frac{ndF}{(\Delta F)^2}. \quad (9)$$

Combining equations (7) and (9) we find that

$$\delta X = -\frac{ndF}{(\Delta F)^2 p[\sin(\theta_1) - \sin(\theta_2)]} \quad (10)$$

where δX is the inferred shot spacing and θ_1 and θ_2 are the azimuths to Bayanaul and Karkaralinsk (and equal $+24.6^\circ$

and -24.6° , respectively). In Fig. 11 we observe 11 cycles present in a frequency band of 30 ± 1 Hz in both the recordings of this event. Thus, using equation (10), and considering a typical crustal ray with a slowness of $1/7 \text{ s km}^{-1}$ we infer a shot spacing of 100 m or less. Clearly many assumptions have been made in this calculation so it should be regarded as a crude estimate at best. We have no *a priori* information on what blasting techniques (shot geometry and timing) the Soviet mining engineers employ in their quarry blasts. Combining this fact with the observations that the spectral modulations are regular in frequency and independent of time and source-receiver azimuth it seems inappropriate to attempt a more sophisticated modelling by allowing spatial offsets. We can adequately model these Soviet quarry blasts by employing either of the two models proposed earlier in this paper.

Assuming linear superposition (and the first quarry blast model), it is a simple matter to synthesize a quarry blast by linearly superposing a Green's function upon itself after offsetting by a delay time prior to each addition. By chance it turns out that Chemex 2 is at nearly the same distance from Bayanaul as is event d, and thus it is eligible for use as a 'Green's function' if lateral variations of crustal structure are small. This observed rather than synthesized Green's function has the obvious drawback of being produced by a significantly larger source than a likely subevent in a typical quarry blast, so that its corner frequency will be lower. This

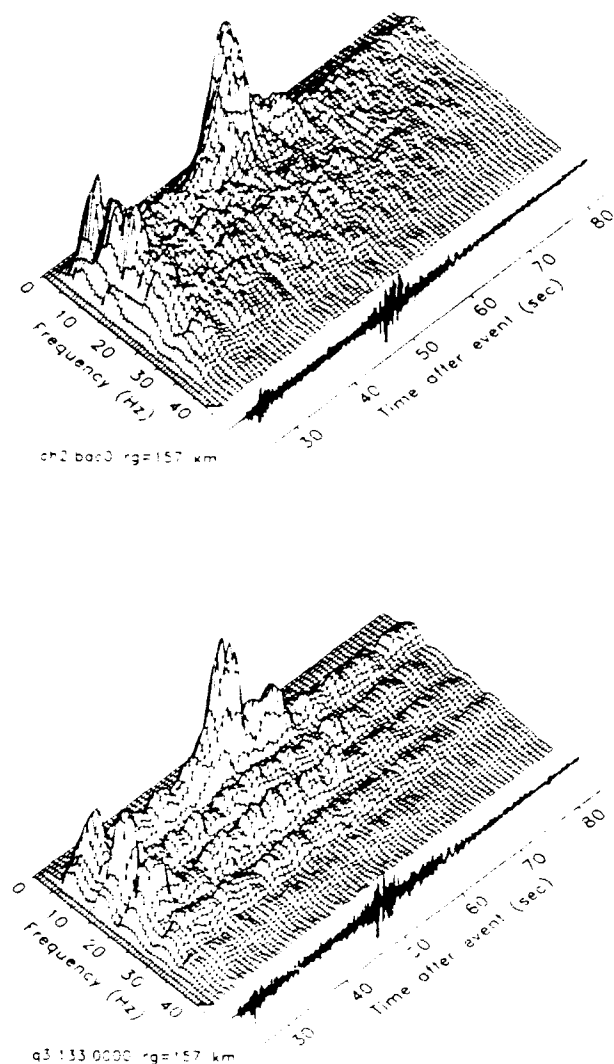


Figure 12. (a) Time series and sonogram corresponding to Chemex 2 recorded at Bayanaul. (b) Time series and sonogram representing a 'synthetic' quarry blast involving three shots spaced in time by 133 ms.

should not be a significant problem since, as Evernden, Archambeau & Cranswick (1986) note, the Sharpe explosion model (Sharpe 1942), predicts the corner frequency of a tamped explosion of this size to be 30–35 Hz. This is approximately the upper frequency limit in all binary sonograms considered in this study. The usefulness in general of such a Green's function is limited because it is only available at a small number of ranges (defined by the offsets between the two events and the two receivers). It has the distinct advantage *vis-à-vis* synthetics that the propagation transfer function is nearly exact (assuming horizontal layers). By taking the vertical component of motion from Chemex 2 observed at Bayanaul (Fig. 4) and stacking it upon itself twice after offsetting each successive trace by 133 ms, we obtain the 'synthetic' quarry blast displayed in Fig. 12. The binary sonogram corresponding to a synthetic quarry blast consisting of three shots offset by 382 ms, displayed in Fig. 13, compares well with the actual binary sonogram computed from event d. Although non-linear effects must clearly occur during a quarry blast,

simple linear theory can be very effective in reproducing the observed modulation. In principle, we can time an observed ripple-fired quarry-blast repetition rate with this method. In this case we have illustrated a likely offset time (382 ms) for event d.

DISCRIMINATION BETWEEN SINGLE AND MULTIPLE SHOT EXPLOSIONS

The method described above of reducing sonograms to binary matrices provides simple patterns that allow visual discrimination between quarry blasts and simpler events (single-event explosions and perhaps earthquakes). Clearly there are a number of mathematical operations we can employ to reduce these matrices to scalars which reflect the presence or absence of time-independent spectral banding. Two methods seem promising at this time but have not yet been developed. One involves the comparison of three-component binary matrices by performing a three-way cross-correlation. As discussed above the quarry-blast modulation is a source effect and is not dependent on the recorded component. We expect a relatively high cross-correlation between the three components of recorded motion resulting from a quarry blast relative to that computed from simpler events. In an alternate method the 2-D Fourier transform of the binary sonogram matrix is computed. We expect the presence or absence of time-independent modulation would be reflected in the distribution of power levels, those events with time-independent modulation should show a distinctive pattern. For the present purposes, however, we feel it is sufficient to recognize simply that distinct time versus frequency pattern differences between quarry blasts and calibration explosions exist. By comparing individual columns in the binary sonogram matrices calculated from single- and multiple-event explosions we can assess the enhanced discrimination potential of binary sonogram matrices over that of single spectral estimates. In Fig. 8 many of the columns possess a regular modulation comparable to that seen in single columns computed from the coda resulting from a quarry blast (for example Fig. 9). Individual spectral estimates computed from even simple single-event explosions can have significant regular modulation and thus distinguishing between these and more complex multiple-event explosions using single spectra is expected to be difficult. The profound differences between these two types of events becomes obvious when many spectra offset from each other in time are computed. The persistence of spectral features through time in the coda of multiple-source events, but not single-source events, is what sets them apart.

A weakness of this discriminant and indeed any algorithm which seeks to separate quarry blasts from other events on the basis of their unusual spectral colour is that time-independent spectral modulation can be acquired during propagation. The binary sonogram matrix of Chemex 2 recorded at Bayanaul possesses a faint but undeniable time-independent structure at about 5 Hz. Comparison of this figure with the binary sonogram computed from Chemex 2 recorded at Karkaralinsk reveals that the two stations have recorded essentially the same patterns. The same exercise performed on the Chemex 1 recordings at Bayanaul and Karkaralinsk revealed faint but strikingly

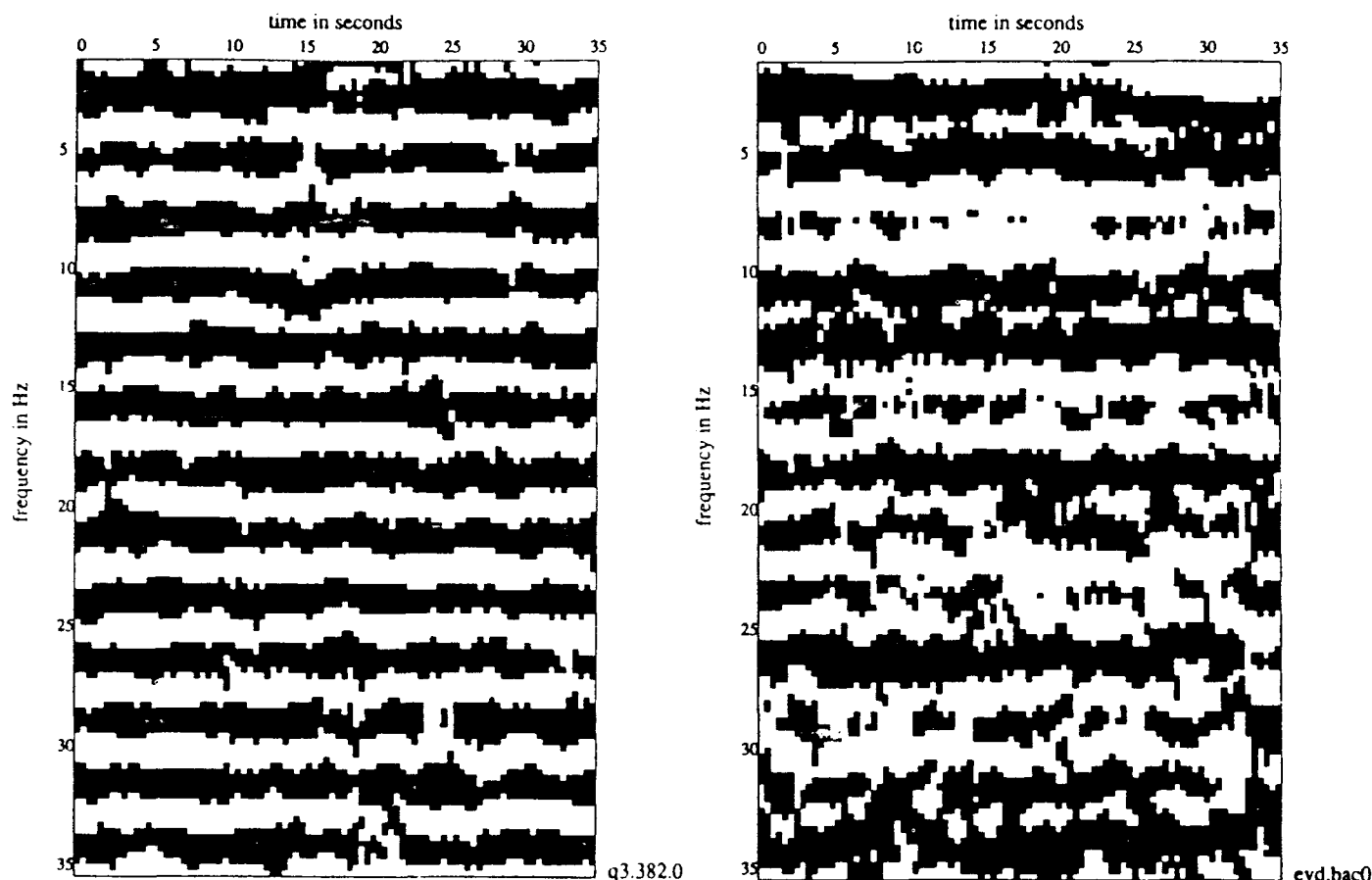


Figure 13. (a) Vertical component binary sonogram matrix corresponding to a synthetic quarry blast consisting of three subevents spaced in time by 382 ms. (b) Vertical component binary sonogram matrix corresponding to event d recorded at Bayanaul.

similar time-independent patterns distinct from the Chemex 2 patterns. These features are most likely a source effect since similar patterns have sources, not receivers, in common. Since the Chemex events are known to be single-source events, the most plausible explanation is that the patterns are due to reverberations occurring in a shallow, near-source horizon. Although these time-independent effects are faint they are worth considering further. Reverberations can occur at any time during propagation from the source to the receiver, but the two points at which the effects are going to be most noticeable and most likely are near the source and near the receiver. These are the only two points at which the recorded body wave energy is most likely to encounter a low velocity horizon. Prior to using the discriminant, we are proposing that a receiver must be shown to be free of reverberations by recording single-event explosions. If the site is able to record these events with no time-independent effects then it is eligible for this type of work. Fortunately the Chemex events have not produced significant time-independent structure (the high frequency overtones have not developed), but they do indicate that it may be possible to disguise a single-event explosion as a quarry blast by detonating it in a low-velocity horizon.

A second problem exists when events have been recorded at a time of high noise levels, especially when the events are

small and/or distant and when spectral spikes exist in the noise. Prominent features in ground or instrumental noise can emerge from the signal after the onset and be misinterpreted as time-independent features due to the source, especially if more than one harmonic is present. To combat this problem it is necessary to obtain and analyse pre-event noise samples to permit the identification of time-independent features in the coda that are really due to noise. In this study, all time-independent features attributed to the source are seen on both the Karkaralinsk and Bayanaul records. It is also true that while signal spectra between the two receivers have high coherence, the pre-event noise spectra do not.

In practice it is clearly desirable that more than one station be used when attempting to discriminate quarry blasts from simpler events. As discussed earlier, if the quarry blast subshot array is not infinitely small we expect the modulation pattern to show an azimuthal dependence. There are certain array geometries, for example linear arrays, that will produce, at certain source-receiver azimuths, negligible apparent time offsets between the subshots and thus little or no time-independent spectral structure. It is extremely unlikely that a second receiver simultaneously recording this event at a different azimuth will also have such a problem. None of the quarry blasts we have examined show evidence for such azimuthal effects.

CONCLUSIONS

We have observed a significant difference between events which consist of a number of subexplosions closely grouped in space and time and simpler, single explosion, events. The former type of event (a quarry blast) possesses a distinctive time-independent spectral structure that can be easily explained assuming linear superposition of the wavefields produced by each of the subevents. The latter type of source does not cause a regular organization of the energy and thus the distribution of energy in the coda is controlled by the propagating medium. The observed randomness of this energy as a function of frequency and time suggests that the dominant mechanism of coda generation in this region of the continental crust involves scattering by small-scale inhomogeneities. We conclude these two types of events can be most effectively distinguished from each other by exploiting the expected differences in the time and frequency evolution of energy in the onsets and coda. We propose a time versus frequency pattern-based discriminant.

Although we have no *a priori* information on the mining practice employed by the Soviet quarry-blast engineers we infer regular offsets in time and small spatial array dimensions by observing that the modulations are regular in frequency and independent of time and source-receiver azimuth.

In the future we will expand this analysis to include earthquakes and explosions in other regions. We expect we can demonstrate the independence of the algorithm on mining practice and geological setting. We hope to extend the pattern-based discriminant by reducing the binary sonogram matrices to scalars which reflect the presence or absence of time-independent modulation.

ACKNOWLEDGMENTS

We thank Dr Clifford Thurber at the State University of New York, Stony Brook, for his helpful review and comments and for providing us with the satellite photos and event locations. We also express our appreciation to Dr Alan Chave, currently at AT & T Bell Laboratories, for supplying us with the multitaper algorithm that was used to compute spectral estimates. This research was sponsored by the Defense Advanced Research Projects Agency (DARPA)/Air Force Geophysical Laboratory (AFGL) under Contracts No. F19628-87-K-0013 and F19628-88-K-0044. The Kazakh stations were installed and operated by the Institute of Physics of the Earth of the Soviet Academy of Sciences and the Natural Resources Defence Council. We thank the team of scientists who set up these stations.

REFERENCES

- Aviles, C. A. & Lee, W. H. K., 1986. Variations in signal characteristics of small quarry blasts and shallow earthquakes, *Eos, Trans. Am. geophys. Un.* **67**, 1093.
- Balyaevsky, N. A., Borisov, A. A., Fedynsky, V. V., Fotiadi, E. E., Subbotin, S. I. & Volvosky, I. S., 1973. Structure of the Earth's crust on the territory of the USSR, *Tectonophysics*, **20**, 35-45.
- Baumgardt, D. R. & Ziegler, K. A., 1988. Spectral evidence for source multiplicity in explosions: application to regional discrimination of earthquakes and explosions, *Bull. seism. Soc. Am.*, **78**, 1773-1795.
- Bell, A. G. R., 1977. A digital technique for detection of multiple seismic events, *Eos, Trans. Am. geophys. Un.* **57**, 444.
- Berger, J., Eissler, H. K., Vernon, F. L., Nersesov, I. L., Gokhberg, M. B., Stolyrov, O. A. & Tarasov, N. D., 1987. Studies of high-frequency seismic noise in eastern Kazakhstan, *Bull. seism. Soc. Am.*, **78**, 1744-1758.
- Bratt, S. R. & Bache, T. C., 1988. Locating events with a sparse network of regional arrays, *Bull. seism. Soc. Am.*, **78**, 780-798.
- Eissler, H. K., Tarasov, N. T., Zhuravlev, V., Thurber, C. H., Vernon, F. L., Berger, J. & Nersesov, I. L., 1989. High-frequency seismic observations of chemical explosions of known location and yield in eastern Kazakhstan, USSR, *J. geophys. Res.*, in press.
- Evernden, J. F., Archambeau, C. B. & Cranswick, E., 1986. An evaluation of seismic decoupling and underground nuclear test monitoring using high-frequency seismic data, *Rev. Geophys.*, **24**, 143-215.
- Gupta, I. N., Burnetti, J. A., Wagner, R. A. & Marshall, M., 1984. Discrimination between quarry blasts, nuclear explosions and earthquakes, *Unclassified DoD report*.
- Hedlin, M. A. A., Orcutt, J. A. & Minster, J. B., 1988. A comparative study of high frequency signal and noise in oceanic and continental environments, paper presented at the 10th Ann. AFGL/DARPA Seism. Res. Symp.
- Leith, W., 1987. Geology of NRDC seismic stations in eastern Kazakhstan, USSR, *USGS Open-File Report* 87-597.
- Markel, J. D. & Gray, A. H., Jr, 1976. *Linear Prediction of Speech*, Springer-Verlag, Berlin, Heidelberg, New York.
- Park, J., Lindberg, C. R. & Vernon, F. L., 1987. Multitaper spectral analysis of high-frequency seismograms, *J. geophys. Res.*, **92**, 12675-12684.
- Sereno, T. J., Jr, 1986. The propagation of high frequency seismic energy through oceanic lithosphere, *PhD thesis*, University of California.
- Sereno, T. J., Jr. & Orcutt, J. A., 1985a. Synthetic seismogram modelling of the oceanic Pn phase, *Nature*, **316**, 246-248.
- Sereno, T. J., Jr & Orcutt, J. A., 1985b. Synthesis of realistic oceanic Pn wave trains, *J. geophys. Res.*, **90**, 12755-12776.
- Sharpe, J. A., 1942. The production of elastic waves by explosion pressures, I. Theory and empirical field observations, *Geophysics*, **7**, 144-154.
- Smith, A. T., 1989. High-frequency seismic observations and models of chemical explosions: implications for the discrimination of ripple-fired mining blasts, *Bull. seism. Soc. Am.*, **79**, 1089-1110.
- Stump, B. W. & Reamer, S. K., 1988. Temporal and spatial source effects from near-surface explosions, Paper presented at the 10th Ann. AFGL/DARPA Seism. Res. Symp.
- Thompson, D. J., 1982. Spectrum estimation and harmonic analysis, *IEEE Proc.*, **70**, 1055-1096.
- Tribolet, J. M., 1979. *Seismic Applications of Homomorphic Signal Processing*, Prentice-Hall Signal Processing Series.
- Thurber, C. H., Eissler, H., Berger, J., Zhuravlev, V. & Tarasov, N., 1988. Location of regional explosions and earthquakes with the NRDC-Soviet Academy of Sciences seismic network in Kazakhstan, *Eos, Trans. Am. geophys. Un.*, **69**, 1332.

**An automatic means to discriminate between
earthquakes and quarry blasts**

Michael A.H. Hedlin

J. Bernard Minster

John A. Orcutt

Institute of Geophysics and Planetary Physics

Scripps Institution of Oceanography

La Jolla CA 92093 U.S.A.

Submitted, Bull. Seismol. Soc. Am. , February 1990

Revised May 1990

The U.S. Government is authorized to reproduce and sell this report.
Permission for further reproduction by others must be obtained from
the copyright owner.

Abstract

In this paper we discuss our efforts to use the NORESS array to discriminate between regional earthquakes and ripple-fired quarry blasts (events that involve a number of sub-explosions closely grouped in space and time). The method we describe is an extension of the time versus frequency "pattern-based" discriminant proposed by Hedlin et al. (1989b). At the heart of the discriminant is the observation that ripple-fired events tend to give rise to coda dominated by prominent spectral features that are independent of time and periodic in frequency. This spectral character is generally absent from the coda produced by earthquakes and "single-event" explosions. The discriminant originally proposed by Hedlin et al. (1989b) used data collected at 250 s^{-1} by single sensors in the 1987 NRDC network in Kazakhstan, U.S.S.R.. We have found that despite the relatively low digitization rate provided by the NORESS array (40 s^{-1}) we have had good success in our efforts to discriminate between earthquakes and quarry blasts by stacking all vertical array channels to improve signal to noise ratios.

We describe our efforts to automate the method, so that visual pattern recognition is not required, and to make it less susceptible to spurious time-independent spectral features not originating at the source. In essence we compute a Fourier transform of the time-frequency matrix and examine the power levels representing energy that is periodic in frequency and independent of time. Since a double Fourier transform is involved, our method can be considered as an extension of "cepstral" analysis (Tribolet, 1979). We have found, however, that our approach is superior since it is cognizant of the time independence of the spectral features of interest. We use earthquakes to define what cepstral power is to be expected in the absence of ripple firing and search for events that violate this limit. The assessment of the likelihood that ripple firing occurred at the source is made automatically by the computer and is based on the extent to which the limit is violated.

1. Introduction

There is a peculiar breed of seismic event known as a ripple-fired explosion. Such an event differs markedly from a standard "single-event" explosion since it involves the detonation of numerous sub-explosions closely, and generally regularly, grouped in space and time. Ripple-firing is a technique commonly used in quarry blasting (Langefors and Kihlström, 1978) where mine operators are striving to reduce ground motions in areas proximal to the mine, enhance rock-fracturing and reduce the amount of material thrown into the air - "fly" or "throw" rock - (Dowding, 1985). Ripple-firing is in widespread use, being employed both in the Americas and in Europe (Stump et al., 1989).

There has been increased interest in recent years in discriminating mining events from earthquakes and nuclear explosions. A reduced Threshold Test Ban Treaty could potentially bring the magnitude of the largest nuclear explosions down to that of large "engineering" explosions otherwise known as quarry blasts (Stump and Reamer, 1988). Aggravating the problem is the existence of numerous quarries in the vicinity of the Semipalatinsk nuclear test site in the Soviet Union (Thurber *et al.*, 1989; Hedlin *et al.*, 1989b). There have been a number of studies dealing directly and indirectly with this problem. Looking primarily at Scandinavian events recorded by the NORESS array, Baumgardt and Ziegler (1988) found prominent spectral modulation in events believed to involve ripple-firing, but not in the spectra computed from earthquake seismograms. Hedlin *et al.* (1989b) observed similar spectral modulation in the coda produced by suspected quarry blasts in Kazakhstan, U.S.S.R., but not in the coda produced by single-event calibration explosions detonated at similar ranges. They found further that the modulation, when present, was independent of time from the onset, well into the Lg coda. This time-independent character has also been observed in the coda produced by quarry blasts and recorded in Scandinavia (Hedlin *et al.*, 1989a). Both Baumgardt and Ziegler (1988) and Hedlin *et al.* (1989b) found that the spectral modulation observed in the coda produced by mine explosions could be reproduced effectively by assuming that all sub-explosions produce the same, common, waveform and that the motions superpose linearly. Stump and Reinke (1988) have investigated the validity of the assumption of linear superposition. They produced strong evidence supporting the assumption when wavefields from small, closely spaced, explosions are observed in the nearfield. Baumgardt and Ziegler (1988), Hedlin *et al.* (1989a,b), Stump and Reamer (1988) and Smith (1989) - who also observed prominent peaks in the spectra of phases produced by some quarry blasts - all concluded that the unusual spectral color could be used to discriminate quarry blasts from other events with "whiter" spectra.

In this work we are extending the study described in Hedlin *et al.* (1989b) - hereafter referred to as paper 1 - in a number of ways. We examine recordings of earthquakes, not single-event explosions, to determine if they can be discriminated from quarry blasts with a similar degree of success. We seek to determine the sensitivity of the method to the recording "environment". The recordings examined in the current study have been made at 40 s^{-1} by the NORESS small aperture-array in Norway (Ringdal and Husebye, 1982; Mykkeltveit *et al.*, 1983). The data considered in paper 1 were recorded by single sensors and digitized at 250 s^{-1} . We feel that any successful discriminant should not depend strongly on the local geologic setting and mining practice. In paper 1 we examined events that occurred in central Asia, in this paper we consider Scandinavian events. We have automated the algorithm to the point where discrimination can be carried out solely by the computer. This type of problem has also been investigated by Baumgardt and Ziegler

(1989). Their approach also relies heavily on the expected time-independence of spectral modulation in the coda produced by ripple-fired events. In both the present work and Baumgardt and Ziegler (1989) the underlying premise of this automation is that in the future, if lower thresholds are realized, and thus a significantly greater dataset must be examined, it will be beneficial and desirable to distance the human element from the discrimination process.

2. The data set

The bulk of the data used by this study were collected by sensors in the NORESS small-aperture array - located in south-eastern Norway - from 1985 to 1986 (see Figure 1 and table 1). The NORESS array is composed primarily of 25 vertical component sensors deployed roughly 2 m deep in shallow vaults arranged in a set of concentric rings (Mykkeltveit *et al.*, 1983). The fourth and outermost ring is roughly 3 km across. The signal, collected by GS-13 seismometers which have a flat response to ground velocity between 1 and 10 Hz, is digitized at 40 s^{-1} . NORESS is actually part of a significantly larger array, known as NORSAR, and is situated within element 06C at this array, a site known to be particularly sensitive to signals propagating from Semipalatinsk (Richards, 1988). The seismometers are deployed in competent igneous rocks of granitic, rhyolitic and gabbroic composition (Mykkeltveit, 1987) and Precambrian or Paleozoic age (Bungum *et al.*, 1985). The site is thus relatively immune to the near-surface resonance of seismic energy. A more complete description of the array can be found in Mykkeltveit *et al.* (1983).

In addition to the NORESS data, we shall use an event recorded by the NRDC high-frequency stations deployed in Kazakhstan, U.S.S.R. in 1987 (Given *et al.*, 1990). The recording we have chosen is of the calibration explosion, Chemex 2, and was made by the surface sensor at Bayanaul.

The events recorded by the NORESS array consist of earthquakes and quarry blasts which, with the exception of one event, occurred within a range of 700 km from the array. Only regional events are considered here since the analysis depends on the retention of high-frequency energy in the coda. All events fall within a local magnitude range of $1.6 \leq M_L \leq 3.0$. Event magnitudes, locations, origin times and identifications were obtained from Baumgardt and Ziegler (1988) and Sereno *et al.* (1987). All frequency-spectral estimates have been computed using a multi-taper algorithm. The rationale behind the choice of this algorithm is described in paper 1, and the theory describing this approach can be found in numerous papers, including Park *et al.* (1987) and Thompson (1982).

3. The effect of ripple-firing

At least at the macroscopic scale, the practice of ripple-firing appears to have little systematic effect on the seismic waveforms. It is well known, however, that ripple-fired events tend to give rise to seismic coda possessing highly colored spectra, that is, spectra enriched in power in certain, preferred, frequency bands and depleted in power in others (Bell, 1977; Baumgardt and Ziegler, 1988; Stump and Riemer, 1988; Smith, 1989). This spectral color is due to the interaction of the time-offset wavefields produced by each sub-explosion. Briefly, the regular repetition and superposition of similar seismic motions in the time domain leads to regular amplification and suppression of power in the frequency domain. The manner in which the wavefields interact undoubtedly involves nonlinear processes; however, we feel that simple linear theory is sufficient to describe the most obvious result, specifically the pronounced spectral modulation. As described in paper 1, and by numerous other authors (Baumgardt and Ziegler, 1988; Stump and Reinke, 1988; Smith, 1989; Stump *et al.*, 1989) this model makes the assumptions that the wavefields produced by each sub-explosion $w(t)$ are identical and they superpose linearly. Forcing all shots to occur at regular time-intervals T we can construct the wavelet produced by the ensemble of sub-explosions (lasting a total of D seconds) by the equation:

$$x(t) = w(t) * \left[\frac{1}{T} III\left(\frac{t}{T}\right) \bullet B\left(\frac{t}{D}\right) \right] \quad (1)$$

where \bullet represents multiplication, $*$ represents convolution. Here, III is the shah function (Bracewell, 1986) and B is the boxcar function. Hereafter we refer to this representation as model 1. By Fourier transforming this expression we see that the spectrum of the entire seismogram equals that of an individual event multiplied by a set of equispaced sinc functions - collectively referred to as the modulation function:

$$\tilde{X}(f) = \tilde{W}(f) \bullet \left[III(fT) * \frac{\sin(\pi f D)}{\pi f} \right] \quad (2)$$

In Figure 2 we display the modulation function resulting when 39 sub-explosions spaced at 25 ms are superposed in this manner. Primary reinforcement occurs at multiples of 40 Hz (the loci of the main-lobes of the sinc functions). The side-lobes have insignificant amplitudes relative to the main-lobes. They can, however, in theory allow us to compute the duration of the entire quarry blast. The duration, D , is given by the inverse of the width of a single sidelobe. In the event displayed in Figure 2, this value is .975 seconds, the known duration of the set of explosions.

As discussed in paper 1, using the model described above, we predict the modulation produced by ripple firing should be independent of time in the coda. In paper 1 we found that this predicted character can be investigated efficiently by the computation of frequency-time displays known as sonograms (Markel and Gray, 1976; paper 1). In Figures 3 and 4 are displayed the sonograms computed from the coda generated by an earthquake and a quarry blast respectively. The quarry blast (Figure 4) clearly shows a time-independent spectral modulation whereas the earthquake (Figure 3) does not. Often the two types of events do not contrast as well as these examples do when presented in this format. For this reason we have found it beneficial to convert the spectral estimates to binary form. The means by which we accomplish this conversion is discussed fully in the paper 1, and involves comparing a relatively unsmoothed version of each spectrum with a more heavily smoothed one that resolves only the large scale structure, in order to extract the regular modulation. In practice, when analyzing the events considered in this paper, we simply convolved the spectra with boxcar functions spanning 1.0 and 2.5 Hz respectively. We then represent all sections of the spectra where the local power is high relative to the more regional average power by a value of +1 and where it is low by a -1. In this manner the bulk of the magnitude information is discarded and the spectra are "flattened" to very simple binary patterns. When analyzing array data, we generalize the procedure by computing such a binary pattern for each trace individually, and then stacking all the patterns. Because the procedure is quite nonlinear, this is very different from computing binary sonograms from beams as in figures 3 and 4. As illustrated below, stacking after reduction to binary patterns is a more effective approach for our present purposes. In Figures 5 and 6 we display array stacks of the binary sonograms computed for the events displayed in Figures 3 and 4 respectively. Since typically 25 vertical sensors simultaneously record each event, the values in these binary stacks typically range from -25 to +25. The original spectral estimates have been corrected for noise by subtracting an average pre-event sample. Time-independent spectral modulation is present after the onset in the coda of the quarry blast only. This spectral character is not unique to this event but is shared by virtually all the events identified in table 1 as explosions.

4. The cause of the observed spectral modulation

The simplest explanation of the observed spectral modulation is, as discussed in the previous section, that it is due to ripple-firing. The main argument against this explanation is that the inferred delay times at the source are extremely long. Spectra computed from a typical event (030 - pictured in Figures 4 and 6) have power highs spaced at roughly 5 Hz leading to an inferred average shot spacing of 200 ms. In paper 1 we inferred delay times as high as 400 ms at quarries in Kazakhstan, U.S.S.R. As Baumgardt and

Ziegler (1988) mention, "slow delays" (from 500 to 1000 ms) are used in subsurface mining where the intent is to use a shot to remove material prior to the next shot. We have reason to believe, however, that the explosions considered in paper 1 and the current dataset did not occur in the subsurface. With the aid of satellite (SPOT) photos we know that a number of the mines in Kazakhstan are at the free surface (Thurber *et al.*, 1989). The Blasjo explosions are known to be associated with the construction of a dam (Baumgardt and Ziegler, 1988). As discussed by several authors (including Langefors and Kihlström, 1978) the short delays employed at free-surface mining operations generally fall in the range from 1 to 100 ms and are typically on the order of 20 to 30 ms. Using the model described in the previous section, and 30 ms offsets, we predict spectral amplification at multiples of 33 Hz - well beyond the Nyquist frequency of the NORESS dataset. It is conceivable that the closely spaced modulations (shown in Figures 4 and 6) could be an artifact of multiple-row blasting where short delays are used between successive shots in each row, but adjacent rows are spaced by significantly greater delays. Synthetic experiments, in which modulation functions are computed for a variety of quarry blast configurations, suggest that this is a plausible argument; however, realistic examples taken from the literature do not. For example, Stump *et al.* (1989) describe multiple-row quarries which have interrow time spacings of 42 ms. This argument does not rule out slow delays, either between successive shots or adjacent rows, but suggests we should look for alternative explanations for the observed spectral modulation.

As discussed in paper 1 and Hedlin *et al.* (1988) it is possible for a wavefield to acquire a time-independent spectral modulation during propagation by resonating in low velocity layers. The most likely locations of layer resonance are in low velocity sediments or weathered strata near the free-surface close to the source and/or the array. Considering that many of the recorded events have given rise to unmodulated spectra it is clear that no significant near-receiver resonance is taking place. Furthermore, since different modulation patterns are commonly produced by different events with the same location (such as successive mine explosions at the same mine), the modulations are clearly not due to near source resonance. We conclude that the spectral modulation is most likely due to intrinsic source processes.

A third explanation relies again on source multiplicity. The modulation function produced by model 1 is dominated by the main-lobes of the sinc functions. These are the only features that can realistically be expected to produce observable spectral peaks when the time delays are perfectly regular. Model 1, however, does not describe a very likely quarry blast. As discussed by many authors (including Langefors and Kihlström, 1978; Dowding, 1985 and Stump *et al.*, 1989) ripple-fired shots in quarries are spatially offset, usually in a regular pattern. At each shot location there are sometimes several vertically offset

(decked) charges. The time-delays between the shots, especially in multiple row blasting, are not necessarily going to be consistent. Actual shot times often deviate a considerable amount from the intended times (Stump and Reamer, 1988). Knowing the near-surface velocity and the slowness (p) of the energy under consideration we can replace actual time and space offsets (δT_i and $\delta X_i, \delta Y_i$) with apparent time offsets δT_i^a by employing the formula of Smith (1989):

$$\delta T_i^a = p \sqrt{\delta X_i \cos^2 \theta + \delta Y_i \sin^2 \theta} + \delta T_i \quad (3)$$

The azimuth from the quarry to the receiver is given by θ . All the aforementioned factors can cause a considerable deviation of the apparent times of the sub-explosions from a common value. Using these apparent time-offsets, and assuming linear superposition and commonality of basis wavelet $w(t)$, we can construct the wavelet due to a more general quarry blast.

$$x(t) = \sum_{i=1}^n w(t - \delta T_i^a) \quad (4)$$

In the frequency domain this expression is equivalent to:

$$\tilde{X}(f) = \tilde{W}(f) \cdot \left[\left(\sum_{i=1}^n \cos(2\pi f \delta T_i^a) \right)^2 + \left(\sum_{i=1}^n \sin(2\pi f \delta T_i^a) \right)^2 \right]^{\frac{1}{2}} \quad (5)$$

Scatter in the apparent times of the sub-explosions reduces the dominance of the main lobes, or equivalently, lets the side-lobes rise into prominence (paper 1). To illustrate this point we have computed a theoretical modulation pattern for a quarry blast layout adapted from that of a real life quarry, the San Vel quarry, described and studied by Stump and Reimer (1988) and Stump *et al.* (1989). As displayed in Figure 7 the sub-explosions are arranged in an en echelon pattern. The shots in each row are spaced at 25 ms proceeding from west to east. The row detonations are separated by 42 ms proceeding from south to north. The modulation functions, computed for energy traveling to observation points due north and east of the quarry with a slowness of 1/7 s/km, are displayed in Figure 8. Although the dominant delay time is 25 ms, the 40 Hz peak does not dominate either modulation function. The function for the station to the north can be constructed by multiplying the modulation function due to 13 shots spaced at 25 ms (representing the intershot delays) with the function corresponding 3 shots spaced at roughly 42 ms (representing the interrow delays after taking into account the delay associated with the propagation of the energy between the rows). The two functions are in competition and the result is that the broad main-lobes of the latter

accentuate the side-lobes of the former to a point where they can be expected to have a significant impact on the spectrum of the quarry blast.

Using a technique employed in paper 1 we synthesize a quarry blast using the apparent sub-explosion times occurring in the event described above. We assume a common waveform is generated by each sub-explosion and for that waveform we select the calibration explosion Chemex 2 detonated in Kazakhstan, U.S.S.R. and recorded at the station at Bayanaul. (We have resorted to this dataset simply because the 40 Hz NORESS data do not have adequate resolution in time to permit the millisecond offsets required by this quarry.) The Chemex 2 recording was made at 250 s^{-1} . This "Green's function" is linearly stacked upon itself 39 times after including the offsets appropriate for the observation point due north of the quarry. Although we have chosen to create the synthetic quarry blast by offsetting and stacking a Green's function in the time domain, the equivalent result could be achieved by multiplying the spectrum of the Green's function by the complex modulation function which underlies the solid curve pictured in Figure 8. Prior to computing the sonogram, the "synthetic" seismogram was low-pass filtered between 0 and 20 Hz and decimated to one point in 5 to mimic a NORESS recording. The sonogram (displayed in Figure 9) is dominated by time-independent structure. Assuming this modulation pattern was due to main-lobe activity, one would estimate a dominant delay time to be roughly 170 ms (the inverse of 6 Hz). We know, however, that this structure is due to side-lobe activity and is controlled in this case by the total duration of the quarry blast. Because of the manner in which the sonogram is calculated, the frequency estimates are heavily smoothed. Longer time windows would allow a more accurate estimate of the frequency spacing of the modulation. In fact we know that the average sidelobe width is roughly 2.6 Hz (see Figure 8) and that the duration of the quarry blast is 384 ms.

It seems that there is a fundamental ambiguity in the spectral modulation produced by ripple-fired, and hence non-instantaneous, events. Without *a priori* information about what occurred at the source we cannot be sure if the modulation spacing is controlled by the duration of the entire set or by the dominant inter-shot apparent time spacing. This experiment shows that our discriminant, perhaps, will not recognize quarry blasts because they are ripple fired *per se*, but because they last an intermediate length of time. Instantaneous events give rise to unmodulated spectra. Extremely long events (for example large earthquakes) should produce very finely modulated spectra, such that the modulation is masked by scattering and noise.

In paper 1 we considered two types of events - calibration explosions which were detonated by American and Soviet scientists (Given *et al.*, 1990) and did not involve ripple firing. Using *a priori* information we strongly suspected the rest of the events were quarry blasts. This information included satellite photos,

provided by Prof. Clifford Thurber (at the University of Wisconsin), which showed surface mining activity in the vicinity of some of the events. In addition it is known that the region has little natural seismicity (Leith, 1987). Time independent spectral modulation was only observed in the latter set of events and was attributed to the source multiplicity. The current study and the previous one are consistent in suggesting that quarry blasts can be discriminated from non ripple-fired events.

5. The automatic discriminant

For our purposes it is irrelevant whether the time independent spectral features observed in the coda produced by quarry blasts are due to main lobes, or sidelobes in the modulation functions. Ripple fired events tend to give rise to time independent spectral modulation, the earthquakes examined in this study do not. To examine this modulation we have developed a means to "expand" a time series into a matrix of numbers depending on frequency and time. Typical patterns obtained from recordings of an earthquake and a quarry blast (Figures 5 and 6) illustrate that it can be very easy to discriminate visually between these two types of events given these time-frequency displays. In paper 1, using the same approach, we found a similar degree of success in discriminating between quarry blasts and single-event explosions. Given the current interest in the problem of discriminating quarry blasts from earthquakes and single-event explosions and the large numbers of events involved we feel it is important to extend the algorithm so that human intervention is distanced from the discrimination process - to a point where the patterns can be recognized automatically by the computer. One method we have found to be very effective involves the computation of a two-dimensional Fourier transform of the sonogram matrices. This can be considered as an extension of *cepstral* analysis (Tribolet, 1979). In the standard cepstral analysis a Fourier transform of the log of the amplitude spectrum is computed to highlight any regular spectral modulation regardless of its longevity. The independent variable is known as the *quefrecy* and has units of time. The form of cepstral analysis we are proposing is more demanding, however. A given point in the 2-D cepstral matrix not only represents spectral modulation at a certain quefrecy, but periodic along the time axis at a certain frequency. It is thus a simple matter to isolate energy periodic in frequency and independent of time.

To illustrate our point we display two 2-D cepstra in Figures 10 and 11. The first was computed from the first 100 seconds of coda of event 030 (Figures 4 and 6), the second was computed from the coda of the earthquake 094 (Figures 3 and 5). The quarry blast has significantly more energy at zero frequency (along the time axis) than the earthquake. The quefrecy at which the power is concentrated in the 2-D cepstrum computed from the coda produced by the quarry blast is roughly 0.2 seconds (reflecting the

spectral modulation with 5 Hz spacing. Slices at zero time-frequency through 2-D cepstra computed from the coda produced by a quarry blast (event 507) and all the earthquakes in the dataset are shown in Figure 12. As expected, the quarry blast is a singular event. The most noticeable feature in the quarry blast cepstrum is, obviously, the significant peak at a quefreny of 0.2 seconds. We expect that ripple-fired events should give rise to significantly larger extreme cepstral values than earthquakes. Supporting this thesis are the histograms in Figure 13 showing the observed distributions of cepstral extremes for the entire earthquake and quarry blast populations examined in this study.

Although we are most interested in the quarry blast cepstra, we can gain some important insight from the earthquake cepstra which illustrate the 2-D cepstral structure that can be expected in the absence of source multiplicity. These cepstra show what time-independent structure will be acquired by a propagating wavelet or, in other words, they are indicative of the region's natural level of resonance. We propose to identify events as quarry blasts by searching for anomalously high global extrema in the time-independent segments of the 2-D cepstra. To calibrate the algorithm, to account for the natural resonance in the region, we make the judgement of what is a large value on the basis of what extrema non-ripple-fired events produce. The consideration of global extrema in these 2-D cepstra is a problem that is well suited for analysis using the statistics of extremes (Gumbel, 1958). In Figure 13 it is clear that the logs of the extreme amplitudes are centrally distributed and there are no significant outliers. The Kolmogorov-Smirnov test suggests that the earthquake cepstral extremes follow a log-normal distribution. However we would like to avoid the adoption of a specific underlying distribution since we have no fundamental reason for choosing one and since we only have 16 earthquakes. It is known (e.g. Gumbel, 1958 and Weissman, 1978) that when dealing with observations of extreme values the underlying distribution need not be assumed, but the behavior can be modeled using functions that are asymptotically valid as the number of samples examined and the number of points in each sample approaches infinity (Kennedy and Neville, 1974). Selecting the exponential asymptote, the cumulative probability (P) that an extremum belonging to the earthquake population will be less than the one observed is given by:

$$P = e^{[-e^{(-y)}]} \quad (6)$$

where the expression for the reduced variate (y) is:

$$y = a(u - \hat{u}) \quad (7)$$

The terms a and \hat{u} are the dispersion parameter and the mode of the distribution respectively and are estimated directly from the population of earthquake extremes shown in Figure 13 (Kennedy and Neville, 1974). The log of the cepstral extremum of interest is represented by u . We find that for this distribution a and \hat{u} equal 7.204 and 3.55 respectively.

Given this probability function we can pose the discrimination problem in terms of a standard hypothesis test: Let the null hypothesis (H_0) be that a newly recorded event belongs to the population of earthquakes used to calibrate the technique. If the cepstral extremum calculated for this event exceeds a certain threshold determined from the distribution (8), then we can reject the null hypothesis (H_0) at a preset confidence level, and conclude that the event is probably a quarry blast. For example, on Figure 14, this threshold was selected such that for points that plot above the threshold line, the null hypothesis is rejected with only a 5% risk of doing so erroneously. In other words, we state that events above the line do not belong to the earthquake population, at the 95% confidence level. In spite of the apparent efficiency of the discriminant illustrated on Figure 14, we must remember that the calibration of the distribution (8) is based on our (small) sample of 16 identified earthquakes, so that the test is in fact "data fitted". Confirmation of our claim of success will have to be based on an independent sample. In this figure the symbol size is directly proportional to the signal to noise ratio (derived from average spectra encompassing the time from 50 seconds before and after the compressional onset). Of the 26 quarry blasts considered, 23 lie above the 95% confidence level. Of the two that fall well below this limit, one (event 505 - located in northern Sweden) had extremely low signal to noise levels (less than 10 dB) and the other (event 504) produced only a very broad spectral modulation. The three earthquakes located above a probability of 0.8 (events 112, 523 and 208) all suffered from signal to noise ratios less than 10 dB.

6. Conclusions

In a previous paper (Hedlin *et al.*, 1989b) we advanced the preliminary observation that ripple-fired events tend to give rise to coda dominated by time-independent spectral features and that this quality should be exploited to discriminate these events from earthquakes and single-event explosions.

In this paper we have demonstrated that this can also be done with a high degree of success when considering earthquakes and quarry blasts. We have found that quarry blasts tend to produce modulated spectra, but the modulations may not result directly from the ripple-firing; they may exist simply because the event is non-instantaneous. We have produced an empirical, calibrated, approach to the discrimination problem which allows for local seismic resonance. We have automated the approach to the point where

discrimination can be carried out solely by the computer. We have examined a dataset consisting of 26 quarry blasts and 16 earthquakes and have found that with few exceptions the two populations are well separated by our approach. The events which failed to be identified with a high degree of confidence generally suffered from low signal to noise ratios.

By comparing our current results with those in the earlier work we have illustrated the ability of the algorithm to accommodate changes in the recording environment, local geologic setting and mining practice. Based on the results presented in paper 1, we expect that we would have a similar degree of success in discriminating between single-event explosions and quarry blasts.

7. Acknowledgments

We thank Dr Thomas Carter at the Center for Seismic Studies for providing us with the bulk of the events used in this study. Dr Thomas Sereno, at Science Applications International Corporation in San Diego, helped us obtain the rest of the NORESS events. We thank Graham Kent and an anonymous reviewer for helpful suggestions. The Kazakh event was recorded by a station installed and operated by the Institute of Physics of the Earth of the Soviet Academy of Sciences and the Natural Resources Defense Council. This research was sponsored by the Defense Advanced Research Projects Agency (DARPA)/ Air Force Geophysics Laboratory (AFGL) under contracts No. F19628-89-K-0018 and F19628-88-K-0044.

8. References

- Baumgardt, D. R. and Ziegler, K. A. (1988). Spectral Evidence for Source Multiplicity in Explosions: Application to Regional Discrimination of Earthquakes and Explosions. *Bull. Seismol. Soc. Am.*, **78**, 1773-1795.
- Baumgardt, D. R. and Ziegler, K. A. (1989). Automatic recognition of economic and underwater blasts using regional array data. *unpublished report to Science Applications Incorporated*, 11-880085-51.
- Bell, A. G. R. (1977). A Digital Technique for Detection of Multiple Seismic Events. *EOS, Trans. of the American geophys. Union*, **57**, 444.
- Bracewell, R. N. (1986). *The Fourier transform and its applications*. McGraw-Hill Book Company.
- Bungum, H., Mykkeltveit, S. and Kværna, T. (1985). Seismic noise in Fennoscandia, with emphasis on

- high frequencies. *Bull. Seismol. Soc. Am.* , 75, 1489-1513.
- Dowding, C.H. (1985). *Blast vibration monitoring and control*. Prentice-Hall international series in civil engineering and engineering mechanics.
- Given, H.K., Tarasov, N.T., Zhuravlev, V., Vernon, F.L., Berger, J. and Nersesov, I.L. (1990). High-Frequency Seismic Observations in Eastern Kazakhstan, U.S.S.R., with emphasis on chemical explosion experiments. *J. Geophys. Res.* , 95, 295-307.
- Gumbel, E. J. (1958). *Statistics of extremes*. Columbia University Press, New York and London.
- Hedlin, M. A. H., Orcutt, J. A. and Minster, J. B. (1988). A Comparative Study of High Frequency Signal and Noise in Oceanic and Continental Environments. Contributed paper at "10th annual AFGL/DARPA seism. Res. Symp", held in Falbrook, CA.
- Hedlin, M. A. H., Orcutt, J. A., Minster, J. B. and Gurrola, H. (1989a). The time-frequency characteristics of quarry blasts, earthquakes and calibration explosions recorded in Scandinavia and Kazakhstan, U.S.S.R.. Contributed paper at "11th Annual AFGL/DARPA Seismic Research Symposium", held in San Antonio, TX.
- Hedlin, M. A. H., Minster, J. B. and Orcutt, J. A. (1989b). The time-frequency characteristics of quarry blasts and calibration explosions recorded in Kazakhstan, U.S.S.R.. *Geophys. J.* , 99, 109-121.
- Kennedy, J. B. and Neville, A. M (1974). *Basic statistical methods for engineers and scientists*. Harper and Row.
- Langefors, U. and Kihlström, B. (1978). *The modern technique of rock blasting*. Halsted Press, John Wiley and sons, New York.
- Leith, W. (1987). Geology of NRDC seismic stations in Eastern Kazakhstan, U.S.S.R.. *U.S.G.S. Open-File Report 87-597*.
- Markel, J. D. and Gray, A. H. Jr. (1976). *Linear Prediction of Speech*. Springer-Verlag, Berlin Heidelberg New York.

- Mykkeltveit, S. (1987). Local geology of the regional array sites in Norway. *Norsar Semiannual Technical Summary, Scientific Report No. 1-87/88*.
- Mykkeltveit, S., Åstebol, K., Doornbos, D.J. and Husebye, E.S. (1983). Seismic array configuration optimization. *Bull. Seismol. Soc. Am.* , **73**, 173-186.
- Park, J., Lindberg, C. R. and Vernon, F. L. (1987). Multitaper Spectral Analysis of High-Frequency Seismograms. *J. Geophys. Res.* , **92**, 12675-12684.
- Richards, P. (1988). Nuclear test ban treaties and seismic monitoring of underground nuclear explosions: an overview of the historical, technical and political issues. *the Alan S. Attardo Symposium on Science and Society*.
- Ringdal, F. and Husebye, E. S. (1982). Application of arrays in the detection, location, and identification of seismic events. *Bull. Seismol. Soc. Am.* , **72**, S201-S224.
- Sereno, T. J. Jr., Bratt, S.R. and Bache, T.C. (1987). Regional wave attenuation and seismic moment from the inversion of NORESS spectra. *unclassified semiannual report, Air Force Geophysics Laboratory, AFGL-TR-87-0237. ADA187399*.
- Smith, A. T. (1989). High-Frequency Seismic Observations and Models of Chemical Explosions: Implications for the Discrimination of Ripple-Fired Mining Blasts. *Bull. Seismol. Soc. Am.* , **79**, 1089-1110.
- Stump, B. W. and Reamer, S. K. (1988). Temporal and Spatial Source Effects from Near-Surface Explosions. Contributed paper at "10th annual AFGL/DARPA seism. Res. Symp", held in Falbrook, CA.
- Stump, B.W. and Reinke, R.E. (1988). Experimental confirmation of superposition from small-scale explosions. *Bull. Seismol. Soc. Am.* , **78**, 1059-1073.
- Stump, B. W., Reamer, S. K., Anderson, D., Olsen, K. and Reinke, R. (1989). Quantification of explosion source characteristics from near source, regional and teleseismic distances. *unclassified final report, Geophysics Laboratory, GL-TR-89-0194. ADA216218*.

- Thompson, D. J. (1982). Spectrum Estimation and Harmonic Analysis. *IEEE Proc*, **70**, 1055-1096.
- Tribolet, J. M. (1979). *Seismic Applications of Homomorphic Signal Processing*. Prentice-Hall Signal Processing Series.
- Thurber, C. H., Given, H. and Berger, J. (1989). Regional seismic event location with a sparse network: application to eastern Kazakhstan U.S.S.R.. *J. Geophys. Res.* , **94**, 17767-17780.
- Weissman, I. (1978). Estimation of parameters and large quantiles based on the k largest observations. *Journal of the American Statistical Association*, **73**, 812-815.

9. Table and Figure captions

Table 1. Event locations, origin times, local magnitudes and types.

Figure 1. Map showing the locations of the earthquakes (stars), explosions (octagons) and the NORESS array (dark triangle).

Figure 2. Spectral modulation predicted for an event consisting of 39 sub-explosions located at the same point in space and offset evenly in time at 25 ms.

Figure 3. Seismogram resulting from an earthquake located 342 km from NORESS (event 094) and corresponding sonogram. In Figures 3 through 6 the sonograms have been computed from a stack of 25 spectra, each computed from an individual vertical channel in the NORESS array. The stacks were computed after offsetting the seismograms to beamform for the Pg phase. In addition all spectral estimates have been corrected for noise and the instrument response. The spectral amplitudes in figures 3 and 4 are shown on a linear scale.

Figure 4. Seismogram resulting from a quarry blast located 301 km from NORESS (event 030) and corresponding sonogram.

Figure 5. Seismogram resulting from the earthquake presented in Figure 3 (094) and corresponding binary sonogram. The conversion to binary form was performed on each channel before stacking.

Figure 6. Seismogram resulting from the quarry blast presented in Figure 4 (030) and corresponding binary sonogram.

Figure 7. The layout of sub-explosions in an en echelon quarry blast. Shooting within the rows is spaced in time at 25 ms. Adjacent rows are separated by 42 ms in time. This pattern is adapted from Stump *et al.* (1989).

Figure 8. The amplitude of modulation functions resulting from the shot introduced in Figure 7. The solid and dashed curves represent energy traveling at a slowness of $1/7$ s/km to stations due north and east of the quarry respectively.

Figure 9. Time series and sonogram representing a "synthetic" quarry blast. The synthetic was constructed by linearly stacking a seismogram produced by the Chemex 2 explosion in Kazakhstan U.S.S.R. upon itself after offsetting in time to mimic the quarry pictured in Figure 7 when observed from a point to the north (see Figure 8). The original seismogram was sampled at 250 s^{-1} . The synthetic was low pass filtered and decimated to simulate recording conditions similar to the NORESS array.

Figure 10. Two-dimensional cepstrum computed from the coda produced by a quarry blast (event 030). The first 100 seconds of the coda were considered.

Figure 11. Two-dimensional cepstrum computed from the coda produced by an earthquake (event 094). The first 100 seconds of the coda were considered.

Figure 12. Slices through the time-independent portions of two-dimensional cepstra computed from a quarry blast (event 507) and all the earthquakes considered in this study. The quarry blast is shown as the solid line.

Figure 13. Histograms showing the observed distributions of global extreme cepstral values computed from the coda produced by earthquakes (top) and quarry blasts (bottom).

Figure 14. The cumulative probabilities of extreme cepstral values derived from the coda produced by all events in the dataset. The quarry blasts are denoted by octagons, the earthquakes are represented by stars. The likelihood that the assumption that the event is an earthquake is invalid increases with this probability. For points above the 0.95 threshold, the hypothesis that the corresponding events belong to the earthquake population is rejected at the 5% risk level. The event number (along the horizontal axis) indicates the location of the event in table 1. The symbol size scales with the signal to noise ratio (see insert).

Event	Latitude	Longitude	Origin Time	M I	Event type
	°N	°E	y/d-h:m:s (UTC)		
030	59.31	06.95	1985/302-10:22:52.8	1.9	Blasjo ex
039	59.31	06.95	1985/310-14:50:51.4	2.4	Blasjo ex
501	58.34	06.43	1985/313-14:42:45.0		Titania ex
094	59.73	05.71	1985/331-04:53:32.1	3.0	earthquake
099	61.55	04.65	1985/334-19:05:13.4	3.0	earthquake
111	60.19	05.25	1985/341-14:15:43.2	2.2	earthquake
112	58.90	05.98	1985/341-14:39:09.9	1.9	earthquake
158	58.34	06.43	1985/365-13:36:49.6	2.1	Titania ex
196	58.34	06.43	1986/031-14:17:35.7	1.9	Titania ex
522	62.74	04.50	1986/036-23:35:41.0	2.6	earthquake
523	62.90	04.86	1986/037-06:19:52.0	2.3	earthquake
208	62.90	04.86	1986/037-06:20:05.4	1.9	earthquake
216	66.45	14.89	1986/038-21:03:21.1	2.2	earthquake
524	62.40	05.28	1986/044-13:39:00.0	2.5	earthquake
525	62.61	05.07	1986/044-19:03:48.0	2.6	earthquake
504	58.34	06.43	1986/045-14:13:25.0	2.7	Titania ex
505	67.10	20.60	1986/045-16:44:08.0	2.6	explosion
506	58.34	06.43	1986/045-17:54:11.0	2.3	Titania ex
526	61.69	04.90	1986/047-18:19:41.0	2.0	earthquake
239	62.76	05.29	1986/057-02:11:58.5	1.9	earthquake
247	61.67	02.58	1986/067-16:21:18.3	1.9	earthquake
266	61.66	04.53	1986/089-03:22:48.7	1.6	earthquake
270	58.34	06.43	1986/094-13:12:43.9	1.9	Titania ex
298	59.31	06.95	1986/120-10:18:48.2	2.2	Blasjo ex
507	59.31	06.95	1986/147-18:36:14.0	2.3	Blasjo ex
508	59.31	06.95	1986/148-17:51:57.0	2.4	Blasjo ex
509	58.34	06.43	1986/157-13:14:28.0	1.7	Titania ex
510	59.31	06.95	1986/170-03:55:08.0	2.5	Blasjo ex
511	58.34	06.43	1986/174-13:12:54.0	1.8	Titania ex
512	59.31	06.95	1986/191-20:10:42.0	2.3	Blasjo ex
513	59.31	06.95	1986/197-17:49:28.0	2.3	Blasjo ex
514	59.31	06.95	1986/204-20:47:10.0	2.2	Blasjo ex
515	59.31	06.95	1986/210-13:13:41.0	2.3	Blasjo ex
516	59.31	06.95	1986/211-17:59:39.0	2.4	Blasjo ex
517	58.34	06.43	1986/226-13:14:39.0	1.9	Titania ex
518	59.31	06.95	1986/226-14:39:57.0	2.4	Blasjo ex
519	59.31	06.95	1986/245-12:53:51.0	2.1	Blasjo ex
520	59.31	06.95	1986/252-17:55:58.0	2.4	Blasjo ex
503	58.34	06.43	1986/274-14:15:10.0	1.9	Titania ex
521	58.34	06.43	1986/282-14:13:52.0	2.0	Titania ex
407	61.97	02.33	1986/283-19:56:29.1	2.1	earthquake
422	61.46	03.29	1986/299-11:44:54.1	2.4	earthquake

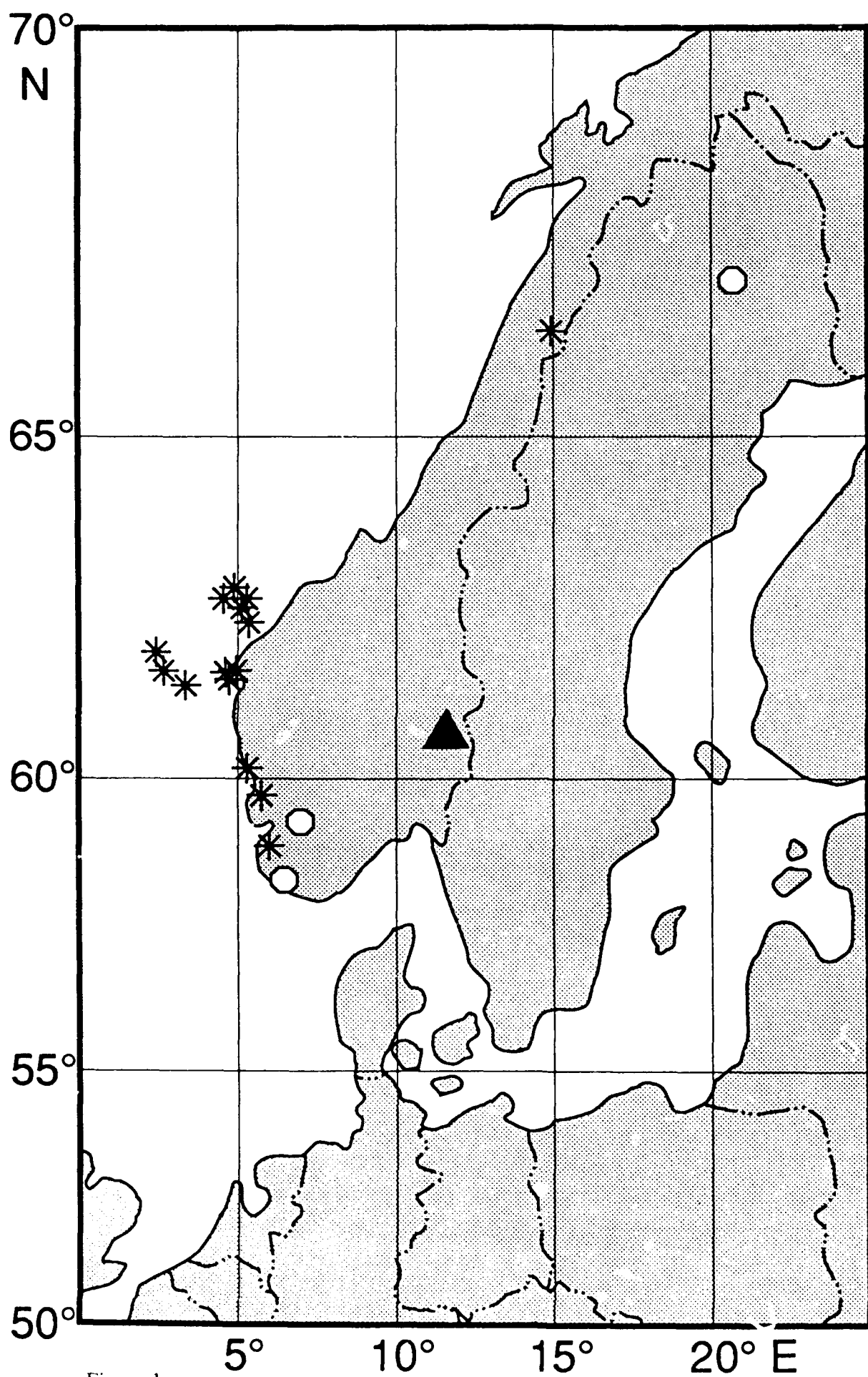


Figure 1

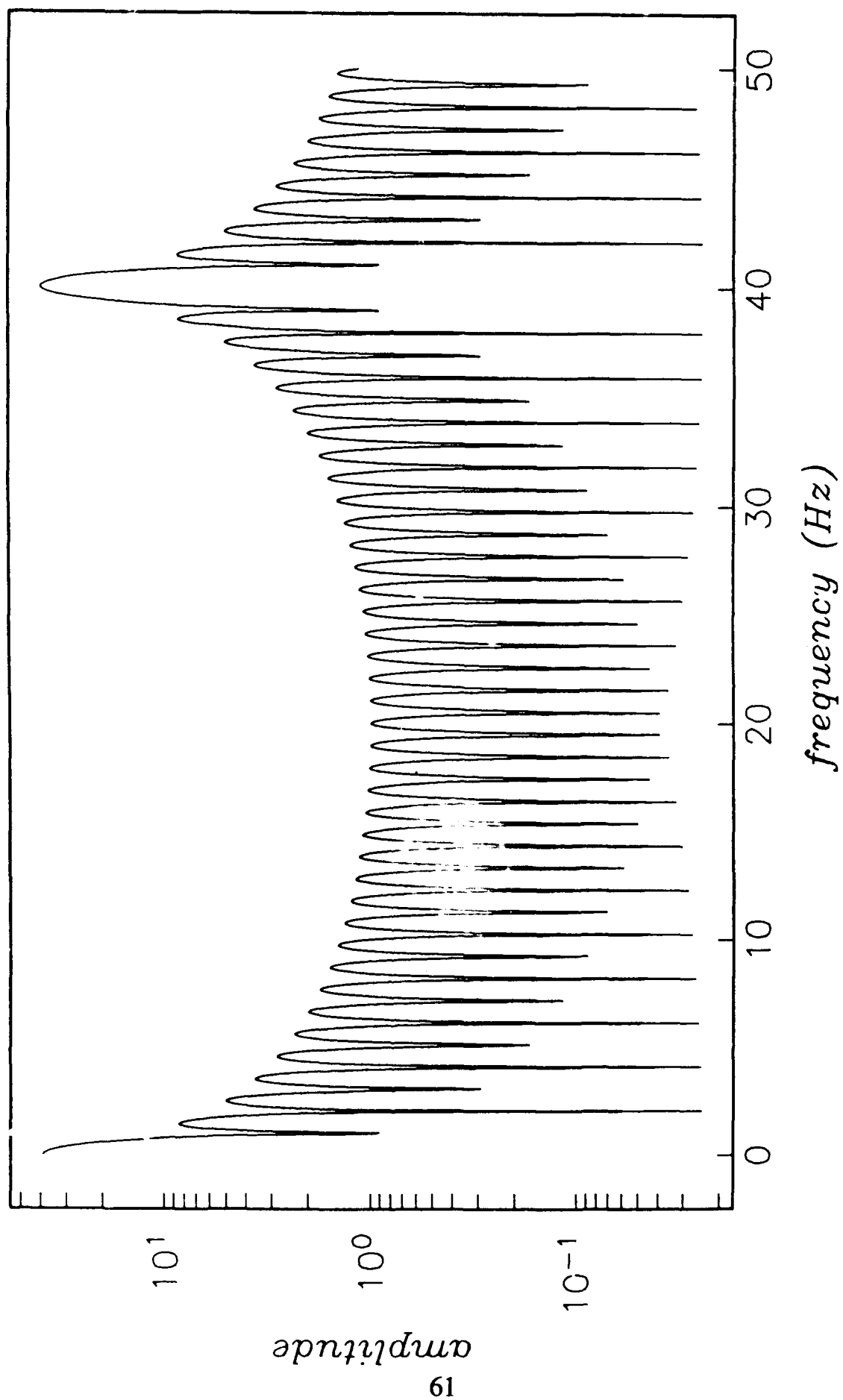


Figure 2

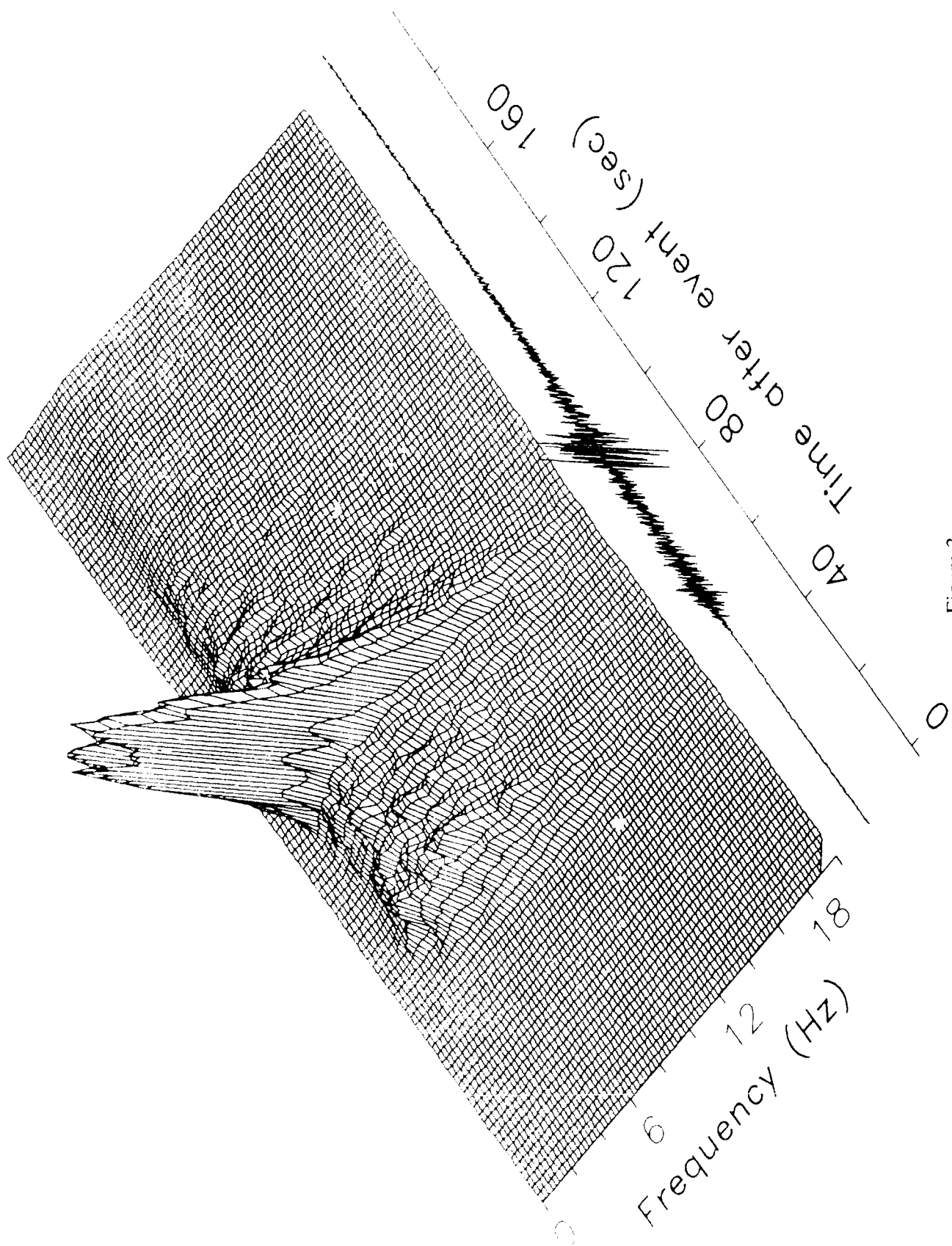


Figure 3

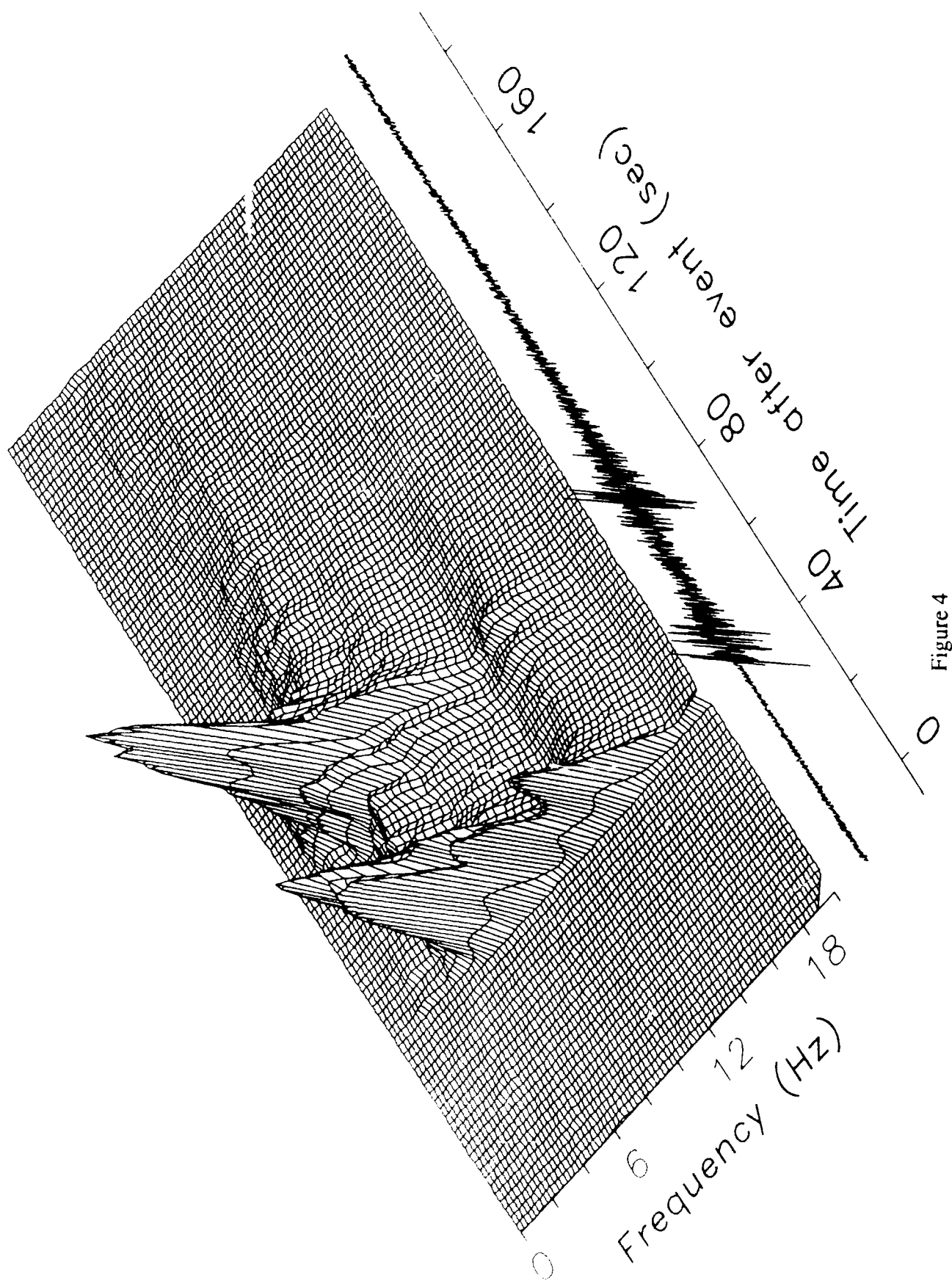


Figure 4

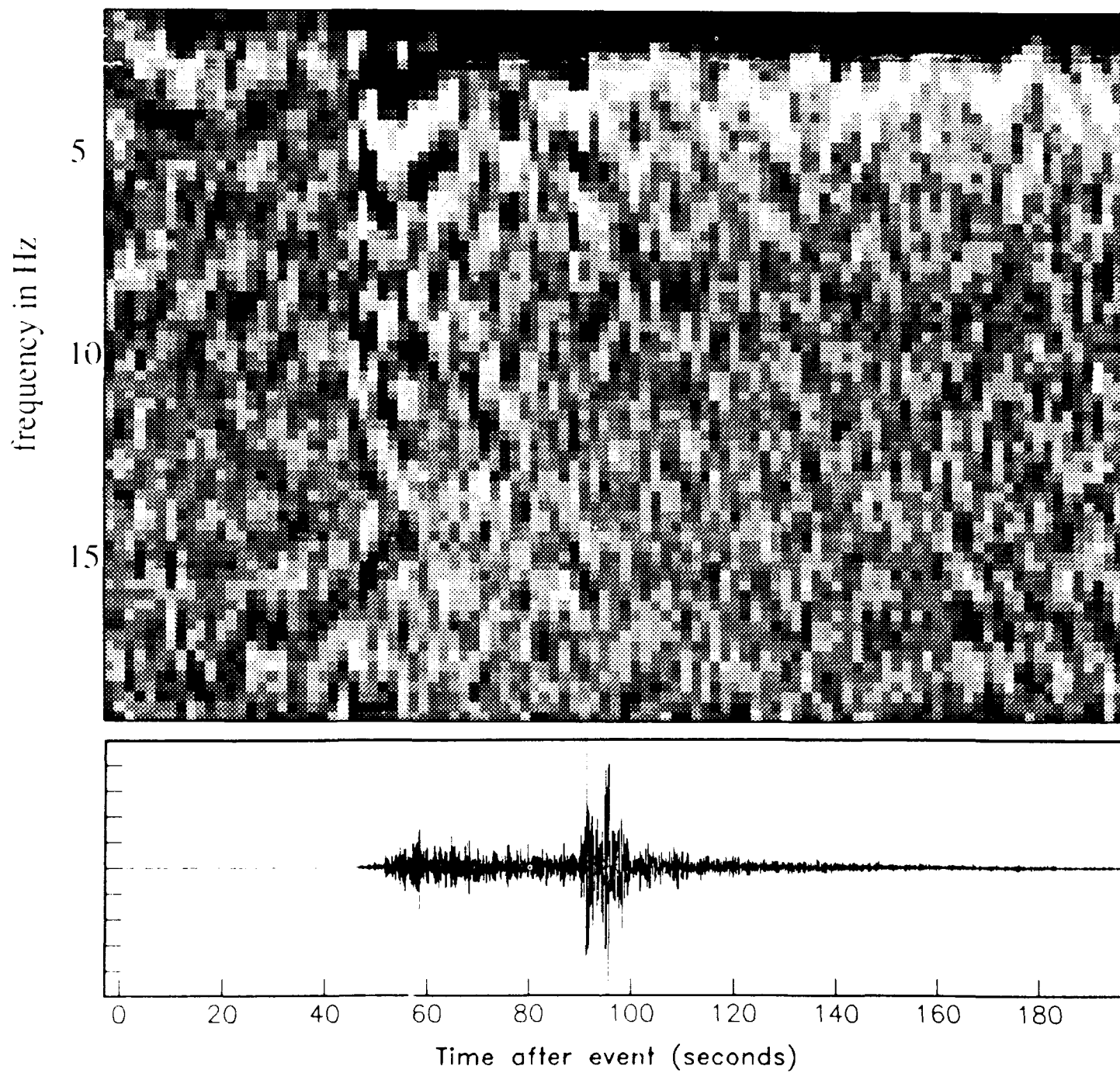


Figure 5

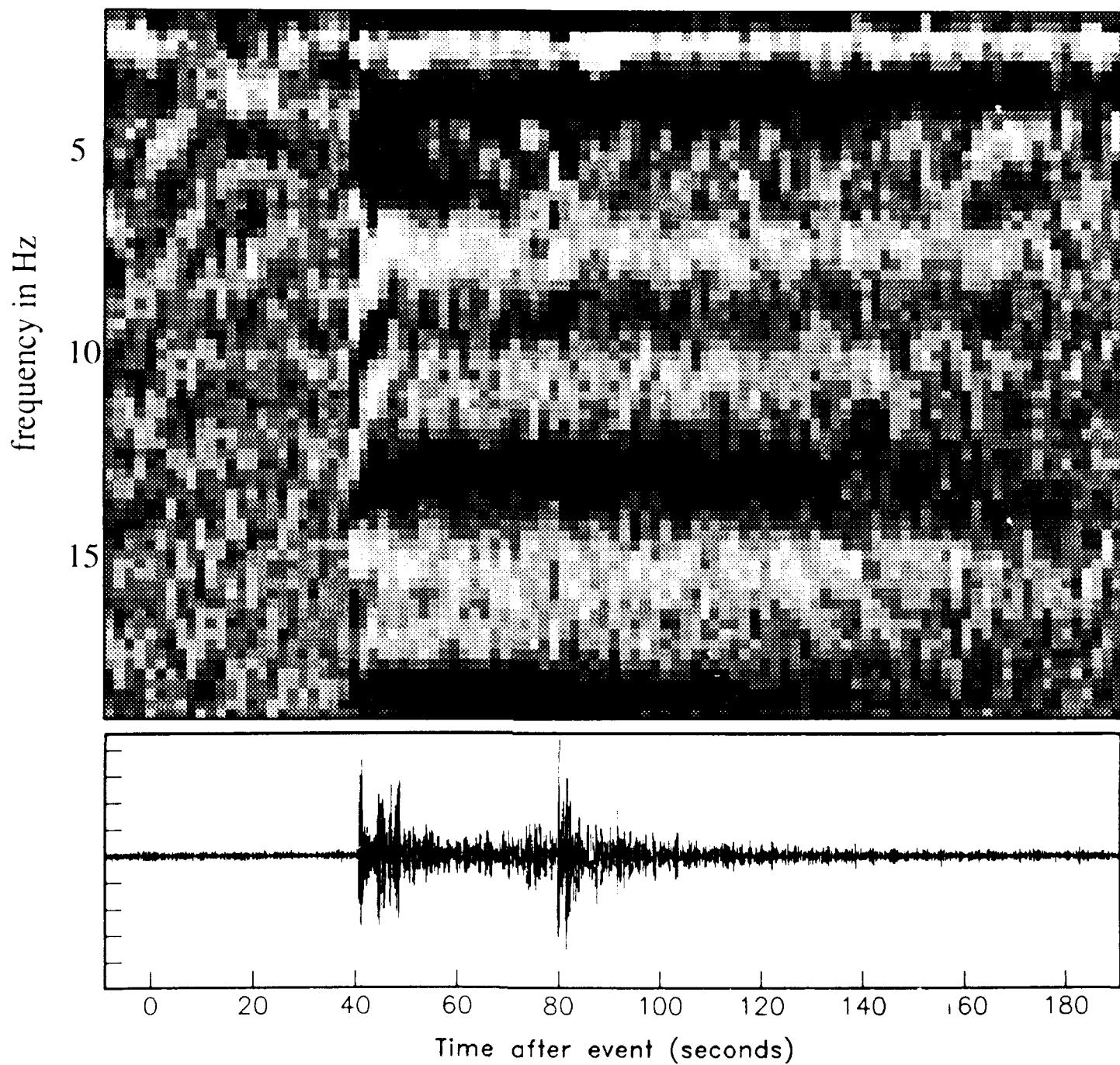


Figure 6

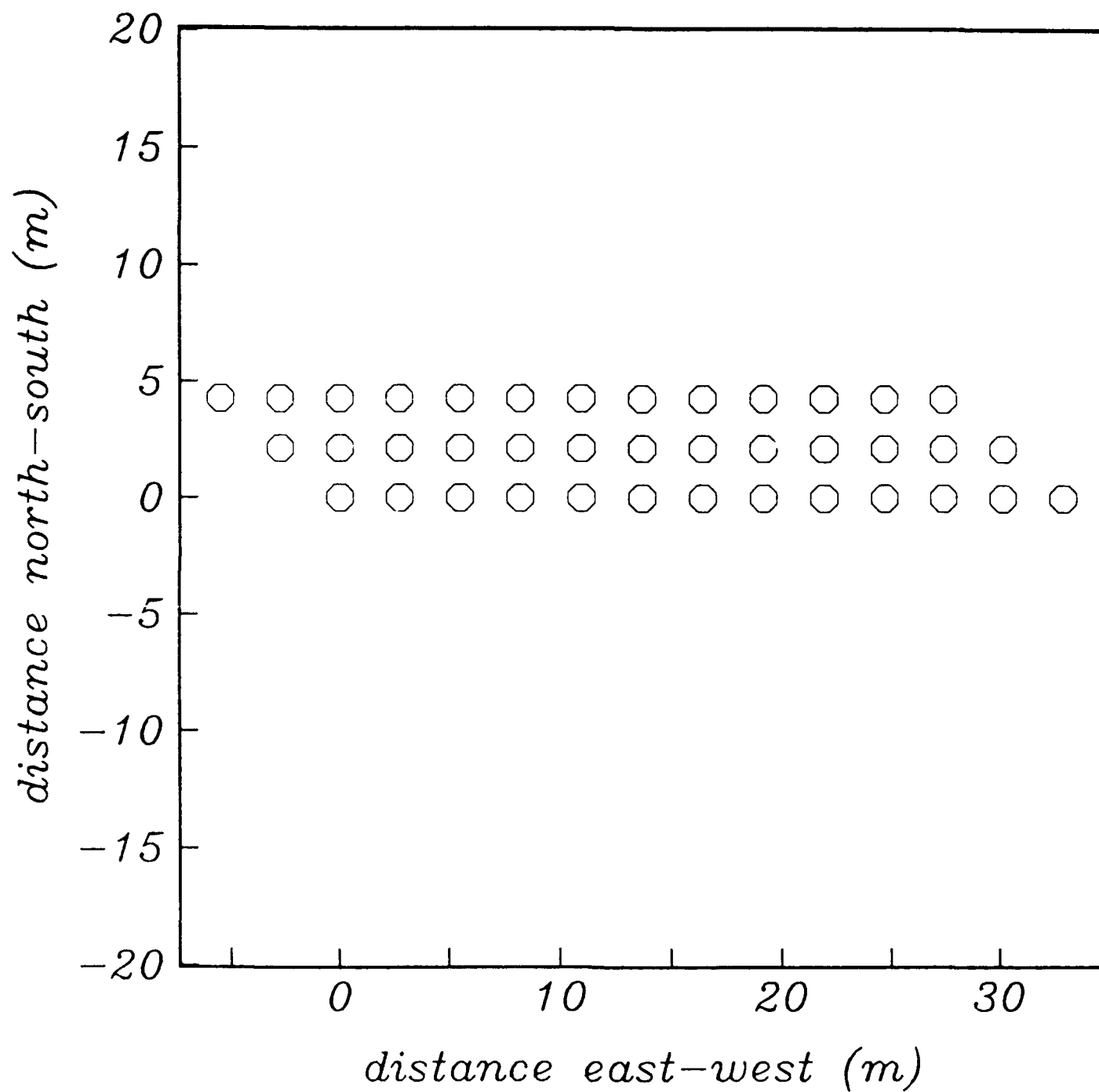


Figure 7

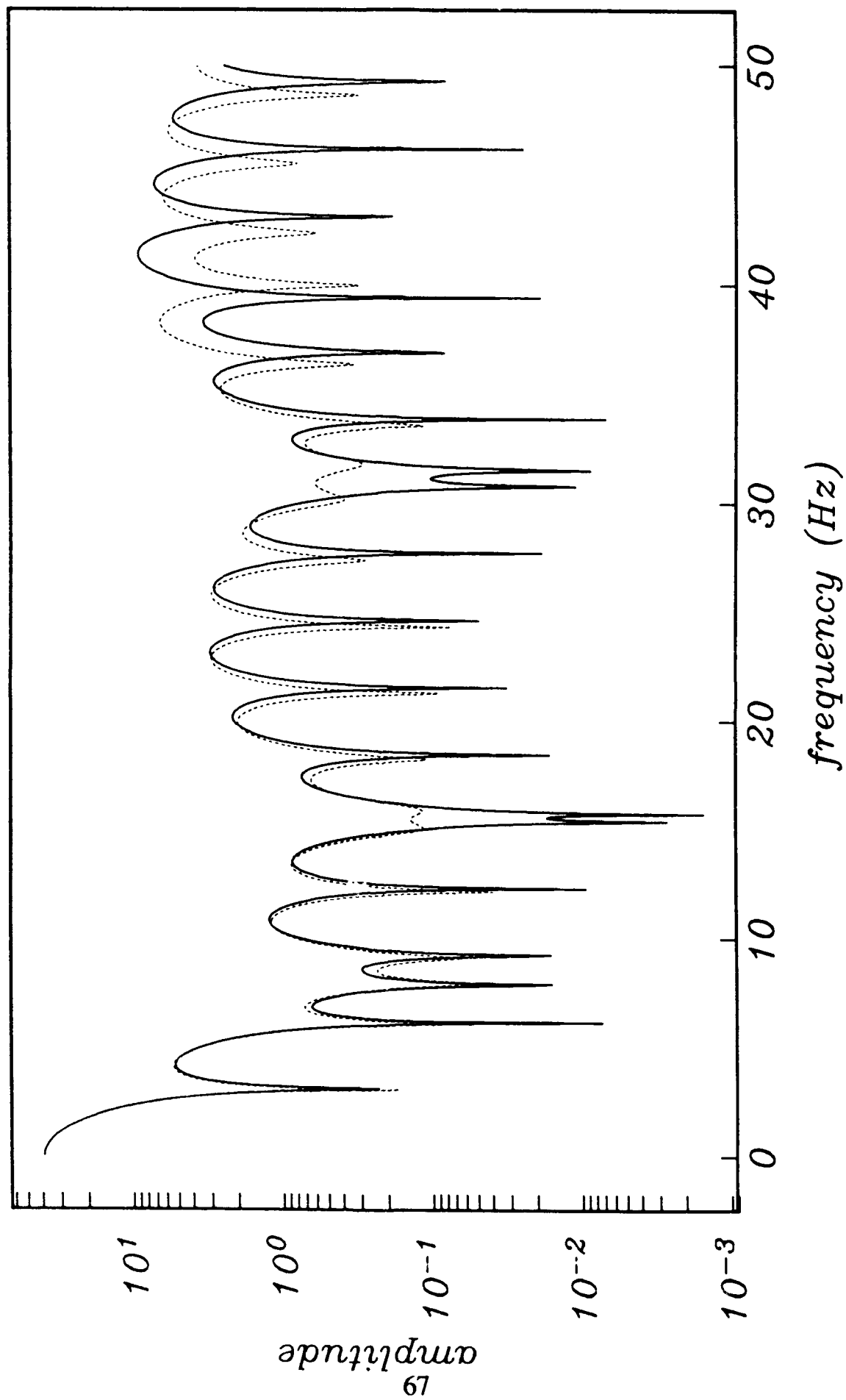


Figure 8

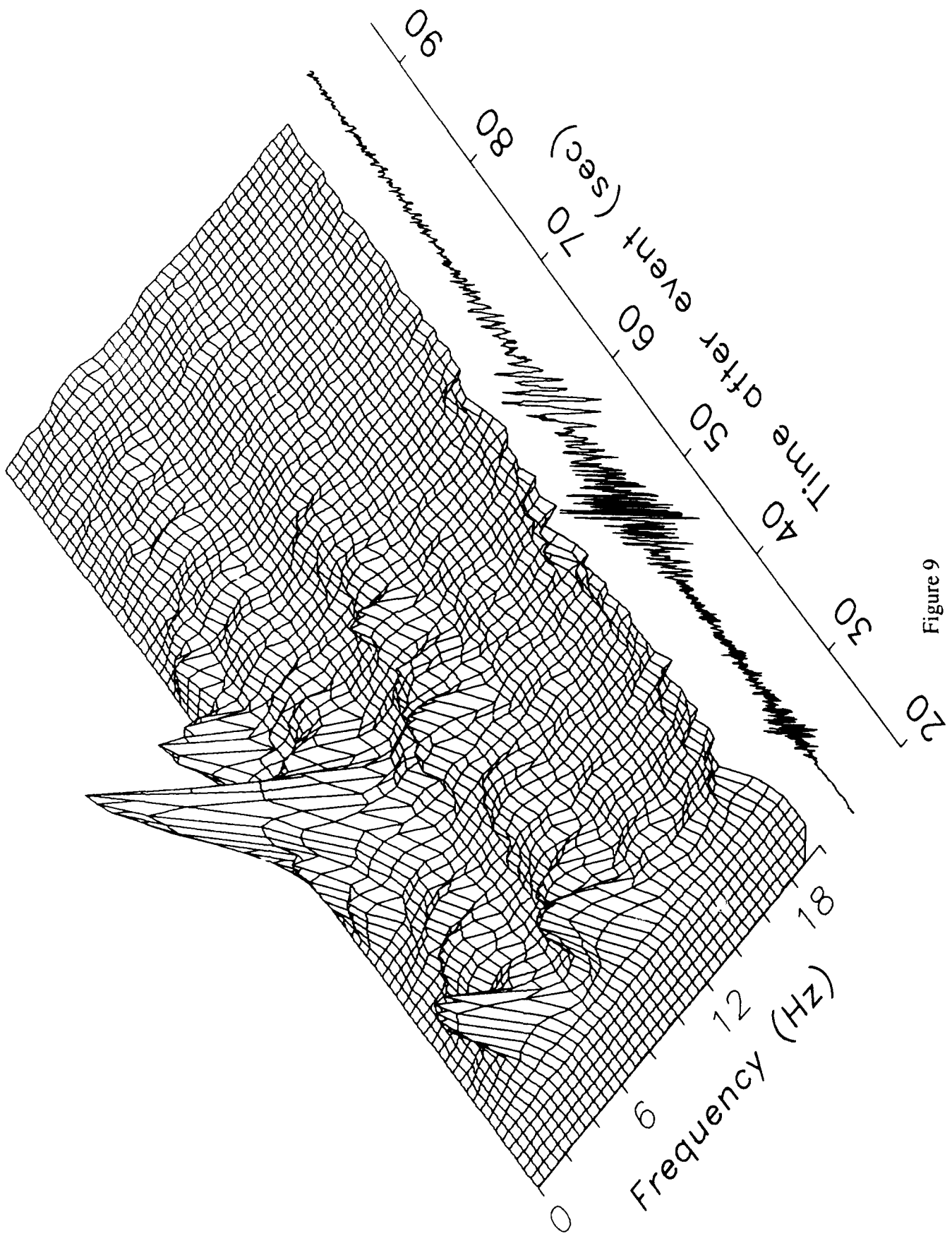


Figure 9

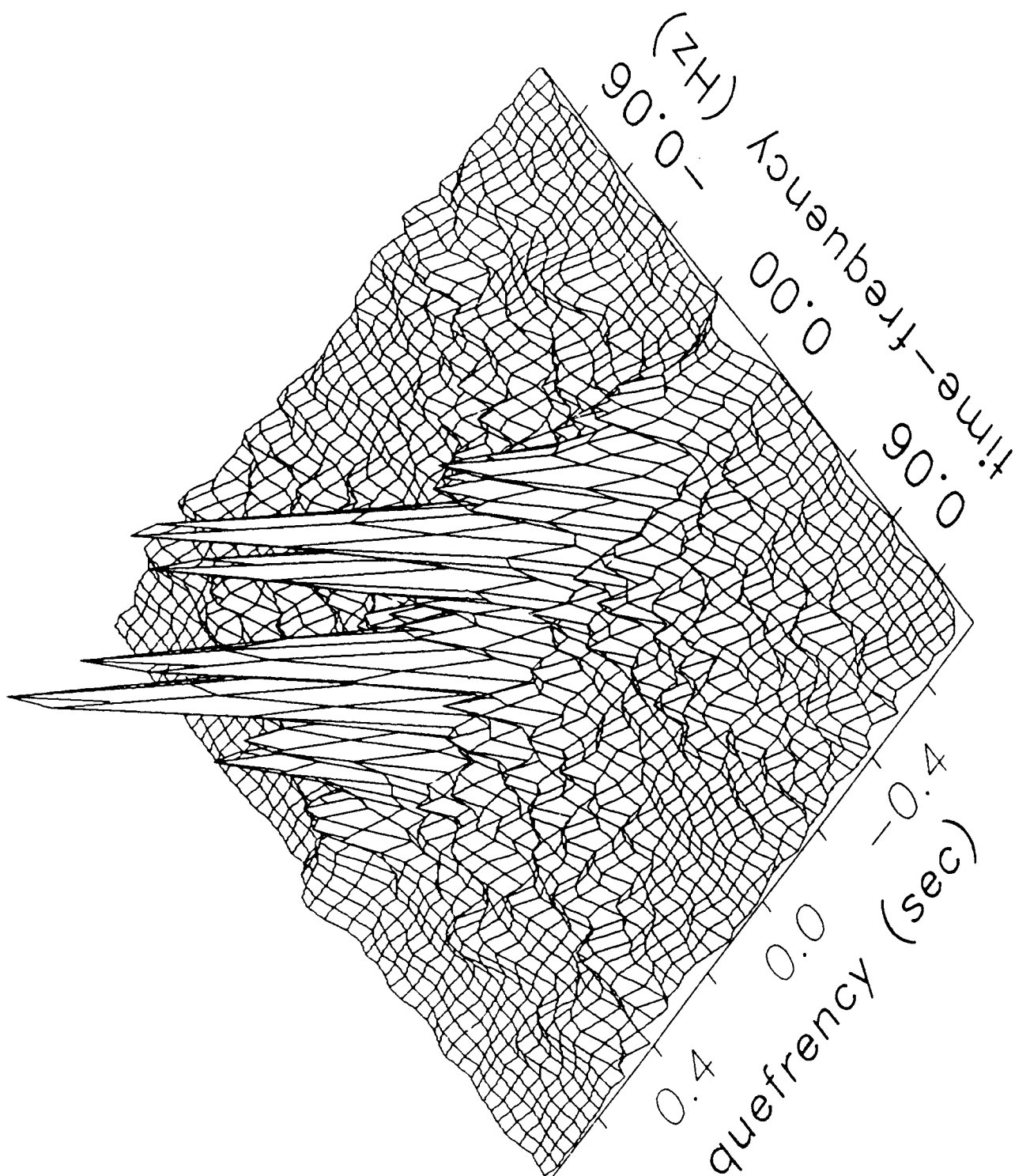


Figure 10

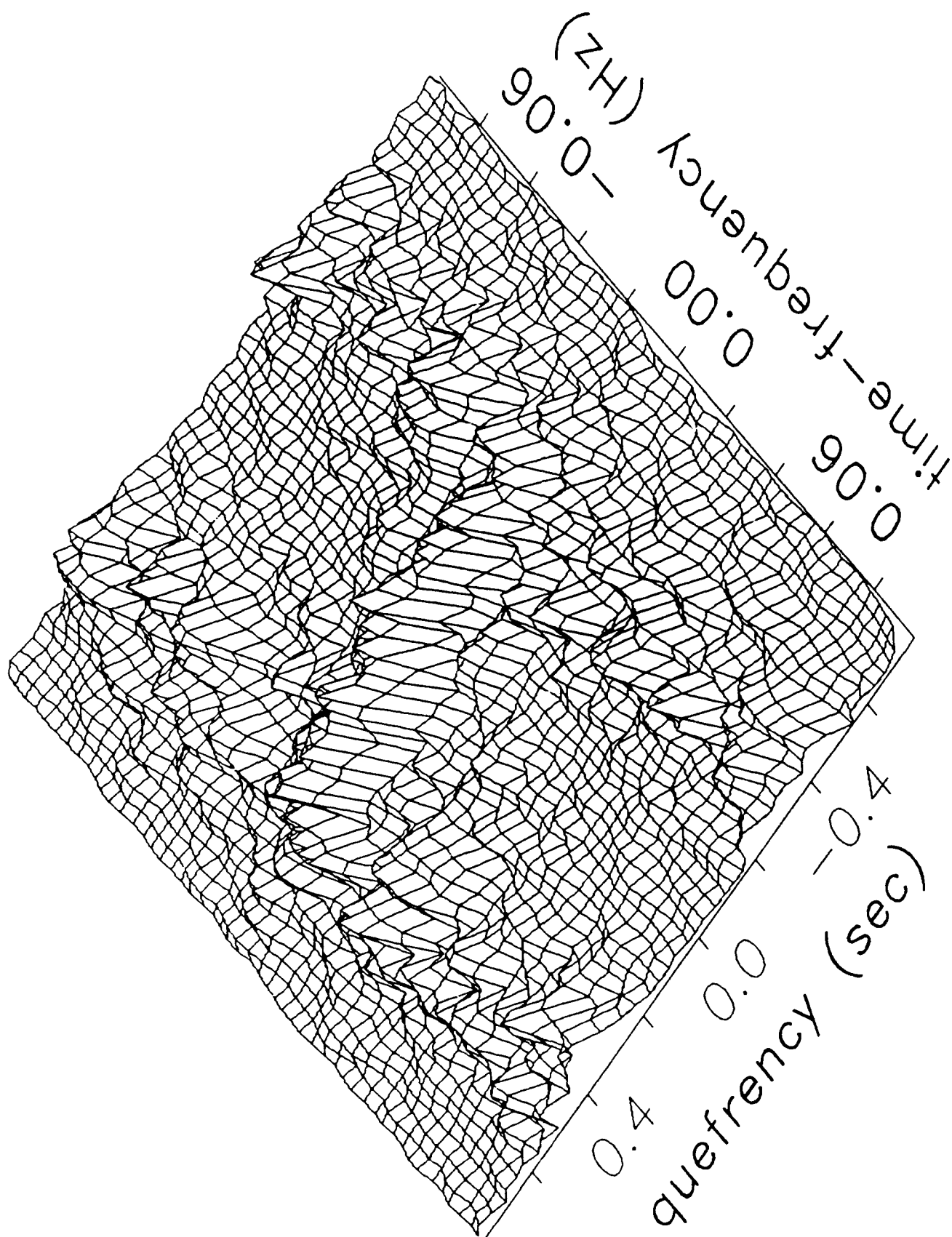


Figure 11

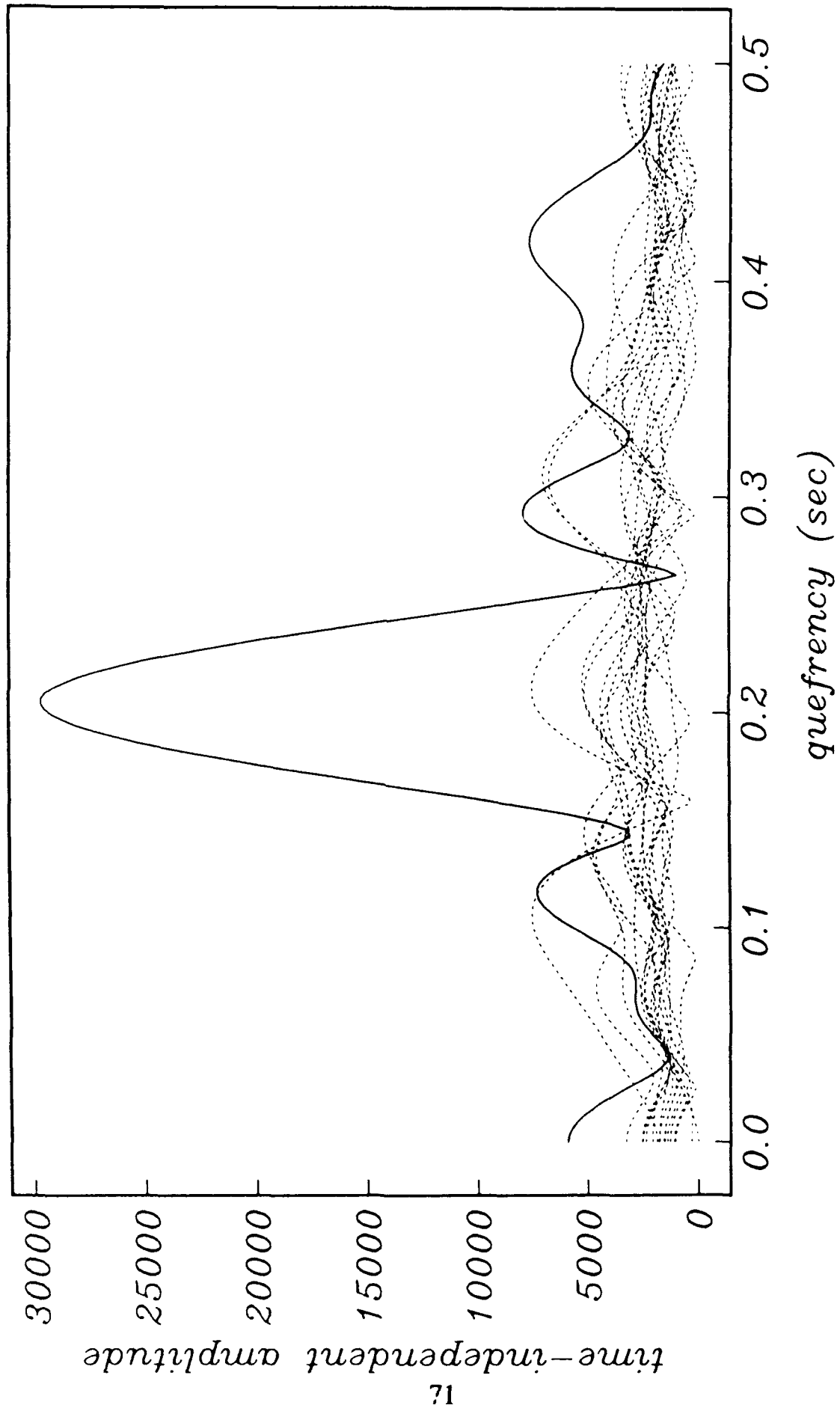


Figure 12

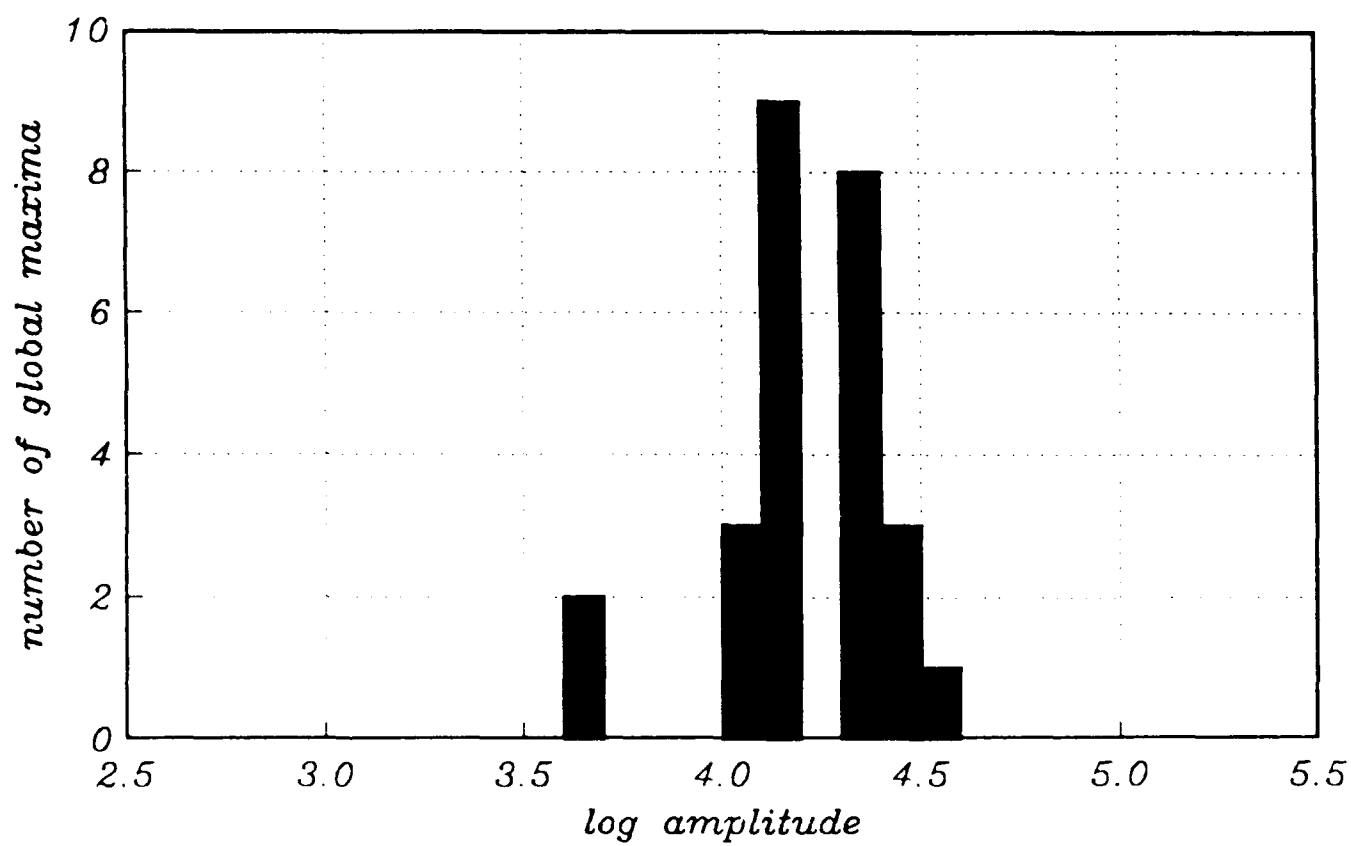
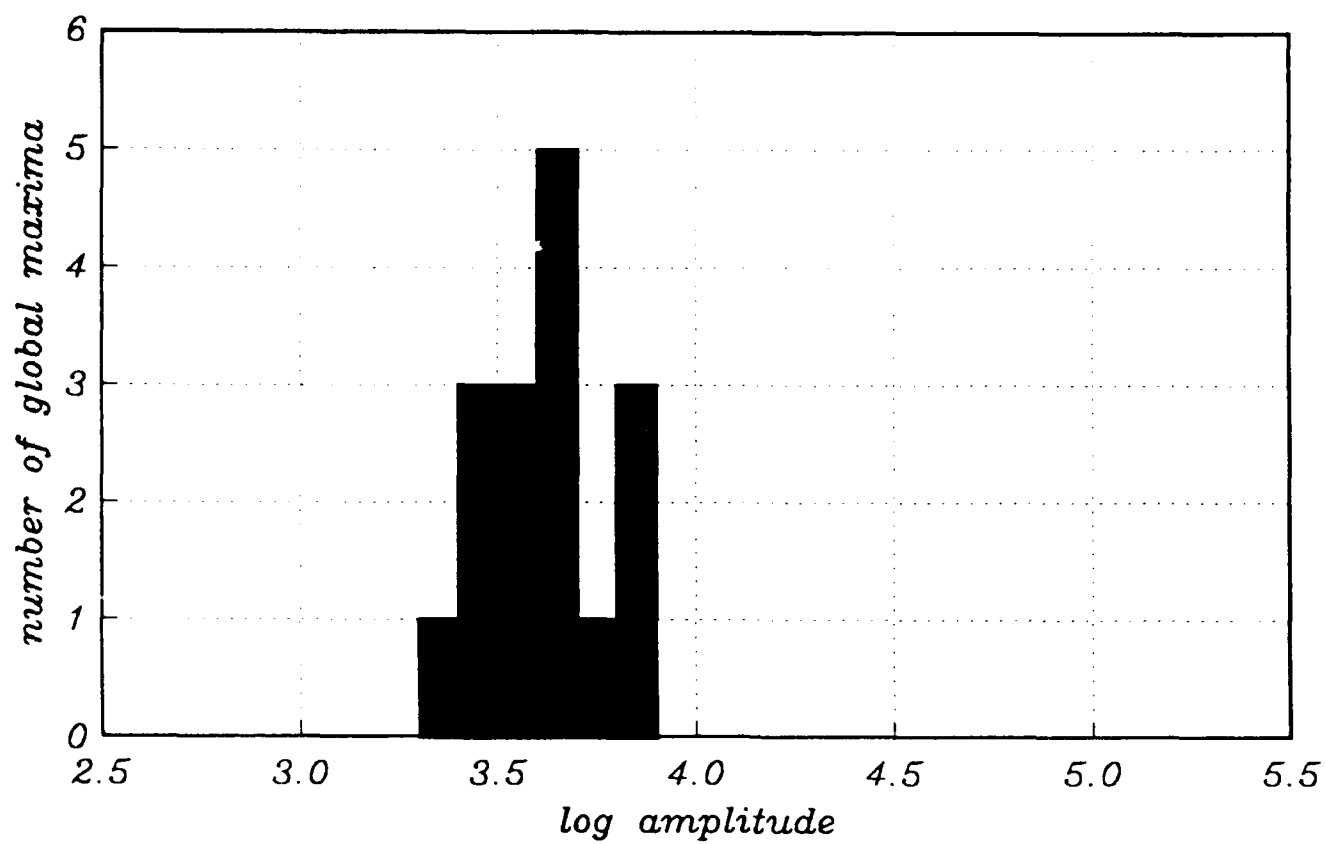


Figure 13

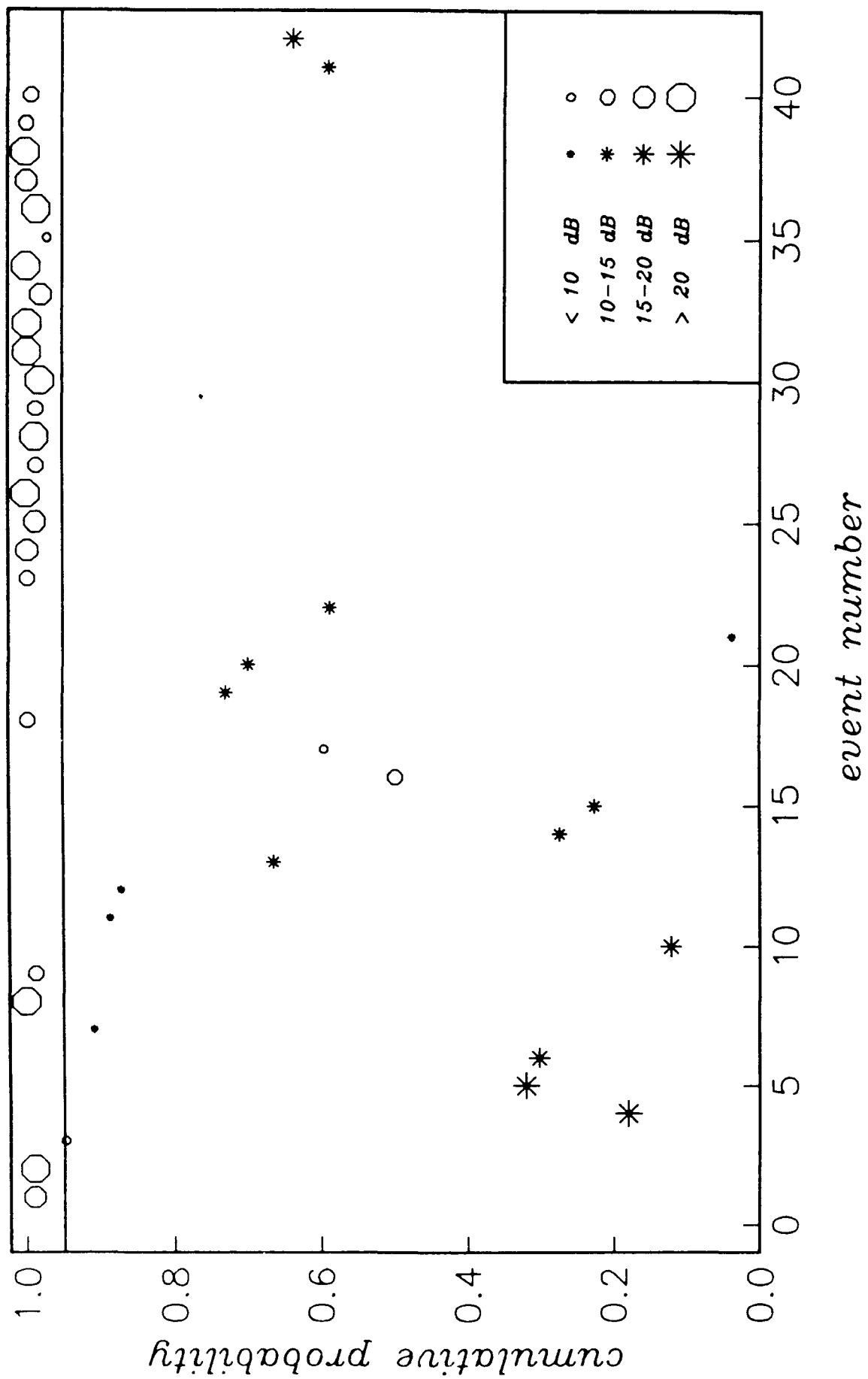


Figure 14

Beam-stack imaging using a small aperture array

Michael A.H. Hedlin

J. Bernard Minster

John A. Orcutt

Institute of Geophysics and Planetary Physics

Scripps Institution of Oceanography

La Jolla CA, 92093, U.S.A.

Revised manuscript submitted to Geophys. Res. Lett. , March, 1991

The U.S. Government is authorized to reproduce and sell this report.
Permission for further reproduction by others must be obtained from
the copyright owner.

Abstract

We seek to gain a fuller understanding of seismic coda generation in the continental crust, by identifiable secondary (scattering) sources illuminated by a distant primary source. We have developed a technique to scan seismic coda recorded by a small-aperture seismic array for phases generated locally by scattering from large heterogeneities, or topographic undulations. We use a widely distributed suite of seismic events to illuminate the local crustal volume from different directions and produce an image of the local crust. Stable apparent secondary seismic sources are indeed observed, and interpreted as scatterers excited by the primary events.

1. Introduction

One of the important aspects of seismic monitoring is to understand the generation of seismic coda, particularly the near-station mechanisms. Two mechanisms we have investigated include seismic resonance (in low velocity strata) and scattering by inhomogeneities and topographic undulations (both at the free surface and at buried interfaces). The two processes appear to have different relative importance in the continental and oceanic crusts. Recent work (by Sereno and Orcutt, 1985a,b; Sereno and Orcutt, 1987; Mallick and Frazer, 1990) has produced evidence that in the oceanic crust, coda waves are likely dominated by resonance in the water and sedimentary horizons. Other studies (eg. Aki, 1969; Aki and Chouet, 1975) have argued that coda waves generated in the continental crust are most likely due to scattering by heterogeneities. Although studies quantifying the effects of scattering have mostly been statistical and have dealt with the influence of small-scale random scatterers, some deterministic studies (Key, 1967; Key, 1968; Gupta *et al.*, 1990a,b; Bannister *et al.*, 1990; Lay, 1987; Lynnes and Lay, 1989) have produced compelling evidence that large features are capable of producing significant amounts of scattered energy, principally in the form of large identifiable seismic phases, which affect nuclear monitoring and discrimination: These prominent scattered phases may be confused with direct arrivals. Being able to identify these "secondary" sources is the first step toward being able to reduce this confusion.

Several attempts have been made to locate the sources of scattered phases both near the receiver (Key, 1967; Gupta *et al.*, 1990a,b; Bannister *et al.*, 1990) and near the source (Lay, 1987; Lynnes and Lay, 1989). The work to date suggests that the most significant sources of identifiable phases are topographic features at the free-surface.

2. The imaging technique

Recently, we (Hedlin *et al.*, 1990) have examined a suite of synthetic and recorded events (observed by the NORESS array in Norway) and developed a systematic technique to image nearby large scatterers. The underlying premise is that incident seismic waves impinging on a scatterer generate coda waves recorded by the array. From this point of view each scatterer may be treated as a secondary source which is excited with a delay estimated from elementary ray theory. We have applied a modified beamforming technique to array records to enhance signals radiated by such faint secondary sources. A suite of broadly distributed seismic sources is used to achieve a more "balanced" illumination of the population of scatterers in the shallow crust surrounding the array than is provided by a single event. We use the suite of events to scan the crustal volume for stable apparent sources.

To image a region of the crust, the technique subdivides the area into small segments and considers them individually, in sequence. For each crustal sub-area being scanned, the seismograms from the event suite are incoherently stacked after beam-correcting each trace, computing new beams for the crustal sub-area and migrating the recordings by applying appropriate time offsets, τ . The beam correction is effected by subtracting (coherently) the primary source beam from each channel before beamforming for the secondary scattered energy. This is equivalent to masking the more energetic primary source (e.g. Gupta *et al.*, 1990a,b). As is illustrated in figure 1, considering a single event-scatterer pair, the time offset, τ , between the arrivals of energy propagating directly from the source (at vector slowness \mathbf{p}_i) and via the scatterer (vector slowness \mathbf{p}_s) at a vector distance \mathbf{R}_{as} from the array is given by:

$$\tau = \mathbf{R}_{as} \cdot (\mathbf{p}_i - \mathbf{p}_s) \quad (1)$$

Considering a suite of broadly distributed events it is possible to estimate \mathbf{p}_s by computing a number of preliminary images while slowly varying this parameter and selecting the value that brings the image into the sharpest focus. The slowness of the incident energy, \mathbf{p}_i , is well constrained by the first breaks on the array records. By systematically scanning the crustal volume about the array, we can generate an image which is interpreted as a map of local scatterers. To date, we have considered scattering interactions excited by P waves, using both synthetic and real datasets.

Since we use multiple sources, for which the time offsets τ are different, scatterers are in effect imaged through a "synthetic aperture array". Another analogy is with "hyperbola summation" migration - applied to seismic reflection data to enhance images of subsurface structure (Yilmaz, 1987). Since a delay-and-sum operation is involved, this method is akin to standard beamforming techniques and bears some resemblance

to f-k analysis. This technique is distinguished, however, by its cognizance of not only the wavenumber but the onset time of a seismic arrival. As a result, the technique can be used to infer the likely geographic location of the secondary source. This method differs from previous attempts to locate large near-receiver scatterers since it is designed to accommodate simultaneously many primary events from different azimuths, to give a balanced illumination of local scatterers while suppressing the influence of near-source scatterers. The method is a "whole waveform" technique since it simultaneously considers all coda that could be influenced by scattering interactions within the region of interest.

3. Analysis of Synthetic Data - Imaging Resolution

The resolution of the imaging technique can be gauged from experiments with synthetics. Using wavenumber integration (Apsel and Luco, 1983; Luco and Apsel, 1983) we consider a localized omnidirectional scatterer (delta function in space) illuminated by an impulsive incident wave (delta function in time), and compute synthetic vertical seismograms individually for each of the sensors in the array. This yields a perfectly beam-corrected image (figure 2). This, and all subsequent images, have been computed by subdividing the area shown into 1681 blocks 3 km on a side. In the preliminary analysis of synthetic and recorded data we have chosen a surface wave slowness of .304 s/km (the slowness of the dominant phase in the synthetic R_g packet) and have bandpass filtered the records between 1 and 3 Hz. In practice we found that applying a gain to correct for geometrical spreading resulted in an unacceptable amount of noise amplification at extreme ranges so we did not do it. In general, considering dispersion and instability problems, it is necessary to average the stacks over a time window centered on the predicted onset of scattered energy. We have varied the window length by up to 5 seconds. As illustrated in figure 2 the radial resolution is limited to some extent by the dispersion of the surface wave packet (displayed in the lower half of the figure) and to a greater extent by the time-averaging (in this case 5 seconds). The azimuthal resolution of the synthetic source is very poor primarily because the coherence of the surface waves, computed with only a small degree of numerical noise, is very high and because we are employing incoherent beams. Energy is aliased away from the actual location of the scatterer to locations which share the same delay time. By manipulation of the first equation, it can be shown that scatterers which share a common delay time τ lie on a curve described by:

$$|\mathbf{R}_{12}| = \frac{\tau}{|\mathbf{p}_s| - |\mathbf{p}_1| \cos(\theta)} \quad (2)$$

When \mathbf{p}_s is greater than \mathbf{p}_1 (eg. P to R_g scattering) this describes an ellipse with one focus at the center of the array, major axis pointing to the primary source and eccentricity proportional to \mathbf{p}_1 . In this synthetic

calculation the primary source was located directly beneath the array ($p_i = 0$) and thus the curves of constant τ have degenerated into circles centered on the array.

The imaging algorithm assumes that all excitation of a scatterer located at \mathbf{R}_s , occurs at $\tau = \mathbf{R}_s \cdot \mathbf{p}_i$ (the scatterer is illuminated by a single arrival). This condition is met by the synthetic data, and as a result it is possible to infer the geographic location of the synthetic source, not just the time of excitation and angle of approach. If this is not the case, and the incoming wavetrain consists of a protracted sequence of arrivals, then a single scatterer will be illuminated, and emit energy, for a longer time. In theory, this will result in a "tail" of energy extending outward from the actual location of the scatterer along a radial line. In such cases it is more appropriate to plot the image as a function of time, not space.

4. Analysis of Recorded Data

We have applied this technique to a dataset consisting of 105 earthquakes and nuclear explosions recorded by the NORESS array in southern Norway. The events range in magnitude from $m_b = 5.4$ to 6.8 and epicentral distances up to 80° from NORESS. This dataset includes 15 Semipalatinsk nuclear explosions. To test the resolving power of events coming from a single azimuth (and thus to gauge the improvement we can expect by using a widely distributed suite of events) we have computed the images using a single Semipalatinsk nuclear explosion (1984, day 351). Although all Semipalatinsk explosions produce images that are remarkably similar, we chose this event because it has been previously considered by Gupta *et al.*, (1990a,b) who also applied beam-correction, and f-k analysis in their search for large scatterers. This gives us a chance to compare both techniques. Due to the protracted incident P train estimated by beam steering to the primary source (lower part of figures 3 and 4), we plotted the images as functions of time. The first image (figure 3), computed with 1 second of time averaging, is badly smeared along ellipses of constant τ . Not surprisingly, the ability of a single primary event to resolve structure along arcs of constant τ is poor. As in synthetic tests, the smearing is due to the high coherence of the low frequency scattered phases across the array. We can decrease the smearing by increasing time-averaging so that several cycles of less coherent scattered energy are included in the window. By increasing the time span to 5 seconds of coda centered on the predicted onset we obtain the result displayed in figure 4. The smearing is still present, but has been significantly reduced, and two apparent energy sources are clearly resolved. The cost of increasing the azimuthal resolution in this manner is a loss of resolution along radial lines. The trade off between azimuthal and radial resolution can, in theory, be mitigated by using a broadly distributed suite of events. In figure 5 we show the image produced by stacking the full set of 105 teleseismic nuclear explosions

and earthquakes. The stacking was performed after weighting each event by its signal to noise ratio. A focusing analysis (varying p_s between .30 and .43 s/km) yields the sharpest images for $p_s \sim .36$ s/km, indicating that the bulk of the energy produced propagates as surface waves. This is in agreement with E. Husebye (personal communication). The final image implies the presence of two prominent scatterers close to the array - both of which have been previously observed and related to prominent topographic features near NORESS. The anomaly in the third quadrant, now less azimuthally smeared, is in the same location (roughly 11 s, or 30 km, from the array) as the Skreikampen feature previously identified by Gupta *et al.* (1990a,b) and Bannister *et al.* (1990). Another feature roughly 4 seconds (or 11 km) from NORESS at a back-azimuth of 80° is likely due to the Bronkeberget topographic relief discussed by Bannister *et al.* (1990). We believe that an additional feature in the first quadrant (roughly 15 seconds from the array) may be due to the late excitation of the Bronkeberget relief.

5. Conclusion

By employing an incoherent hyperbola summation migration to broadly distributed teleseismic events recorded by the NORESS array we have constructed images of crustal scatterers near the array. We have found that the highest radial and azimuthal resolution can be obtained using events broadly distributed in azimuth. Images constructed using single and broadly distributed events indicate the presence of two prominent scatterers to the southwest and northeast of the NORESS array. These results are consistent with those of Gupta *et al.* (1990a,b) and Bannister *et al.* (1990). To refine the algorithm further will require deconvolution of the incident wavetrain (Hedlin *et al.*, in preparation). This will allow us to test more stringently the stability of our images.

6. Acknowledgments

We thank Dr. Thomas Carter at the Center for Seismic Studies for providing us with the bulk of the events used in this study. This research was sponsored by the Defense Advanced Research Projects Agency (DARPA)/Air Force Geophysics Laboratory (AFGL) under contracts No. F19628-89-K-0018 and F19628-88-K-0044.

7. References

- Aki, K., Analysis of the seismic coda of local earthquakes as scattered waves. *J. Geophys. Res.*, **74**, 615-631, 1969.

- Aki, K. and Chouet, B., Origin of coda waves: source, attenuation, and scattering effects. *J. Geophys. Res.* , **80**, 3322-3342, 1975.
- Apsel, R.J. and Luco, J.E., On the Green's functions for a layered half-space, part II. *Bull. Seismol. Soc. Am.* , **73**, 931-951, 1983.
- Bannister, S.C., Husebye, E.S. and Ruud, B.O., Teleseismic P coda analyzed by three-component and array techniques: Deterministic location of topographic P-to- R_g scattering near the NORESS array. *Bull. Seismol. Soc. Am.* , **80B**, 1969-1986, 1990.
- Gupta, I.N., Lynnes, C.S., McElfresh, T.W. and Wagner, R.A., F-K analysis of NORESS array and single station data to identify sources of near-receiver and near-source scattering. *Bull. Seismol. Soc. Am.* , **80B**, 2227-2241, 1990a.
- Gupta, I.N., Lynnes, C.S. and Wagner, R.A., Broadband F-K analysis of array data to identify sources of local scattering. *Geophys. Res. Lett.* , **17**, 183-186, 1990b.
- Hedlin, M.A.H., Minster, J.B. and Orcutt, J.A. (1990). Beam-stack imaging of scatterers near a small aperture array. Contributed paper at "12th annual AFGL/DARPA seism. Res. Symp", held in Key West, FL.
- Key, F.A., Signal-generated noise recorded at the Eskdalemuir seismometer array station. *Bull. Seismol. Soc. Am.* , **57**, 27-37, 1967.
- Key, F.A., Some observations and analysis of signal generated noise. *Geophys. J. R. Astron. Soc.* , **15**, 377-392, 1968.
- Lay, T., Analysis of near-source contributions to early P-wave coda for underground explosions. III. Inversion for isotropic scatterers. *Bull. Seismol. Soc. Am.* , **77**, 1767-1783, 1987.
- Luco, J.E. and Apsel, R.J., On the Green's functions for a layered half-space, part I. *Bull. Seismol. Soc. Am.* , **73**, 909-929, 1983.
- Lynnes, C.S. and Lay, T., Inversion of P coda for isotropic scatterers at the Yucca Flat test site. *Bull.*

Seismol. Soc. Am. , **79**, 790-804, 1989.

Mallick, S. and Frazer, L.N., Po/So synthetics for a variety of oceanic models and their implications for the structure of the oceanic lithosphere. *Geophys. J. Int.* , **100**, 235-253, 1990.

Sereno, T. J. Jr. and Orcutt, J. A., Synthetic seismogram modelling of the oceanic Pn phase. *Nature*, **316**, 246-248, 1985a.

Sereno, T. J. Jr. and Orcutt, J. A., Synthesis of Realistic Oceanic Pn Wave Trains. *J. Geophys. Res.* , **90**, 12755-12776, 1985b.

Sereno, T. J. Jr. and Orcutt, J. A., Synthetic P_n and S_n phases and the frequency dependence of Q in oceanic lithosphere. *J. Geophys. Res.* , **92**, 3541-3566, 1987.

Yilmaz, O., *Seismic data processing*. Society of Exploration Geophysicists, investigations in geophysics, volume 2, 1987.

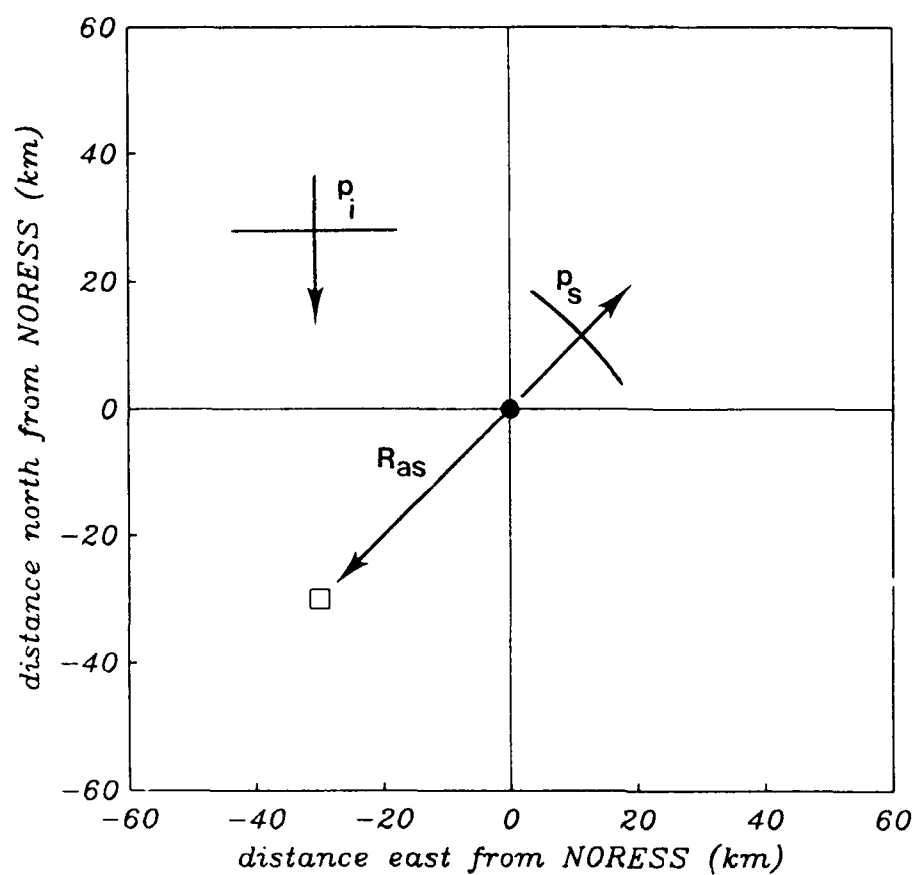


Figure 1

The vectors appearing in equation 1 are illustrated in this figure. The incident wavefront arrives from the north at a vector slowness of \mathbf{p}_i . A scattered wavefield originates within the small box (3 km on a side) and propagates outward to the NORESS array (dark circle at the center of the figure) at vector slowness \mathbf{p}_s . The vector from the array to a sample block is \mathbf{R}_{as} . Both the array and the sample block are shown to scale.

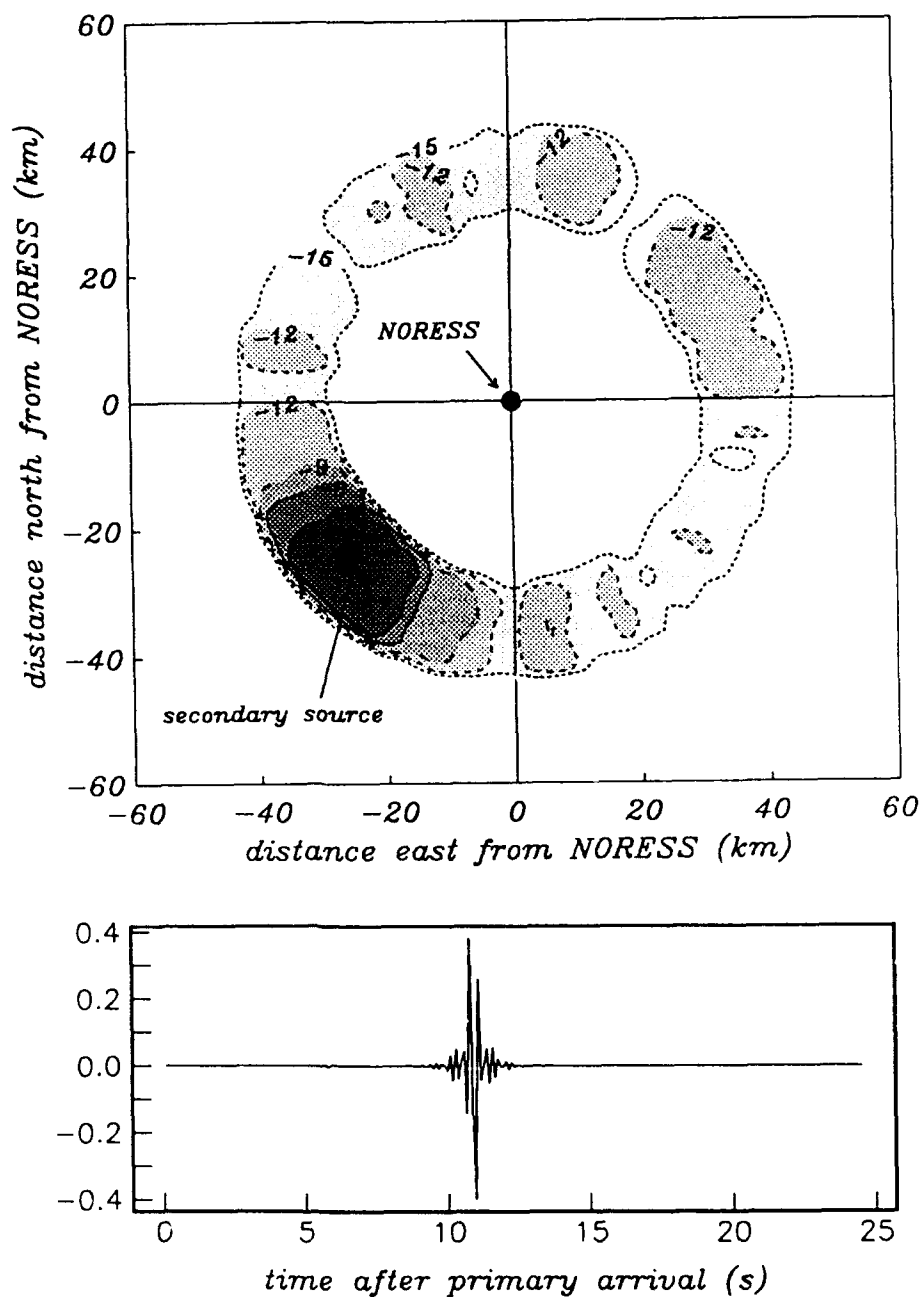


Figure 2

Image of a synthetic point source located 35 km from the array at a back azimuth of 225° . Wavenumber Integration was used to generate synthetic seismograms individually for each of the 25 vertical component sensors in the NORESS array (illustrated is the synthetic computed for the center station). Contour values indicate amplitudes in dB relative to the largest value in the image. In this and all following images, cylindrical propagation of scattered wavefronts was assumed.

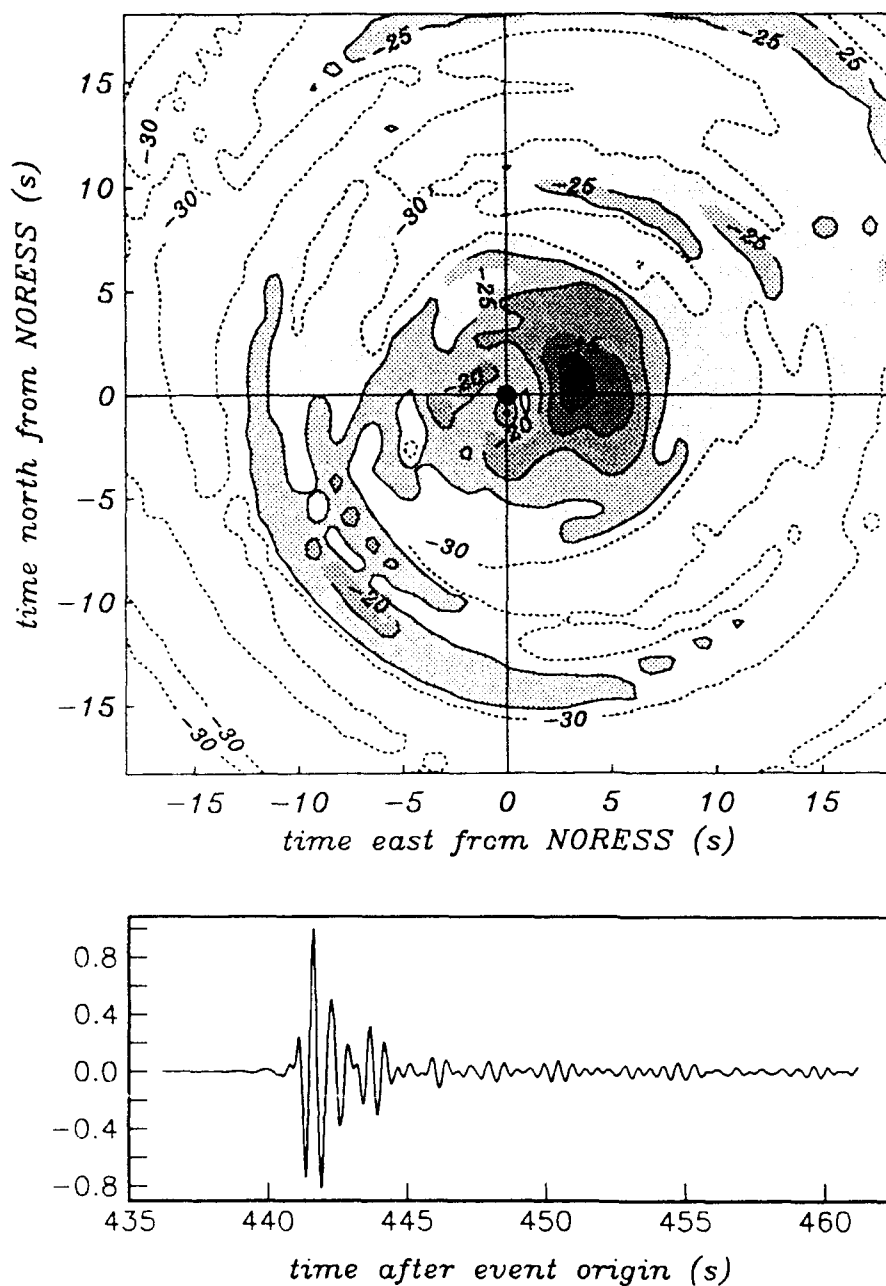


Figure 3

Image of the scattering field in the vicinity of the NORESS array obtained using a single Semipalatinsk nuclear explosion (1984, day 351). The image was generated by integrating over 1 second of data centered on the predicted onsets of the scattered energy. The test site is located at a back azimuth of 75° . Due to the protracted form of the incoming wavefield (estimated by the beam pictured in the lower half of the figure), the image has been plotted as a function time. In this and all subsequent images, contour values indicate amplitudes in dB relative to the largest value in the image obtained without beam correction.

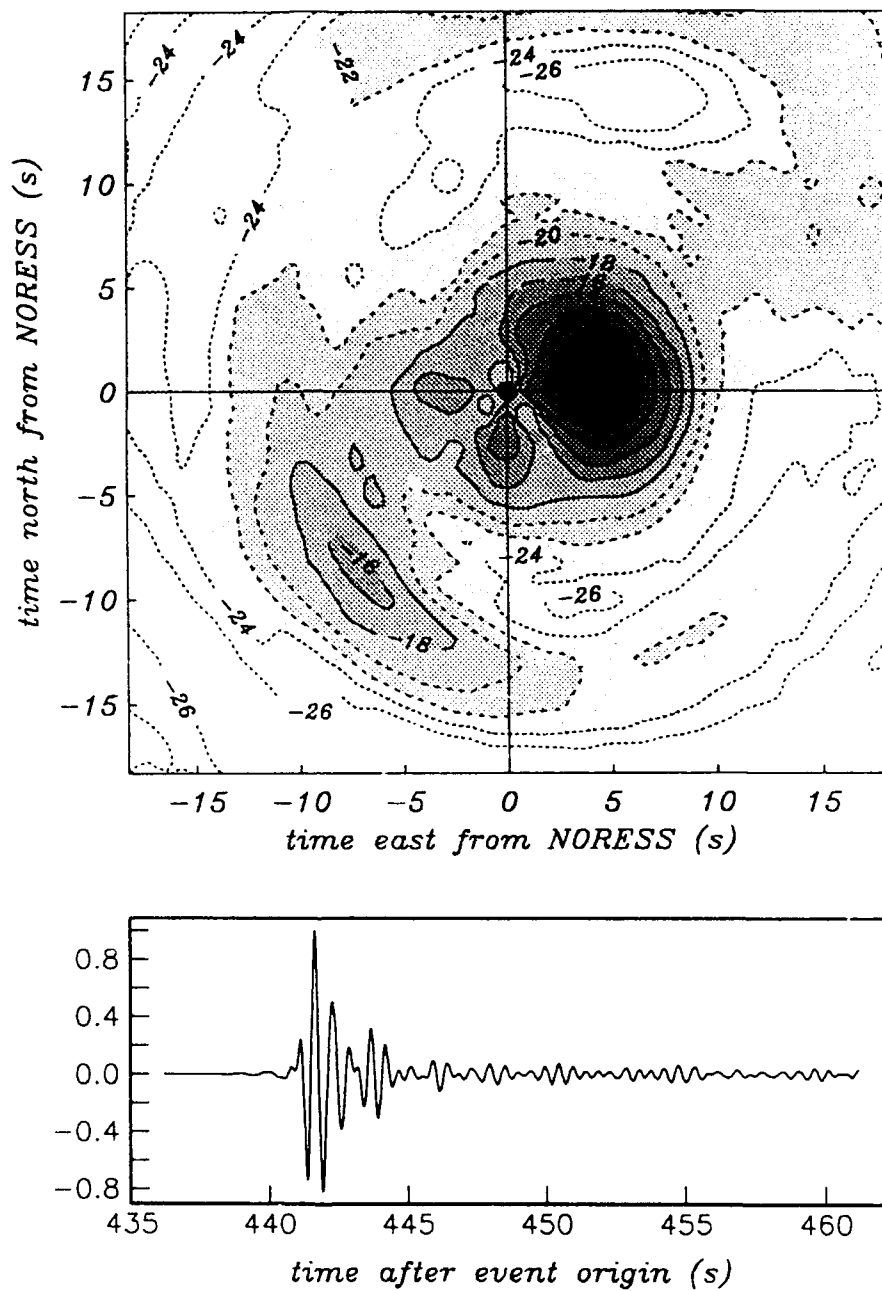


Figure 4

Image of the scattering field in the vicinity of the NORESS array obtained using a single Semipalatinsk nuclear explosion (1984, day 351). Time averaging was performed over 5 seconds centered on the predicted onset time of the scattered energy. The beam computed for the test site is pictured in the lower half of the figure.

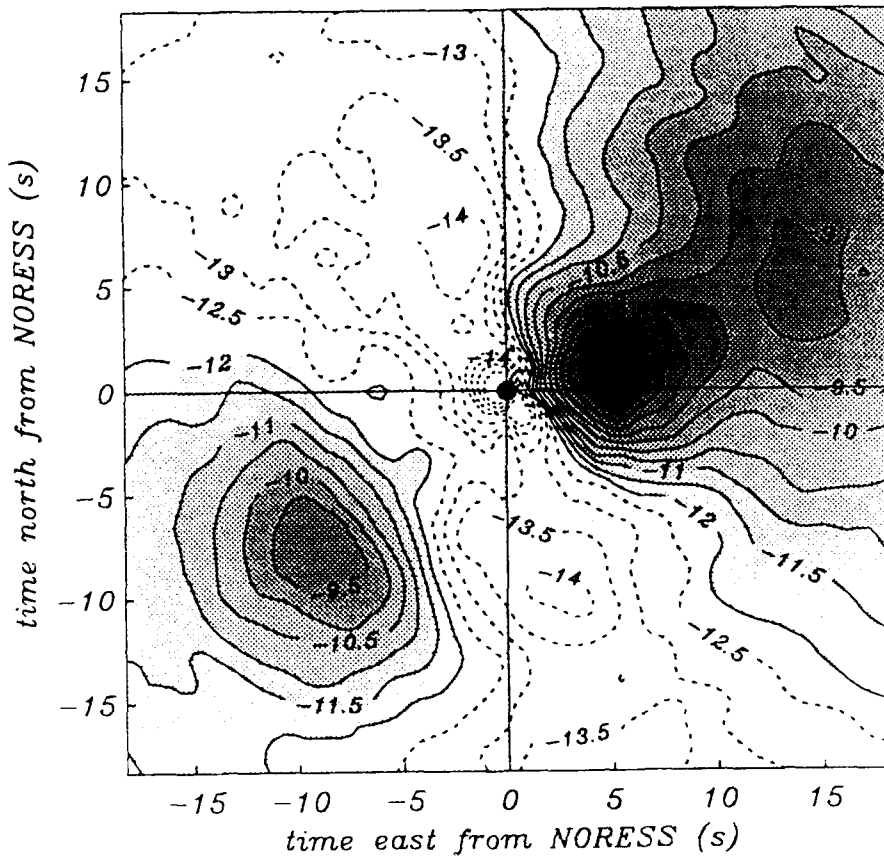


Figure 5

Image of the scattering field local to the NORESS array obtained using a broadly dispersed set of 105 teleseismic earthquakes and nuclear explosions. The stack was time-averaged over 5 seconds centered on the predicted onset of the scattered energy.

**High-Frequency Borehole Seismograms
Recorded in the
San Jacinto Fault Zone, Southern California**

Part 1: Polarizations

**Richard C. Aster
Peter M. Shearer**

**Institute of Geophysics and Planetary Physics,
University of California, San Diego**

**Submitted to *B.S.S.A.*
September 24, 1990
Revised February 27, 1991**

The U.S. Government is authorized to reproduce and sell this report.
Permission for further reproduction by others must be obtained from
the copyright owner.

Abstract

Two borehole seismometer arrays (KNW-BH and PFO-BH) have been established in the Southern California Batholith region of the San Jacinto Fault zone by the U.S. Geological Survey. The sites are within 0.4 km of Anza network surface stations and have three-component seismometers deployed at 300 m depth, 150 m depth, and at the surface. Downhole horizontal seismometers can be oriented to an accuracy of about 5° using regional and near-regional initial P-wave particle motions.

Shear waves recorded downhole at the KNW-BH indicate that the strong alignment of initial S-wave particle motions previously observed at the (surface) KNW Anza site (KNW-AZ) is not generated in the near-surface weathered layer. The KNW-BH surface instrument, which sits atop a highly weathered zone, displays a significantly different ($\approx 20^\circ$) initial S-wave polarization direction from that observed downhole and at KNW-AZ, which is bolted to an outcrop. Although downhole initial shear-wave particle motion directions are consistent with a shear-wave splitting hypothesis, observations of orthogonally-polarized slow shear-waves are generally elusive, even in seismograms recorded at 300 m. A cross-correlation measure of the apparent relative velocities of S_{fast} and S_{slow} horizontally-polarized S-waves suggests shallow shear-wave anisotropy, consistent with the observed initial S-wave particle motion direction, of $2.3\% \pm 1.7\%$ between 300 and 150 m and $7.5\% \pm 3.5\%$ between 150 and 0 m.

Introduction

Numerous recent studies have produced evidence for shear-wave anisotropy in the shallow continental crust. These studies indicate that shear-wave anisotropy occurs in a wide variety of geological situations. Evidence arises from essentially two types of experiments.

- (1) Controlled source studies using borehole sensors and artificial shear-wave sources. Such measurements sample the near-surface down to the maximum depth of instrumented boreholes (typically ≤ 1.5 km) (*e.g.*, Daley and McEvilly, 1990; Winterstein, 1990; Majer *et al.*, 1988; Shearer, 1988; Aieford, 1986).
- (2) Polarization analysis of shear-wave signals from shallow earthquakes. Such studies have primarily relied on three-component surface stations deployed in seismogenic regions, which can record nearby earthquakes with sufficient high-frequency content to resolve the first ≈ 0.1 s of the shear wave. It is also desirable to record events with near-vertical ray paths, so that waveform complications from converted phases arising at or near the free surface are minimized (*e.g.*, Crampin and Booth, 1985; Peacock *et al.*, 1988; Savage *et al.*, 1989; Savage *et al.*, 1990; Aster *et al.*, 1990; Gledhill, 1990).

Malin *et al.* (1988) examined shear-wave polarizations from nearby earthquakes using borehole seismometers, a scheme which we adopt in this study. Although this type of experiment is logistically more daunting than those using surface instrumentation alone, there are several distinct advantages. Recording below the surface weathered layer results in significantly improved high-frequency signal-to-noise levels, due both to lower noise levels and to lower attenuation along the ray path (*e.g.*, Aster and Shearer, this issue). Additionally, when borehole

instruments are deployed at several depths, the resulting vertical seismic array may be used to directly estimate near-surface seismic anisotropy and attenuation for vertically travelling waves as in controlled source experiments. A disadvantage relative to controlled source experiments is that the earthquake source may have a poorly constrained radiation pattern. A distinct advantage for shear-wave studies, however, is that earthquakes are very efficient sources of shear-wave energy.

Specific questions to be addressed in this paper are:

- (1) How well can we orient downhole horizontal sensors of unknown orientation using earthquake signals?
- (2) How consistent are initial shear-wave particle motions observed by borehole instruments with those observed at the surface?
- (3) Is evidence for distinct slow quasi-shear waves clearer in recordings made below the weathered layer?

The Anza Borehole Installations

Earthquakes discussed in this paper were recorded in the Anza seismic gap region of the San Jacinto Fault zone (Thatcher *et al.*, 1975; Sanders and Kanamori, 1984; Rockwell and Loughman, 1990) using the U.S.G.S. borehole instrumental arrays KNW and PFO (Fletcher *et al.*, 1990). Both installations are sited within 400 m of Anza network stations (Berger *et al.*, 1984; Vernon, 1989). Geodetic measurements (J. Scott, pers. commun.) indicate that the PFO borehole (PFO-BH) is approximately 28 m N268°E of the PFO Anza vault (PFO-AZ; [33.61165°N, 116.45855°W]; 1.286 km above sea level) and the KNW borehole (KNW-BH) is sited 391 m N212°E of the KNW Anza vault (KNW-AZ; [33.71413°N, 116.71107°W]; 1.527 km above sea level). KNW-AZ is bolted to a tonalitic

outcrop with NW-SE lineations, atop a ridge that descends toward the SE. PFO-AZ is located on the grounds of Piñon Flat Observatory (Wyatt *et al.*, 1988) where the topography is flat to within a few meters for several kilometers in all directions. Earthquake locations in the area are routinely provided by the Anza network (operated by the U.S.G.S. and the University of California, San Diego) and by the Southern California Seismic Network (SCSN; operated by the U.S.G.S. and the California Institute of Technology). These borehole sites were selected specifically to investigate high-frequency properties of earthquake signals; stations KNW-AZ and PFO-AZ exhibit the broadest frequency content in the Anza network ($f_{\max} \approx 40$ Hz and ≈ 32 Hz, respectively; Fletcher *et al.*, 1987).

The boreholes are drilled into the bedrock of the Southern California Batholith (Sharp *et al.*, 1967), with drilling results reported by Carroll *et al.* (1991). PFO-BH predominantly penetrates coarse-grained gabbro. Beneath a 2 m-thick layer of *grus* (gravel weathered out of the batholith) is a decomposed zone approximately 15 m thick with biotite as the principal mafic constituent. Below approximately 20 m the rock appears to be unaltered gabbro with numerous hornblende crystals, occasionally intersected by fine-grained dikes. KNW-BH is primarily drilled into medium to coarse-grained tonalite. An approximately 1 m-thick layer of *grus* at the surface is underlain by about 30 m of highly weathered felsic tonalite. A more mafic and fine-grained (possibly gabbroic) zone occurs from 30 m to 45 m. Below approximately 90 m the rock appears to be essentially unaltered, coarse-grained, tonalite, with an increased proportion of mafic constituents (hornblende with some biotite). Televiewer records (Fletcher *et al.*, 1990) indicate that the crack density is higher at KNW (WSW preferential pole direction) than at PFO (no preferred pole direction).

Three 3-component, self-leveling, 2 Hz-resonant, Mark Products L-22D velocity seismometer packages are deployed at depths of 300 m, 150 m and 0 m at each site. The 300-m and 150-m instruments occupy distinct boreholes, which are separated by about 5 m. Each borehole installation thus constitutes a near-vertical, 9-channel, 3-station vertical array. 3-component signals from each depth are recorded by independently-triggered GEOS data loggers (Borcherdt *et al.*, 1985) with 16 bit (≈ 96 dB) resolution at a sampling rate of 400 samples/s. Anti-aliasing is provided by 7-pole (42 dB/octave) Butterworth filters with corner frequencies of 100 Hz. The velocity response of the recording system is thus approximately flat from 2-100 Hz.

Prior to installing the L-22D seismometer packages, both boreholes were velocity logged with a 3-component 8 Hz-resonant Mark Products geophone package at 2.5 m intervals for the initial 50 m and at every 5 m thereafter (Fletcher *et al.*, 1990). A sledgehammer was used to generate P-waves and a horizontal hammer (Liu *et al.*, 1988) was used to generate S-waves. These independent measurements of P- and S-wave vertical travel times proved to be invaluable for our analysis, particularly for Q estimation (Aster and Shearer, this issue), as the relative times between 0 m, 150 m, and 300 m recordings were not generally reliable for our study period due to poor WWVB time signal reception.

Local and Regional Events Studied

We obtained a catalog for events recorded at KNW-BH and PFO-BH by comparing start times of 5820 total triggers from the GEOS recorders from 22 July, 1987 through 29 April, 1989 with source times from two earthquake catalogs. Regional earthquakes out to an epicentral radius of 5° were identified from the Preliminary Determination of Epicenters (PDE) bulletin published monthly by the

National Earthquake Information Center. Local events were identified from the Anza network catalog using the 1-d velocity model locations of Scott *et al.* (1988, 1990). We searched for candidate seismic events by examining a time window ending at the borehole trigger time, using a 1-minute window for the Anza catalog and a 2-minute window for the PDE catalog. For events found in both catalogs, we used the Anza hypocenter if the epicenter was within the aperture of the Anza network, otherwise the PDE location was used. Following this procedure, we obtained nonintersecting catalogs of 31 PDE and 48 Anza events (Table 1; Table 2). Hereafter, we will refer to our PDE-based catalog as the "regional" catalog and to our Anza-based catalog as the "local" catalog. Station locations and epicenters from the regional and local catalogs are plotted in Figures 1 and 2, respectively.

Orientations of Downhole Horizontal Seismometers

During deployment, a gimbal stage was used to level the horizontal components of the downhole sensors to within 0.1° (Liu *et al.*, 1986), but rotations about the vertical axis were not constrained or monitored. We estimated horizontal seismometer orientations using initial P-wave particle motions from the regional catalog (Table 1; Figure 1). We expect these particle motions to be most consistent with the true source azimuth and to be least affected by heterogeneity and anisotropy because of their compressional wave nature, low frequency content, and longer ray paths.

Best-fitting horizontal seismometer orientations were estimated by identifying the angular corrections, ψ_0 , that minimized the L_1 angular error (A11) between back-azimuths and initial P-wave particle motions (see Appendix). Corrected particle motion azimuths versus back-azimuths are shown in Figure 3. Final correction

rotations for each set of horizontal instruments are shown in Table 3.

Self-scaled horizontal projections of the first 0.1 s of the initial P-wave particle motions for the complete oriented data set are shown in Figure 4. Note that horizontal particle motions recorded at surface (0 m) seismometers are considerably less linear than those recorded downhole, especially at KNW. This effect is probably principally due to more vertical rays at 0 m resulting from low-velocity surface material; 0-m horizontal particle motions have larger relative contributions from P-to-P side-scatter and P-to-S conversion, and lesser contributions due to the direct P-wave. These contributions are enhanced in Figure 4 by the self-scaling of each individual particle motion plot. Additionally, there are azimuthally dependent effects that presumably reflect variations in regional structure; particle motions from distant sources are more linear from the north and northwest than from the south and southwest at both stations. This may reflect both the extreme regional topography and differences between the relatively competent geology of the transverse ranges and Mojave block to the north versus the sedimentary fill of Borrego Valley and the Salton Trough to the southeast.

Shear-wave Particle Motions at KNW

Borehole records at KNW are of particular interest for shear-wave observations because both KNW-BH and KNW-AZ have recorded numerous microearthquakes with near-vertical ray paths; the stations at PFO are at a relative disadvantage in this regard (Figure 2; Figure 4). Besides having the shortest (and thus probably minimum-attenuation) ray paths, nearly vertically incident signals also have reduced phase conversions and minimum resulting waveform complication from vertical heterogeneity (*e.g.*, Booth and Crampin, 1985). Furthermore, previous studies (Peacock *et al.*, 1988; Aster *et al.*, 1990) have indicated that recordings

at KNW-AZ provide the clearest evidence for shallow crustal shear-wave anisotropy in the region and have excellent high-frequency signal-to-noise ratios (Frankel and Wennerberg, 1989). We thus concentrate our polarization analysis on recordings from the KNW site.

Initial S-wave particle motions for events with near-vertical (straight-line station-to-hypocenter dip, $d \geq 45^\circ$) ray paths are plotted in Figure 5 for events recorded at KNW-BH (Figure 2; Table 2) and KNW-AZ from July 21 1988 through April 29, 1989. Downhole KNW-BH S-wave particle motions show approximately the same NW-SE trend as those at KNW-AZ. This trend is independent of event azimuth and is suggestive of shear-wave anisotropy. S-wave particle motions at the KNW-BH surface site, on the other hand, exhibit less of a tendency to align than those recorded downhole or at KNW-AZ and show a more N-S orientation (see below).

It has been noted that site responses may exhibit localized directional resonances, particularly at high frequencies. Bonamassa *et al.* (1991) measured resonance effects in afterslack data recorded from the Loma Prieta earthquake in the frequency band from 1-18 Hz, and found that these resonances varied significantly for some stations separated by only 25 m. These resonances seem to affect the initial arrival the least. The general agreement between downhole particle motions at KNW-BH and those observed at the surface by KNW-AZ indicates that this alignment phenomenon is not a directional site response; the borehole instrument is nearly 0.4 km distant from the Anza station. Furthermore, the alignment is more strongly visible downhole than at the KNW-BH surface instrument, which is sited in a clearly weathered zone, suggesting that surface effects near the borehole site degrade rather than enhance the phenomenon. A high-frequency directional resonance does in fact occur at KNW-AZ, but it is almost orthogonally oriented to the

initial shear wave particle motion direction at this station (Aster and Shearer, this issue).

Evidence for shear-wave splitting. Peacock *et al.* (1988) noted that aligned initial shear-wave particle motions observed at surface Anza stations were consistent with a shear-wave splitting hypothesis (*e.g.*, Crampin, 1978) in that the degree of alignment could not be accounted for by shear-wave radiation patterns for selected earthquakes. Aster *et al.* (1990) confirmed this for the entire data set from October, 1982 through April, 1989, but found that unambiguous candidates for slow quasi-shear wave arrivals were not generally observed. This was true even for earthquakes with shear-wave radiation patterns and ray paths that predicted a strong slow quasi-shear wave excitation. Borehole recordings, being relatively removed from surface effects, might provide clearer evidence of incoming slow quasi-shear wave energy.

To optimally orient the KNW-BH data to examine evidence for shear-wave splitting, we first rotated 3-component seismograms from 20 events with near-vertical ray paths (Figure 5a) into an apparent (P, S_V, S_H) coordinate system, specified by a P-wave azimuth, ϕ , and a P-wave dip, θ , using the eigenvalue-eigenvector decomposition of the 3-dimensional variance tensor (*e.g.*, Kanasewich, 1975) of the initial 0.05 s (20 samples) of the P-wave. The 2-dimensional variance tensor (in the plane perpendicular to P of the S-wave signal; see Appendix) was then used to rotate the coordinate system in the (S_V, S_H) plane by an angle ψ , so that energy in the initial 0.05 s of the shear wave was maximized along one component, S_{fast} (Figure 6). An estimate of the initial shear-wave particle motion vector, \hat{S}_{fast} , in the (V,N,E) coordinate system may thus be computed using the vector rotation formula (*e.g.*, Goldstein, 1981) as

$$\hat{S}_{fast} = \begin{bmatrix} -\sin\theta\cos\psi \\ \cos\phi\cos\theta\cos\psi - \sin\phi\sin\psi \\ -\sin\phi\cos\theta\cos\psi + \cos\phi\sin\psi \end{bmatrix}. \quad (1)$$

\hat{S}_{fast} orientations are shown in Figure 7. As suggested by Figure 5a, particle motion azimuths at 150 m and 300 m are consistent with a narrow range of initial shear-wave particle motion azimuths observed over an 8-year period from events with near-vertical ray paths at KNW-AZ by Aster *et al.* (1990). Particle motions at the KNW-BH surface instrument, however, show a clear bias toward a more N-S orientation, an effect also visible in the horizontal particle motions of Figure 5a. Because the orientations of the surface horizontal components were checked twice, once via magnetic compass during deployment and once during our P-wave orientation analysis (Figure 3; Figure 4) and in both cases were found to be within a few degrees of (N,E), this rotation is most likely due to a systematic effect occurring in the upper 150 m.

Rotated seismograms. To examine differences between waveforms at different borehole depths, we projected P- and S-wave 3-component seismograms into (P, S_V, S_H) and (P, S_{fast}, S_{slow}) coordinate systems, respectively. Figure 8 shows seismograms from 20 events time-aligned to less than or equal to 1 sample (2.5 ms) by the cross-correlation maximum of the first 0.05 s (20 samples) of the P and S_{fast} components, for P- and S-waves, respectively (because of timing uncertainties, true relative times were not available between the different depths for this period). It is immediately clear that large modifications occur for both P- and S-wave signals in the shallowest 150 m.

First, note that P- and S-wave attenuation, as manifested in a relative deficit of high frequencies, is much greater between 150 m and the surface than between 300 m and 150 m. We quantify this effect in Aster and Shearer (this issue). Second, there are many instances where energy with a strong P-component polari-

zation is visible approximately 0.1 - 0.2 s after the surface-recorded S-wave. Such arrivals are not generally seen in downhole recordings (*e.g.*, event 881060633), indicating that significant S-to-P conversion and/or S-to-S side-scattering is occurring near the surface. As these ray paths are all nearly vertical, such conversions must be due to shallow 3-dimensional structure.

Fletcher *et al.* (1990) estimated two-way travel times to the surface and back for the 150 m and 300 m KNW-BH sensors to be approximately 120 ms and 180 ms for P-waves and 170 ms and 280 ms for S-waves, respectively. Good candidates for surface reflections are not generally visible in the downhole seismograms near these times, at least partially due to the well-developed P- and S-wave codas. We experimented with low-pass filtering (*e.g.*, Blakeslee and Malin, 1991) and autocorrelation in an attempt to detect reflected phases, but still did obtain any clear examples.

Arrivals in the S_{slow} -component direction generally follow the S_{fast} arrival by 0.025 to 0.080 s (*e.g.*, events 88079026 and 881322211). Waveform variation from depth to depth for individual earthquakes is considerably greater in S_{slow} -component seismograms than in S_{fast} - or P-component seismograms, and clear examples of time-shifted, correlatable S_{fast} and S_{slow} arrivals which would be diagnostic of shear-wave splitting are not generally observed. This is true even for seismograms recorded at 300 m, well beneath the obvious weathered layer. Nevertheless, a few events (*e.g.*, events 881321420 and 881322211) do exhibit distinct slow quasi-shear wave pulses that are consistent with a shear-wave splitting hypothesis.

S_{fast} - and S_{slow} -component seismograms from 300-m, sorted by ray path length (estimated as the straight-line station to hypocenter distance), are plotted in Figure 9. Again, note that pulse shape correlation between fast- and slow-

component arrivals is not generally observed, even well below the weathered zone. Furthermore, the dominant shear-wave frequency is comparable to the shear-wave linearity interval and many arrivals on the slow quasi-shear wave component are emergent, making it problematic to estimate a duration for the linear shear-wave particle motion.

Numerous techniques have been proposed to estimate the time delay, τ , between the initial shear-wave arrival and later phases which may represent either the arrival of the slow quasi-shear wave or the onset of the coda. An overview is provided by MacBeth and Crampin (1990). Aster *et al.* (1990) applied a variance tensor analysis to recordings of shear waves from 125 earthquakes with near-vertical ray paths recorded at KNW-AZ and concluded that path and source variations in the earthquake catalog led to great variability in their τ measurements, making it likely that much of the observed variation was due to scattered energy arriving around the time of the expected arrival of the slow quasi-shear wave. Such scattering makes unambiguous determination of τ difficult (although much more robust estimates of temporal variability are obtainable using a small population of highly similar earthquakes [Poupinet, 1984; Aster *et al.*, 1990, 1991]). The dissimilarity in the majority of fast and slow waveforms illustrated in Figure 9 confirms that these complications also exist in KNW-BH recordings made below the weathered layer, even for events with near-vertical ray paths.

An interesting feature of the data is the extreme similarity and complexity in initial arrivals for many of the 150 m and 300 m seismogram pairs. Event 881032333 of Figure 8, for example, shows a complicated P-wave arrival on both downhole sensors. These waveforms show no large differences which would indicate that this signal was generated by surface or near-surface reflections or scattering. It instead appears that the waveform complexity is due either to deeper

scattering or source complexity and that the seismic transfer function between 150 m and 300 m is transparent up to high frequencies (Aster and Shearer, this issue). Similar arrival character in P- and S_{fast} -component downhole arrivals (*e.g.*, event 881060633) favors a source time function complexity explanation.

Evidence for Shallow Anisotropy

Scattering and attenuation in the near-surface produce dramatic variations between some downhole and surface recordings of the same earthquake (*e.g.*, event 872251032). There exist many examples, however, (*e.g.*, event 880472249) of highly correlated shear-wave seismograms recorded at different levels, particularly for pairs from 150 m and 300 m. Such traces provide an opportunity to estimate the mean velocity anisotropy between sensors.

To obtain such a measure, we calculated cross-correlation functions for S_{fast} -component pairs and S_{slow} -component pairs from individual earthquakes recorded by different sensors, using cosine-tapered time windows of 0.24 s (96 samples). The S_{fast} window began 0.05 s (20 samples) before the shear-wave pick indicated in Figure 8 and the S_{slow} window began at the shear-wave pick. Note that in using this coordinate system, we are assuming that any shallow anisotropy between the sensors has approximately the same orientation as the local anisotropy inferred from initial S-wave particle motion directions at KNW-BH and KNW-AZ.

The cross-correlation was performed in the frequency domain. To interpolate to 1/32 sample ($\approx 78 \mu\text{s}$) time spacing we padded out the high-frequency portion of the discrete Fourier transform of the cross-correlation function with 2976 $((32-1) \cdot 96)$ zeros prior to taking the inverse Fourier transform. This interpolation procedure is invariably stable and introduces no additional frequency content to the cross-correlation function. We then examined the difference between the best lag

of the S_{slow} cross-correlation function, C_{slow} , and the best lag of the S_{fast} cross-correlation function, C_{fast} for component pairs recorded at 300 m and 150 m, 150 m and 0 m, and 300 m and 0 m (Figure 10). The cross-correlation peaks exhibit appreciable scatter, but display a distinct preference for the best C_{slow} lag to be later than the best C_{fast} lag for all component pairs. This relative lag is visible in some seismograms in Figure 8 as a slight moveout between the S_{slow} traces from the same event recorded at different levels (*e.g.*, event 88051549).

300-m and 150-m seismogram pairs, which have the highest frequency content and best cross-correlations, show a mean C_{slow} maximum that is 1.3 ms (with a standard deviation of 1.0 ms) later than the corresponding C_{fast} maximum. If we interpret this lag as being due to azimuthal shear-wave anisotropy, the one-way travel time for shear waves between 300 m and 150 m of 54 ms (Fletcher *et al.*, 1990) suggests a differential shear-wave velocity between the S_{fast} and S_{slow} components of $2.3\% \pm 1.7\%$.

Cross-correlation functions from 150-m and 0-m pairs have maxima that are broader and lower, primarily because of the loss of high frequencies in 0-m seismograms due to near-surface attenuation. Despite this complication, these pairs have unanimously late C_{slow} best lags with a mean value of 6.9 ms and a standard deviation of 3.6 ms. The one-way travel time for shear-waves is 85 ms, and the corresponding implied azimuthal shear-wave anisotropy is $7.5\% \pm 3.5\%$.

The 300 m and 0 m cross-correlations suffer from the greatest amount of scatter, both because of the reduced high frequency content of the surface recordings and because the increased distance between sensors produces correspondingly greater incoherence. We note, however, that despite some outliers, the C_{slow} cross-correlations are also preferentially late. This is again consistent with relatively slow vertical propagation of S_{slow} -polarized energy.

Discussion

The KNW-AZ surface instrument, which is affixed to an outcrop, displays polarization properties that are in close agreement with those made at depth in the borehole, suggesting that the strong initial shear-wave polarization alignment observed at this station is truly indicative of the bedrock anisotropy near this site. The KNW-BH surface instrument, on the other hand, is emplaced atop a weathered zone that is several tens of meters deep (Carroll *et al.*, 1991). This material not only causes severe high-frequency attenuation (Aster and Shearer, this issue), but also alters the initial S-wave polarization direction (Figure 5; Figure 7). Notably, Fletcher *et al.* (1990) examined horizontal shear-wave particle motions from a surface shear-wave generator during velocity logging at KNW-BH and found that the signal acquired a noticeably elliptical particle motion by 7.5 m depth. It thus appears clear that S-wave initial particle motion directions can be significantly influenced by weathered near-surface material.

Consistent evidence for shallow shear-wave anisotropy at KNW-BH is found in relative cross-correlation peaks between S_{fast} - and S_{slow} -polarized energy recorded at pairs of sensors (Figure 10). Estimates of azimuthal shear-wave anisotropy are $2.3\% \pm 1.7\%$ from 300 to 150 m, and $7.5\% \pm 3.5\%$ from 150 to 0 m. The excellent agreement in downhole and KNW-AZ polarization directions, however, indicates that the initial shear-wave polarization alignment exists well below the deepest borehole instrument (300 m).

Recent borehole results from controlled source experiments by Daley and McEvilly (1990) and Winterstein (1990) suggest that shallow azimuthal shear-wave anisotropy on the order of 10% exists in some areas near the San Andreas fault system. If this were also the case for the upper few kilometers at Anza, then the

typical linearity interval (about 0.1 s) between the initial shear-wave arrival and the onset of significantly elliptical or chaotic motion (Peacock *et al.*, 1988; Aster *et al.*, 1990, Crampin *et al.*, 1990), if indicative of the shear-wave splitting delay, could be attributed to a shallow anisotropic layer with an approximate thickness of as little as 3.5 km, assuming a mean S-wave velocity of 3.2 km/s. Our anisotropy estimate of 2.3% between 150 and 300 m, if generally applicable, increases the depth of a uniformly anisotropic layer to about 15 km. A shallow crustal explanation is also consistent with the 40° difference in initial shear-wave particle motion azimuths between the closely-sited Anza stations KNW and WMC (15 km separation; Peacock *et al.*, 1988; Aster *et al.*, 1990) and with variations observed in nearby stations at other networks (*e.g.*, Savage *et al.*, 1989, 1990; Gledhill, 1990).

The S_{fast} direction at KNW-AZ and KNW-BH is approximately consistent with the predominant strike of cracks observed in KNW-BH televiewer logs (Fletcher *et al.*, 1990), with the shear-fabric in the outcrop onto which KNW-AZ is affixed, and with the trace of the nearby Hot Springs fault (Figure 2). A comprehensive discussion of proposed mechanisms for generating shear-wave anisotropy in the crust is outside the scope of this paper, but they include microcracks reflecting the current stress field (*e.g.*, Crampin and Booth, 1985; Shepherd, 1990), microcracks reflecting the paleostress field (*e.g.*, Blenkinsop, 1990), rock fabric (*e.g.*, Kern and Wenk, 1990), and joints (macrocracks) (*e.g.*, Stewart, 1990). It is possible that the shear-wave anisotropy at KNW-AZ and KNW-BH is due to both rock fabric and cracks that extend essentially to the surface. The alignment of the horizontal projection of the fast anisotropic axis at KNW with a strike-slip fault strand favors a paleostress or shear-fabric interpretation rather than a mechanism dependent on the current regional maximum compressional stress direction, which must be between 0° and 90° clockwise with respect to the northwesterly strike of

the San Jacinto fault zone. The exact cause, however, remains obscure, with perhaps several of the above mechanisms contributing to the observed shear-wave polarization directions.

Although the downhole environment at KNW-BH enjoys considerably broader signal bandwidth and higher signal-to-noise levels relative to the surface (Aster and Shearer, this issue), borehole records do not show clear evidence for P- or S-wave surface reflections, nor do they display pervasive candidates for slow quasi-shear waves, even at 300 m. While the lack of clear surface reflections is consistent with Q and velocity estimates (Aster and Shearer, this issue), the lack of slow quasi-shear waves is more problematic. One possibility is that Q for deeper paths at Anza is mostly attributable to scattering rather than to intrinsic attenuation, in which case the slow quasi-shear wave arrival is obscured by multipathing. Such masking of the slow quasi-shear wave could also conceivably be enhanced by anisotropic shear-wave attenuation.

Conclusions

Summarizing our results in terms of the questions of the introduction, we find:

- (1) Horizontal seismometers both downhole and at the surface can be successfully oriented at the KNW and PFO boreholes to an estimated accuracy of approximately $\pm 5^\circ$ using low-pass-filtered initial P-wave particle motions from regional and near-regional earthquakes and one Nevada Test Site explosion.
- (2) An approximately 20° clockwise bias in initial shear-wave polarization directions occurs in surface recordings at the KNW borehole relative to recordings downhole. This rotation is not visible in P-wave particle motion azimuths from regional and near-regional events. Initial shear-wave particle motions at 150 m and 300 m are consistent with those observed over an 8-year period by

a nearby Anza network surface station, indicating that the alignment in initial shear-wave particle motions is not confined to the immediate vicinity of the Anza station and is at least partially due to processes occurring below the deepest borehole instrument (300 m), which is well beneath the weathered zone.

- (3) At the KNW borehole, good candidates for slow quasi-shear waves are only sporadically observed in seismograms from local earthquakes ($M_L \approx 2$) with near-vertical hypocenter-to-station ray paths, even at 300 m (the PFO borehole did not record any events with near-vertical ray paths). KNW-BH data from these earthquakes also do not display readily discernible surface reflections from near-vertical P- or S-waves. Aster and Shearer (this issue) show that this is attributable due to high near-surface attenuation.
- (4) Cross-correlated waveforms from different levels in the KNW borehole are suggestive of azimuthal shear-wave anisotropy, with the fast anisotropic axis having the same orientation as the observed initial S-wave polarization alignment. The initial alignment of S-wave particle motions observed at 300 m suggests that this anisotropy extends beneath the borehole.

References

- Aki, K., and P. Richards (1980). *Quantitative Seismology*, W.H. Freeman, New York.
- Aleford, (1986). Shear data in the presence of azimuthal anisotropy: Dilley, Texas, *Expanded abstract, S.E.G. meeting November 2-6, 1986, Houston, Texas*.
- Aster, R.C., and P.M. Shearer (1990). High-frequency borehole seismograms recorded in the San Jacinto fault zone, Southern California. Part 2: Attenuation and Site Effects, *Bull. Seism. Soc. Am.*, this issue.
- Aster, R.C., P.M. Shearer, and J. Berger, (1990). Quantitative measurements of shear-wave polarizations at the Anza seismic network, southern California — implications for shear-wave splitting and earthquake prediction, *J. Geophys. Res.*, **95**, 12449-12474.
- Aster, R., Shearer, P., Berger, J., (1991). Reply to "Response to comments by Aster et al. [1990] about temporal variations in shear-wave splitting observed by Peacock et al. [1988] and Crampin et al. [1990]", *J. Geophys. Res.*, *in press*.
- Berger, J., L.N. Baker, J.N. Brune, J.B. Fletcher, T.C. Hanks, and F.L. Vernon (1984). The Anza array: a high-dynamic-range, broadband, digitally radiotelemetered seismic array, *Bull. Seism. Soc. Am.*, **74**, 1469-1481.
- Blakeslee, S., and P. Malin, (1991). Near surface attenuation and amplification: Site-effect determination from two borehole stations at Parkfield, California, *Bull. Seism. Soc. Am.*, submitted.
- Blenkinsop, T., 1990. Correlation of paleotectonic fracture and microfracture orientations in cores with seismic anisotropy at Cajon Pass drill hole, southern California, *J. Geophys. Res.*, **95**, 11143-11150.
- Bonamassa, O., J. Vidale, and S. Schwartz, (1991). Directional site resonances observed from aftershocks of the 18 October, 1989 Loma Prieta Earthquake, *Bull. Seism. Soc. Am.*, submitted.
- Booth, D.C., and S. Crampin (1985). Shear-wave polarizations on a curved wave-front at an isotropic free-surface, *Geophys. J. R. astr. Soc.*, **83**, 31-45.
- Borcherdt, R., J. Fletcher, E. Jensen, G. Maxwell, J. Van Schaack, R. Warrick, E. Cranswick, M. Johnson, and R. McClearn (1985). GEOS: a general earthquake observation system, *Bull. Seism. Soc. Am.*, **75**, 1783-1802.
- Carroll L., J. Fletcher, H. Liu, and R. Porcella (1991). Implications of site response on determination of f_{\max} : results from a borehole experiment at Anza, CA, *Bull. Seism. Soc. Am.*, submitted.
- Crampin, S. (1978). Seismic-waves propagating through a cracked solid: Polarization as a possible dilatancy diagnostic, *Geophys. J. R. Astron. Soc.*, **53**, 467-496.
- Crampin, S., D.C. Booth, R. Evans, S. Peacock, and J. Fletcher (1990). Changes in shear wave splitting at Anza near the time of the North Palm Springs earthquake, *J. Geophys. Res.*, **95**, 11197-11212.
- Crampin, S., and D.C. Booth (1985). Shear wave polarizations near the North Anatolian fault, II, Interpretation in terms of crack-induced anisotropy, *Geophys. J. R. Astron. Soc.*, **83**, 75-92.
- Daley, T.M., and T.V. McEvilly (1990). Shear Wave Anisotropy in the Parkfield Varian Well VSP, *Bull. Seis. Soc. Am.*, **80**, 857-869.
- Fletcher, J., L. Haar, T. Hanks, L. Baker, F. Vernon, J. Berger, and J. Brune (1987). The digital array at Anza, California: processing and initial interpretation of source parameters, *J. Geophys. Res.*, **92**, 369-382.
- Fletcher, J., T. Fumal, H. Liu, and R. Porcella (1990). Near-surface velocities and

- attenuation at two boreholes near Anza, CA from logging data. *Bull. Seis. Soc. Am.*, **80**, 807-831.
- Frankel, A., and L. Wennerberg (1989). Microearthquake spectra from the Anza network., *Bull. Seis. Soc. Am.*, **79**, 581-609.
- Gledhill, K.R. (1990). A shear-wave polarization study in the Wellington region, New Zealand, *Geophys. Res. Lett.*, *in press*.
- Goldstein, H. (1981). *Classical Mechanics*, 672 pp., Addison-Wesley, Reading, MA.
- Kanasewich, E. (1975). *Time Sequence Analysis in Geophysics*, University of Alberta Press, Edmonton.
- Kern, H., and H.-R. Wenk (1990). Fabric-related velocity anisotropy and shear wave splitting in rocks from the Santa Rosa mylonite zone, California, *J. Geophys. Res.*, **95**, 11213-11224.
- Liu, H.-P., R.E. Westerlund, J.B. Fletcher, and R.E. Warrick (1986). A borehole geophone leveling device, *U.S.G.S. Open File Rep. 86-351*, 15 pp.
- Liu, H.-P., R.E. Warrick, R.E. Westerlund, J.B. Fletcher, and G.L. Maxwell (1988). An air-powered impulsive shear-wave source with repeatable signals, *Bull. Seism. Soc. Am.*, **78**, 355-369.
- Malin, P., J.A. Waller, R.D. Borchardt, E. Cranswick, E.G. Jensen, and J. Van Schaack (1988). Vertical seismic profiling of Oroville microearthquakes: Velocity spectra and particle motion as a function of depth, *Bull. Seism. Soc. Am.*, **78**, 401-420.
- MacBeth, C., and S. Crampin (1990). Utility of automatic techniques for estimating the effects of anisotropy in VSP data, *Geophys. Prospecting*, *submitted*.
- Majer, E., T.V. McEvilly, F. Eastwood, and L. Myer (1988). Fracture detection using P-wave and S-wave vertical seismic profiling at The Geysers, *Geophysics*, **53**, 76-84.
- Peacock, S., S. Crampin, D.C. Booth, and J. Fletcher (1988). Shear wave splitting in the Anza seismic gap, Southern California: temporal variations as possible precursors, *J. Geophys. Res.*, **93**, 3339-3356.
- Poupinet, G., W. Ellsworth, and J. Frechet (1984). Monitoring velocity variations in the crust using earthquake doublets: An application to the Calaveras fault, California, *J. Geophys. Res.*, **89**, 5719-5731.
- Rockwell, T., and C. Loughman (1990). Late Quaternary rate of slip along the San Jacinto fault zone near Anza, southern California, *J. Geophys. Res.*, **95**, 8593-8605.
- Sanders, C., and H. Kanamori (1984). A seismotectonic analysis of the Anza seismic gap, San Jacinto fault zone, southern California, *J. Geophys. Res.*, **89**, 5873-5890.
- Savage, M.K., X.R. Shih, R.P. Meyer, and R.C. Aster (1989). Shear wave anisotropy of active tectonic regions via automated S wave polarization Analysis, *Tectonophysics*, **165**, 279-292.
- Savage, M.K., W.A. Peppin, and U.R. Vetter (1990). Shear wave anisotropy and stress direction in and near Long Valley Caldera, California, 1979-1988, *J. Geophys. Res.*, **95**, 11165-11178.
- Scott, J.S., T.G. Masters, and J. Berger, Three-dimensional structure of the San Jacinto Fault Zone near Anza, California, (abstract), *EOS Trans. AGU*, **69**, 1324, 1988.
- Scott, J.S., T.G. Masters, and J. Berger, Earthquake source studies at Anza, California: Requirements for Location Precision and the effect of 3-D structure, (abstract), *EOS Trans. AGU*, **71**, 553, 1990.
- Sharp, R. (1967). San Jacinto fault zone in the Peninsular Ranges of southern California, *Bull. Geol. Soc. Am.*, **78**, 705-730.

- Shearer, P. (1988). Synthetic seismogram modeling of shear-wave splitting in VSP data from the Geysers, California, *Geophys. Res. Lett.*, **15**, 1085-1088.
- Shepard, T.J. (1990). Geological link between fluid inclusions, dilatant microcracks and paleostress field, *J. Geophys. Res.*, **95**, 11115-11120.
- Stewart, R.C. (1990). Seismic-wave velocity anisotropy in a jointed granite. *Abstract, Geophys. J. Int.*, **100**, p. 291.
- Thatcher, W., J.A. Hileman, and T.C. Hanks (1975). Seismic slip distribution along the San Jacinto fault zone, Southern California, and its implications, *Bull. Geol. Soc. Am.* **86**, 1140-1146.
- Vernon, F.L. (1989). *Analysis of Data Recorded on the Anza Seismic Network*, Ph.D. thesis, Scripps Instit. Oceanogr., Univ. of Calif., San Diego, La Jolla.
- Winterstein, D., and M. Meadows (1990). Depth dependence of S-wave polarization azimuth near the San Andreas fault, *Abstract, Fourth International Seismic Workshop on Anisotropy, Edinburgh, U.K.*
- Wyatt, F., D. Agnew, and M. Zumberge (1988). Piñon Flat Observatory: A facility for studies of crustal deformation, *U. S. Geol. Survey. Open File Report 99-673*, 4 pp.

Table and Figure Captions

Table 1. Regional events recorded by the Anza borehole instruments identified from the National Earthquake Information Center PDE report (Figure 1). Columns labeled KNW and PFO indicate which GEOS recorders triggered at each borehole site, where 1 = 300 m, 2 = 150 m, and 3 = 0 m. Depths are below sea level.

Table 2. Local events recorded by the Anza borehole instruments identified from the National Earthquake Information Center PDE report (Figure 2). Columns labeled KNW and PFO indicate which GEOS recorders triggered at each borehole site, where 1 = 300 m, 2 = 150 m, and 3 = 0 m. Depths are below sea level.

Table 3. Best orientations, ψ_0 (degrees E of N) for h_1 downhole components estimated from event back-azimuths and P-wave particle motions (see Appendix). The orientation error is taken as the minimum of the 1-norm angular error function (A11), *i.e.*, as the mean weighted angular deviation between the optimally rotated particle motion azimuths and the back-azimuths. $n_{0.9}$ indicates the number of regional and near-regional earthquakes used in each estimate, all of which have horizontal particle motion linearities, l (A5), of greater than or equal to 0.9.

Fig. 1. Regional geography, borehole locations, and regional and near-regional epicenters from 22 July, 1987 through 29 April, 1989 recorded by one or more borehole instruments (Table 1).

Fig. 2. Local and regional geography, borehole locations, and local event epicenters from 22 July, 1987 through 29 April, 1989 recorded by one or more borehole instruments (Table 2).

Fig. 3. Event back-azimuths, ϕ , plotted versus P-wave particle motion (initial

0.1 s) azimuth estimates (A8), θ (degrees E of N), corrected by the estimated horizontal seismometer orientations, ψ_0 (degrees E of N) (Table 3). Dashed lines at $\phi = \theta - \psi_0$ and at $\phi = \theta - \psi_0 \pm 180^\circ$ indicate ideal trends for dilatational and compressional sources, respectively, in a laterally-homogeneous isotropic Earth. The estimated orientation error, $\epsilon(\psi_0)$, for each horizontal coordinate system determination (Table 3) is the average angular deviation of the corrected azimuth estimates from a perfect fit to these trends.

Fig. 4. Self-scaled horizontal P-wave particle motions (initial 0.1 s) for all identified events recorded at the KNW and PFO. The projection is polar; the particle motion origin for each event is plotted at the event back-azimuth, and at a radius proportional to the straight-line emergence angle between station and source. The perimeter corresponds to an emergence angle of 95° (slightly above horizontal so as not to interfere with the plotting of distant events).

Fig. 5. (a) Self-scaled horizontal velocity particle motions for the first 0.1 s of the shear wave for 20 events with near-vertical ray paths to the KNW borehole site, KNW-BH, recorded between 22 July, 1987 and 29 April, 1989. The projection is identical to that of Figure 4, but the perimeter corresponds to an emergence angle of 45° . Note the general agreement between the 300 m and 150 m horizontal S-wave polarization directions and the $\approx 20^\circ$ clockwise rotation of the initial S-wave direction at the surface instrument relative to the other instruments.

(b) Self-scaled horizontal velocity particle motions for the first 0.1 s of the shear wave for 125 events with near-vertical ray paths to the Anza network surface seismometer KNW-AZ, recorded between 1 October, 1982 and 24 November, 1989 (After Aster *et al.*, 1990), plotted as in Figure 5a. Note the general agreement between the horizontal S-wave polarization directions in this figure and the 300 m

and 150 m particle motions shown in (a).

Fig. 6. (P, S_{fast}, S_{slow}) particle motion-based coordinate system, where ϕ is the azimuth (E of N) of the P-wave first motion, θ is the emergence angle of the P-wave first motion, and ψ is the angle of the S-wave first motion in the (S_V, S_H) plane as shown in the inset. Note that all angles are defined solely by the initial particle motion directions, and are not to be confused with those of Figure 3.

Fig. 7. Dip and azimuth (degrees E of N) values of initial S-wave velocity particle motion vectors for 20 events with near-vertical ray paths recorded by KNW borehole instruments (Figure 5a). Dashed lines at azimuths of $320 \pm 7.5^\circ$ indicate 95% confidence limits for the distribution of initial S-wave particle motion azimuths from 125 events recorded at the surface Anza Network station KNW-AZ (Figure 5b; Aster *et al.*, 1990). Note that KNW borehole instrument initial shear wave particle motion azimuths at 150 m and 300 m agree well with those observed at KNW-AZ, but those recorded at 0 m at the borehole site show increased scatter and a clockwise rotation of approximately 20° relative to those recorded downhole and at KNW-AZ.

Fig. 8. (a) P-wave velocity seismograms (0.5 s) for the 20 near-vertical ray path events of Figure 5a, projected into the (P, S_V, S_H) coordinate system determined by the initial P-wave particle motion (Figure 6). Each box shows seismograms recorded at 0, 150, and 300 m (from top to bottom, respectively) for the labeled event and component. Individual components for each event and depth have correct relative amplitudes. Seismograms for each event are aligned on the maximum cross-correlation of 0.05 s (20 samples) of the P component. Local magnitudes for these events range from 1.4 (event 872251032) to 2.5 (event 872521021) (Table 2).

(b) S-wave velocity seismograms (0.5 s) for the 20 borehole-recorded events of Figure 5a, projected into the (P, S_{fast}, S_{slow}) coordinate system determined by the initial P-wave and S-wave particle motions (Figure 6). Components for each event and depth have correct relative amplitudes. Seismograms for each event are aligned on the maximum cross-correlation of 0.05 s (20 samples) of the S_{fast} component.

Fig. 9. 300-m S_{fast} -component (solid) and S_{slow} -component (dashed) S-wave velocity seismograms recorded by the 300-m KNW borehole instrument (expanded time scale from Figure 8b), sorted by decreasing (straight-line station-to-hypocenter) range. Note that even for these 300-m recordings from below the weathered layer, similar pulse shapes between S_{fast} - and S_{slow} -component seismograms predicted by a simple shear wave splitting model are not generally observed (with the notable exception of event 881322211).

Fig. 10. Cross-correlation function main lobes from S_{slow} -component (C_{slow}) and S_{fast} -component (C_{fast}) S-wave velocity seismograms recorded at the KNW borehole (Figure 8b). C_{fast} cross-correlations are centered on zero lag. Each C_{slow} maximum is plotted relative to the maximum of its corresponding C_{fast} function, with its peak highlighted by a triangle. Note that all three sets of cross-correlations exhibit a preference for the upward propagation of S_{slow} -polarized energy to be slow relative to S_{fast} -polarized energy.

Appendix: Estimating Horizontal Seismometer Orientations Using Initial Particle Motions

Initial particle motion directions were estimated using a 2-dimensional variance tensor analysis (*e.g.*, Kanasewich, 1975) using 0.1 s-segments (40 samples) of the P-wave time series in the horizontal plane, $\{\vec{x}\}$, expressed in a coordinate system H of unknown orientation and handedness.

The data variance tensor is the expectation value of the outer product

$$\mathbf{V} = \langle \vec{x} \vec{x}^T \rangle . \quad (\text{A1})$$

which has a decomposition

$$\mathbf{V} = \mathbf{a} \cdot \Lambda \cdot \mathbf{a}^T \quad (\text{A2})$$

where \mathbf{a} is the 2-dimensional orthogonal matrix of (unit) eigenvectors

$$\mathbf{a} = (\hat{e}_1, \hat{e}_2) \quad (\text{A3})$$

and Λ is a diagonal matrix composed of the real, non-negative eigenvalues of \mathbf{V}

$$\Lambda_{ij} = \eta_i \delta_{ij} , \eta_1 \geq \eta_2 \geq 0 . \quad (\text{A4})$$

The linearity (Aster *et al.*, 1990) is:

$$l = \frac{\eta_1 - \eta_2}{\eta_1 + \eta_2} . \quad (\text{A5})$$

and is a measure of the degree to which the energy in the windowed segment of $\{\vec{x}\}$ is confined to a single direction. For the two dimensional case considered here, where the variance tensor defines an ellipse, l is just the square of the center-to-focus distance, where the semimajor axis is

$$a = \left[\frac{\eta_1}{\eta_1 + \eta_2} \right]^{1/2} \quad (\text{A6})$$

and the semiminor axis is

$$b = \left[\frac{\eta_2}{\eta_1 + \eta_2} \right]^{1/2} \quad (\text{A7})$$

The eigenvector corresponding to η_1 , \hat{e}_1 , is the best fit L_2 -norm axial vector to the data points; the axis from which the sum of the squares of the perpendicular distances of the data points is minimized, or equivalently, is the axis of minimum rotational inertia for the (unit weighted) data points. Because \hat{e}_1 is an axial vector (due to the quadratic form of V), it may point parallel to or antiparallel to the actual particle motion, depending upon the conventions of the particular eigenvector-eigenvalue decomposition routine used. We therefore adjust \hat{e}_1 to indicate the actual particle motion direction by comparing \hat{e}_1 with the average of $\langle \vec{x} \rangle$ over the windowed time series, which is dominated by the first swing for the regional and near-regional signals used in this paper. The orientation azimuth, θ for the i^{th} event is then

$$\theta_i = \tan^{-1}[(\hat{e}_{1i})_x/(\hat{e}_{1i})_y] \in [0, 2\pi) . \quad (\text{A8})$$

For a (N,E) coordinate system convention and isotropic and laterally homogeneous media, the relationship between observed particle motions and geographically-determined back-azimuths is

$$\theta = \phi + m\pi \quad (\text{A9})$$

where $\phi \in [0, 2\pi)$ is the (known) event back-azimuth obtained from station and hypocenter coordinates, and the source polarity factor $m \in \{-1, 0, 1\}$. $m = 0$ is appropriate for dilatational sources, where the first swing of the particle motion is in the back-azimuth direction, and $m = \pm 1$ models the required inversion of particle motion for compressional sources, where the initial particle motion is away from the source.

We wish to rotate the observed particle motion azimuths (recorded in the unknown coordinate system H) into a set of azimuths that best agree with the set

of geographic back-azimuths. By convention, if H is left handed ($h_1 \times h_2 = -\text{vertical}$), we seek the azimuthal correction angle, $\psi = \psi_0 \in [0, 2\pi)$, so that

$$\theta - \psi = \phi \pm m\pi \quad (\text{A10})$$

is best satisfied. If H is right handed, we interchange the h_1 and h_2 components before fitting (A9), to maintain consistency with (A8).

We minimize a weighted L1 angular error function

$$\epsilon(\psi) = \frac{1}{n} \sum_{i=1}^n l_i \cdot |\theta_i - \phi_i - \psi \pm m\pi| \quad (\text{A11})$$

to estimate ψ_0 , where n is the number of particle motion observations and the weighting factor l is the particle motion linearity (A5). The integer m characterizes the source polarity and is free to vary to minimize each term. Note that (A11) is simply an average of n sawtooth functions, each with a period of 180° and an amplitude range of $\pm 90^\circ$. The consistency of the orientation data is reflected in the phase agreement of these terms.

The error function, $\epsilon(\psi)$, has a 180° ambiguity that requires source polarity information for its resolution. One possibility would be to incorporate polarity information directly into the error function by including terms with 360° periodicities and an amplitude range of 0° to 180° for sources of known polarity (e.g., Nevada Test Site explosions). We chose instead to calculate ϵ as in (A11) and then restrict the range of ψ by matching polarities of seismograms recorded both by the surface borehole instruments and by nearby surface Anza network instruments of known polarity. This procedure had the added benefit of enabling us to verify the polarity of the downhole vertical sensors.

To reduce noise in initial particle motion azimuth estimates (A8), all seismograms were low-pass-filtered using a finite impulse response realization (Kaiser and

Reed, 1977) with a corner frequency of 20 Hz, a transition bandwidth of 5 Hz, and a stop band level of -20 dB at 30 Hz. Only those signals with linearities (A5) $l \geq 0.9$ were used in evaluating the error function (A11). A negative $d\phi/d\theta$ was observed for the 150-m and 300-m instruments at KNW, indicating that these instruments were data logged with right handed coordinate systems, which result when components are interchanged or when a single component is inverted. Horizontal records from these depths were interchanged prior to final evaluation of the error function.

Acknowledgments

We especially thank J. Fletcher, who generously provided borehole data and system information. Borehole sites were maintained by L. Carroll, J. Batti, J. Babcock and J. Scott. F. Vernon assisted in the data processing. D. Betts assisted in preparing the figures. The authors thank A. Frankel and J. Vidale for helpful reviews. Funding was provided by Institute of Geophysics and Planetary Physics, Lawrence Livermore National Laboratory grants 89-14 and GS90-45, by U. S. Geological Survey grant 14-08-0001-G1767, and by AFGL contract F19628-88-K-0044.

Regional Events							KNW	PFO
Year	Day	Time (UTC)	Longitude	Latitude	Depth (km)	M _L		
1987	216	02:40:10.19	-117.780	32.970	6.0	3.0 (Oceanside)	1,2,3	-
1987	276	23:23:17.20	-118.050	34.060	8.0	3.0 (Whittier)	1,2,3	-
1987	277	02:55:15.21	-118.076	34.077	10.0	2.6 (Whittier)	1,2,3	-
1987	277	10:59:38.10	-118.100	34.070	8.0	5.3 (Whittier)	1,2,3	-
1987	277	14:05:52.40	-118.110	34.080	11.0	3.5 (Whittier)	1,2,3	-
1987	278	07:05:11.50	-118.100	34.080	9.0	3.2 (Whittier)	1,3	-
1987	310	23:36:45.20	-117.780	33.000	6.0	3.1 (Oceanside)	1,3	-
1987	335	07:03:47.70	-117.860	33.660	12.0	3.0	1,2,3	1,3
1987	335	08:23:07.79	-115.850	32.740	6.0	3.1 (Sstn. Hills)	-	1,3
1987	336	04:03:05.64	-115.830	33.126	5.0	4.0 (Sstn. Hills)	1,3	1,2,3
1987	337	19:04:36.50	-115.870	33.010	2.0	3.8 (Sstn. Hills)	1,3	1,2
1987	338	05:23:54.00	-115.810	32.990	3.0	3.1 (Sstn. Hills)	1,3	1,2
1987	338	20:18:10.70	-115.840	32.990	6.0	3.1 (Sstn. Hills)	-	1,2
1987	347	15:02:39.40	-115.700	32.910	6.0	3.6 (Sstn. Hills)	1	1,3
1987	351	01:51:58.80	-117.760	33.030	6.0	3.5 (Oceanside)	3	1,2,3
1987	351	07:26:25.60	-116.680	33.980	9.0	3.1 (N. Plm. Sp.)	3	1,2,3
1987	363	10:17:18.20	-117.200	33.550	6.0	3.1	1,3	1,3
1987	365	21:08:14.90	-116.400	34.180	6.0	3.0	-	1,3
1987	365	21:34:01.29	-116.420	34.180	2.0	3.9	-	1,3
1988	002	19:40:51.78	-116.405	34.173	5.0	3.3	-	1,3
1988	002	19:43:00.90	-116.410	34.180	2.0	3.1	-	1,3
1988	092	18:52:53.29	-116.220	32.930	9.0	3.4	1,2,3	1,3
1988	093	23:43:01.09	-117.730	32.920	6.0	3.1 (Oceanside)	1,2,3	1,3
1988	094	03:34:04.60	-117.730	32.920	6.0	3.0 (Oceanside)	1,2,3	1,3
1988	104	06:52:38.80	-117.790	32.980	6.0	3.2 (Oceanside)	1,2,3	-
1988	105	13:03:09.29	-116.300	33.270	11.0	3.0	1,2,3	1,3
1988	120	05:29:14.80	-116.760	34.030	11.0	3.5 (N. Plm. Sp.)	1,3	1,3
1988	138	19:38:37.90	-116.250	33.240	8.0	3.8	-	1
1988	158	08:06:26.20	-116.310	33.300	13.0	3.1	1,3	1
1988	173	20:02:50.40	-116.410	32.070	6.0	3.3 (Baja)	1,3	-
1988	230	17:00:00.09	-116.307	37.297	0.0	5.5 (NV Test Site)	1,2,3	3

Table 1

Local Events								
Year	Day	Time (UTC)	Longitude	Latitude	Depth (km)	M _L	KNW	PFO
1987	203	22:54:47.276	-116.569	33.459	10.57	2.6	1,2,3	-
1987	224	23:38:07.160	-116.747	33.492	13.37	1.6	1,3	-
1987	225	10:32:36.233	-116.714	33.611	17.55	1.4	1,3	-
1987	238	08:24:57.154	-116.860	33.359	15.11	2.4	1,3	-
1987	252	10:21:53.387	-116.682	33.588	17.56	2.5	3	-
1987	307	22:11:06.899	-116.705	33.687	20.94	1.6	1,2,3	3
1987	310	18:06:23.598	-116.918	33.553	14.36	2.8	1,3	1,2
1987	335	00:11:11.063	-116.721	33.662	18.74	2.1	1,2,3	3
1987	337	11:15:02.511	-116.713	33.906	18.07	1.9	1,3	1
1987	363	11:08:27.592	-116.890	33.600	5.19	2.9	1,3	1,3
1987	365	06:16:43.073	-116.394	33.372	12.49	1.8	-	1,3
1988	047	14:46:33.167	-116.736	33.646	17.00	1.5	1,2,3	1
1988	047	22:49:57.811	-116.765	33.664	15.64	1.4	1,2,3	-
1988	048	02:01:45.947	-116.619	33.579	15.32	1.4	1,2,3	1
1988	050	15:49:00.702	-116.723	33.649	18.35	-	1,2,3	-
1988	079	06:28:33.790	-116.712	33.639	15.84	1.8	1,3	1,3
1988	080	16:23:28.730	-116.739	33.901	13.80	2.7	1,2,3	3
1988	084	04:01:04.028	-116.725	33.666	18.87	1.8	-	1,3
1988	088	15:09:01.431	-116.547	33.969	11.49	2.5	1,2,3	1,3
1988	089	09:09:20.806	-116.719	33.694	21.92	1.9	1,2,3	3
1988	089	20:50:40.041	-116.509	33.512	16.64	2.3	1,2,3	1,3
1988	093	12:50:49.035	-116.951	33.890	13.38	2.5	1,2,3	3
1988	095	19:40:33.313	-116.808	33.594	9.95	1.8	1,3	-
1988	103	23:33:03.716	-116.752	33.709	19.81	1.4	1,2,3	1
1988	106	06:33:13.758	-116.800	33.690	17.48	1.9	1,2,3	1,3
1988	106	14:17:36.170	-116.744	33.702	19.04	1.6	1,2,3	3
1988	107	03:09:52.696	-116.797	33.569	4.77	-	1,2,3	1
1988	108	00:22:24.904	-116.760	33.548	5.41	2.2	1,2	1,3
1988	110	09:57:11.166	-116.580	33.475	14.32	1.9	-	1,2,3
1988	116	19:45:29.961	-116.678	33.889	13.29	2.7	1,3	1,3
1988	117	21:27:17.176	-116.628	33.592	16.03	1.6	1,3	1,3
1988	118	22:22:11.867	-116.759	33.547	5.06	1.7	1,3	1
1988	120	03:11:25.066	-116.507	33.511	16.17	2.5	-	1,3
1988	120	22:43:44.091	-116.549	33.976	13.60	2.9	1,3	1,2,3
1988	122	11:14:02.531	-116.760	33.547	5.31	2.5	-	1,2,3
1988	132	08:38:07.856	-116.458	33.512	9.09	1.9	1,3	1,2
1988	132	14:20:02.420	-116.759	33.658	19.10	1.5	1,3	-
1988	132	22:11:59.174	-116.751	33.621	18.36	-	1	-
1988	158	08:14:59.825	-116.318	33.301	14.33	2.6	1,3	1,2
1988	158	08:58:07.746	-116.319	33.300	14.42	2.1	1,3	1
1988	161	06:35:00.138	-116.808	33.594	9.92	1.4	3	-
1988	171	09:17:29.024	-116.211	33.347	13.43	2.4	1,3	-
1988	172	03:23:28.787	-116.254	33.239	9.58	2.6	1,3	-
1988	201	11:13:04.048	-116.938	33.752	17.05	2.1	1,3	-
1988	201	22:54:24.273	-116.790	33.652	16.86	1.6	1,3	3
1988	229	12:41:33.405	-116.861	33.872	10.19	2.3	1,2,3	3
1989	116	06:31:33.239	-116.731	33.662	16.62	1.9	1,2	1,3
1989	119	15:30:46.952	-116.723	33.645	19.26	1.7	1,2	1,3

Table 2

Instrument Orientation Determinations						
Station	0 m		150 m		300 m	
	ψ_0	$n_{0.9}$	ψ_0	$n_{0.9}$	ψ_0	$n_{0.9}$
KNW	$4.1 \pm 4.9^\circ$	16	$305.6 \pm 7.6^\circ$	9	$57.0 \pm 5.7^\circ$	19
PFO	$354.3 \pm 5.4^\circ$	21	$232.1 \pm 4.8^\circ$	8	$188.5 \pm 4.7^\circ$	12

Table 3

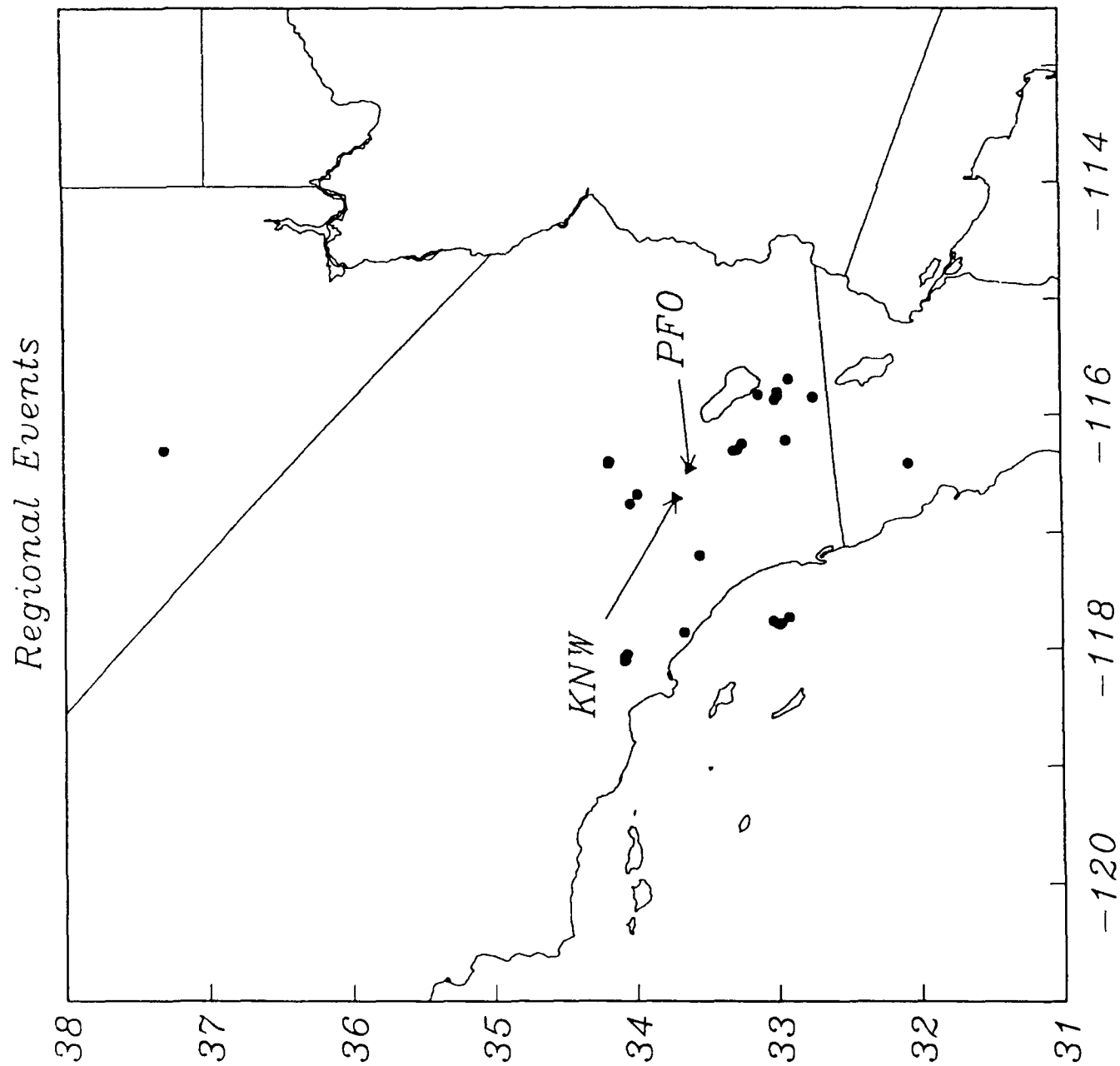


Figure 1

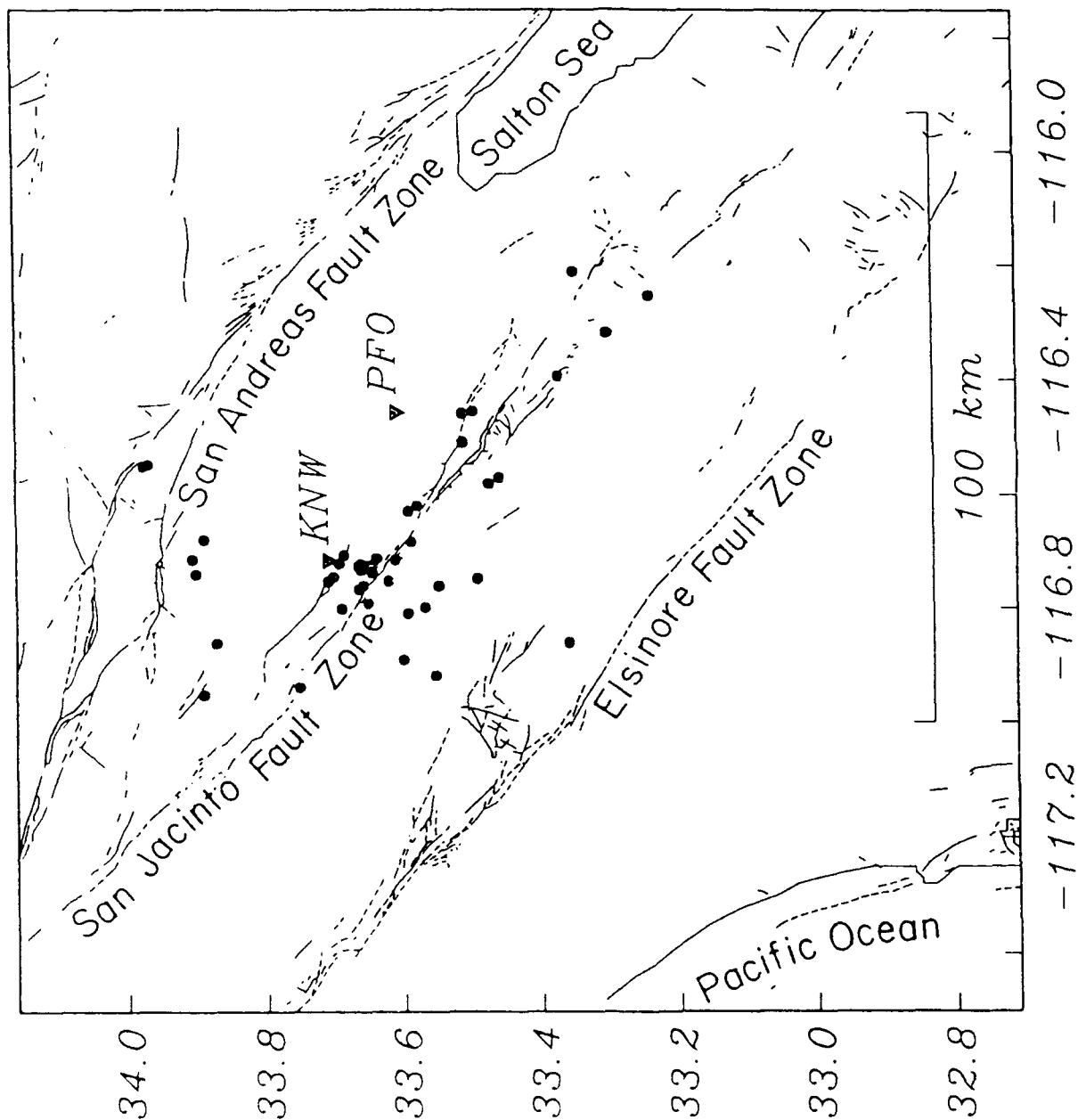


Figure 2

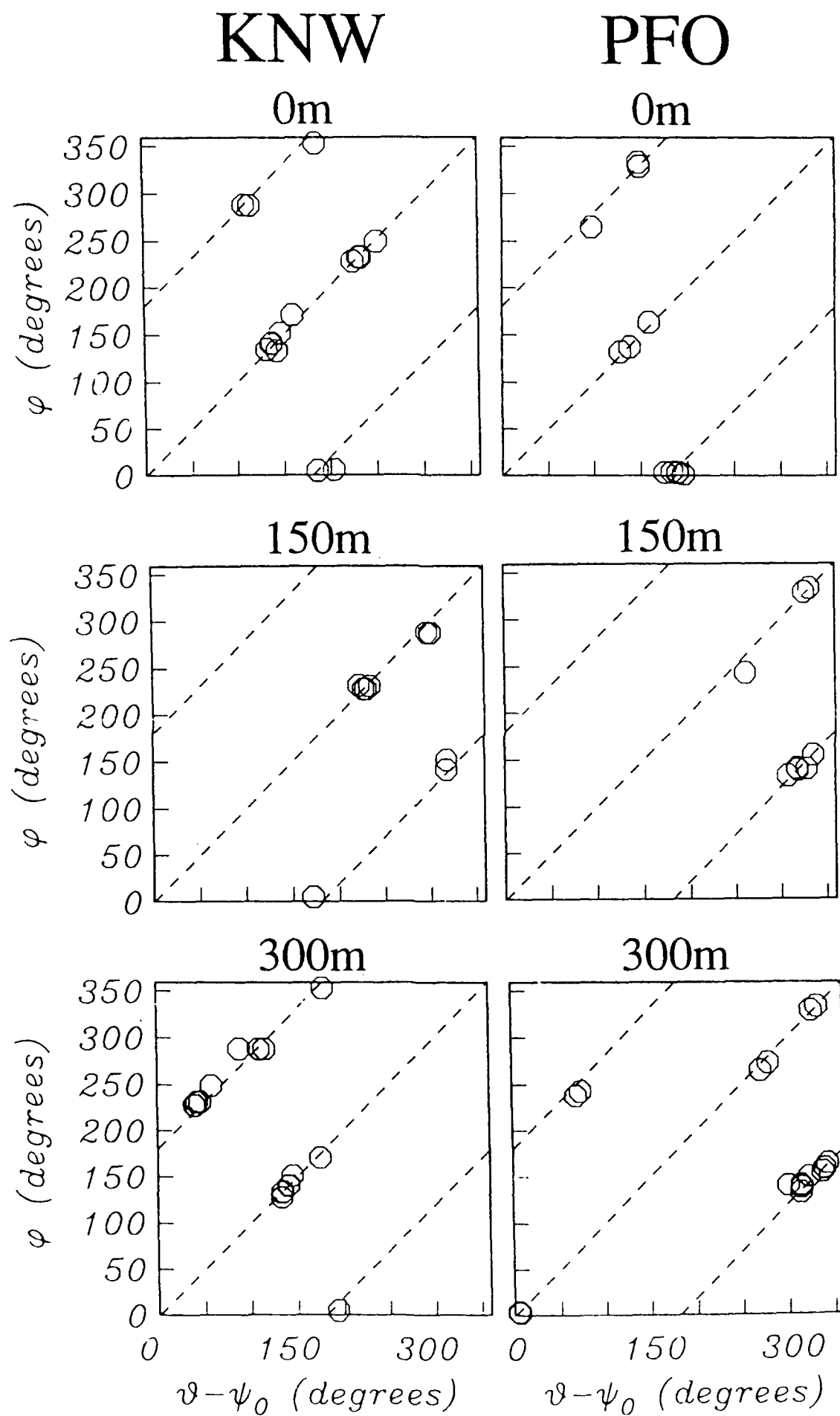
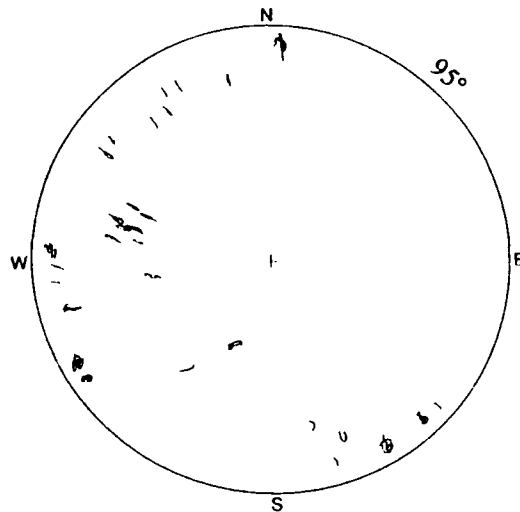
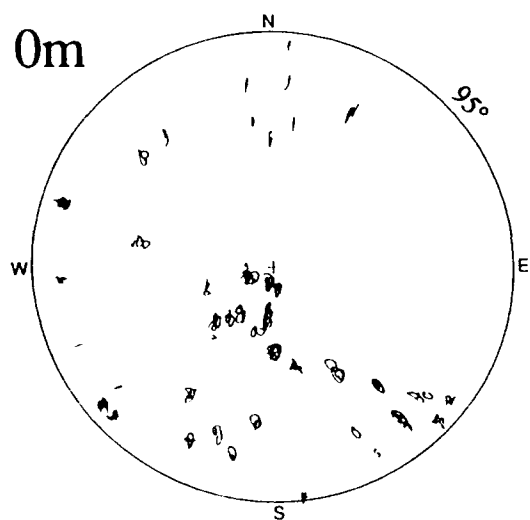


Figure 3

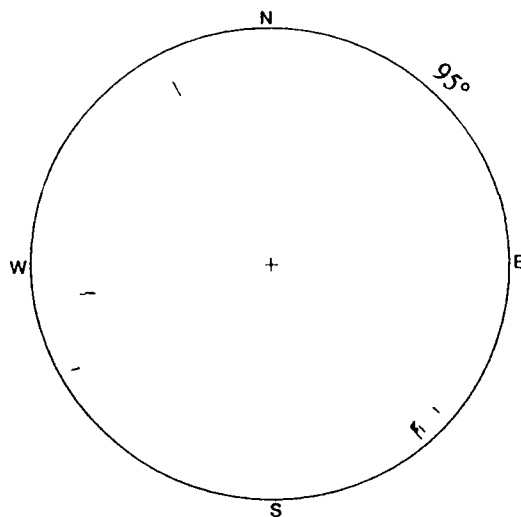
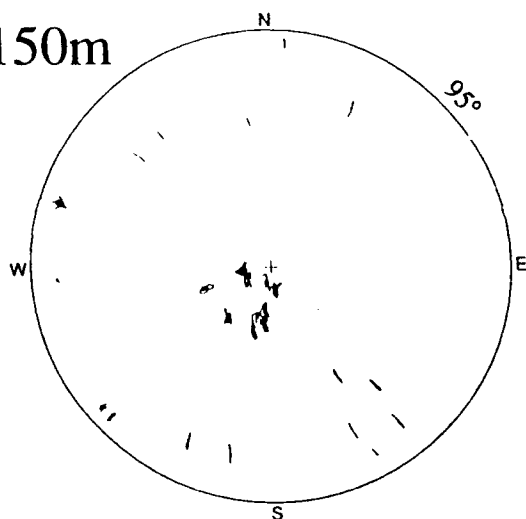
KNW

PFO

0m



150m



300m

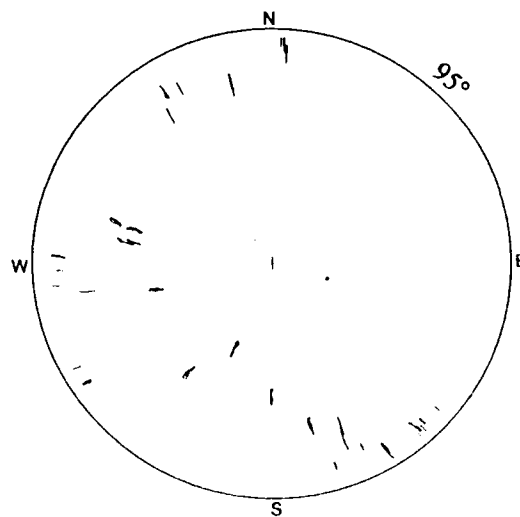
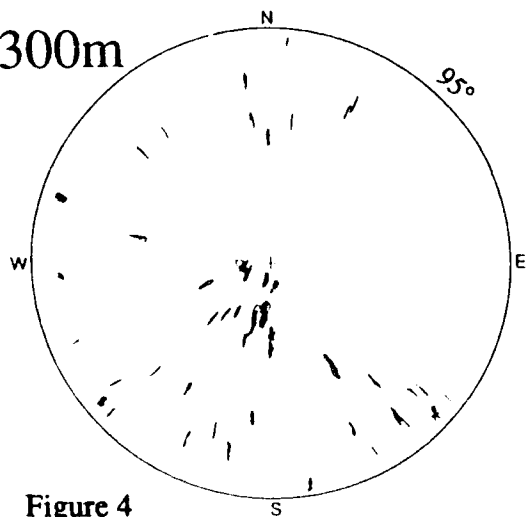
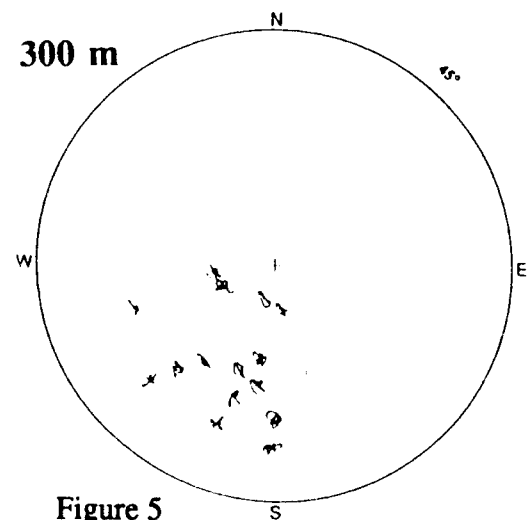
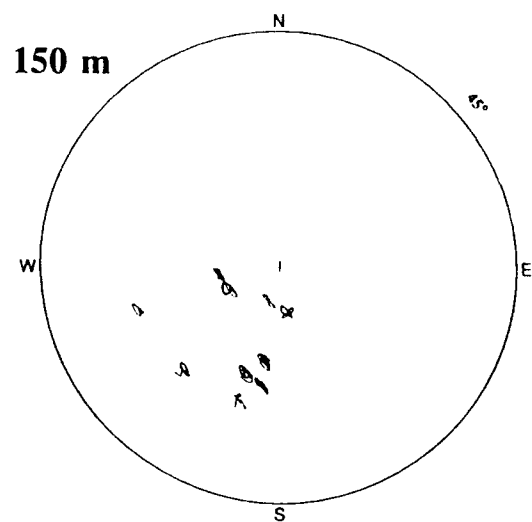
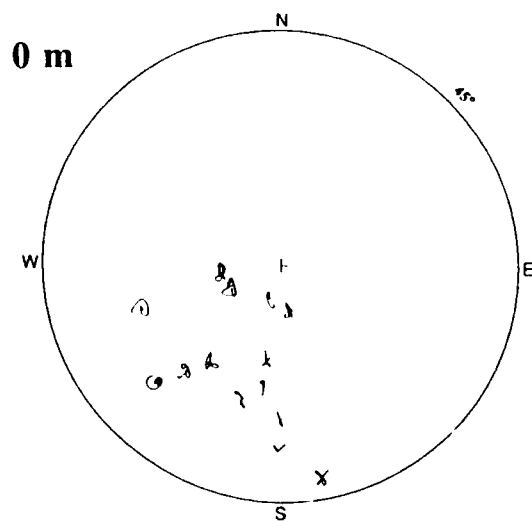


Figure 4

(a)

KNW-BH



(b)

KNW-AZ

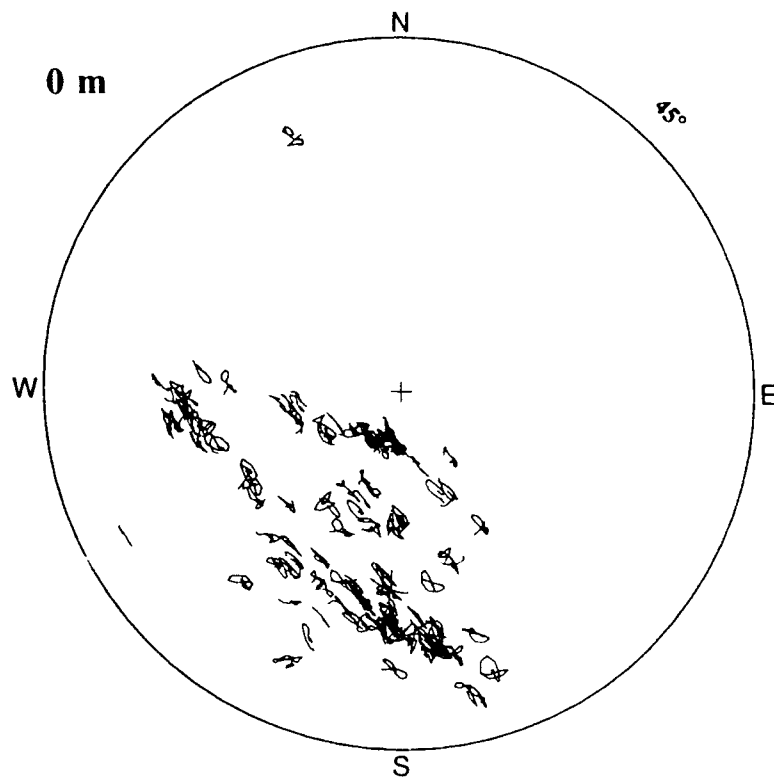


Figure 5

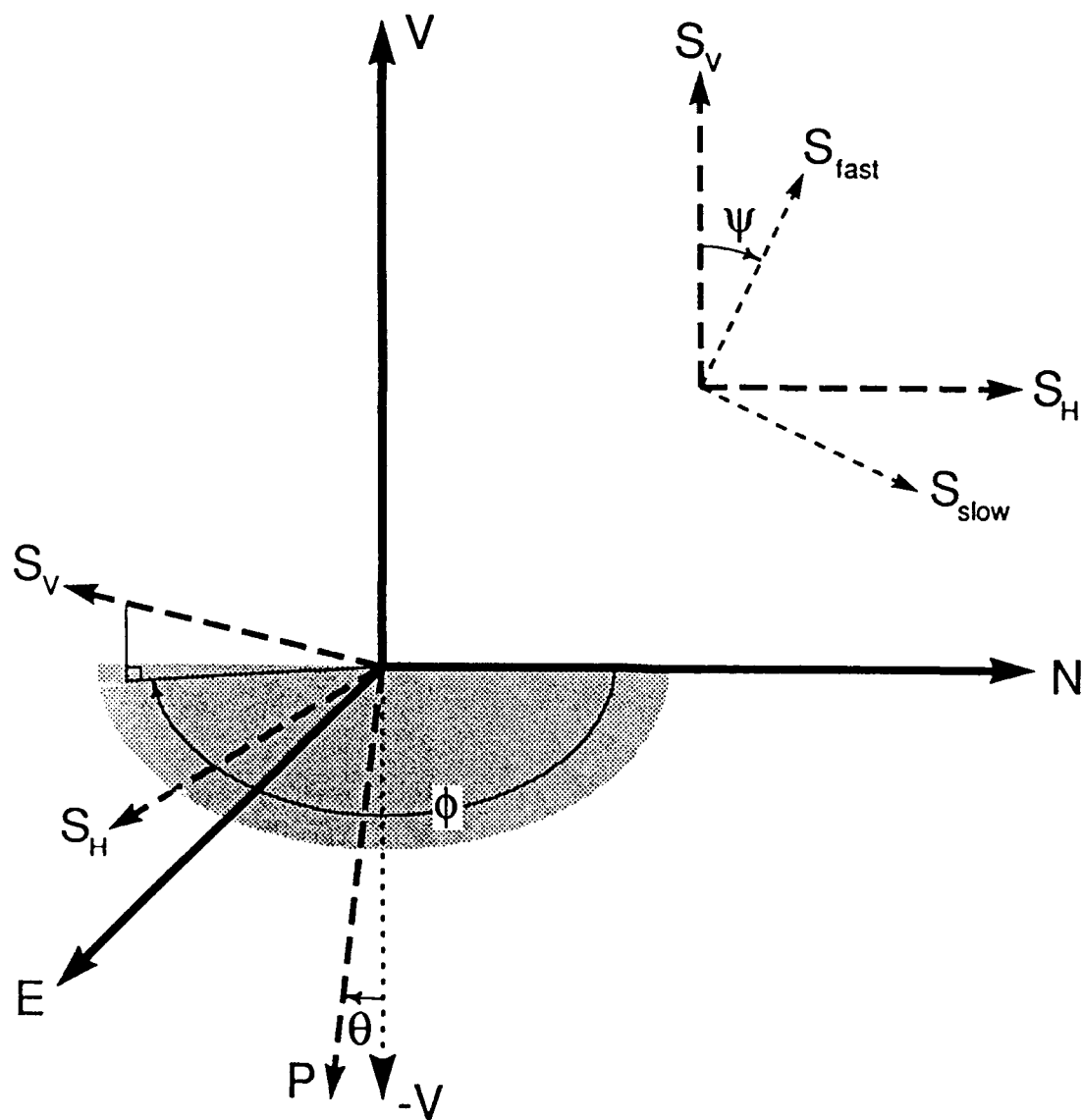


Figure 6

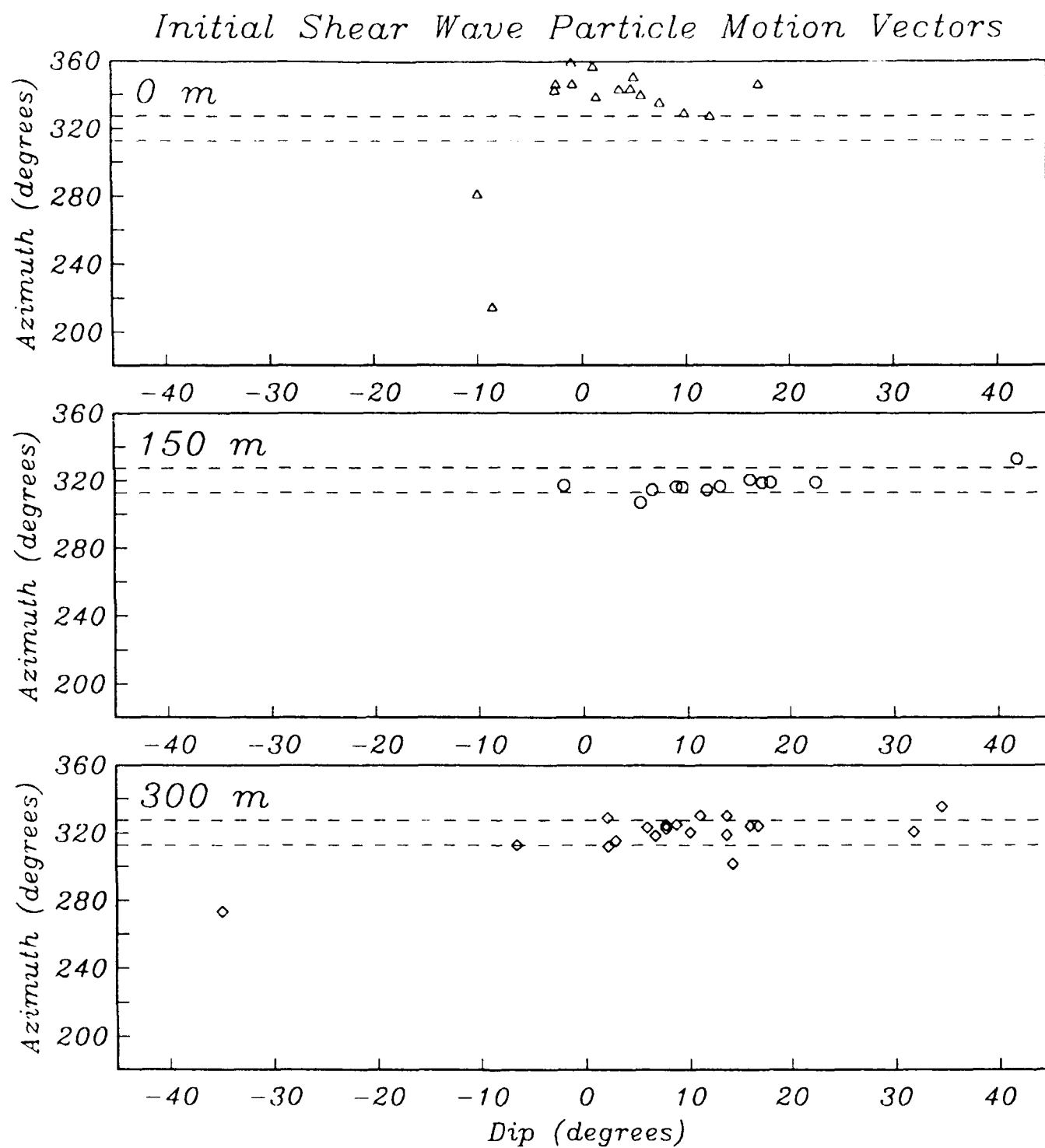


Figure 7

P-WAVE

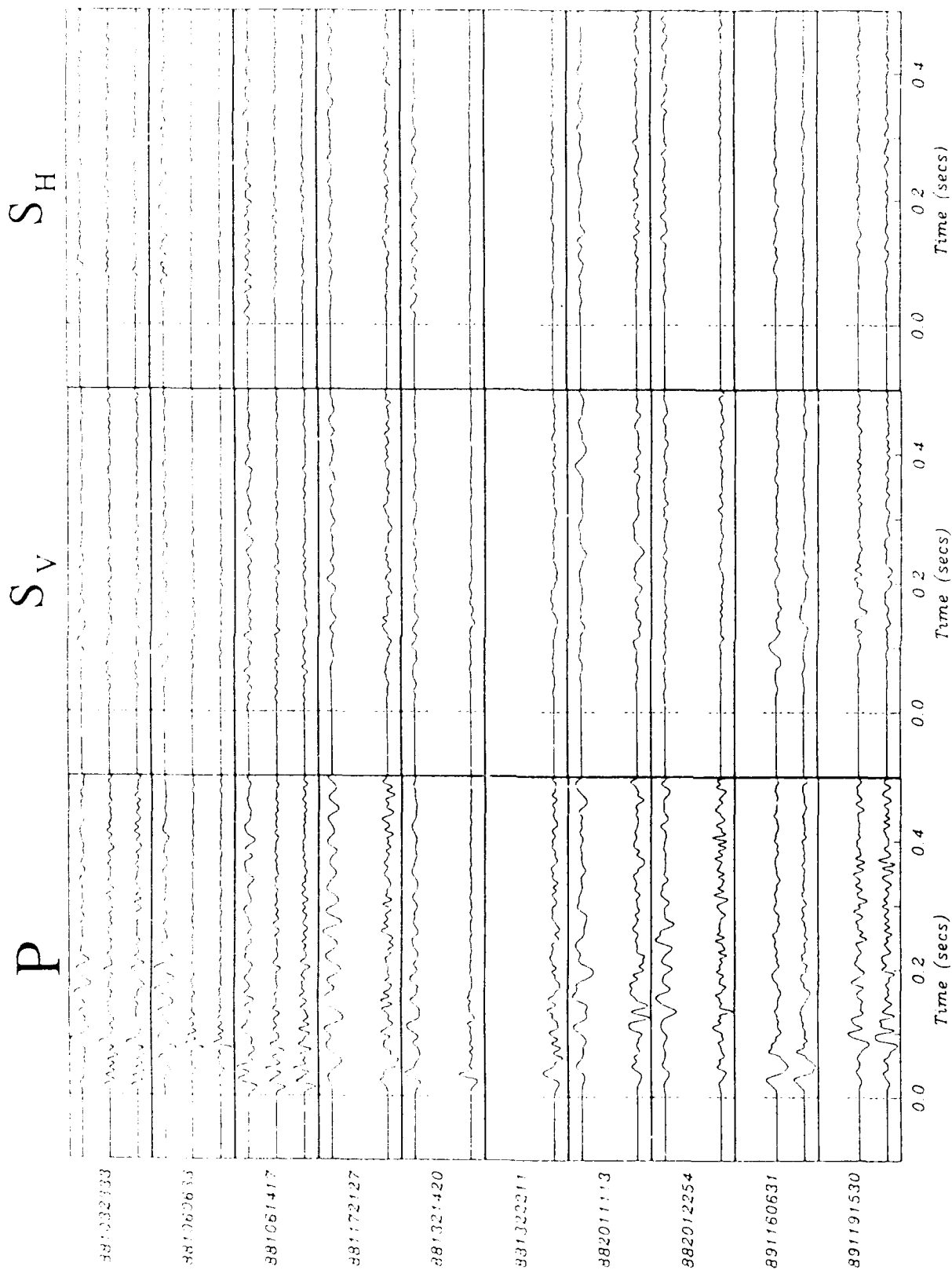


Figure 8(a)

P-WAVE

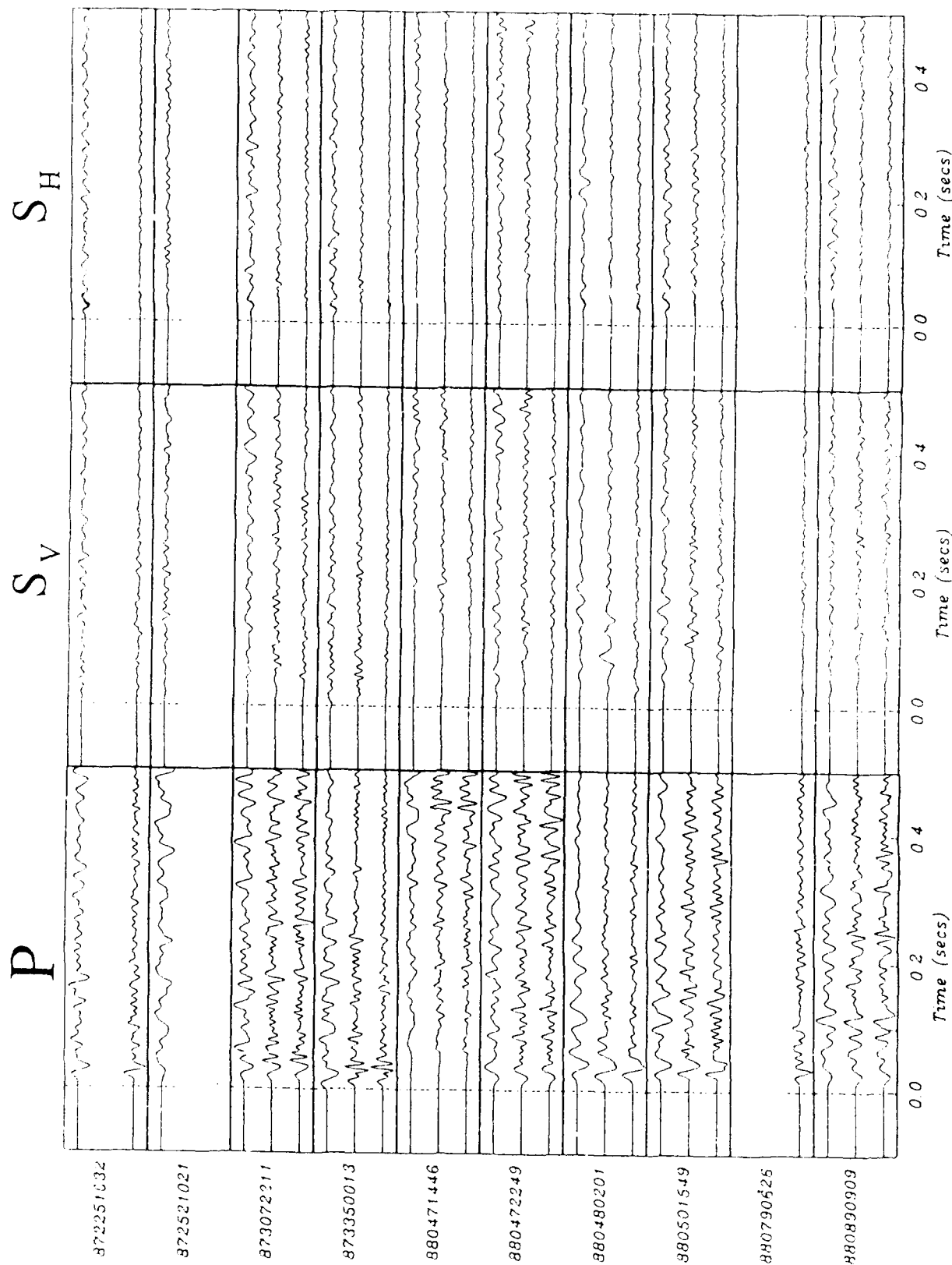


Figure 8(a) continued

S-WAVE

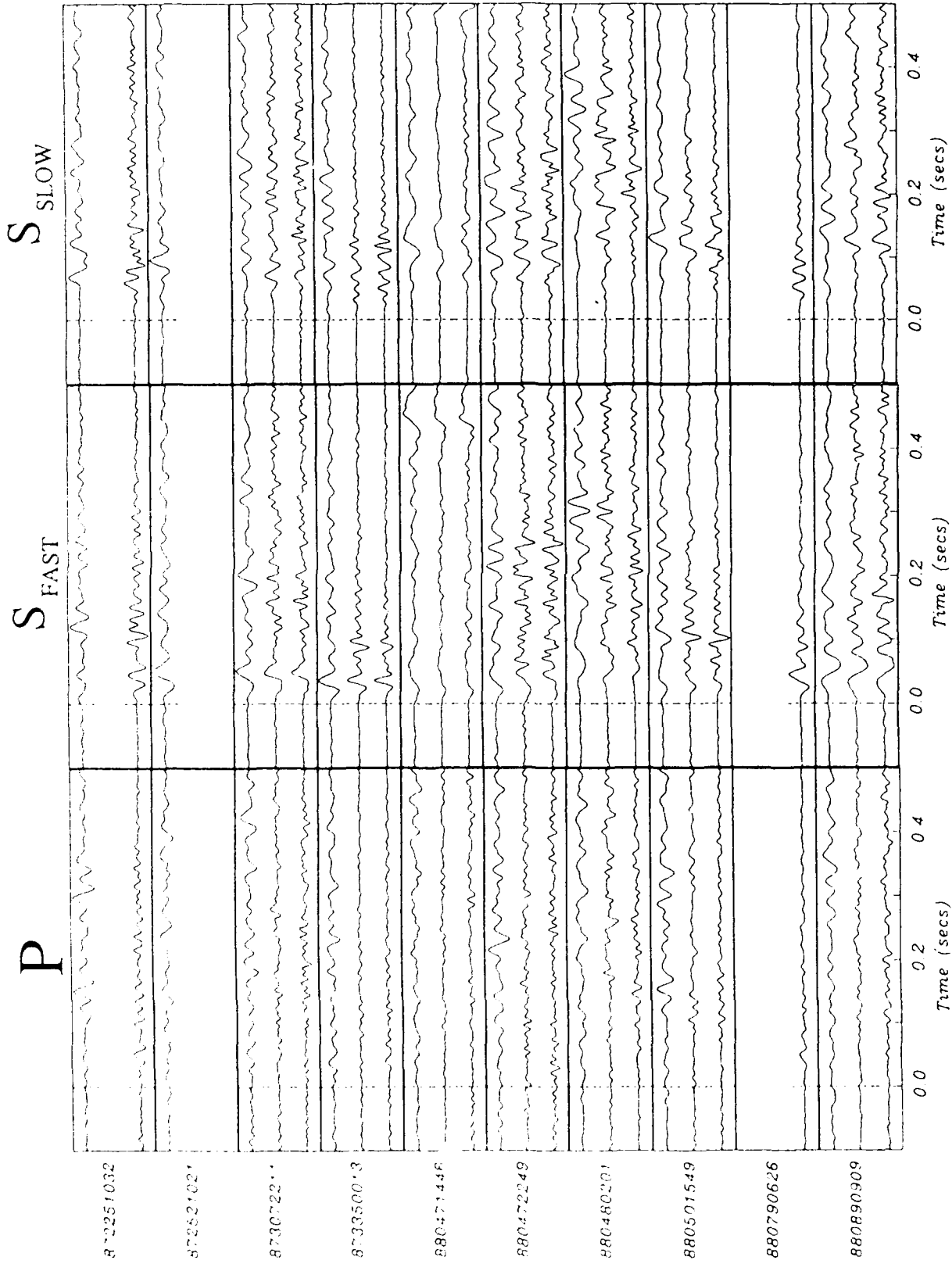


Figure 8(b)

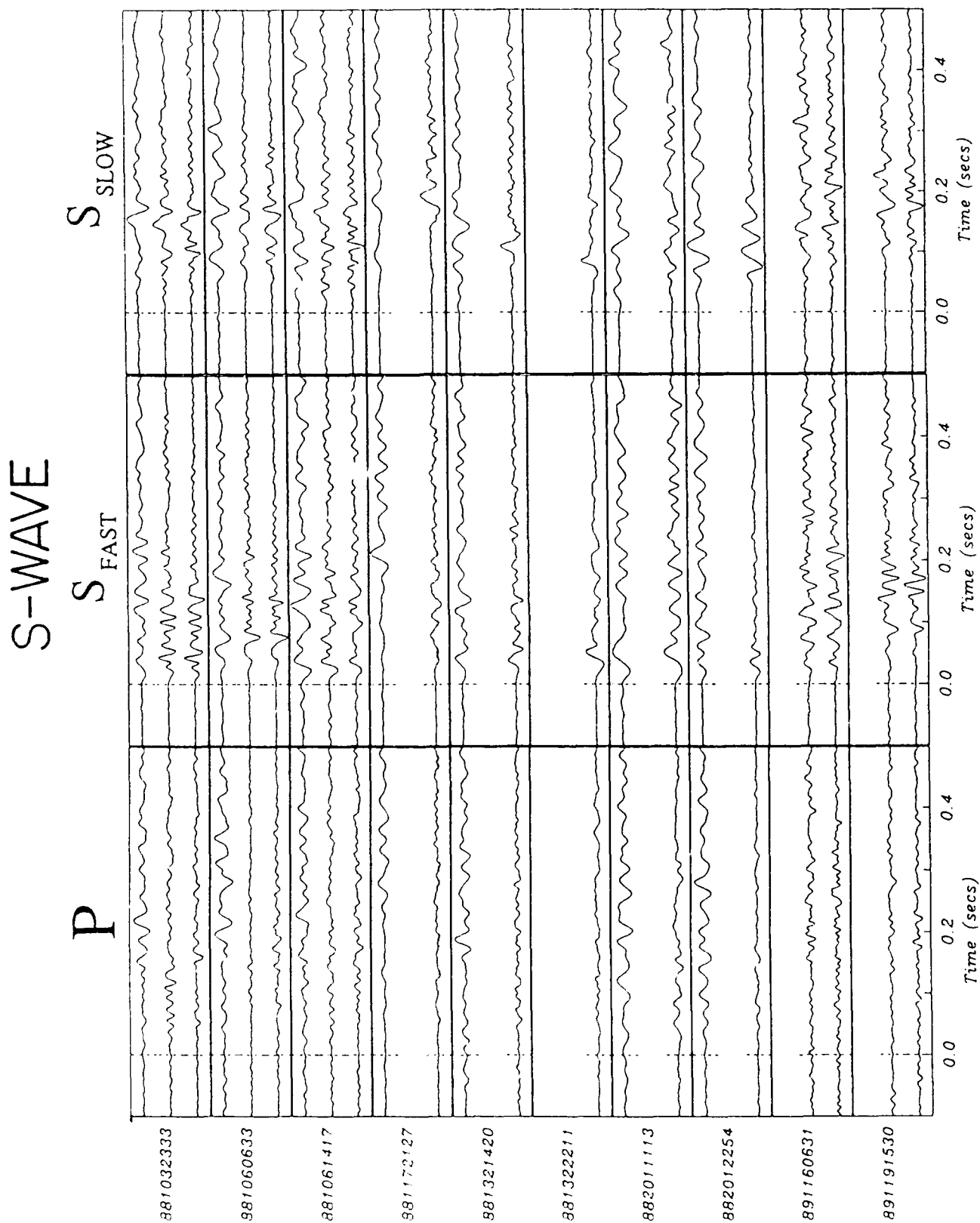


Figure 8(b) continued

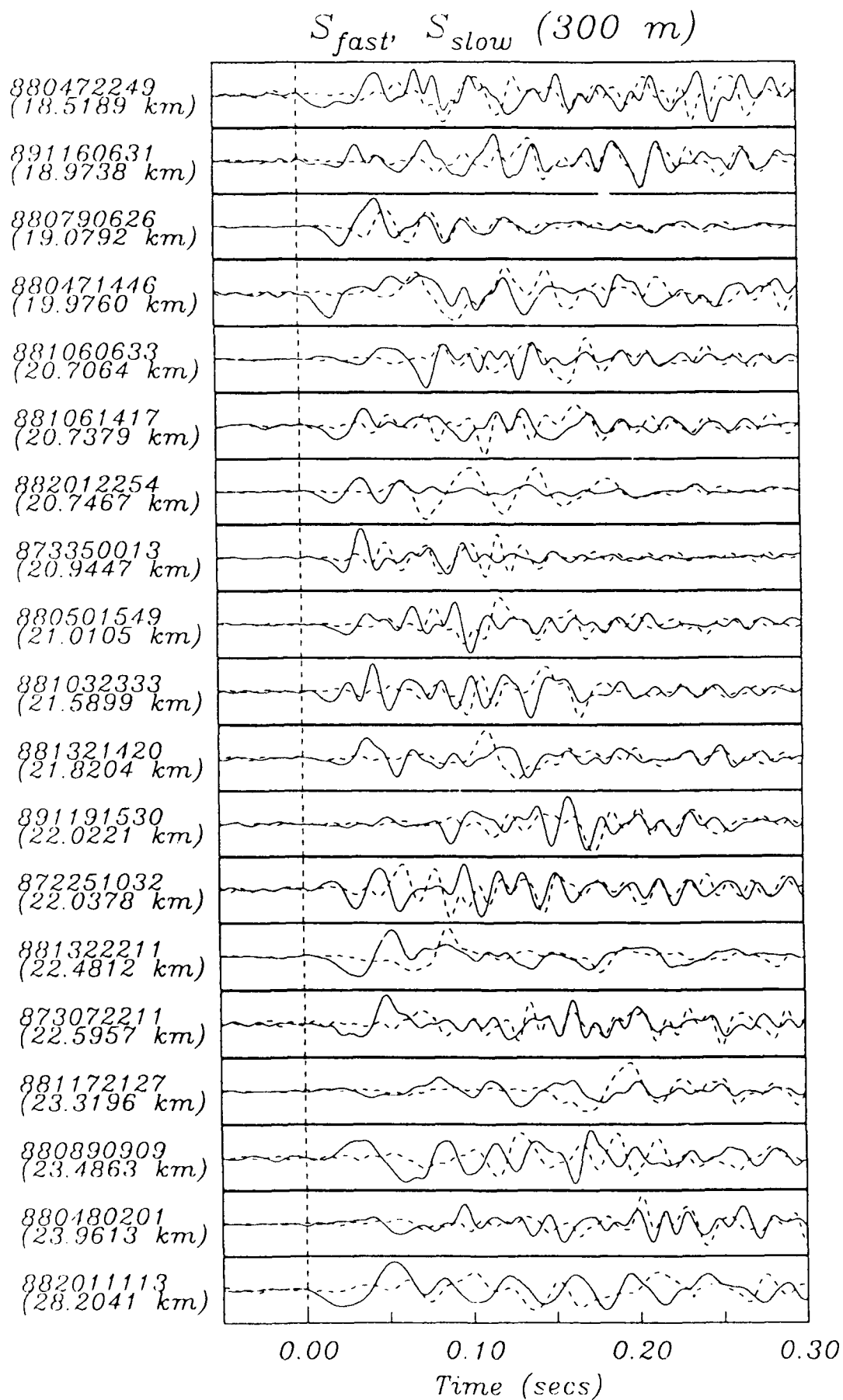


Figure 9

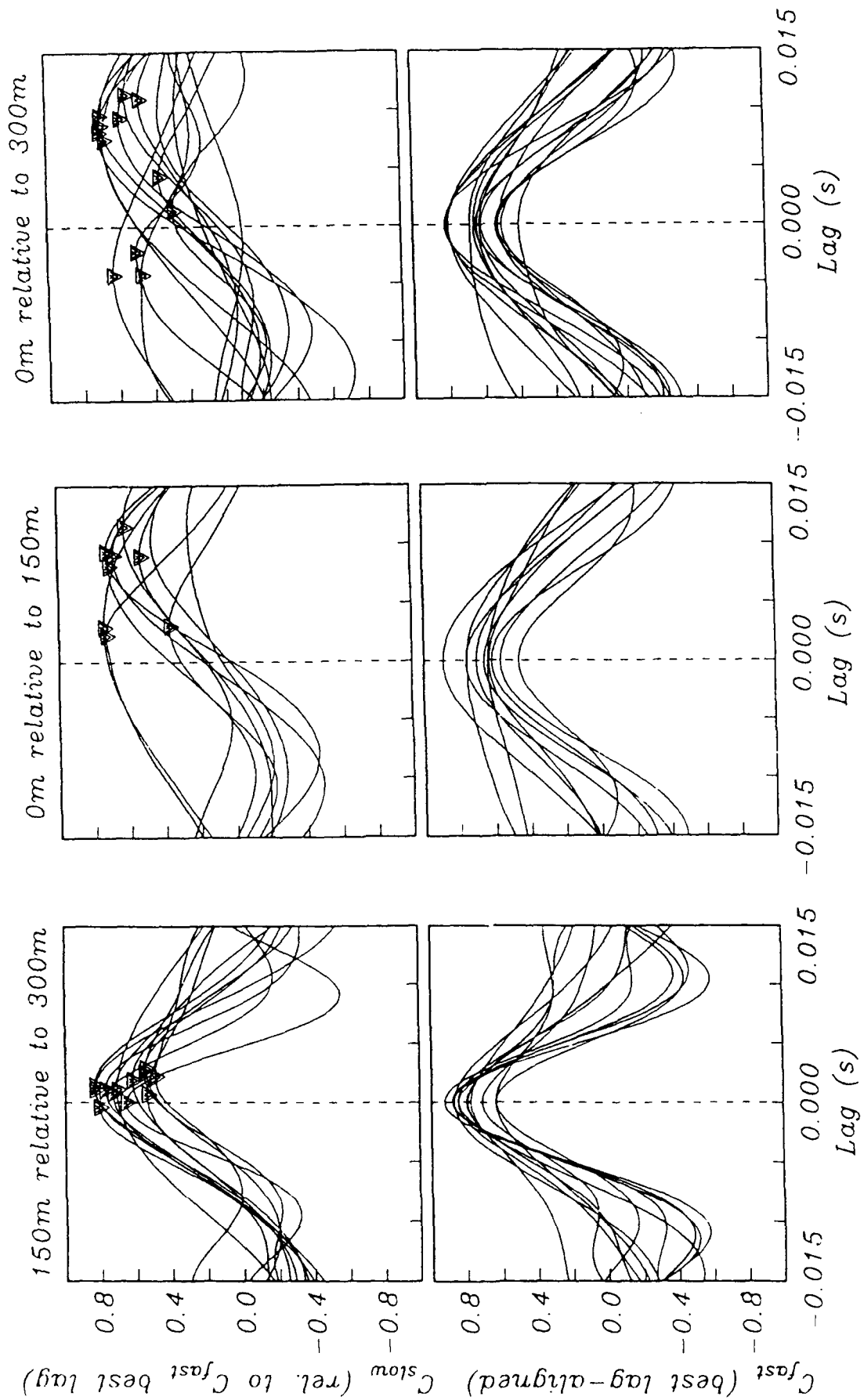


Figure 10

**High-Frequency Borehole Seismograms
Recorded in the
San Jacinto Fault Zone, Southern California**

Part 2: Attenuation and Site Effects

**Richard C. Aster
Peter M. Shearer**

**Institute of Geophysics and Planetary Physics,
University of California, San Diego**

**Submitted to *B.S.S.A.*
September 24, 1990
Revised February 27, 1991**

The U.S. Government is authorized to reproduce and sell this report.
Permission for further reproduction by others must be obtained from
the copyright owner.

Abstract

We examine surface and downhole P- and S-wave spectra from local earthquakes recorded at two borehole seismometer arrays (KNW-BH and PFO-BH) installed in the Southern California Batholith region of the San Jacinto Fault zone by the U.S. Geological Survey to assess the influence of the weathered layer on the spectral content of high-frequency (2-200 Hz) seismic signals.

Earthquake signals recorded downhole at both sites show significantly improved seismic bandwidth due to both a reduction in ambient noise levels and (especially) to dramatically increased levels of high-frequency signal. Significant seismic signal is observed up to approximately 190 Hz for P-waves at KNW-BH. Stacked spectral ratios from these signals indicate that the highly weathered near-surface (between 0 and 150 m) at KNW-BH and PFO-BH exerts a much larger influence on seismic signals than deeper (between 150 and 300 m) material. Modeling of uphole/downhole spectral ratio data suggests $Q_\alpha \approx 6.5$ and $Q_\beta \approx 9$ between 0 and 150 m, increasing to $Q_\alpha \approx 27$ and $Q_\beta \geq 26$ between 150 and 300 m. An outcrop-mounted Anza network station, deployed approximately 0.4 km from KNW-BH, displays roughly similar high-frequency content to the KNW-BH downhole sensors, but exhibits spectra that are significantly colored by directional resonances.

Low- Q and low-velocity near-surface material forms a lossy boundary layer at these borehole sites that is advantageous to the high-frequency downhole environment; not only are noise levels reduced, but reflections from the surface and near-surface are greatly attenuated. As a result, high-frequency recordings from below the weathered zone more nearly resemble those recorded in a whole space than would otherwise be expected.

Introduction

Numerous borehole studies (*e.g.*, Boatwright *et al.*, 1986; Hauksson *et al.*, 1987, Malin *et al.*, 1988; Seale and Archuleta, 1989; Blakeslee and Malin, 1991) indicate that weathered, near-surface material commonly has low velocity and extremely low Q (≈ 10) for both P- and S-waves. Consequently, the shallowest material in the earth exerts a disproportionately large influence on the frequency and phase characteristics of high-frequency seismic signals. Surface seismometer studies indicate that even "hard-rock" sites on apparently unaltered bedrock exhibit resonance and attenuation effects. For example, Cranswick *et al.* (1985) described site effects for seismometers sited on glacially scoured bedrock in New Brunswick, and Frankel and Wennerberg (1989) found that spectra from the Anza network in Southern California display distinct site-specific spectral characteristics, independent of the seismic source region.

Instruments deployed in boreholes that penetrate below the weathered material of the near-surface thus potentially provide a considerably more transparent window through which to observe source processes and deeper path effects that may be masked by a strong near-surface transfer function. A second advantage of borehole stations is their relative isolation from surface noise. Finally, observations in boreholes enable an assessment of local site effects at nearby surface stations, which are far more convenient and economical to deploy.

We analyze microearthquake recordings from two 300 m-deep borehole arrays, KNW-BH and PFO-BH, located near Anza network stations PFO-AZ and KNW-AZ (Berger *et al.*, 1984; Vernon, 1989). These boreholes penetrate the Southern California Batholith (Sharp, 1967) near the San Jacinto Fault zone. For a full description of instrumentation, geological setting, and seismicity, see Aster and

Shearer (this issue) and Carroll et al. (1991). We address the following questions:

- (1) How much is the usable seismic bandwidth improved in these boreholes relative to surface sites?
- (2) What do uphole/downhole spectral ratios indicate about the seismic response of near-surface material to near-vertically traveling P- and S-waves?
- (3) How well can we model observed spectral behavior using an assumption of flat-lying layers?
- (4) How does the seismic response differ between downhole sites and a nearby surface hard-rock site at KNW?

Borehole and Surface Signal and Noise Levels

Borehole instruments generally operate at significantly lower ambient noise levels than surface instruments (*e.g.*, Rodgers *et al.*, 1987; Gurrola *et al.*, 1990). This advantage is partially due to the amplification of low-impedance surface material and the free surface, which affect signal and noise equally, but also arises because of the physical separation of borehole instruments from surface noise sources and from the high attenuation of the near-surface. To assess signal and noise levels for the borehole instrument velocity seismograms, we estimated power spectral densities (PSD's) from 0.5-s (200 sample) time windows preceding and following P- and S-wave arrivals. KNW-BH signal and noise levels at 0 m, 150 m, and 300 m were estimated for 20 events with near-vertical ray paths (P- and S-wave seismograms for these events are shown in Figure 8 of Aster and Shearer, this issue). Due to a lack of nearby events, PFO-BH signal and noise levels were estimated for 25 more distant events in the Anza catalog. As PFO-BH recorded few events on the 150-m instrument and had indistinct S-wave arrivals,

we evaluated only P-wave pre-event and signal noise, and only for the 0-m and 300-m instruments at this station. Signal levels from individual events scale with size and range, the KNW events examined were $M_L = 1.4$ to 2.5 and had (straight-line hypocenter-to-station) ranges from 18.5 to 28.2 km (Figure 9 of Aster *et al.*, this issue). The PFO events were $M_L = 1.4$ to 3.8 and had (straight line hypocenter-to-station) ranges from 15.1 to 79.5 km.

We analyze data in the frequency domain using a coordinate system that facilitates plane-layer modeling of spectral characteristics, (V, S_1, S_2) , where V is the vertical component. At KNW, S_1 is the horizontal projection of the predominant initial S-wave polarization direction from earthquakes with near-vertical ray paths (N40°W; approximately San Jacinto Fault-parallel), observed at nearby Anza network station KNW-AZ by Peacock *et al.* (1988) and at both KNW-AZ and KNW-BH by Aster *et al.* (1990) and Aster and Shearer (this issue). At PFO (which lacks large numbers of events with near-vertical ray paths) the S_1 -direction is arbitrarily taken to be N, close to the predominant initial S-wave polarization direction for Anza stations. In both cases, S_2 is the left-hand perpendicular to V and to S_1 .

Mean and $\pm 1\sigma$ signal levels were estimated by stacking individual component spectra using a 0.5-s (200 sample), cosine-tapered time window beginning 0.125 s before the pick time. Assuming that pre-signal noise levels are statistically stationary, we obtained lower-variance PSD estimates for each event by section averaging (*e.g.*, Welch, 1967; Priestly *et al.*, 1981) across three 50%-overlapping, 0.5-s time windows, thus using a total of 1.0 s of pre-arrival noise. As S-P times for seismograms observed at KNW-BH were all greater than 1.8 s, pre-signal PSD's for S-waves (*i.e.*, the P-wave coda) were estimated using energy beginning well after the P-wave arrival. (V, S_1, S_2) -component PSD's for signal and pre-arrival noise are shown out to the 200 Hz Nyquist frequency for KNW-BH P- and S-waves in

Figures 1a and 1b, respectively, and for PFO-BH P-waves in Figure 1c.

P- and S-wave signal and noise levels at KNW-BH. P-wave pre-event noise levels are generally 10-20 dB lower at the downhole instruments than at the surface. This is 4-14 dB better than could be attributable to free surface amplification alone (see below). Surface noise levels have maxima of about -160 dB (relative to $1 \text{ m}^2/\text{s}^2/\text{Hz}$) near 20 Hz, a peak which is absent downhole. An approximately 6 dB difference in the high-frequency asymptotes of the noise spectra between surface (≈ -180 dB) and downhole (≈ -186 dB) instruments probably reflects differences in digitizer noise; the surface and downhole GEOS gains were set at 48 dB and 54 dB, respectively, thus making a surface digital least count 6 dB more significant than a downhole digital least count. Noise levels at 300 m are only marginally lower (1-2 dB) than at 150 m.

Downhole P-waves at the 150-m and 300-m KNW-BH sensors generally have signal and noise PSD's that asymptotically approach each other near the Nyquist frequency (200 Hz). Apparently there is significant seismic energy from nearby earthquakes above the 100 Hz antialiasing corner frequency at these depths that could be recorded by an even broader-bandwidth system. In contrast, surface-recorded P-waves are relatively deficient in high frequencies and approach background noise levels near 120 Hz. The reduction in useful bandwidth in surface seismograms is exacerbated by higher noise levels, but is mostly due to strong near-surface attenuation. Surface spectra also exhibit more narrow-band structure below about 60 Hz than downhole spectra, a feature suggestive of surface resonances.

Signal-to-noise levels for S-waves at KNW-BH (Figure 1b) are much poorer than for P-waves (Figure 1a). This is partly because of the generally lower corner frequency of the S-wave (e.g., Savage, 1972; Hanks, 1981), but is predominantly

due to the P-wave coda, which is typically about 40 dB above P-wave pre-event noise levels. S-wave signal and P-wave coda PSD's merge at about 120 Hz on the downhole horizontal components and at about 80 Hz at the surface. There is an approximately 6-10 dB preferential partition of P-wave coda energy onto the vertical component at all depths that, along with the nearly horizontal polarization of the shear wave for these events with near-vertical ray paths results in improved S-wave signal-to-noise on the horizontal components. As with P-waves, a clear diminution of high frequencies occurs near the surface, and the 0-m instrument displays narrow-band structure that is suggestive of near-surface resonances.

P-wave signal and noise levels at PFO-BH. 300-m pre-event noise levels at PFO-BH are also appreciably lower than at the surface, although all channels exhibited (easily removable) narrow-band line noise at multiples of 60 Hz (Figure 1c). Surface noise peaks around 20 Hz that is near -150 dB (relative to $1 \text{ m}^2/\text{s}^2/\text{Hz}$), or about 10 dB higher than at the KNW-BH surface site. 300-m noise levels, however, are comparable to those at the KNW-BH downhole instruments. Signals from these more distant events were not as broad-band as those recorded by KNW-AZ due to regional attenuation, a modest increase in usable bandwidth at high frequencies is nevertheless still observed downhole, extending the unity signal-to-noise frequency from about 100 Hz up to near 125 Hz.

The Seismic Response of the Near-Surface

It is clear from Figure 1 that most modification to the seismic signal occurs in the uppermost 150 m at both sites. These changes reflect heterogeneity (including topography) and viscoelasticity that manifest themselves in amplification, resonance, scattering and attenuation. Shearer and Orcutt (1987) provide a more comprehensive summary of plane-wave effects, which we only briefly review here.

The free surface. The zero-traction boundary condition at a free surface introduces an amplification of 6 dB for vertically incident P- and S-waves for instruments deployed within a small fraction of a wavelength of the surface. The general response is a special case of reflection (see below).

Impedance contrast. Energy conservation dictates that amplitudes for completely transmitted waves will vary inversely as the square root of the ratio of the seismic impedances between two dissimilar media.

Reflection and transmission. Velocity variations which introduce a scale length to the model result in frequency-dependent response spectra. In the simplest case, a vertically traveling P- or S_H -wave in a lossless medium reflecting from an interface above a borehole receiver, the response spectrum is the sum of two delta-function spectra with differing phases, resulting in a frequency-periodic interference pattern. Multiple interfaces produce a plethora of resonance and (for non-vertical incidence) phase conversion effects in the response spectrum.

Attenuation. For seismic body waves propagating in a non-dispersive, linear, and homogeneous medium, the energy in a harmonic plane wave at some spatial position, x , is characterized by simple exponential decay, where the exponent is proportional to frequency and x , and is inversely proportional to the quality factor, $Q(f)$. A frequency-independent, finite Q , (the case for models considered in this paper), thus results in a relative loss of energy at higher frequencies. In addition, attenuation produces resonance damping, which results in a "smoother" response function. In this paper we generalize seismic Q to include apparent energy losses due to pulse broadening from scattering (e.g., Dainty, 1981; Richards and Menke, 1983; Frankel and Clayton, 1986).

Uphole versus downhole spectral ratios at KNW-BH. Mean P- and S-wave stacked spectral ratios (0-to-300 m, 0-to-150 m, and 150-to-300 m) with 1σ error

bars estimated using 0.5-s KNW-BH signal spectra (Figure 1) are shown in Figure 2. We also estimated these ratios for window lengths of 1.0 s and 0.25 s to verify that the gross features were not strongly dependent on the window size. The stacked spectral ratios display clearer structure, particularly below 40 Hz, than the stacked signal levels (Figure 1), suggesting that the crude deconvolution obtained by taking spectral ratios was reasonably successful in reducing variability due to source differences.

The stacked spectral ratios of Figure 2 clearly indicate the confinement of gross attenuation and low-frequency amplification at KNW-BH to the uppermost 150 m. 0-to-150 m and 0-to-300 m ratios are quite similar, and display a dramatic high-frequency decay. As all sensors are separated by only a fraction of a kilometer, near-surface attenuation must be very high to account for this energy loss. 150-to-300 m ratios, in contrast, are relatively flat, although some high-frequency roll-off is apparent in the V and S_2 components. The relative flatness of the 150-to-300 m ratios is also reflected in the time domain by similar waveforms for 150-m and 300-m seismograms from the same events (Figure 8 of Aster and Shearer, this issue; Figure 7 of this paper).

Interestingly, there appears to be evidence for preferential attenuation of the S_2 (slow horizontal) component relative to the S_1 (fast horizontal) component in 150-to-300 m spectral ratios, but not in ratios involving the surface instrument. This is suggestive of anisotropic shear-wave attenuation between 150 and 300 m, which is below the obviously weathered layer (Fletcher *et al.*, 1990). This effect could partially account for the clear fast quasi-shear waves and the general lack of distinct slow quasi-shear waves, even at 300 m, noted by Aster and Shearer (this issue) and Aster and Shearer (1990).

Fletcher *et al.* (1990) estimated layered P- and S-wave velocity models from logging at the KNW and PFO boreholes using P- and S-wave surface sources (Table 1). We note that although these velocity models fit the P- and S-wave velocity logging data to within experimental error, they have interfaces at different depths, resulting in widely varying values of V_P/V_S which are unlikely to closely reflect the true structure.

Because of the tradeoff between model layer thicknesses and Q values, we only estimated the mean Q between sensors. Thus, all Q models in this paper consist of two constant- Q layers over a lossless half-space, with the interfaces fixed at 150 m and 300 m. To obtain initial estimates of the average Q between sensors for P-waves and for S_1 - and S_2 -polarized S-waves, we first fitted maximum likelihood slopes (*e.g.*, Press *et al.*, 1986) to the high-frequency portion (from 20 Hz up to the approximate frequency where the signal-to-noise approaches unity; Figure 1) of the stacked spectral ratio data (Figure 2). The spectral ratio bounds were taken as approximate 1σ Gaussian-distributed errors superimposed on a linear trend. A χ^2 -based measure of goodness-of-fit indicated that linear fits with these error bounds were highly acceptable (>99%) in all cases. This estimation procedure carries the assumption (which we shall justify later in this paper) that downward-reflected energy is weak at high frequencies. In this case, high-frequency spectral ratios can be modeled to first order by simple exponential decay. Q values can then be estimated as:

$$Q = \frac{10}{\ln 10} \cdot \frac{-2\pi T}{dR(f)/df} \quad (1)$$

where $dR(f)/df$ is the estimated power spectral ratio slope (dB/Hz), f is frequency (Hz), and T is the one-way travel time between the sensors (s) calculated from the velocity model given in Table 1.

Using the 0-to-150 m and 150-to-300 m high-frequency spectral slope Q estimates as starting models, we further refined our Q estimates by inverting for best-fit 2-layer Q models, minimizing the L_1 -norm error (in dB) between synthetic and observed spectral ratios over the entire usable frequency range. The contribution to the total error at each frequency was weighted by the inverse standard deviation of the corresponding data point. The minimum-error model was found using Powell's method, as implemented by Press *et al.* (1986). Synthetic plane-wave spectral ratios for the forward problem were calculated using generalized reflection/transmission modeling. This approach is numerically stable and solves for the complete (P, S_V) and S_H plane-wave impulse response. More complete discussions of the technique and its application are found in Kennett (1974, 1983) and in Shearer and Orcutt (1987). The P- and S-wave velocity models (Table 1) were kept fixed during the inversion. Ray parameters were chosen to be consistent with the mean initial P-wave emergence angle at 300 m of 20.4° , although results were not distinctly different when a ray parameter of zero (vertical incidence) was used. Estimated Q values from spectral slope fitting and from the two-layer inversion are shown in Table 2.

P-wave synthetic spectral ratios, using the Q inversion results of Table 2, are shown along with 1σ error bounds from the stacked spectral ratios in Figure 3a. The remarkably low Q_α model ($Q_\alpha = 6.5$ between 0 and 150 m, $Q_\alpha = 26.6$ between 150 and 300 m) fits the observed high-frequency trends well, although a large surface resonance near 30 Hz remains poorly modeled.

S-wave spectral ratio data are more difficult to fit consistently (Figures 3a and 3b). High-frequency spectral slopes suggest a dramatic difference in Q_β between 150 and 300 m for S_1 and S_2 polarizations, with the S_1 ratio showing essentially no attenuation and the S_2 ratio showing significant decay corresponding to a Q_β of

about 26. The 0-to-150 m S-wave ratios, on the other hand, suggest a reversal of this Q_β discrepancy, with the S_2 component showing somewhat less apparent attenuation than the S_1 component ($Q_\beta = 9.8$ and 7.8 , respectively). The net result is that the 0-to-300 m spectral ratios (and implied intersensor attenuation, see below) are similar for the two S-wave polarizations. As a 90° rotation with depth in any azimuthal Q_β anisotropy seems unlikely, the possibility of variable coupling in the horizontal sensors cannot be ruled out, especially as the horizontal seismometers at 150 m and 300 m are both deployed within 20° of a (S_1, S_2) coordinate system (Table 3 of Aster and Shearer, this issue). Such coupling differences can theoretically be eliminated using reversed spectral ratios (e.g., Smith, 1989). We note that our estimated low near-surface Q_β values are consistent with those estimated from borehole logging by Fletcher *et al.* (1990) and Carroll *et al.* (1991), who suggested an average Q_β of about 8 for the upper 50 m using pulse rise times and spectral ratios, respectively.

To examine the time-domain predictions of the near-surface model, we calculated synthetic impulse responses at borehole instrument depths for vertically incident plane waves (Figure 4). These calculations confirm that reflected phases, even for the plane layer models considered here, are highly attenuated by the lossy surface layer and contribute very little high-frequency energy to the signal, thus justifying the use of high-frequency spectral ratios in obtaining approximate intersensor Q values and providing a plausible explanation for the lack of clear surface reflections in downhole seismograms noted by Aster and Shearer (this issue).

Comparison of Borehole Spectra with Surface Spectra from Anza Station KNW

The KNW-BH borehole surface instrument is sited on a clearly decomposed bench, with grus weathered out of the Southern California batholith covering the surface. We are fortunate to have a comparative surface site in Anza network station KNW-AZ (Berger *et al.*, 1984; Vernon, 1989) located 391 m N148°E of KNW-BH. The surface environment at KNW-AZ differs significantly from that of KNW-BH in that the seismometer vault is bolted to a visibly unaltered outcrop. KNW-AZ recorded 17 of the 20 nearby events recorded by KNW-BH and examined above. Figures 5a and 5b show signal and noise power spectral density estimates for these earthquakes up to the 125 Hz Nyquist frequency, in the same format as Figure 1. Pre-event noise levels at KNW-AZ are comparable to those observed at KNW-BH (0 m), but this is potentially misleading, as the gain was probably not high enough during this period to adequately register ground noise (F. Vernon, personal communication). P- and S-wave signal spectra at KNW-AZ have remarkable high-frequency content for an Anza network surface site, as noted in previous studies of Anza network spectra (*e.g.*, Anderson and Hough, 1984; Fletcher *et al.*, 1986, 1987; Frankel and Wennerberg, 1989). Figure 5 also reveals a strongly directional resonance centered near 60 Hz and concentrated on the V and S_2 components. The breadth of this resonance and the fact that it is not seen in the pre-event (electronic) noise spectra indicate that it arises from seismic excitation rather than from instrument noise. Swapping the horizontal components (which are deployed within 5° of a $[S_1, S_2]$ coordinate system) showed no tendency for the resonance to migrate between channels and an examination of the site showed no obvious local structures which could oscillate near 60 Hz. Although the rectangular vault has its long axis oriented approximately in the S_1 direction,

identical Anza vaults deployed at other stations exhibit no comparable resonances. We conclude that this effect is a near-site directional resonance (*e.g.*, Bonamassa *et al.*, 1991). Figure 6 shows stacked spectral ratios between KNW-AZ and KNW-BH recordings, adjusted for the differing sampling rates and antialiasing systems between the two instruments. Note that, although spectra of nearby earthquakes at KNW-AZ show far more high-frequency energy than the KNW-BH surface instrument, the KNW-AZ spectrum is highly colored, especially by the resonance noted above. A P-wave seismogram comparison for an earthquake recorded at KNW-AZ and at all three depths at KNW-BH, in which both surface and directional site resonance effects are visible is shown in Figure 7.

Discussion

The picture that emerges for the KNW-BH vertical array is one of remarkably low and comparable Q_α and Q_β in the upper 150 m. This is in stark contrast to the relatively efficient high-frequency propagation observed between the 300-m and 150-m instruments and indicates that the 150-m instrument is sufficiently deep to avoid most of the waveform modification occurring near the surface. Hough *et al.* (1988) and Hough and Anderson (1988) determined average ray path Q values at Anza by examining the high-frequency spectral decay slope of earthquake seismograms as a function of distance. They estimated Q_α and Q_β , averaged over the upper 5 km, to be greater than several hundred. A similar result was obtained by Fletcher *et al.* (1986), using earthquake signal spectral ratios from pairs of stations in the Anza network. These results indicate that our Q estimates of about 26 for material between 300 and 150 m (where borehole cuttings indicated that the rock was not visibly altered) are significantly lower than Q for the bulk of the batholith (with the notable exception of Q_β for the S_1 component). This is perhaps due to a

greater number of open cracks and/or inhomogeneities between 300 and 150 m than at greater depth.

The percentage of attenuation for a nearby earthquake signal which takes place in the uppermost 300 m at KNW-BH can be estimated by comparing observed t^* values in the borehole with those estimated for a complete ray path, where

$$t^* = \int_{path} \frac{dr}{v(r)Q(r)} . \quad (2)$$

We find that, for probable sub-borehole Q_α and Q_β values of greater than a few hundred, more than 50% of all attenuation for surface signals recorded at KNW-BH (as parameterized by t^*) occurs in the uppermost 300 m (Figure 8). We also note that the t^* values for the 0-to-300 m interval are remarkably similar for P- and S-waves, all being close to 0.01 s.

Surface seismograms at KNW-BH, besides exhibiting high attenuation, demonstrate clear evidence of strong scattering in the near-surface from lateral inhomogeneities. This phenomenon is apparent in wave polarized energy following the S-wave arrival and in horizontally polarized energy following the P-wave arrival (Figure 8b of Aster and Shearer, this issue; Figure 7 of this paper). This suggests that the observed near-equality of shallow Q_α and Q_β is due to a scattering-dominated mechanism (*e.g.*, Richards and Menke, 1983; Blakeslee and Malin, 1991) rather than to intrinsic shear losses alone, which would predict $Q_\alpha > Q_\beta$ (*e.g.*, Anderson *et al.*, 1965). Determination of a specific attenuation mechanism, however, remains problematic; most scattering models predict $Q_\beta \geq Q_\alpha$, but the relative size of Q_α and Q_β can vary with proposed intrinsic mechanisms (*e.g.*, see Hough and Anderson, 1988).

Aster and Shearer (this issue) and Aster *et al.* (1990) note that slow quasi-shear waves are not generally visible following the S-wave arrival at KNW-AZ or KNW-BH, despite strong initial S-wave particle motion alignments which probably indicate the horizontal projection of the fast anisotropic shear wave direction. This is true even for signals recorded at 300 m which is well below the weathered layer (Figure 9 of Aster and Shearer, this issue). One possibility is that the slow quasi-shear phase is obscured by deep scattering, but these data also suggest that anisotropic attenuation could play a part in obscuring shear waves polarized perpendicular to the S_{fast} direction, although horizontal seismometer coupling differences provide an alternative explanation.

Simple plane-layer models are successful in matching high-frequency behavior and approximate low-frequency amplification seen in the borehole spectral ratios at KNW-BH, but some significant low-frequency resonance peaks are not successfully modeled. A laterally homogeneous velocity model may indeed exist which is consistent with both the travel-time and the stacked spectral ratio at all frequencies. Alternatively, lateral heterogeneity, including topography, may be required to fit the data to within the error bounds. In this case, velocity horizons encountered in a single borehole will not necessarily be those best included in a minimum-error laterally homogeneous model and an array of boreholes, perhaps allied with a surface array, might be needed to obtain a suitable model.

Interestingly, intersensor Q values determined by high frequency slope fitting are generally lower than those obtained by fitting the entire usable spectral band in an iterative inversion (Table 2). Although suggestive of frequency-dependent Q , this is predominantly due to the inversion scheme fitting low-frequency resonances in the data by increasing Q at the expense of the high-frequency fit.

These borehole sites offer a significant advantage in usable bandwidth relative to surface sites. The desirable qualities of decreased ambient noise levels, increased usable signal at high frequencies, and lack of strong interference from surface reflections all arise from siting beneath a very low- Q surface layer. Low- Q , low-velocity near-surface material at KNW is actually advantageous to the borehole instrument environment because it acts as a lossy boundary layer to alleviate both noise and reflections from the surface. As a result, the downhole seismic response at high frequencies more closely resembles that of a whole-space than would otherwise be expected.

Conclusions

Summarizing our results in terms of the questions of the introduction, we find:

- (1) Downhole recording in the Southern California Batholith offers a considerable improvement in usable seismic bandwidth relative to nearby surface sites. Downhole noise is reduced not only by physically separating the sensors from the surface, but also by attenuation from very low- Q , low-velocity near-surface material (see below). Surface velocity power noise at the borehole sites peaks near 20 Hz, and is ≈ 20 dB higher at PFO-BH than KNW-BH. Downhole noise levels display no strong peaks and are similar at the KNW-BH 150 m, KNW-BH 300-m, and PFO-BH 300-m sites, with a maximum velocity power spectral density of approximately -180 dB relative to $1 \text{ m}^2/\text{s}^2/\text{Hz}$. P-wave signals at KNW-BH from $M_L \approx 2$ earthquakes with near-vertical ray paths have approximately 70 Hz more (up to 190 Hz) usable bandwidth at 150 m and 300 m than at the surface. Shear wave signals from these events have considerably poorer signal-to-noise levels and usable bandwidth due to interference from the P-wave coda. Nevertheless, S-wave

signal-to-noise levels also improved downhole due to both increased signal bandwidth and reduced P-wave coda levels; the maximum usable S-wave frequency on the horizontal components at KNW-BH increased from approximately 80 to 120 Hz. Downhole P-wave earthquake signals at PFO-BH (from more distant earthquakes than those examined at KNW-BH) also display a modest increase in the highest usable frequency over surface recordings, from approximately 100 Hz to 125 Hz.

- (2) Uphole/downhole spectral ratios indicate that the KNW-BH surface instrument suffers from extreme near-surface attenuation. Average Q_α values in the upper and lower 150 m of the borehole are estimated by a two-layer Q inversion to be approximately 6.5 and 27, respectively. Estimates of average Q_β are approximately 8-10 in the upper 150 m, and ≥ 26 in the lower 150 m, with some suggestion of preferential attenuation of the slow (S_2) S-wave component, although this discrepancy could conceivably be due to uncorrected coupling differences in the horizontal seismometers. Low- Q and low-velocity near-surface material, besides shielding the downhole instruments from surface-generated noise, also attenuates reflections from the free surface and from the near-surface velocity gradient. The seismic response at depth is thus more nearly that of a whole-space than would otherwise be expected. t^* values for the entire 300 m sampled by the borehole are similar (≈ 0.01 s) for P- and S-waves.
- (3) Forward modeling using a layered half-space velocity model derived from borehole logging and average intersensor Q values obtained from stacked spectral ratios is reasonably successful in fitting low and high-frequency spectral ratio data, but leaves some low-frequency structure unmodeled. It remains an open question as to whether significantly better modeling of the

spectral ratio data requires the introduction of a 3-dimensional structure or merely further adjustment of flat-layer model parameters.

- (4) The hard-rock Anza surface station KNW-AZ displays gross frequency content comparable to that seen by the 150 m and 300 m KNW-BH instruments, indicating that much of the very high attenuation associated with surface sites such as KNW-BH (0 m) can be avoided by siting on outcrops. The seismic response at KNW-AZ is, however, significantly colored by strong resonances that are not observed downhole at KNW-BH. The largest resonance is clearly directional, and results in significantly more high-frequency energy being recorded on the vertical and S_2 components than on the S_1 component.

References

- Anderson, D.L., A. Ben-Menahem, and C.B. Archambeau (1965). Attenuation of seismic energy in the upper mantle, *J. Geophys. Res.*, **70**, 1441-1445.
- Aster, R.C. and P.M. Shearer (1990). High-frequency borehole seismograms recorded in the San Jacinto fault zone, Southern California. Part 1: Polarizations, *Bull. Seism. Soc. Am.*, this issue.
- Aster, R.C., P.M. Shearer, and J. Berger (1990). Quantitative measurements of shear-wave polarizations at the Anza seismic network, southern California — implications for shear-wave splitting and earthquake prediction, *J. Geophys. Res.*, **95**, 12449-12474.
- Berger, J., L.N. Baker, J.N. Brune, J.B. Fletcher, T.C. Hanks, and F.L. Vernon (1984). The Anza array: a high-dynamic-range, broadband, digitally radiotelemetered seismic array, *Bull. Seism. Soc. Am.*, **74**, 1469-1481.
- Blakeslee, S. and P. Malin (1991). Near surface attenuation and amplification: Site-effect determination from two borehole stations at Parkfield, California, *Bull. Seism. Soc. Am.*, submitted.
- Blenkinsop, T., 1990. Correlation of paleotectonic fracture and microfracture orientations in cores with seismic anisotropy at Cajon Pass drill hole, southern California, *J. Geophys. Res.*, **95**, 11143-11150.
- Boatwright, J., R. Porcella, T. Fumal, and H.-P. Lui (1986). Direct estimates of shear wave amplification and attenuation from a borehole near Coalinga, California, *Earthquake Notes*, **57**, 8.
- Bonamassa, O., J. Vidale, and S. Schwartz (1991). Directional site resonances observed from aftershocks of the 18 October, 1989 Loma Prieta Earthquake, *Bull. Seism. Soc. Am.*, submitted.
- Carroll, L., J. Fletcher, H. Liu, and R. Porcella (1991). Implications of site response on determination of f_{\max} : results from a borehole experiment at Anza, CA, *Bull. Seism. Soc. Am.*, submitted.
- Cranswick, E., R. Wetmiller, and J. Boatwright (1985). High-frequency observations and source parameters of microearthquakes recorded at hard-rock sites, *Bull. Seism. Soc. Am.*, **75**, 1535-1567.
- Dainty, A. (1981). A scattering model to explain seismic Q observations in the lithosphere between 1 and 30 Hz, *Geophys. Res. Lett.*, **8**, 1126-1128.
- Fletcher, J., L. Haar, F.L. Vernon, J.N. Brune, T. Hanks, and J. Berger (1986). The effects of attenuation on the scaling of source parameters for earthquakes at Anza, California, *Earthquake Source Mechanics, AGU geophysical monograph 37 (Maurice Ewing 6)*, 331-338.
- Fletcher, J., L. Haar, T. Hanks, L. Baker, F.L. Vernon, J. Berger, and J.N. Brune (1987). The digital array at Anza, California: processing and initial interpretation of source parameters, *J. Geophys. Res.*, **92**, 369-382.
- Fletcher, J., T. Fumal, H. Liu, and R. Porcella (1990). Near-surface velocities and attenuation at two boreholes near Anza, CA from logging data. *Bull. Seis. Soc. Am.*, **80**, 807-831.
- Frankel, A., and R. Clayton (1986). Finite difference simulations of seismic scattering: Implications for the propagation of short-period seismic waves and models of crustal heterogeneity., *J. Geophys. Res.*, **91**, 6465-6489.
- Frankel, A., and L. Wennerberg (1989). Microearthquake spectra from the Anza network., *Bull. Seis. Soc. Am.*, **79**, 581-609.
- Gurrola, H., J.B. Minster, H. Given, F. Vernon, J. Berger, and R. Aster (1990). Analysis of high frequency seismic noise in the western U.S. and eastern Kazakhstan, *Bull. Seis. Soc. Am.*, **80**, 951-970.
- Hanks, T. (1981). The corner frequency shift, earthquake source models, and Q ,

- Bull. Seis. Soc. Am.*, **71**, 597-612.
- Hauksson, E., T. Ta-liang, and T. Henyey (1987). Results from a 1500 m deep, three-level downhole seismometer array: Site response, low Q values and f_{\max} , *Bull. Seis. Soc. Am.*, **77**, 1883-1903.
- Hough, S., J. Anderson, J.N. Brune, F.L. Vernon, J. Berger, J. Fletcher, L. Haar, T. Hanks, and L. Baker (1988). Attenuation near Anza, California, *Bull. Seis. Soc. Am.*, **78**, 676-691.
- Hough, S., and J. Anderson (1988). High frequency spectra observed at Anza, California: Implications for Q structure. *Bull. Seis. Soc. Am.*, **78**, 692-707.
- Kennett, B. (1974). Reflections, rays and reverberations, *Bull. Seism. Soc. Am.*, **64**, 1685-1696.
- Kennett, B. (1983). *Seismic wave Propagation in Stratified Media*, Cambridge University Press, New York.
- Malin, P., J.A. Waller, R.D. Borchardt, E. Cranswick, E.G. Jensen, and J. Van Schaack (1988). Vertical seismic profiling of Oroville microearthquakes: Velocity spectra and particle motion as a function of depth. *Bull. Seism. Soc. Am.*, **78**, 401-420.
- Peacock, S., S. Crampin, D.C. Booth, and J. Fletcher (1988). Shear wave splitting in the Anza seismic gap, Southern California: temporal variations as possible precursors, *J. Geophys. Res.*, **93**, 3339-3356.
- Press, W., B. Flannery, S. Teukolsky, and W. Vetterling (1986). *Numerical Recipes*, Cambridge University Press, Cambridge.
- Priestley, M.B. (1981). *Spectral Analysis and Time Series*, Academic Press Inc., London.
- Richards, P., and W. Menke (1983). The apparent attenuation of a scattering medium, *Bull. Seism. Soc. Am.*, **73**, 1005-1021.
- Rodgers, P., S. Taylor, and K. Nakanishi (1987). System and site noise in the Regional Seismic Test Network from 0.1 to 20 Hz, medium, *Bull. Seism. Soc. Am.*, **77**, 663-678.
- Savage, J.C. (1972). Relation of corner frequency to fault dimensions, *J. Geophys. Res.*, **27**, 3788-3795.
- Seale, S., and R. Archuleta (1989). Site amplification and attenuation of strong ground motion, *Bull. Seism. Soc. Am.*, **79**, 1673-1696.
- Sharp, R. (1967). San Jacinto fault zone in the Peninsular Ranges of southern California, *Bull. Geol. Soc. Am.*, **78**, 705-730.
- Shearer, P., and J. Orcutt (1987). Surface and near-surface effects on seismic waves — theory and borehole seismometer results, *Bull. Seism. Soc. Am.*, **77**, 1168-1196.
- Smith, A.T. (1989). Estimating high-frequency crustal attenuation in eastern Kazakhstan, USSR, using reversed spectral ratios of P_g and P_n . LLNL UCRL-99549 (preprint).
- Vernon, F.L. (1989). *Analysis of Data Recorded on the Anza Seismic Network*, Ph.D. thesis, Scripps Instit. Oceanogr., Univ. of Calif., San Diego, La Jolla.
- Welch, P. (1967). The use of the fast Fourier transform for the estimation of power spectra: A method based on time averaging over short, modified periodograms, *IEEE Trans. on Audio and Electroacoust.*, **Au-15**, No. 2., 70-73.

Table and Figure Captions

Table 1. P-wave (a) and S-wave (b) velocity structure estimated for KNW-BH from seismic logging (after Fletcher *et al.*, 1990).

Table 2. Q estimated from high-frequency spectral slope fitting and two-layer inversion of the data shown in Figure 2. f_{\min} and f_{\max} indicate the range of frequency fitting for each determination.

Fig. 1. Power spectral density (PSD) estimates of signal and pre-arrival noise (dB relative to $1 \text{ m}^2/\text{s}^2/\text{Hz}$) for P-waves (a) and S-waves (b) recorded at KNW-BH, and for P-waves recorded at PFO-BH (c). Solid traces indicate mean and $\pm 1\sigma$ bounds for signal PSD obtained from stacking individual estimates from cosine-tapered, 0.5-s (200 sample) time windows. Signals were windowed beginning 0.125 s (50 samples) before the phase pick so the taper would not grossly affect the first arrival. Stacked pre-arrival noise PSD's with $\pm 1\sigma$ bounds are indicated by dashed curves, where an estimate for each event was obtained from section averaging three 0.5-s, cosine-tapered, 50% overlap windows. N is the number of events used in each spectral stack. Note the reduced pre-event noise levels, increased high-frequency signal, and consequent increase in usable seismic bandwidth at the downhole instruments for both sites. Narrow-band noise peaks at PFO-BH are due to electronic noise. The PFO-BH 150-m instrument did not record a sufficient number of records for meaningful PSD stacking. Reduction of signal and noise above 100 Hz is dominated by the 7-pole antialiasing filter. The Nyquist frequency is 200 Hz.

Fig. 2. Stacked power spectral density ratios for P-waves (vertical component) and S-waves (S_1 and S_2 components) at KNW-BH. Note the extreme high-frequency

spectral decay between surface and downhole seismograms due to low near-surface Q .

Fig. 3. Predicted power spectral density ratios at KNW-BH (solid curve), obtained from the velocity model of Table 1 and the two-layer inversion Q model of Table 2, for P-waves, vertical-component (a), and for S-waves, S_1 component (b) and S_2 component (c). $\pm 1\sigma$ envelopes from the observed spectral ratios (Figure 2) are indicated by dashed curves.

Fig. 4. Synthetic impulse response functions for KNW-BH, shown in both the frequency and time domain, for vertically incident P-waves (a) and S-waves (S_1 component [b] and S_2 component [c]), using the layered velocity models of Table 1 and the two-layer inversion Q results of this paper (Table 2). Note the high attenuation of reflected energy from shallow layers and from the free-surface.

Fig. 5. Signal and noise power spectral densities (dB relative to $1 \text{ m}^2/\text{s}^2/\text{Hz}$) for P-waves (a) and S-waves (b) recorded by Anza network station KNW-AZ, displayed in the same format as the borehole spectra of Figure 1. Note the strongly directional resonance near 60 Hz, primarily visible on the V and S_2 components. Reduction of signal and noise above 62.5 Hz is dominated by the 6-pole antialiasing filter. The Nyquist frequency is 125 Hz.

Fig. 6. Stacked power spectral density ratios for P-waves (vertical component) and S-waves (S_1 and S_2 components) between Anza network station KNW-AZ and the three depths recorded at KNW-BH, displayed as in Figure 2. Note that although the outcrop-mounted KNW-AZ instrument displays much better high-frequency content than the 0-m KNW-BH instrument, the response is also significantly colored relative to the KNW-BH downhole sites, especially by a strongly direc-

tional resonance near 60 Hz (Figure 5). A broadband offset of approximately +6 dB in the Anza/downhole ratios is due to free-surface amplification. KNW-AZ spectra were resampled at 400 hz and adjusted to KNW-BH response prior to taking spectral ratios.

Fig. 7. Three-component P-wave seismograms (1 s) from an earthquake ($M_L = 1.9$) recorded by both the Anza network station KNW-AZ and by the borehole array KNW-BH at 9:09 UT, 29 March, 1988. The hypocenter was approximately 23.5 km below and 2 km N195°E of KNW-BH. The schematic section (strike of N212°E from left to right) shows the relative sensor locations. Frequency-domain features discussed in the text are visible in these seismograms, specifically: (1) High attenuation between downhole and surface signals at KNW-BH. (2) Lack of strong attenuation or scattering between 150 m and 300 m at KNW-BH. (3) Preferential partition of P-wave coda at KNW-BH onto the vertical component, especially in the downhole recordings. (4) Lack of obvious surface reflections in the downhole recordings (two-way travel times for P-wave surface reflections are about 0.122 s and 0.178 s at 150 m and 300 m, respectively). (5) Relatively robust high-frequency content of seismograms recorded at the outcrop-mounted KNW-AZ site compared to seismograms recorded at KNW-BH (0 m). (6) High-frequency directional resonance at KNW-AZ, predominantly visible on the V and S_2 components.

Fig. 8. Percentage attenuation (as measured by t^* ; equation 2) occurring in the shallowest 300 m at KNW-BH relative to attenuation along a complete 20 km ray path (the approximate range to the closest earthquakes recorded by this station). Attenuation is parameterized in the borehole segment by $t^* = 10$ ms, and in the batholith segment by a variable frequency-independent Q . Note that for probable

batholith Q values of greater than several hundred, the majority of attenuation occurs in the uppermost 300 m. Vertical-incidence t^* values for the shallowest 300 m, computed from the velocity models of Table 1 and from the two-layer inversion Q estimates of Table 2, are $t_P^* = 10.5$ ms, $t_{S_1}^* = 10.9$ ms, and $t_{S_2}^* = 10.7$ ms.

Acknowledgments

We especially thank J. Fletcher, who generously provided borehole data and system information. Borehole sites were maintained by L. Carroll, J. Batti, J. Babcock and J. Scott. F. Vernon assisted in the data processing. D. Betts assisted in preparing the figures. The authors thank A. Frankel and J. Vidale for helpful reviews. Funding was provided by Institute of Geophysics and Planetary Physics, Lawrence Livermore National Laboratory grants 89-14 and GS90-45, by U. S. Geological Survey grant 14-08-0001-G1767, and by AFGL contract F19628-88-K-0044.

(a)

KNW P Velocity Structure			
V_P (m/s)	ρ (g/cc)	h (m)	z_{bottom} (m)
300	1.50	5.0	5.0
900	2.67	10.0	15.0
2100	2.67	10.0	25.0
3800	2.67	45.0	70.0
4800	2.67	90.0	160.0
5400	2.67	∞	∞

(b)

KNW S Velocity Structure			
V_S (m/s)	ρ (g/cc)	h (m)	z_{bottom} (m)
200	1.50	2.5	2.5
900	2.67	20.0	22.5
1900	2.67	27.5	50.0
2800	2.67	20.0	70.0
2800	2.67	∞	∞

Table 1

KNW Q Estimates									
Signal (comp.)	Ratio	Spectral Slope Fitting					Two-layer Inversion		
		Q	Q _{min}	Q _{max}	f _{min} (Hz)	f _{max} (Hz)	Q	f _{min} (Hz)	f _{max} (Hz)
P (V)	0 m/300 m	6.2	5.7	6.8	20	120	-	-	-
	0 m/150 m	5.0	4.7	5.4	20	120	6.5	2	120
	150 m/300 m	18.7	13.7	29.6	20	160	26.6	2	160
S (S ₁)	0 m/300 m	8.8	9.5	12.6	20	80	-	-	-
	0 m/150 m	5.2	4.5	6.1	20	80	7.8	2	80
	150 m/300 m	∞	64.0	∞	20	120	∞	2	120
S (S ₂)	0 m/300 m	10.5	8.8	13.0	20	80	-	-	-
	0 m/150 m	9.2	7.4	12.0	20	80	9.8	2	80
	150 m/300 m	14.7	11.1	21.8	20	120	25.9	2	120

Table 2

KNW-BH P-WAVE SIGNAL AND NOISE

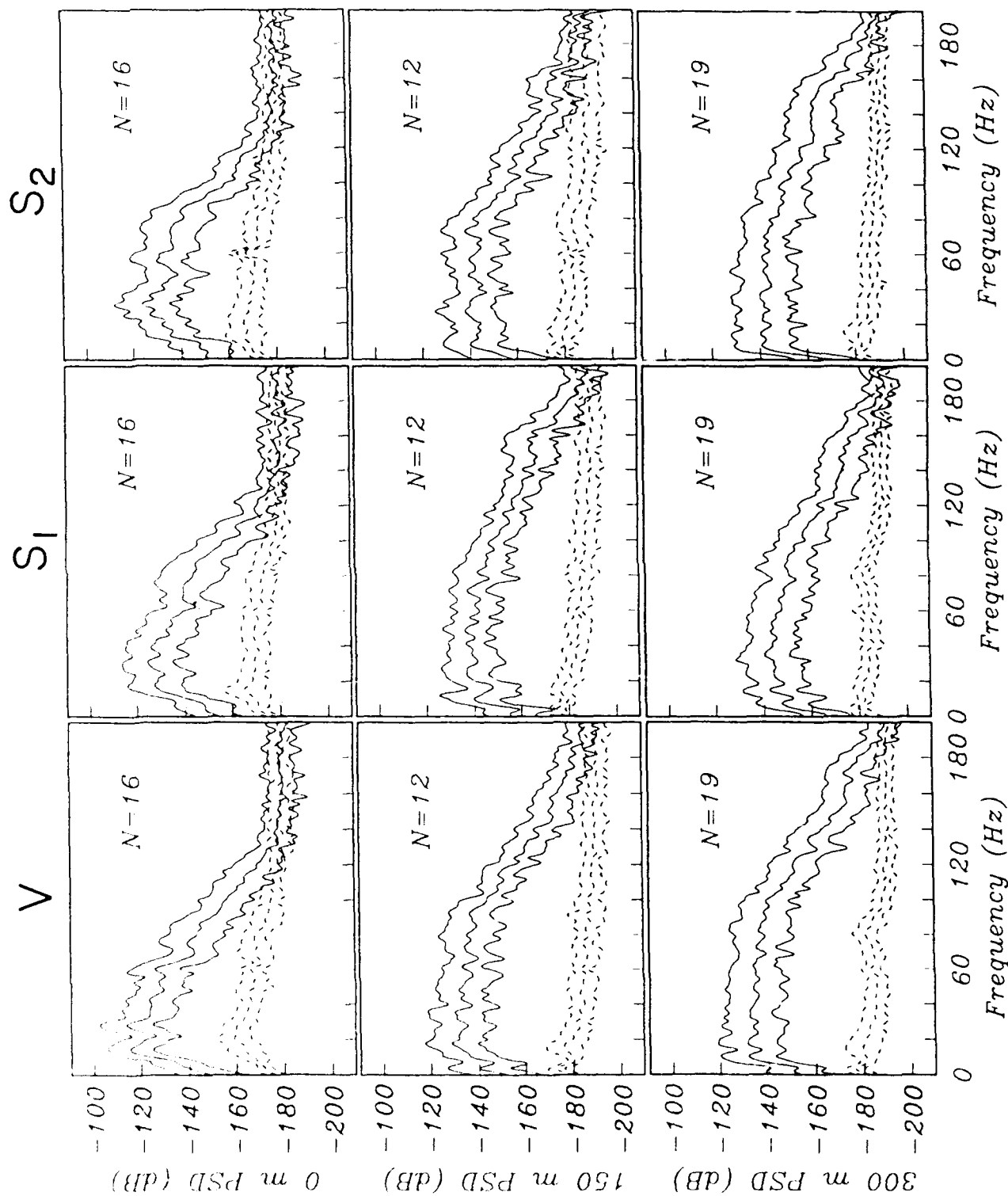


Figure 1(a)

KNW-BH S-WAVE SIGNAL AND NOISE

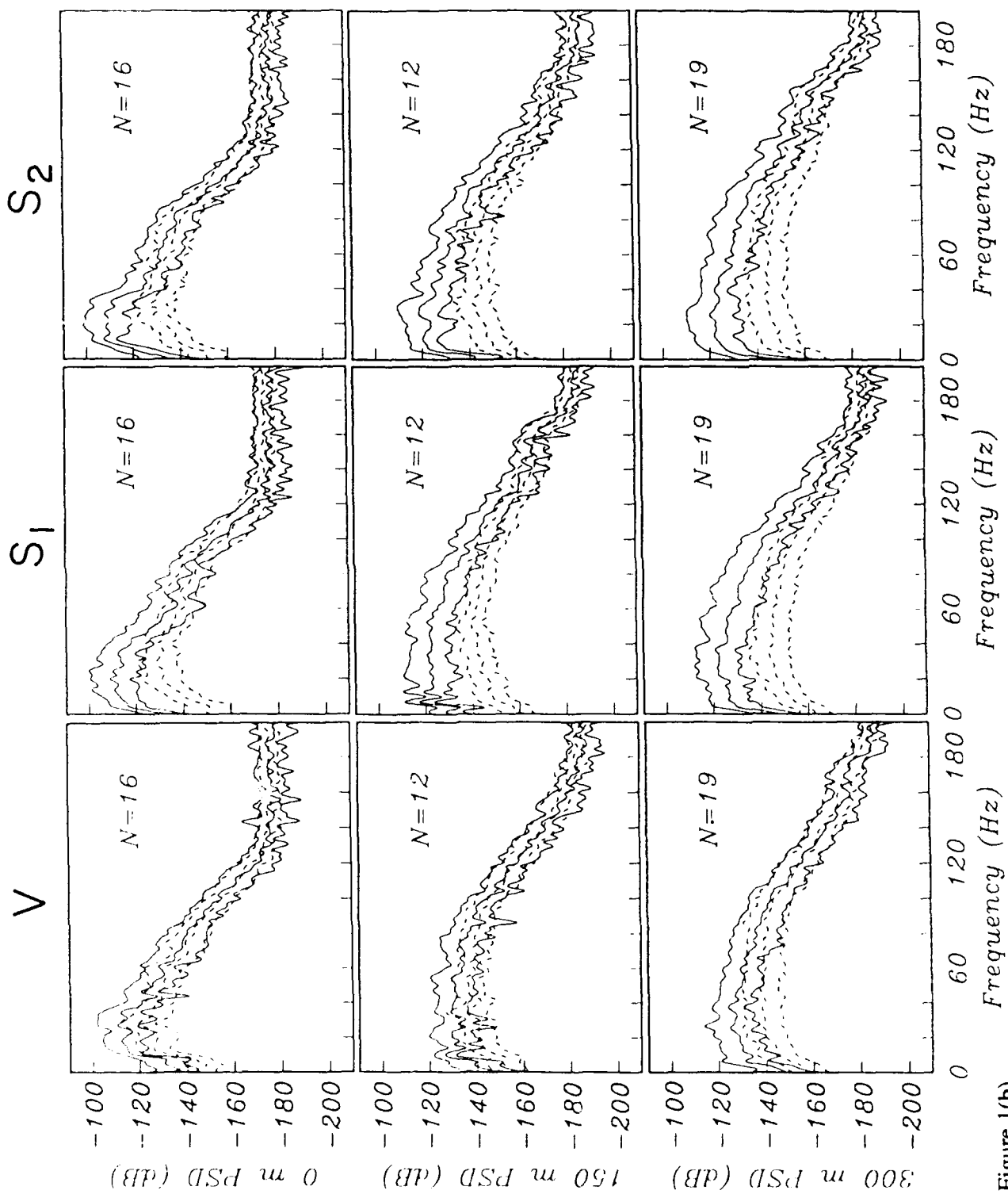


Figure 1(b)

PFO-BH P-WAVE SIGNAL AND NOISE

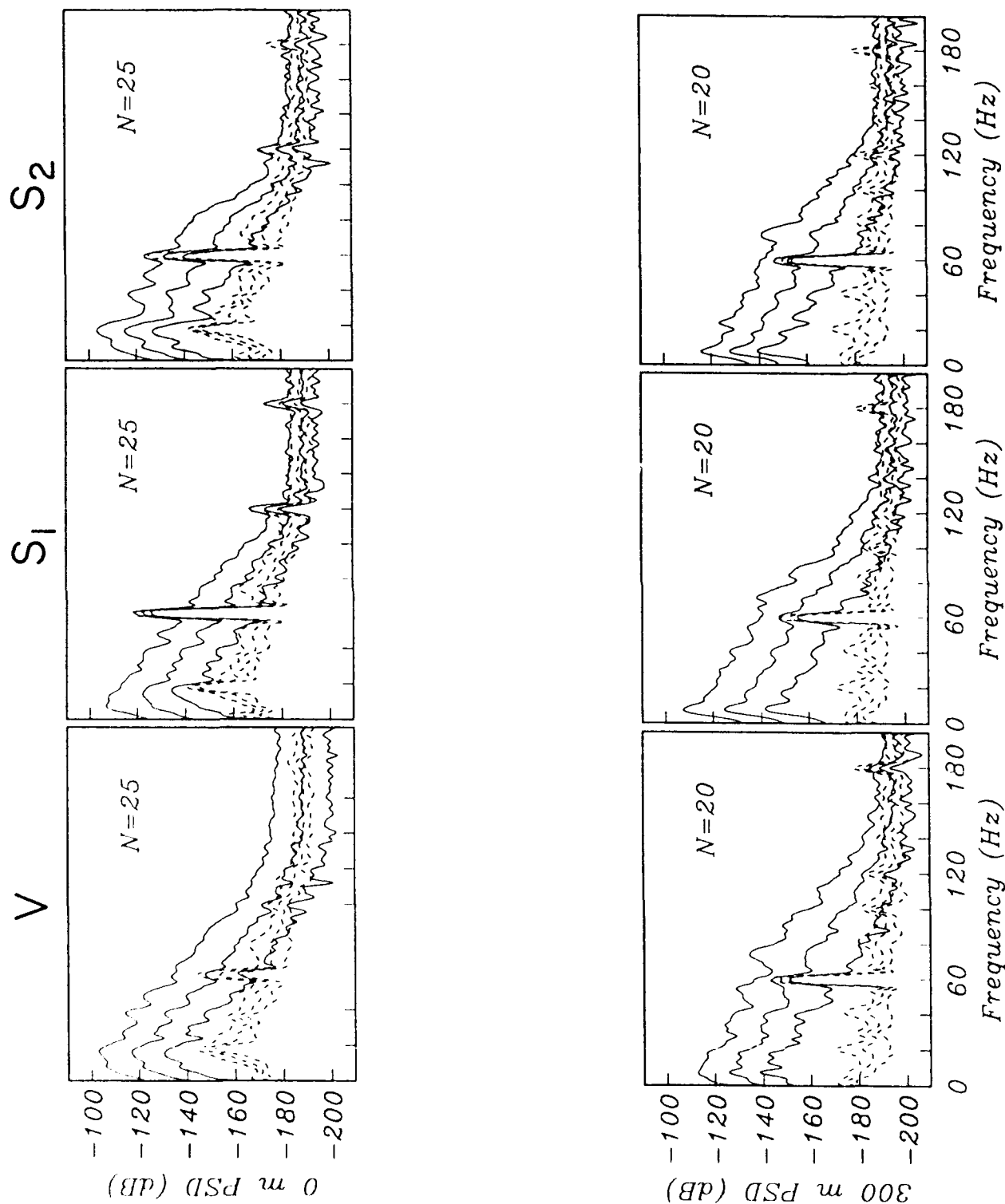


Figure 1(c)

KNW-BH POWER SPECTRAL RATIOS

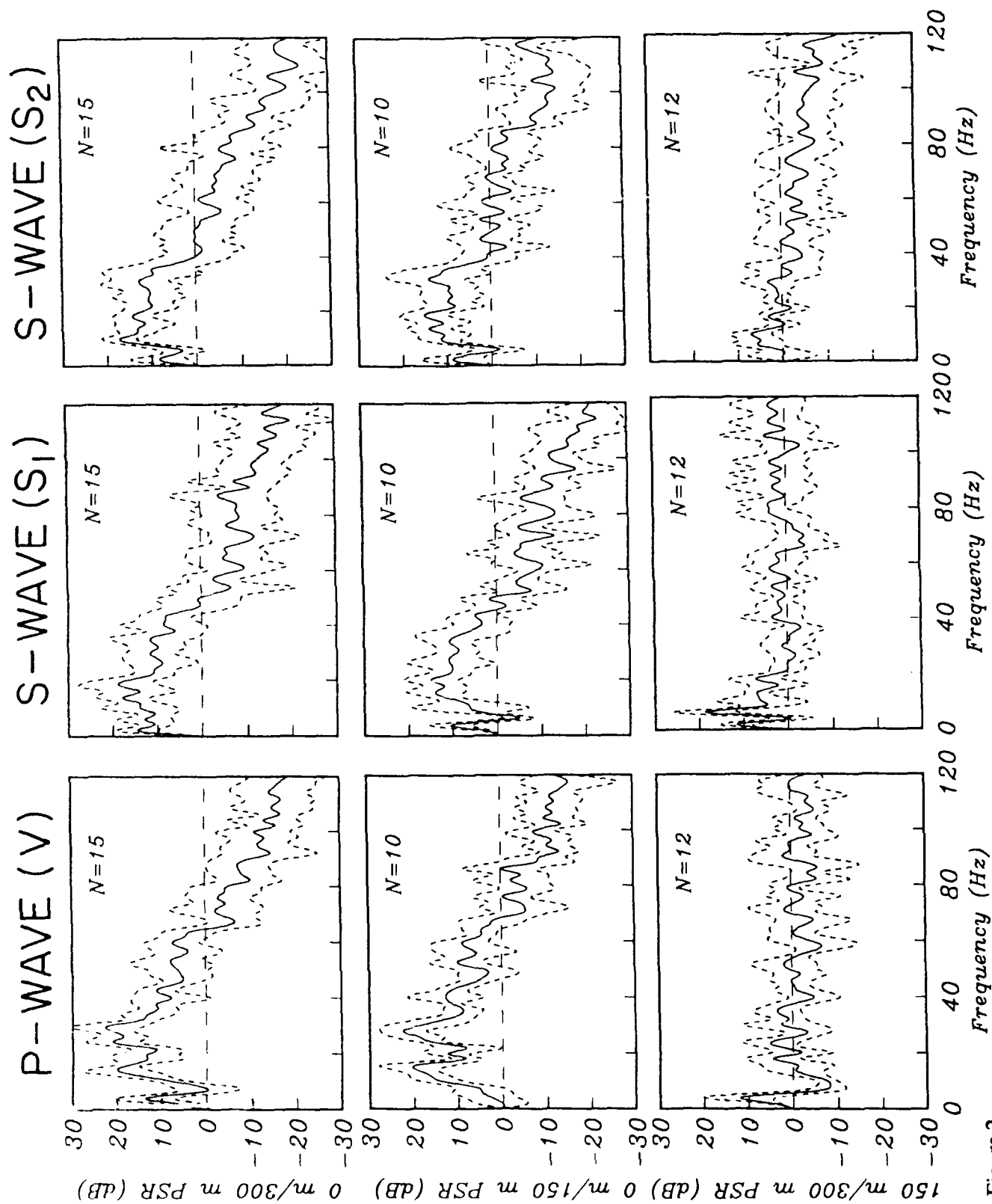


Figure 2

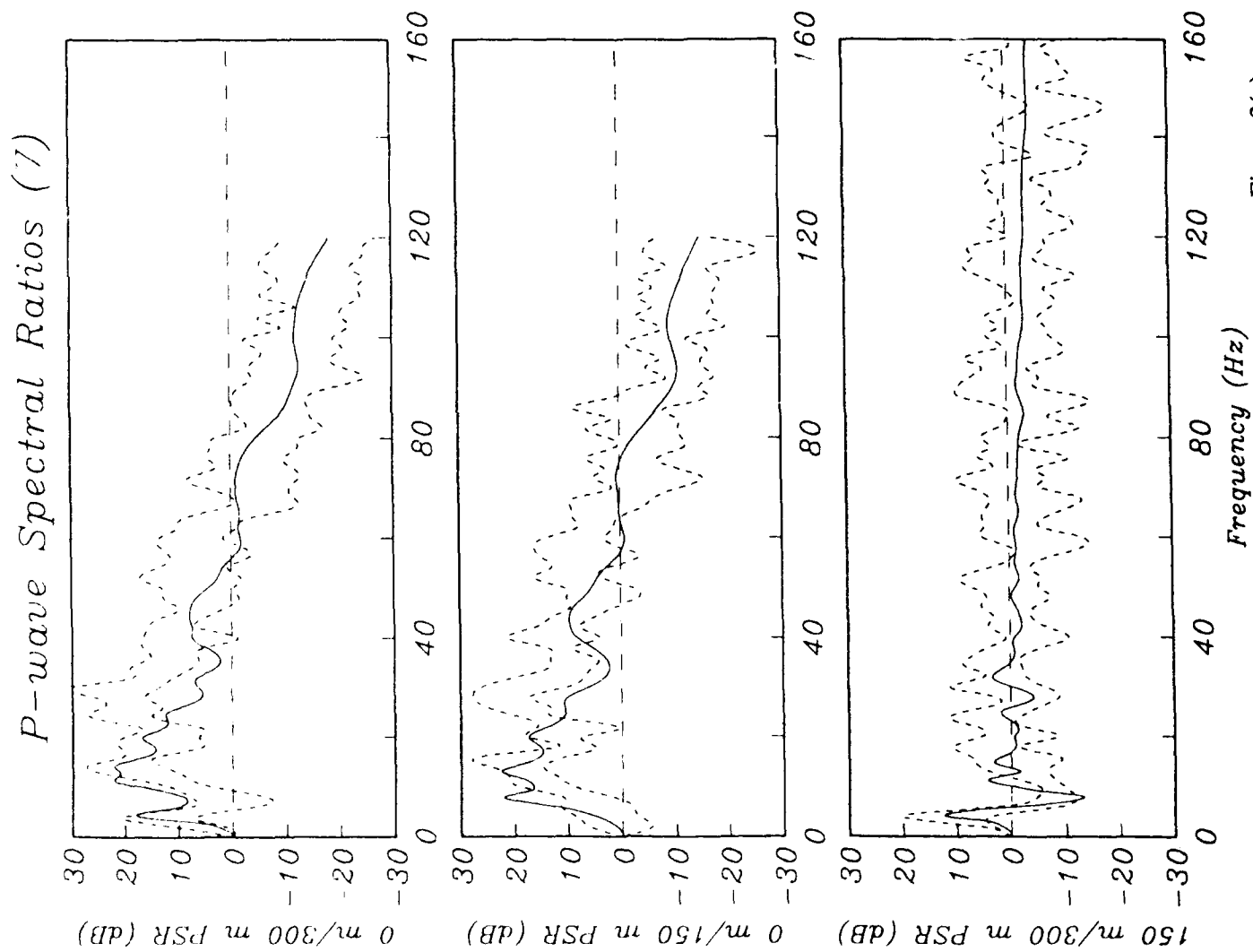
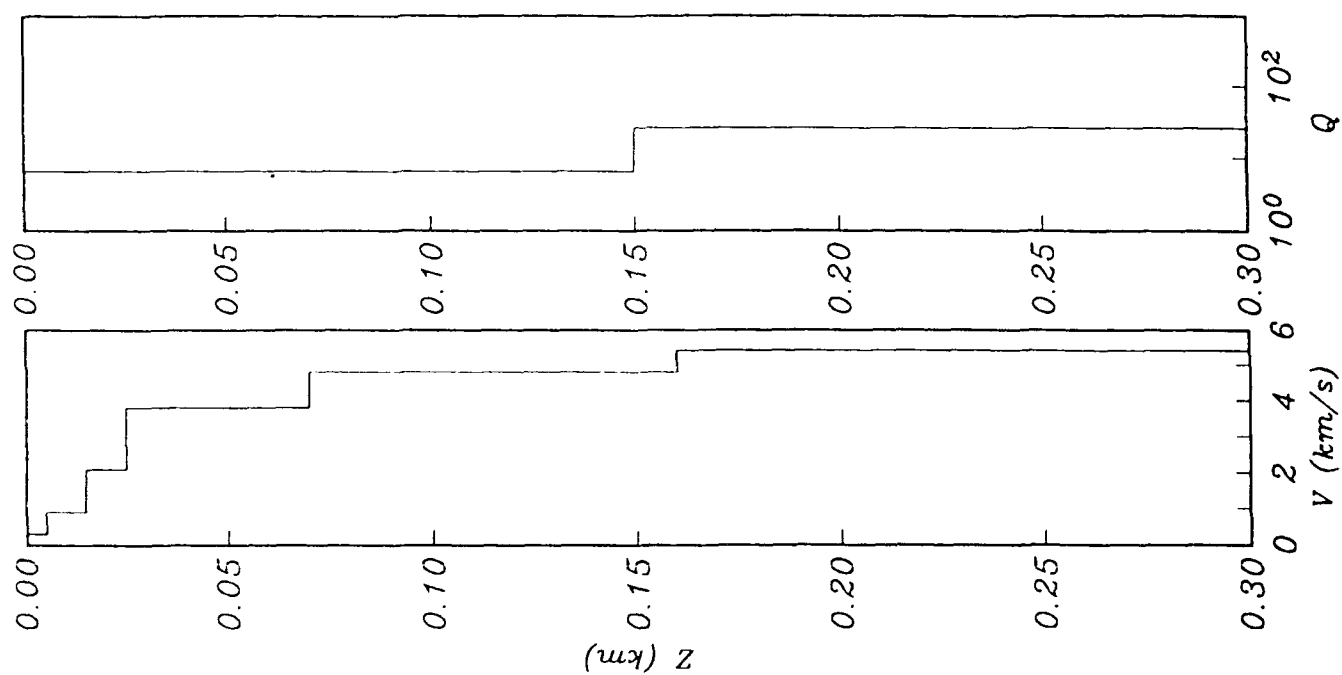


Figure 3(a)



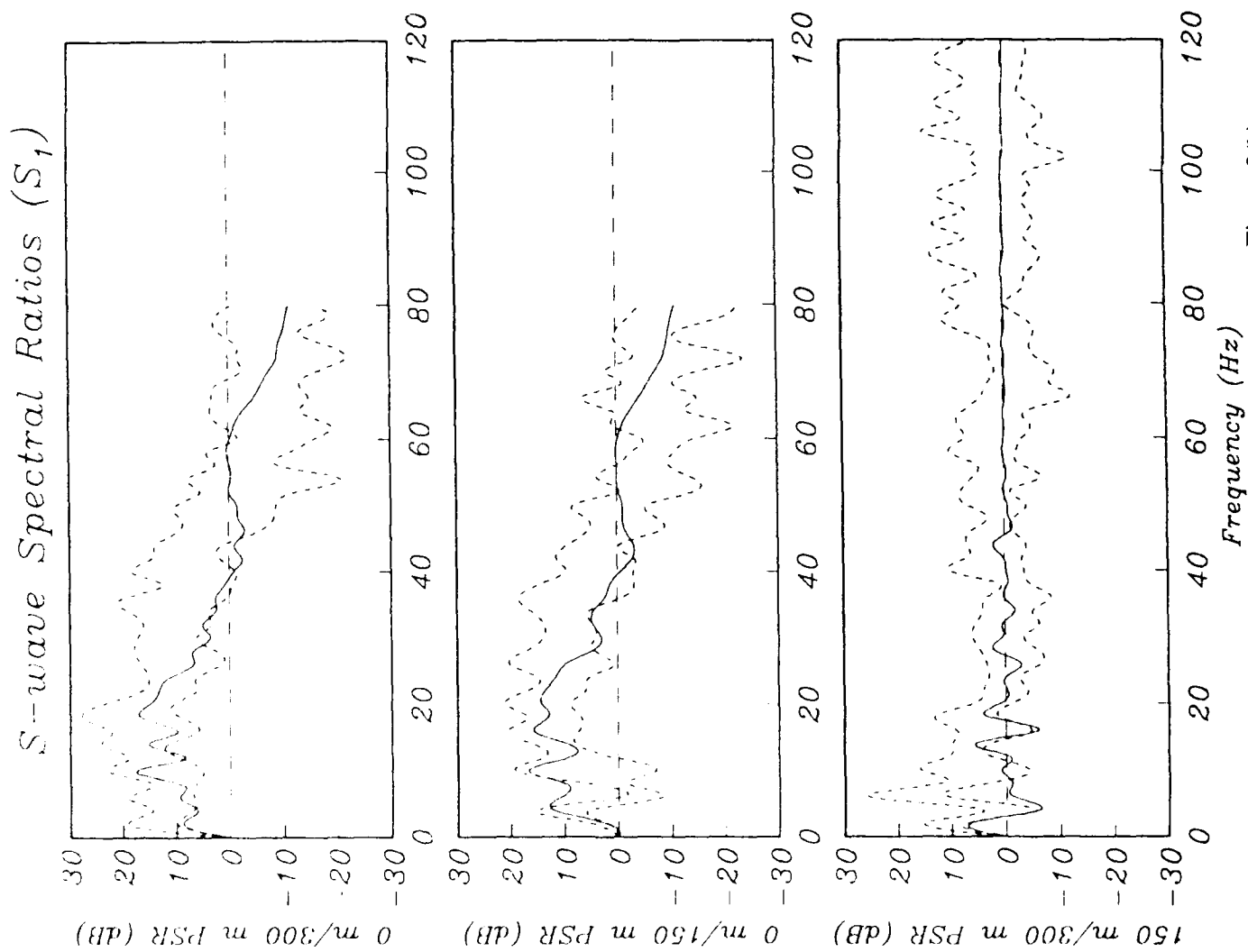
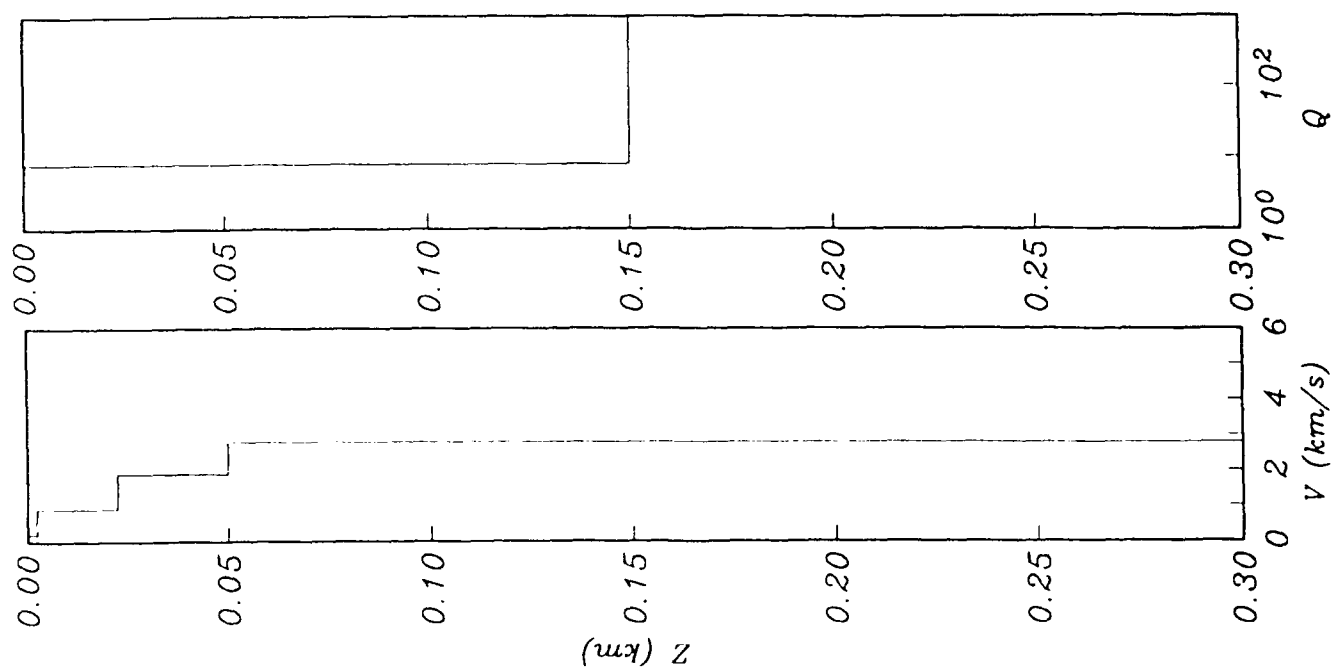


Figure 3(b)



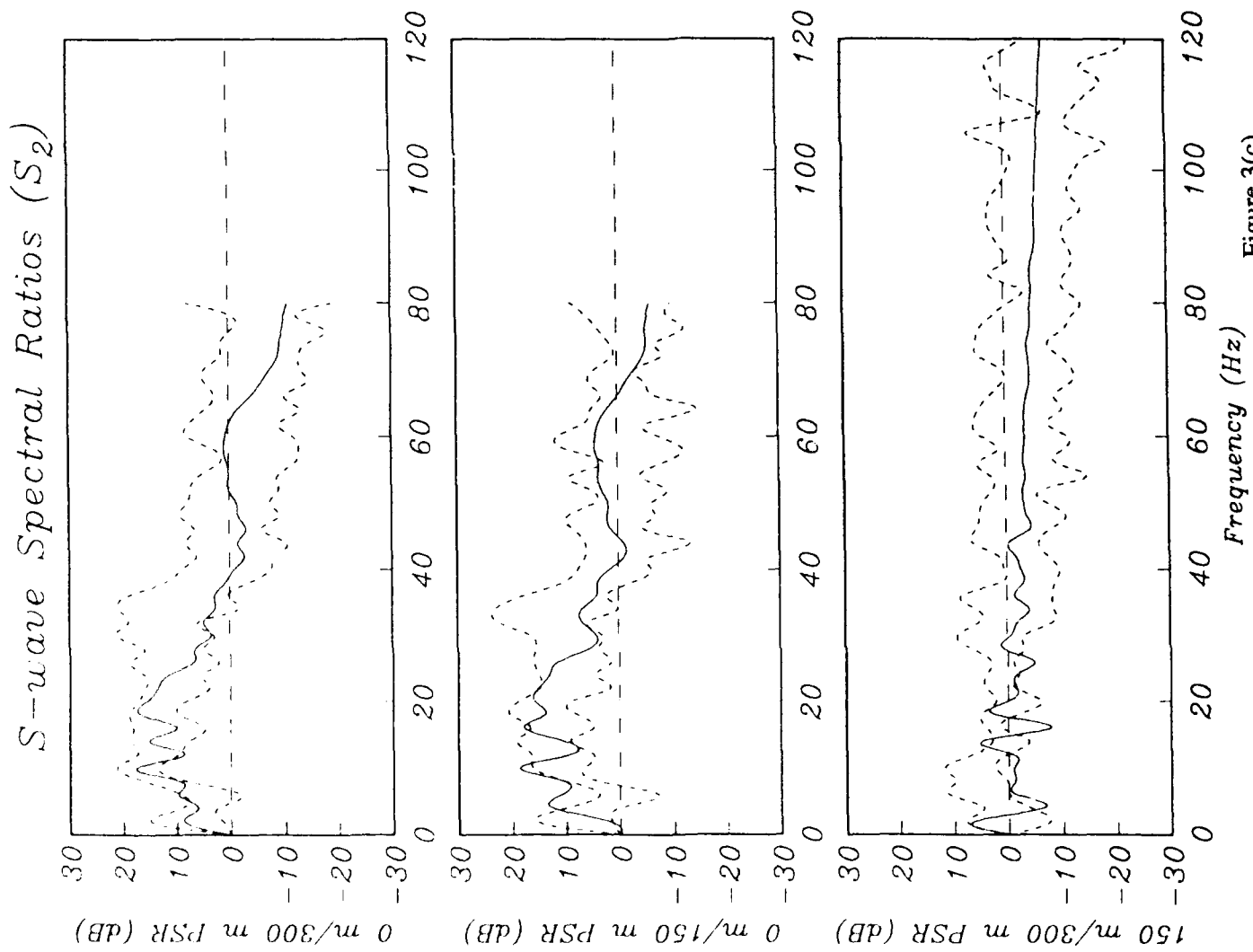
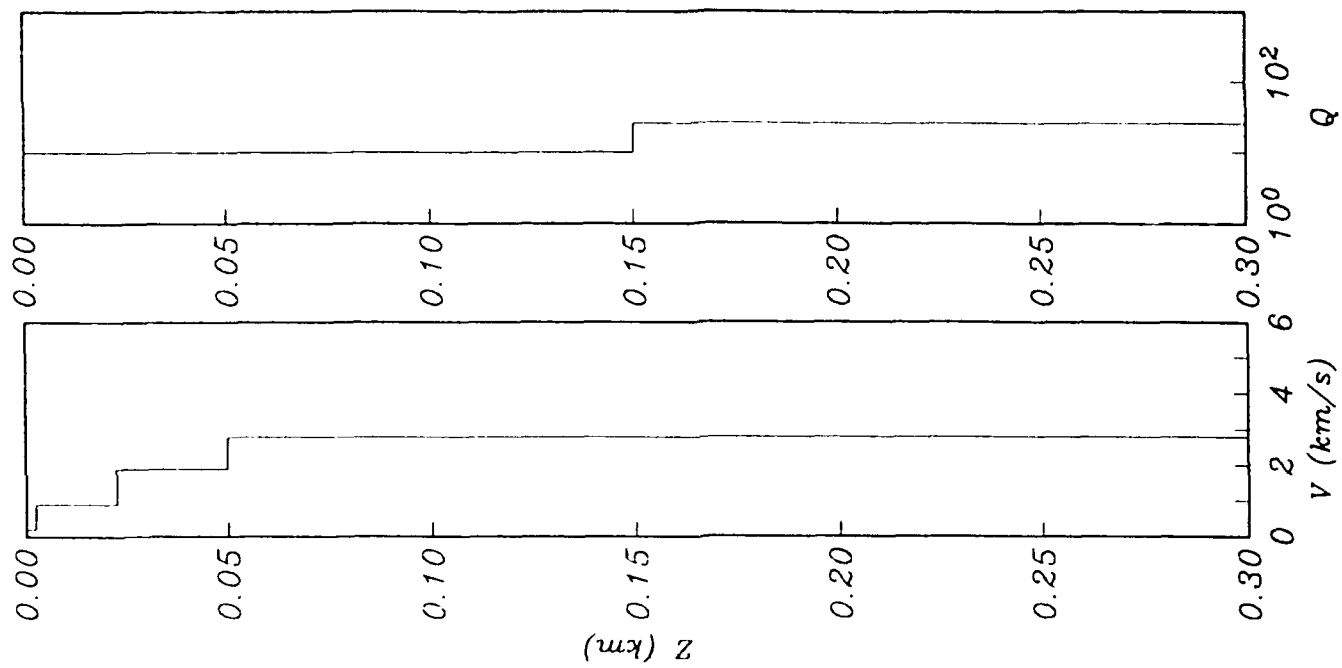


Figure 3(c)



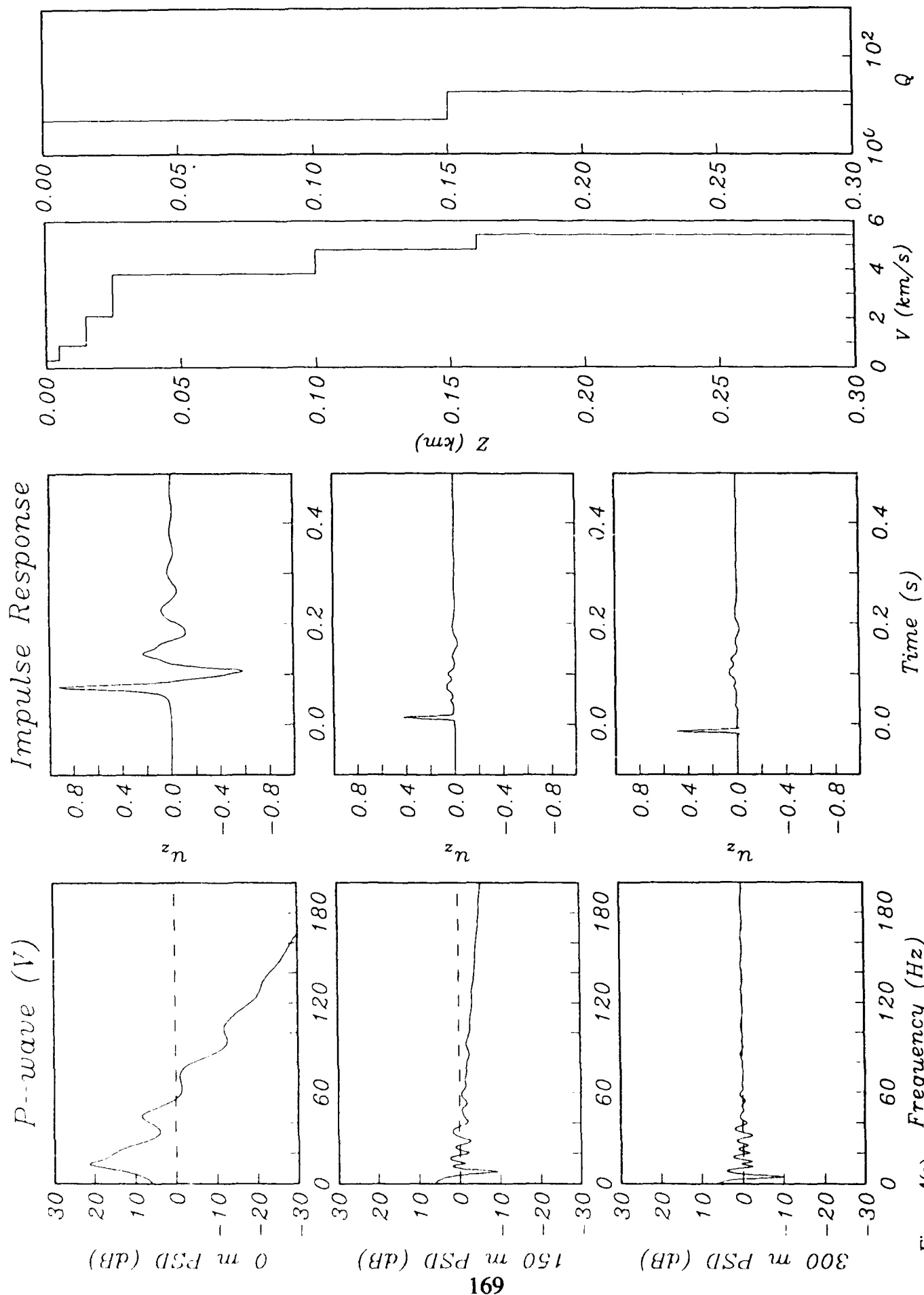


Figure 4(a)

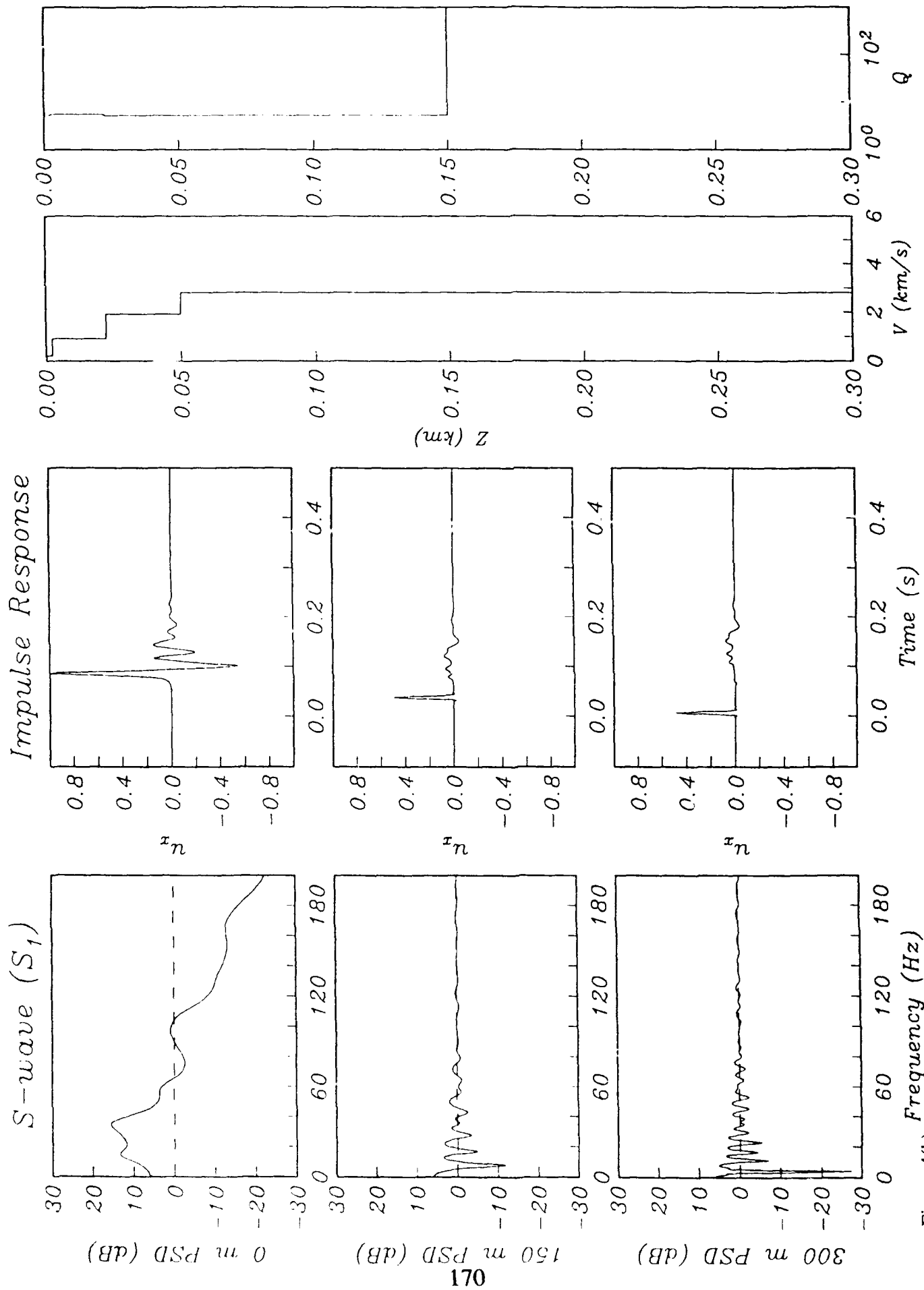


Figure 4(b)

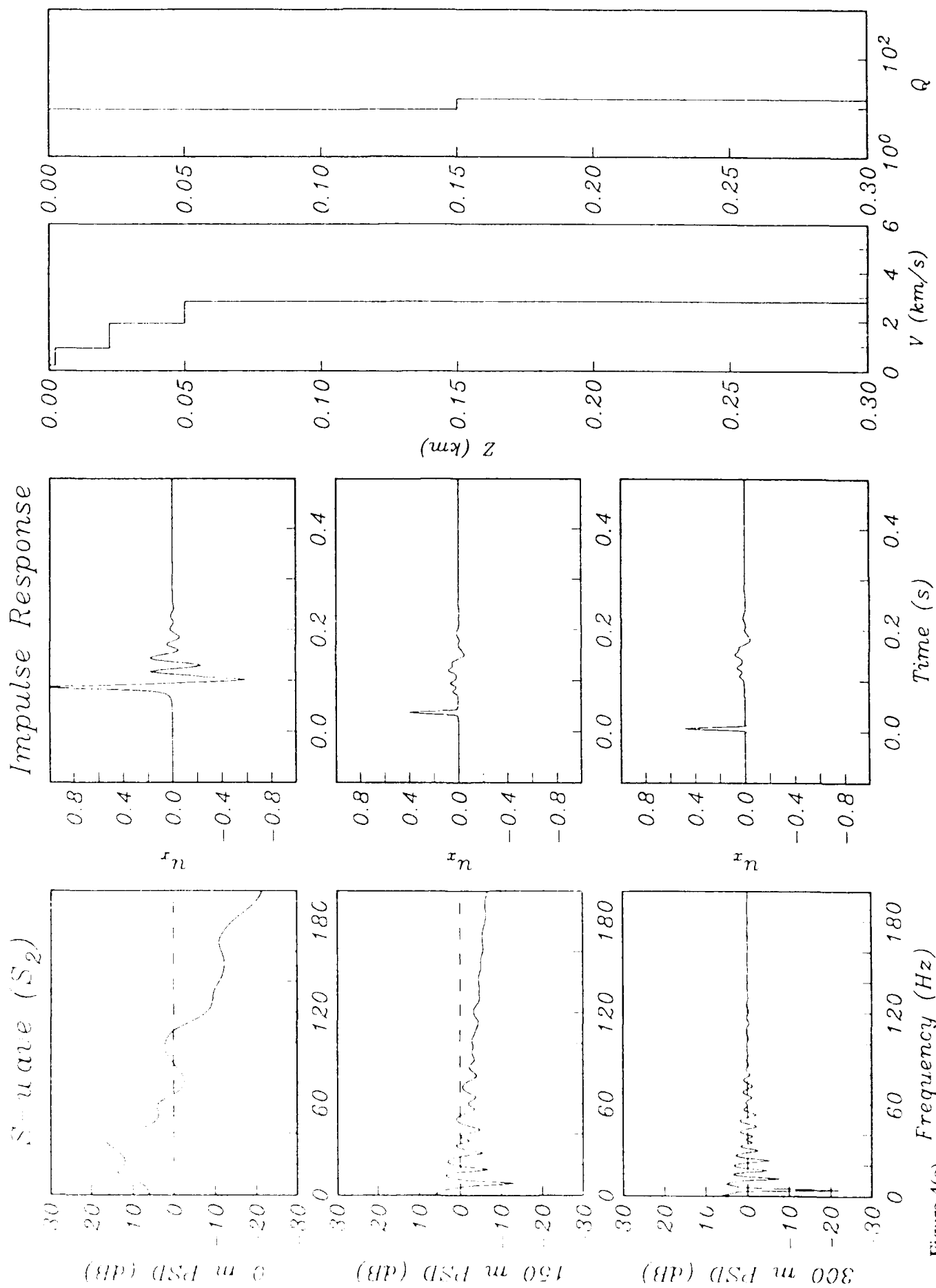


Figure 4(c)

KNW-AZ P-WAVE SIGNAL AND NOISE

V

S₁

S₂

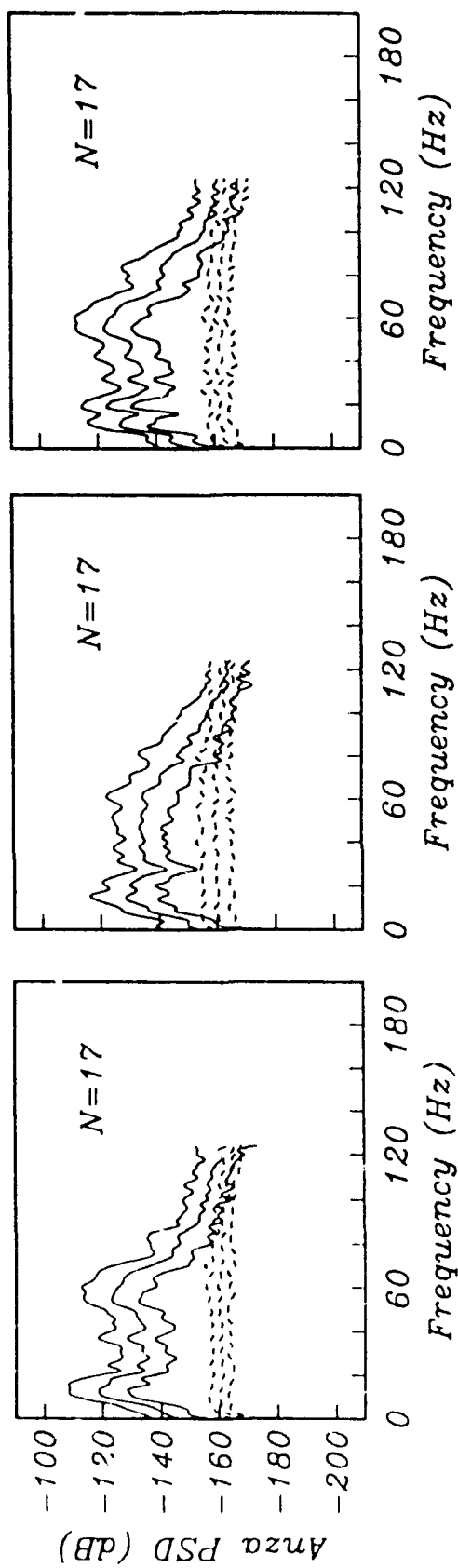


Figure 5(a)

KNW-AZ S-WAVE SIGNAL AND NOISE

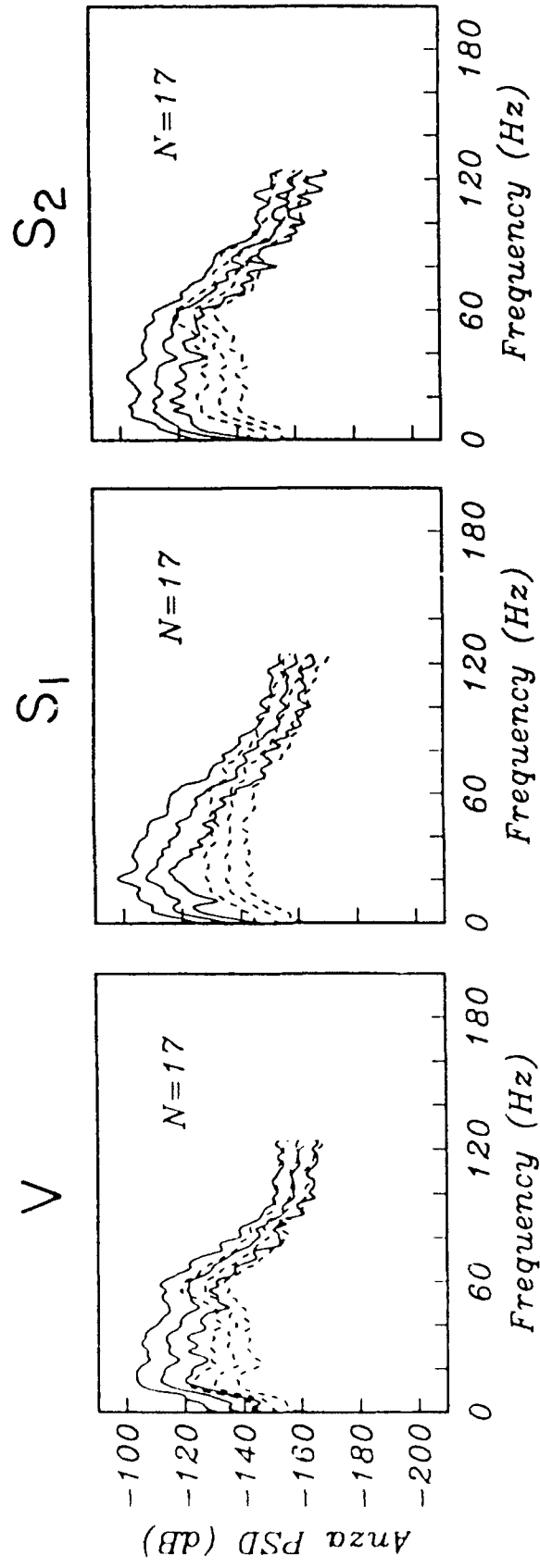


Figure 5(b)

KNW-AZ POWER SPECTRAL RATIOS

P-WAVE (V) S-WAVE (S_1) S-WAVE (S_2)

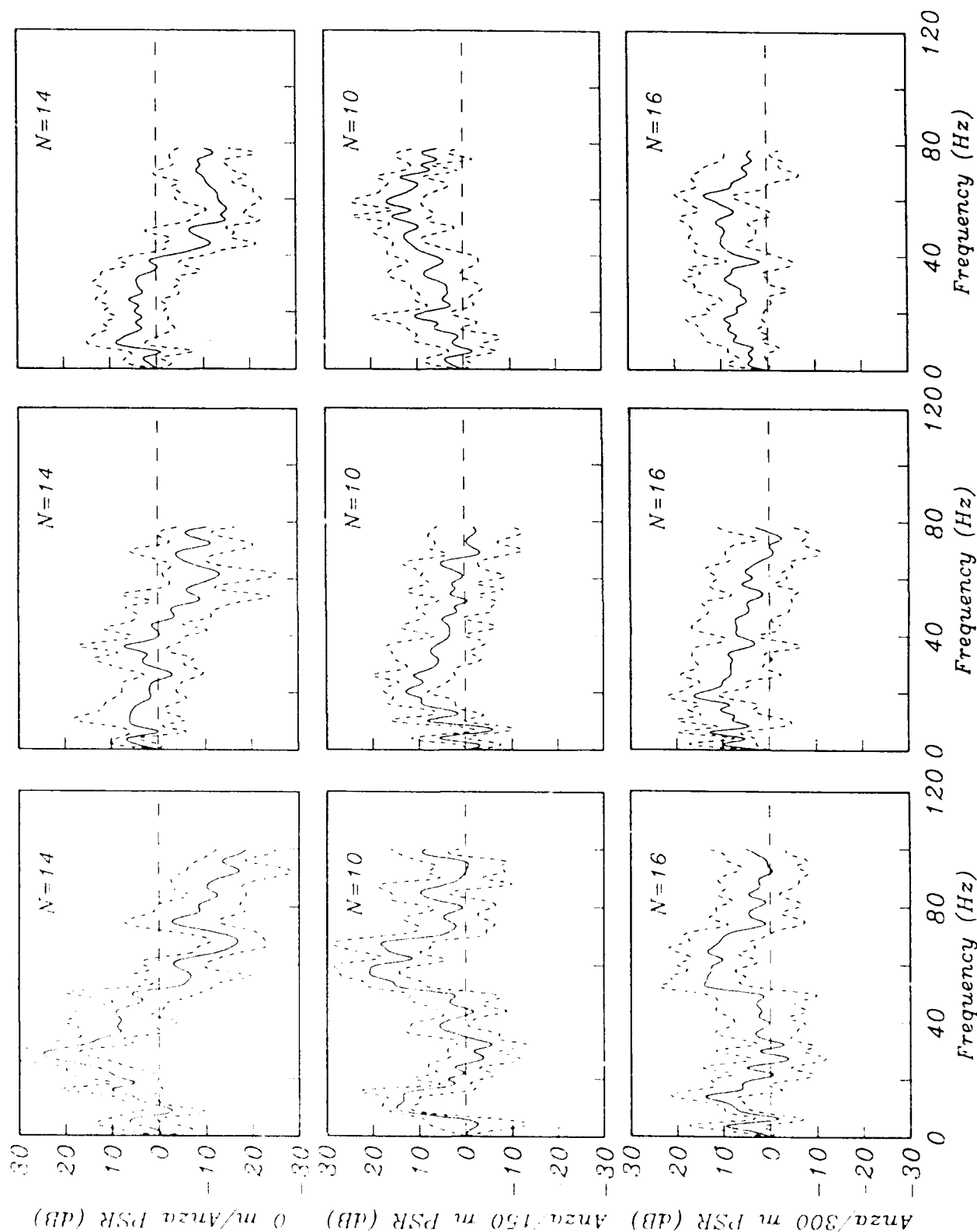
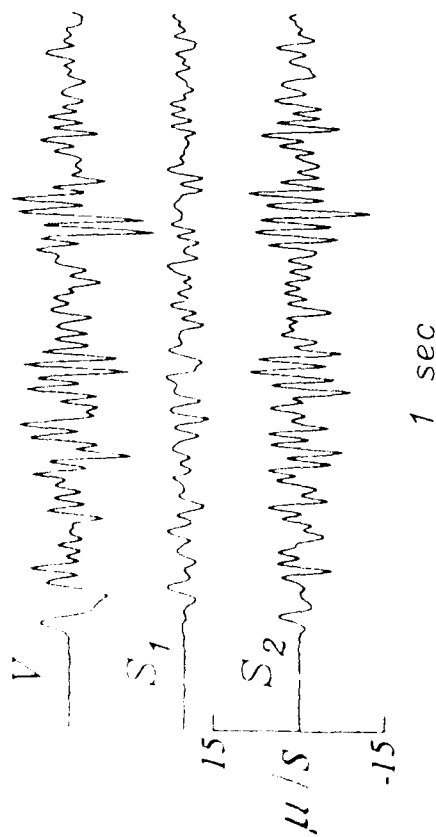
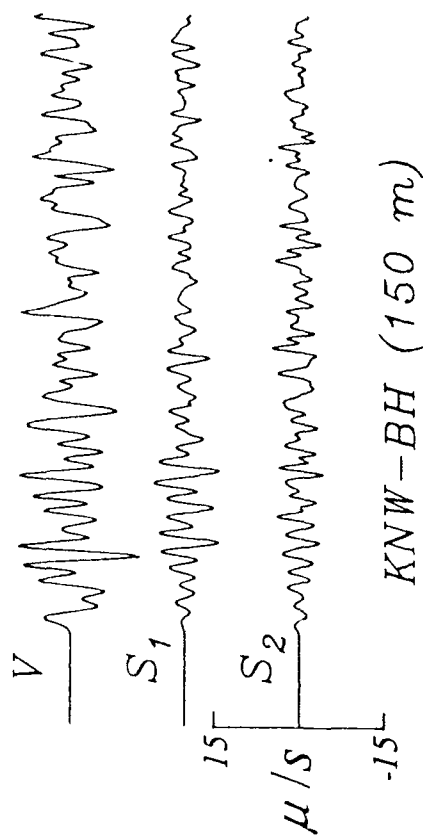


Figure 6

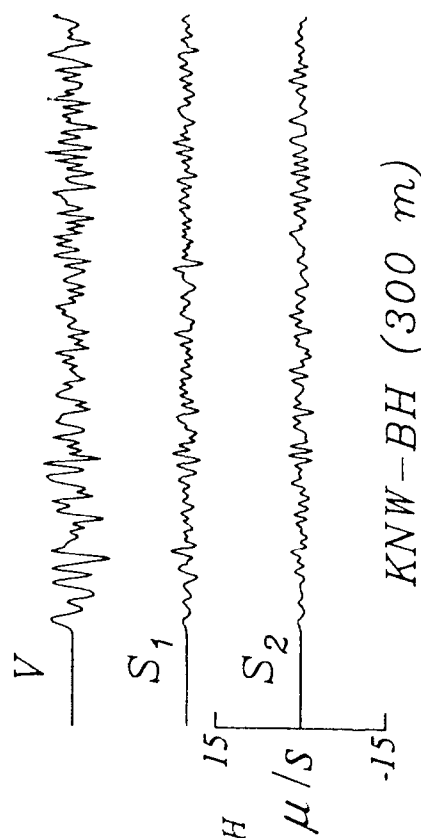
KNW-AZ



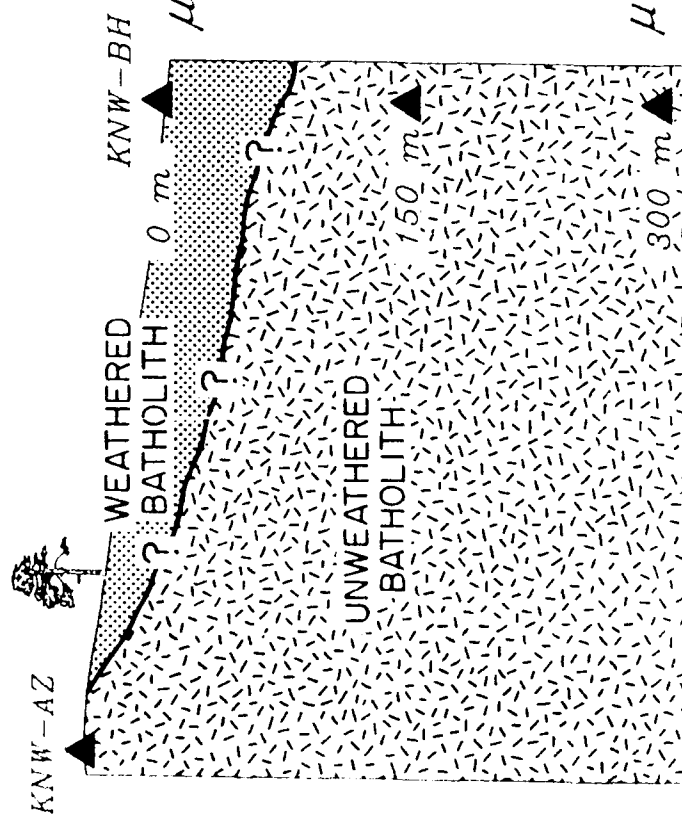
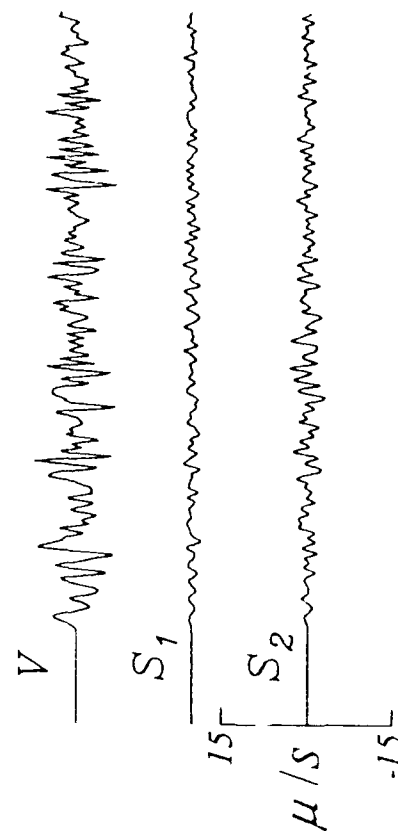
KNW-BH (0 m)



KNW-BH (150 m)



KNW-BH (300 m)



1 sec

Figure 7

Effect of Uppermost 300 m Relative to Batholith (20 km ray path)

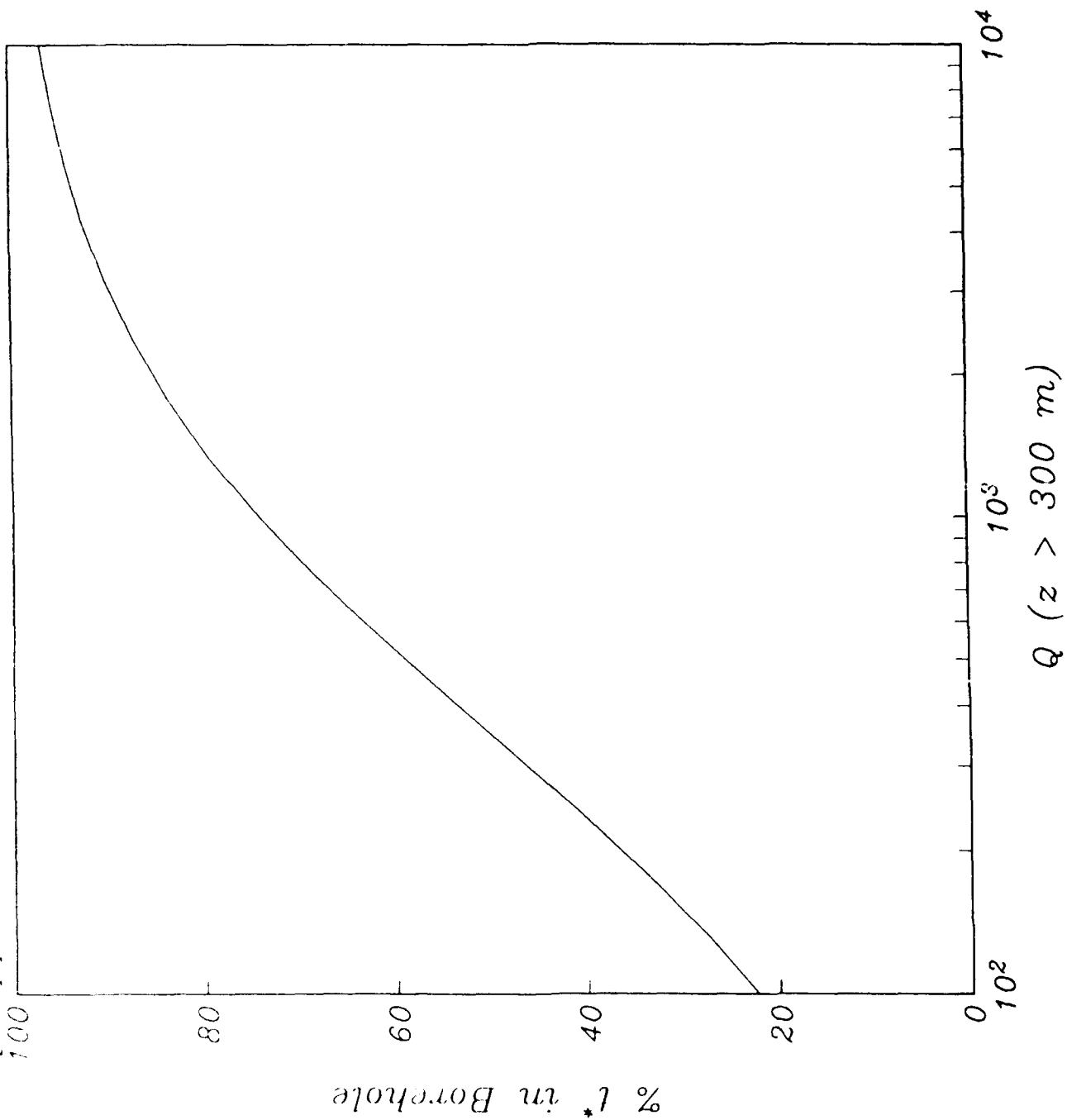


Figure 8

Prof. Thomas Ahrens
Seismological Lab, 252-21
Division of Geological & Planetary Sciences
California Institute of Technology
Pasadena, CA 91125

Prof. Charles B. Archambeau
CIRES
University of Colorado
Boulder, CO 80309

Dr. Thomas C. Bache, Jr.
Science Applications Int'l Corp.
10260 Campus Point Drive
San Diego, CA 92121 (2 copies)

Prof. Muawia Barazangi
Institute for the Study of the Continent
Cornell University
Ithaca, NY 14853

Dr. Jeff Barker
Department of Geological Sciences
State University of New York
at Binghamton
Vestal, NY 13901

Dr. Douglas R. Baumgardt
ENSCO, Inc
5400 Port Royal Road
Springfield, VA 22151-2388

Prof. Jonathan Berger
IGPP, A-025
Scripps Institution of Oceanography
University of California, San Diego
La Jolla, CA 92093

Dr. Gilbert A. Bollinger
Department of Geological Sciences
Virginia Polytechnical Institute
21044 Derring Hall
Blacksburg, VA 24061

Dr. Lawrence J. Burdick
Woodward-Clyde Consultants
566 El Dorado Street
Pasadena, CA 91109-3245

Dr. Jerry Carter
Center for Seismic Studies
1300 North 17th St., Suite 1450
Arlington, VA 22209-2308

Dr. Karl Coyner
New England Research, Inc.
76 Olcott Drive
White River Junction, VT 05001

Prof. Vernon F. Cormier
Department of Geology & Geophysics
U-45, Room 207
The University of Connecticut
Storrs, CT 06268

Professor Anton W. Dainty
Earth Resources Laboratory
Massachusetts Institute of Technology
42 Carleton Street
Cambridge, MA 02142

Prof. Steven Day
Department of Geological Sciences
San Diego State University
San Diego, CA 92182

Dr. Zoltan A. Der
ENSCO, Inc.
5400 Port Royal Road
Springfield, VA 22151-2388

Prof. Lewis M. Duncan
Dept. of Physics & Astronautics
Clemson University
Clemson, SC 29634-1901

Prof. John Ferguson
Center for Lithospheric Studies
The University of Texas at Dallas
P.O. Box 830688
Richardson, TX 75083-0688

Dr. Mark D. Fisk
Mission Research Corporation
735 State Street
P. O. Drawer 719
Santa Barbara, CA 93102

Prof. Stanley Flatte
Applied Sciences Building
University of California
Santa Cruz, CA 95064

Dr. Alexander Florence
SRI International
333 Ravenswood Avenue
Menlo Park, CA 94025-3493

Dr. Holy K. Given
IGPP, A-025
Scripps Institute of Oceanography
University of California, San Diego
La Jolla, CA 92093

Prof. Henry L. Gray
Vice Provost and Dean
Department of Statistical Sciences
Southern Methodist University
Dallas, TX 75275

Dr. Indra Gupta
Teledyne Geotech
314 Montgomery Street
Alexandria, VA 22314

Prof. David G. Harkrider
Seismological Laboratory
Division of Geological & Planetary Sciences
California Institute of Technology
Pasadena, CA 91125

Prof. Danny Harvey
CIRES
University of Colorado
Boulder, CO 80309

Prof. Donald V. Helmberger
Seismological Laboratory
Division of Geological & Planetary Sciences
California Institute of Technology
Pasadena, CA 91125

Prof. Eugene Herrin
Institute for the Study of Earth and Man
Geophysical Laboratory
Southern Methodist University
Dallas, TX 75275

Prof. Bryan Isacks
Cornell University
Department of Geological Sciences
SNEE Hall
Ithaca, NY 14850

Dr. Rong-Song Jih
Teledyne Geotech
314 Montgomery Street
Alexandria, VA 22314

Prof. Lane R. Johnson
Seismographic Station
University of California
Berkeley, CA 94720

Dr. Richard LaCoss
MIT-Lincoln Laboratory
M-200B
P. O. Box 73
Lexington, MA 02173-0073 (3 copies)

Prof Fred K. Lamb
University of Illinois at Urbana-Champaign
Department of Physics
1110 West Green Street
Urbana, IL 61801

Prof. Charles A. Langston
Geosciences Department
403 Deike Building
The Pennsylvania State University
University Park, PA 16802

Prof. Thorne Lay
Institute of Tectonics
Earth Science Board
University of California, Santa Cruz
Santa Cruz, CA 95064

Prof. Arthur Lerner-Lam
Lamont-Doherty Geological Observatory
of Columbia University
Palisades, NY 10964

Dr. Christopher Lynnes
Teledyne Geotech
314 Montgomery Street
Alexandria, VA 22314

Prof. Peter Malin
Department of Geology
Old Chemistry Bldg.
Duke University
Durham, NC 27706

Dr. Randolph Martin, III
New England Research, Inc.
76 Olcott Drive
White River Junction, VT 05001

Prof. Thomas V. McEvelly
Seismographic Station
University of California
Berkeley, CA 94720

Dr. Keith L. McLaughlin
S-CUBED
A Division of Maxwell Laboratory
P.O. Box 1620
La Jolla, CA 92038-1620

Prof. William Menke
Lamont-Doherty Geological Observatory
of Columbia University
Palisades, NY 10964

Stephen Miller
SRI International
333 Ravenswood Avenue
Box AF 116
Menlo Park, CA 94025-3493

Prof. Bernard Minster
IGPP, A-025
Scripps Institute of Oceanography
University of California, San Diego
La Jolla, CA 92093

Prof. Brian J. Mitchell
Department of Earth & Atmospheric Sciences
St. Louis University
St. Louis, MO 63156

Mr. Jack Murphy
S-CUBED, A Division of Maxwell Laboratory
11800 Sunrise Valley Drive
Suite 1212
Reston, VA 22091 (2 copies)

Prof. John A. Orcutt
IGPP, A-025
Scripps Institute of Oceanography
University of California, San Diego
La Jolla, CA 92093

Prof. Keith Priestley
University of Cambridge
Bullard Labs, Dept. of Earth Sciences
Madingley Rise, Madingley Rd.
Cambridge CB3 0EZ, ENGLAND

Dr. Jay J. Pulli
Radix Systems, Inc.
2 Taft Court, Suite 203
Rockville, MD 20850

Prof. Paul G. Richards
Lamont Doherty Geological Observatory
of Columbia University
Palisades, NY 10964

Dr. Wilmer Rivers
Teledyne Geotech
314 Montgomery Street
Alexandria, VA 22314

Prof. Charles G. Sammis
Center for Earth Sciences
University of Southern California
University Park
Los Angeles, CA 90089-0741

Prof. Christopher H. Scholz
Lamont-Doherty Geological Observatory
of Columbia University
Palisades, NY 10964

Thomas J. Sereno, Jr.
Science Application Int'l Corp.
10260 Campus Point Drive
San Diego, CA 92121

Prof. David G. Simpson
Lamont-Doherty Geological Observatory
of Columbia University
Palisades, NY 10964

Dr. Jeffrey Stevens
S-CUBED
A Division of Maxwell Laboratory
P.O. Box 1620
La Jolla, CA 92038-1620

Prof. Brian Stump
Institute for the Study of Earth & Man
Geophysical Laboratory
Southern Methodist University
Dallas, TX 75275

Prof. Jeremiah Sullivan
University of Illinois at Urbana-Champaign
Department of Physics
1110 West Green Street
Urbana, IL 61801

Prof. Clifford Thurber
University of Wisconsin-Madison
Department of Geology & Geophysics
1215 West Dayton Street
Madison, WI 53706

Prof. M. Nafi Toksoz
Earth Resources Lab
Massachusetts Institute of Technology
42 Carleton Street
Cambridge, MA 02142

Prof. John E. Vidale
University of California at Santa Cruz
Seismological Laboratory
Santa Cruz, CA 95064

Prof. Terry C. Wallace
Department of Geosciences
Building #77
University of Arizona
Tucson, AZ 85721

Dr. William Wortman
Mission Research Corporation
8560 Cinderbed Rd.
Suite # 700
Newington, VA 22122

Prof. Francis T. Wu
Department of Geological Sciences
State University of New York
at Binghamton
Vestal, NY 13901

OTHERS (United States)

Dr. Monem Abdel-Gawad
Rockwell International Science Center
1049 Camino Dos Rios
Thousand Oaks, CA 91360

Michael Browne
Teledyne Geotech
3401 Shiloh Road
Garland, TX 75041

Prof. Keiiti Aki
Center for Earth Sciences
University of Southern California
University Park
Los Angeles, CA 90089-0741

Mr. Roy Burger
1221 Serry Road
Schenectady, NY 12309

Prof. Shelton S. Alexander
Geosciences Department
403 Deike Building
The Pennsylvania State University
University Park, PA 16802

Dr. Robert Burrige
Schlumberger-Doll Research Center
Old Quarry Road
Ridgefield, CT 06877

Dr. Kenneth Anderson
BBNSTC
Mail Stop 14/1B
Cambridge, MA 02238

Dr. W. Winston Chan
Teledyne Geotech
314 Montgomery Street
Alexandria, VA 22314-1581

Dr. Ralph Archuleta
Department of Geological Sciences
University of California at Santa Barbara
Santa Barbara, CA 93102

Dr. Theodore Cherry
Science Horizons, Inc.
710 Encinitas Blvd., Suite 200
Encinitas, CA 92024 (2 copies)

Dr. Susan Beck
Department of Geosciences
Bldg. # 77
University of Arizona
Tucson, AZ 85721

Prof. Jon F. Claerbout
Department of Geophysics
Stanford University
Stanford, CA 94305

Dr. T.J. Bennett
S-CUBED
A Division of Maxwell Laboratory
11800 Sunrise Valley Drive, Suite 1212
Reston, VA 22091

Prof. Robert W. Clayton
Seismological Laboratory
Division of Geological & Planetary Sciences
California Institute of Technology
Pasadena, CA 91125

Mr. William J. Best
907 Westwood Drive
Vienna, VA 22180

Prof. F. A. Dahlen
Geological and Geophysical Sciences
Princeton University
Princeton, NJ 08544-0636

Dr. N. Biswas
Geophysical Institute
University of Alaska
Fairbanks, AK 99701

Mr. Charles Doll
Earth Resources Laboratory
Massachusetts Institute of Technology
42 Carleton St.
Cambridge, MA 02142

Dr. Stephen Bratt
Center for Seismic Studies
1300 North 17th Street
Suite 1450
Arlington, VA 22209

Prof. Adam Dziewonski
Hoffman Laboratory, Harvard Univ.
Dept. of Earth Atmos. & Planetary Sciences
20 Oxford St
Cambridge, MA 02138

Prof. John Ebel
Department of Geology & Geophysics
Boston College
Chestnut Hill, MA 02167

Eric Fielding
SNEE Hall
INSTOC
Cornell University
Ithaca, NY 14853

Dr. John Foley
Phillips Laboratory/LWH
Hanscom AFB, MA 01731-5000

Prof. Donald Forsyth
Department of Geological Sciences
Brown University
Providence, RI 02912

Dr. Cliff Frolich
Institute of Geophysics
8701 North Mopac
Austin, TX 78759

Dr. Anthony Gangi
Texas A&M University
Department of Geophysics
College Station, TX 77843

Dr. Freeman Gilbert
IGPP, A-025
Scripps Institute of Oceanography
University of California
La Jolla, CA 92093

Mr. Edward Giller
Pacific Sierra Research Corp.
1401 Wilson Boulevard
Arlington, VA 22209

Dr. Jeffrey W. Given
SAIC
10260 Campus Point Drive
San Diego, CA 92121

Prof. Stephen Grand
University of Texas at Austin
Department of Geological Sciences
Austin, TX 78713-7909

Prof. Roy Greenfield
Geosciences Department
403 Deike Building
The Pennsylvania State University
University Park, PA 16802

Dan N. Hagedorn
Battelle
Pacific Northwest Laboratories
Battelle Boulevard
Richland, WA 99352

Dr. James Hannon
Lawrence Livermore National Laboratory
P. O. Box 808
Livermore, CA 94550

Prof. Robert B. Herrmann
Dept. of Earth & Atmospheric Sciences
St. Louis University
St. Louis, MO 63156

Ms. Heidi Houston
Seismological Laboratory
University of California
Santa Cruz, CA 95064

Kevin Hutchenson
Department of Earth Sciences
St. Louis University
3507 Laclede
St. Louis, MO 63103

Dr. Hans Israelsson
Center for Seismic Studies
1300 N. 17th Street, Suite 1450
Arlington, VA 22209-2308

Prof. Thomas H. Jordan
Department of Earth, Atmospheric
and Planetary Sciences
Massachusetts Institute of Technology
Cambridge, MA 02139

Prof. Alan Kafka
Department of Geology & Geophysics
Boston College
Chestnut Hill, MA 02167

Robert C. Kemerait
ENSCO, Inc.
445 Pineda Court
Melbourne, FL 32940

William Kikendall
Teledyne Geotech
3401 Shiloh Road
Garland, TX 75041

Prof. Amos Nur
Department of Geophysics
Stanford University
Stanford, CA 94305

Prof. Leon Knopoff
University of California
Institute of Geophysics & Planetary Physics
Los Angeles, CA 90024

Prof. Jack Oliver
Department of Geology
Cornell University
Ithaca, NY 14850

Prof. John Kuo
Aldridge Laboratory of Applied Geophysics
Columbia University
842 Mudd Bldg.
New York, NY 10027

Dr. Kenneth Olsen
P. O. Box 1273
Linwood, WA 98046-1273

Prof. L. Timothy Long
School of Geophysical Sciences
Georgia Institute of Technology
Atlanta, GA 30332

Prof. Jeffrey Park
Department of Geology and Geophysics
Kline Geology Laboratory
P. O. Box 6666
New Haven, CT 06511-8130

Dr. Gary McCartor
Department of Physics
Southern Methodist University
Dallas, TX 75275

Howard J. Patton
Lawrence Livermore National Laboratory
L-205
P. O. Box 808
Livermore, CA 94550

Prof. Art McGarr
Mail Stop 977
Geological Survey
345 Middlefield Rd.
Menlo Park, CA 94025

Prof. Robert Phinney
Geological & Geophysical Sciences
Princeton University
Princeton, NJ 08544-0636

Dr. George Mellman
Sierra Geophysics
11255 Kirkland Way
Kirkland, WA 98033

Dr. Paul Pomeroy
Rondout Associates
P.O. Box 224
Stone Ridge, NY 12484

Prof. John Nabelek
College of Oceanography
Oregon State University
Corvallis, OR 97331

Dr. Norton Rimer
S-CUBED
A Division of Maxwell Laboratory
P.O. Box 1620
La Jolla, CA 92038-1620

Prof. Geza Nagy
University of California, San Diego
Department of Ames, M.S. B-010
La Jolla, CA 92093

Prof. Larry J. Ruff
Department of Geological Sciences
1006 C.C. Little Building
University of Michigan
Ann Arbor, MI 48109-1063

Dr. Keith K. Nakanishi
Lawrence Livermore National Laboratory
L-205
P. O. Box 808
Livermore, CA 94550

Dr. Richard Sailor
TASC Inc.
55 Walkers Brook Drive
Reading, MA 01867

Dr. Susan Schwartz
Institute of Tectonics
1156 High St.
Santa Cruz, CA 95064

John Sherwin
Teledyne Geotech
3401 Shiloh Road
Garland, TX 75041

Dr. Matthew Sibol
Virginia Tech
Seismological Observatory
4044 Derring Hall
Blacksburg, VA 24061-0420

Dr. Albert Smith
Lawrence Livermore National Laboratory
L-205
P. O. Box 808
Livermore, CA 94550

Prof. Robert Smith
Department of Geophysics
University of Utah
1400 East 2nd South
Salt Lake City, UT 84112

Dr. Stewart W. Smith
Geophysics AK-50
University of Washington
Seattle, WA 98195

Donald L. Springer
Lawrence Livermore National Laboratory
L-205
P. O. Box 808
Livermore, CA 94550

Dr. George Sutton
Rondout Associates
P.O. Box 224
Stone Ridge, NY 12484

Prof. L. Sykes
Lamont-Doherty Geological Observatory
of Columbia University
Palisades, NY 10964

Prof. Pradeep Talwani
Department of Geological Sciences
University of South Carolina
Columbia, SC 29208

Dr. David Taylor
ENSCO, Inc.
445 Pineda Court
Melbourne, FL 32940

Dr. Steven R. Taylor
Lawrence Livermore National Laboratory
L-205
P. O. Box 808
Livermore, CA 94550

Professor Ta-Liang Teng
Center for Earth Sciences
University of Southern California
University Park
Los Angeles, CA 90089-0741

Dr. Gregory van der Vink
IRIS, Inc.
1616 North Fort Myer Drive
Suite 1440
Arlington, VA 22209

Professor Daniel Walker
University of Hawaii
Institute of Geophysics
Honolulu, HI 96822

William R. Walter
Seismological Laboratory
University of Nevada
Reno, NV 89557

Dr. Raymond Willeman
Phillips Laboratory - OL-AA/LWH
Hanscom AFB, MA 01731-5000

Dr. Gregory Wojcik
Weidlinger Associates
4410 El Camino Real
Suite 110
Los Altos, CA 94022

Dr. Lorraine Wolf
Phillips Laboratory/LWH
Hanscom AFB, MA 01731-5000

Dr. Gregory B. Young
ENSCO, Inc.
5400 Port Royal Road
Springfield, VA 22151-2388

Dr. Eileen Vergino
Lawrence Livermore National Laboratory
L-205
P. O. Box 808
Livermore, CA 94550

J. J. Zucca
Lawrence Livermore National Laboratory
P. O. Box 808
Livermore, CA 94550

GOVERNMENT

Dr. Ralph Alewine III
DARPA/NMRO
1400 Wilson Boulevard
Arlington, VA 22209-2308

Dr. Dale Glover
DIA/DT-1B
Washington, DC 20301

Mr. James C. Battis
Phillips Laboratory/LWH
Hanscom AFB, MA 01731-5000

Dr. T. Hanks
USGS
Nat'l Earthquake Research Center
345 Middlefield Road
Menlo Park, CA 94025

Harley Benz
U.S. Geological Survey, MS-977
345 Middlefield Rd.
Menlo Park, CA 94025

Dr. Roger Hansen
AFTAC/TT
Patrick AFB, FL 32925

Dr. Robert Blandford
AFTAC/TT
Center for Seismic Studies
1300 North 17th St. Suite 1450
Arlington, VA 22209-2308

Paul Johnson
ESS-4, Mail Stop J979
Los Alamos National Laboratory
Los Alamos, NM 87545

Eric Chael
Division 9241
Sandia Laboratory
Albuquerque, NM 87185

Janet Johnston
Phillips Laboratory/LWH
Hanscom AFB, MA 01731-5000

Dr. John J. Cipar
Phillips Laboratory/LWH
Hanscom AFB, MA 01731-5000

Dr. Katharine Kadinsky-Cade
Phillips Laboratory/LWH
Hanscom AFB, MA 01731-5000

Cecil Davis
Group P-15, Mail Stop D406
P.O. Box 1663
Los Alamos National Laboratory
Los Alamos, NM 87544

Ms. Ann Kerr
IGPP, A-025
Scripps Institute of Oceanography
University of California, San Diego
La Jolla, CA 92093

Mr. Jeff Duncan
Office of Congressman Markey
2133 Rayburn House Bldg.
Washington, DC 20515

Dr. Max Koontz
US Dept of Energy/DP 5
Forrestal Building
1000 Independence Avenue
Washington, DC 20585

Dr. Jack Evernden
USGS - Earthquake Studies
345 Middlefield Road
Menlo Park, CA 94025

Dr. W.H.K. Lee
Office of Earthquakes, Volcanoes,
& Engineering
345 Middlefield Road
Menlo Park, CA 94025

Art Frankel
USGS
922 National Center
Reston, VA 22092

Dr. William Leith
U.S. Geological Survey
Mail Stop 928
Reston, VA 22092

Dr. Richard Lewis
Director, Earthquake Engineering & Geophysics
U.S. Army Corps of Engineers
Box 631
Vicksburg, MS 39180

James F. Lewkowicz
Phillips Laboratory/LWH
Hanscom AFB, MA 01731-5000

Mr. Alfred Lieberman
ACDA/VI-OA State Department Bldg
Room 5726
320 - 21st Street, NW
Washington, DC 20451

Stephen Mangino
Phillips Laboratory/LWH
Hanscom AFB, MA 01731-5000

Dr. Robert Masse
Box 25046, Mail Stop 967
Denver Federal Center
Denver, CO 80225

Art McGarr
U.S. Geological Survey, MS-977
345 Middlefield Road
Menlo Park, CA 94025

Richard Morrow
ACDA/VI, Room 5741
320 21st Street N.W.
Washington, DC 20451

Dr. Carl Newton
Los Alamos National Laboratory
P.O. Box 1663
Mail Stop C335, Group ESS-3
Los Alamos, NM 87545

Dr. Bao Nguyen
AFTAC/TTR
Patrick AFB, FL 32925

Dr. Kenneth H. Olsen
Los Alamos Scientific Laboratory
P. O. Box 1663
Mail Stop D-406
Los Alamos, NM 87545

Mr. Chris Paine
Office of Senator Kennedy
SR 315
United States Senate
Washington, DC 20510

Colonel Jerry J. Perrizo
AFOSR/NP, Building 410
Bolling AFB
Washington, DC 20332-6448

Dr. Frank F. Pilotte
HQ AFTAC/TT
Patrick AFB, FL 32925-6001

Katie Foley
CIA-ACIS/TMC
Room 4X16NHB
Washington, DC 20505

Mr. Jack Rachlin
U.S. Geological Survey
Geology, Rm 3 C136
Mail Stop 928 National Center
Reston, VA 22092

Dr. Robert Reinke
WL/NTESG
Kirtland AFB, NM 87117-6008

Dr. Byron Ristvet
HQ DNA, Nevada Operations Office
Attn: NVCG
P.O. Box 98539
Las Vegas, NV 89193

Dr. George Rothe
HQ AFTAC/TTR
Patrick AFB, FL 32925-6001

Dr. Alan S. Ryall, Jr.
DARPA/NMRO
1400 Wilson Boulevard
Arlington, VA 22209-2308

Dr. Michael Shore
Defense Nuclear Agency/SPSS
6801 Telegraph Road
Alexandria, VA 22310

Mr. Charles L. Taylor
Phillips Laboratory/LWH
Hanscom AFB, MA 01731-5000

Phillips Laboratory
Attn: XO
Hanscom AFB, MA 01731-5000

Dr. Larry Turnbull
CIA-OSWR/NED
Washington, DC 20505

Phillips Laboratory
Attn: LW
Hanscom AFB, MA 01731-5000

Dr. Thomas Weaver
Los Alamos National Laboratory
P.O. Box 1663, Mail Stop C335
Los Alamos, NM 87545

DARPA/PM
1400 Wilson Boulevard
Arlington, VA 22209

Phillips Laboratory
Research Library
ATTN: SULL
Hanscom AFB, MA 01731-5000 (2 copies)

Defense Technical Information Center
Cameron Station
Alexandria, VA 22314 (5 copies)

Phillips Laboratory
ATTN: SUL
Kirtland AFB, NM 87117-6008

Defense Intelligence Agency
Directorate for Scientific & Technical Intelligence
Attn: DT1B
Washington, DC 20340-6158

Secretary of the Air Force
(SAFRD)
Washington, DC 20330

AFTAC/CA
(STINFO)
Patrick AFB, FL 32925-6001

Office of the Secretary Defense
DDR & E
Washington, DC 20330

TACTEC
Battelle Memorial Institute
505 King Avenue
Columbus, OH 43201 (Final Report Only)

HQ DNA
Attn: Technical Library
Washington, DC 20305

DARPA/RMO/RETRIEVAL
1400 Wilson Boulevard
Arlington, VA 22209

DARPA/RMO/Security Office
1400 Wilson Boulevard
Arlington, VA 22209

CONTRACTORS (FOREIGN)

Dr. Ramon Cabre, S.J.
Observatorio San Calixto
Casilla 5939
La Paz, Bolivia

Prof. Hans-Peter Harjes
Institute for Geophysik
Ruhr University/Bochum
P.O. Box 102148
4630 Bochum 1, FRG

Prof. Eystein Husebye
NTNF/NORSAR
P.O. Box 51
N-2007 Kjeller, NORWAY

Prof. Brian L.N. Kennett
Research School of Earth Sciences
Institute of Advanced Studies
G.P.O. Box 4
Canberra 2601, AUSTRALIA

Dr. Bernard Massinon
Societe Radiomana
27 rue Claude Bernard
75005 Paris, FRANCE (2 Copies)

Dr. Pierre Mecheler
Societe Radiomana
27 rue Claude Bernard
75005 Paris, FRANCE

Dr. Svein Mykkeltveit
NTNF/NORSAR
P.O. Box 51
N-2007 Kjeller, NORWAY (3 copies)

FOREIGN (OTHERS)

Dr. Peter Basham
Earth Physics Branch
Geological Survey of Canada
1 Observatory Crescent
Ottawa, Ontario, CANADA K1A 0Y3

Dr. Eduard Berg
Institute of Geophysics
University of Hawaii
Honolulu, HI 96822

Dr. Michel Bouchon
I.R.I.G.M.-B.P. 68
38402 St. Martin D'Heres
Cedex, FRANCE

Dr. Hilmar Bungum
NTNF/NORSAR
P.O. Box 51
N-2007 Kjeller, NORWAY

Dr. Michel Campillo
Observatoire de Grenoble
I.R.I.G.M.-B.P. 53
38041 Grenoble, FRANCE

Dr. Kin Yip Chun
Geophysics Division
Physics Department
University of Toronto
Ontario, CANADA M5S 1A7

Dr. Alan Douglas
Ministry of Defense
Blacknest, Brimpton
Reading RG7-4RS, UNITED KINGDOM

Dr. Manfred Henger
Federal Institute for Geosciences & Nat'l Res.
Postfach 510153
D-3000 Hanover 51, FRG

Ms. Eva Johannisson
Senior Research Officer
National Defense Research Inst.
P.O. Box 27322
S-102 54 Stockholm, SWEDEN

Dr. Fekadu Kebede
Geophysical Observatory, Science Faculty
Addis Ababa University
P. O. Box 1176
Addis Ababa, ETHIOPIA

Dr. Tormod Kvaerna
NTNF/NORSAR
P.O. Box 51
N-2007 Kjeller, NORWAY

Dr. Peter Marshall
Procurement Executive
Ministry of Defense
Blacknest, Brimpton
Reading FG7-4RS, UNITED KINGDOM

Prof. Ari Ben-Menahem
Department of Applied Mathematics
Weizman Institute of Science
Rehovot, ISRAEL 951729

Dr. Robert North
Geophysics Division
Geological Survey of Canada
1 Observatory Crescent
Ottawa, Ontario, CANADA K1A 0Y3

Dr. Frode Ringdal
NTNF/NORSAR
P.O. Box 51
N-2007 Kjeller, NORWAY

Dr. Jorg Schlittenhardt
Federal Institute for Geosciences & Nat'l Res.
Postfach 510153
D-3000 Hannover 51, FEDERAL REPUBLIC OF
GERMANY

Universita Degli Studi Di Trieste
Facolta Di Ingegneria
Istituto Di Miniere E. Geofisica Applicata, Trieste,
ITALY

Dr. John Woodhouse
Oxford University
Dept of Earth Sciences
Parks Road
Oxford OX13PR, ENGLAND